POROUS AND PHASE CHANGE NANOMATERIALS FOR PHOTONIC APPLICATIONS

By

Judson D. Ryckman

Dissertation

Submitted to the Faculty of the

Graduate School of Vanderbilt University

in partial fulfillment of the requirements

for the degree of

DOCTOR OF PHILOSOPHY

in

Electrical Engineering

May, 2013

Nashville, TN

Approved:

Professor Sharon M. Weiss

Professor Richard F. Haglund, Jr.

Professor Dan Fleetwood

Professor Ron Schrimpf

Professor Yaqiong Xu

Copyright © 2013 by Judson D. Ryckman
All Rights Reserved

To Nana and Grandad, Mom and Dad,

for everything.

ACKNOWLEDGMENTS

First and foremost, I wish to thank my PhD advisor and mentor Sharon Weiss. Her support, guidance, and expertise have led me to become not only a stronger researcher and engineer, but a better writer, communicator, and teacher. Since joining her research group as an undergraduate in the summer of 2007, I have had the opportunity to hone both my experimental and theoretical skills while tackling a variety of interesting projects. Along the way, my curiosity and ideas were consistently met with openness and encouragement. From generously supporting group activities, to always having an open door and being there to discuss my research progress (or lack thereof), Sharon has always been a truly great advisor – one for whom I am very thankful.

I also wish to thank the various researchers and collaborators I have had the opportunity to work with, both at Vanderbilt and abroad. Sincere thanks to Richard Haglund for sharing his wealth of knowledge on VO_2 and for playing a vital role in the success of our Si-VO_2 project. Further thanks to Joyeeta Nag for stirring up the conversations and ideas which ultimately lead to the beginning of our Si-VO_2 endeavors and for what became a very enjoyable collaboration. Thanks also to Bob Marvel, Victor Blanco, Kent Hallman, and Sergey Avanesyan, without whom continued progress on the Si-VO_2 project would not have been possible.

Many thanks to John Sipe (U. Toronto) and Marco Liscidini (U. Pavia) for widening my perspective not only beyond the halls of Vanderbilt (and the U.S.A.), but from the world of experiment to the world of theory, and from engineering to its roots in physics. Without their many great ideas, Skype calls, and discussions, neither the DIPS project nor the pSi-DBB would have become a reality.

Special thanks to all the Weiss group members, both past and present. Your continuous help, feedback, discussions, and friendship, have helped make my time as a graduate student both productive and fun. Special thanks to Guoguang Rong for guiding me my first few semesters as beginning researcher, and to Chris Kang for showing me the ropes on everything ranging from fabrication at CNMS, to FDTD simulations, and the best places to

eat on those many trips Oak Ridge.

Special thanks are owed to the facilities and staff where my work was made possible. This includes VINSE and Tony Hmelo, Bo Choi, Bob Geil, Ben Schmidt, and Dmitry Koktysh. At CNMS my thanks go to Laura Edwards, Scott Retterer, Ivan Kravchenko, Dale Hensley, Dayrl Briggs, and Darrell Thomas. Thank you all for instilling the importance of rules and safety, and for always being there, ready to teach, support, or debug. I am also especially thankful for the staff in Featheringill and Electrical Engineering, including Flo Wahidi, Lewis Saettel, Teresa Benedetti, and Linda Koger.

Financial support for my graduate studies was provided in part by a National Science Foundation Graduate Research Fellowship. These research activities were supported by grants from the Army Research Office and Air Force Office of Scientific Research. Work performed at CNMS was sponsored at Oak Ridge National Laboratory by the Scientific User Facilities Division, Office of Basic Energy Sciences, U.S. Department of Energy; while work performed at VINSE was supported in part through renovations funded by the National Science Foundation.

Finally, I wish to thank my family for their never ending love, support, and encouragement. Thank you for always nurturing and being supportive of my interests, both inside and outside the classroom. To my Mom, thanks for teaching me to always chase what I am passionate about and for rubbing off some of your skills as a writer. To my Dad, thanks for teaching me to always act with integrity and for rubbing off some of your skills as an engineer. To my Nana and Grandad, thank you for teaching me to value my studies and for setting such great examples. To my wife, thank you for sharing this life and keeping me balanced.

TABLE OF CONTENTS

Page

DEDICATION ii

ACKNOWLEDGMENTS iii

LIST OF FIGURES ix

Chapter

1. INTRODUCTION 1

1.1 Porous Nanomaterials 1
1.1.1 Characteristics and Production 1
1.1.2 Photonic Properties and Applications 3
1.2 Phase Change Nanomaterials 11
1.2.1 Characteristics and Production 11
1.2.2 Photonic Properties and Applications 16
1.3 Optical Resonators and Light-Matter Interactions 21

2. DIRECT IMPRINTING OF POROUS SUBSTRATES (DIPS) 26

2.1 Introduction. 26
2.2 Experimental Demonstrations and Capabilities of DIPS 28
2.2.1 Preparation of porous nanomaterials 28
2.2.2 Stamp preparation and imprinting 28
2.2.3 DIPS Fabricated Structures 29
2.2.4 Free Standing Microparticle Fabrication and Overstamping 39
2.3 Stamp Reusability 41
2.4 Application: Diffraction-Based Biosensing 45
2.4.1 Principles of Diffraction-Based Biosensing (DBB) 45
2.4.2 pSi-DBB Experiments 47
2.4.3 Real-time Sensing and Fluidic Considerations 51
2.4.4 Conclusion 57
2.5 Summary 58

3. GRAY-SCALE DIPS 59

3.1 Introduction. 59
3.1.1 Introduction to Three-Dimensional Surface Patterning 59
3.2 Experimental Methods. 61
3.2.1 Porous substrate preparation 61

3.2.2 Stamps and imprinting 62
3.2.3 Surface Enhanced Raman Spectroscopy Mapping 63
3.3 Experimental Results 63
3.3.1 Gradient Profiles and Morphologies 65
3.3.2 Morphological Control Over Dielectric Constant and Plasmonic Response 68
3.3.3 Digital Patterns 72
3.3.4 Curvilinear Elements and Lens Shapes 73
3.3.5 Fabrication of Nano-Grooves and Nano-Pits 75
3.3.6 Fabrication of Well Defined Cookie-Cutter Microparticles 76
3.4 Summary 77

4. ULTRA-COMPACT, HYBRID Si-VO_2 PLATFORM. 78

4.1 Motivation 78
4.2 Device Fabrication 80
4.3 Experiment and Analysis 82
4.3.1 Measurement Set-Up and Passive Spectral Measurements 82
4.3.2 Photothermally Induced Optical Modulation 83
4.3.3 Influence of Ring-Size and VO_2 Fractional Coverage 89
4.4 Si-VO_2 Mach-Zehnder Interferometer 94
4.4.1 Concept and Simulation 94
4.4.2 Photothermal Experiments 96
4.5 Discussion 101
4.6 Summary 102

5. OPTICALLY INDUCED, NANOSECOND RECONFIGURATION OF HYBRID Si-VO_2 DEVICES 104

5.1 Introduction. 104
5.2 Si-VO_2 Absorbers and Resonators 107
5.3 Experimental Methods. 108
5.3.1 Device Fabrication 108
5.3.2 All-Optical Pump-Probe Experiments 109
5.4 Pump-Probe Experiments 110
5.4.1 Si-VO_2 Absorbers 110
5.4.2 Si-VO_2 Ring Resonators 111
5.4.3 Relaxation Time and Dependence on VO_2 Patch Length 112
5.5 Si-VO_2 Spectral Reconfiguration 114
5.5.1 Multi-Wavelength Pump-Probe Characterization 114
5.5.2 Analysis 117
5.6 Discussion 119
5.7 Summary 120

6. DESIGNING FOR ENHANCED LIGHT-MATTER INTERACTION 122

6.1 Introduction. 123
6.2 Theoretical Background 124
6.2.1 Bands and Field Properties 124
6.2.2 Field Enhancements and Power Confinement 129
6.3 Experimental Demonstration 133
6.3.1 3D Design and Calculations 134
6.3.2 Fabrication, SEM, and Simulation 136
6.3.3 Measurement and Analysis 138
6.4 Ultra-High Q and Q/V 140
6.4.1 Introduction 140
6.4.2 Deterministic Design 142
6.4.3 Simulation Results 145
6.5 Summary 147

7. CONCLUSION 150

7.1 Summary 150
7.2 Future Work 156
7.2.1 DIPS for Sensing and Drug Delivery 156
7.2.2 Hybrid Si-VO_2 Photonics 159
7.2.3 Slotted PhC Nanobeam Applications 162

Appendix

A. DIPS PROTOCOLS, ADDITIONAL FIGURES, AND RESULTS 166

A.1 Stamp Preparation and Imprinting 166
A.1.1 Cutting Out Stamps and Mounting on Tape 166
A.1.2 Configuring the Tinius Olsen Super L 60K 168
A.1.3 Sample Positioning and Imprinting 170
A.2 Additional Figures 172
A.2.1 Large Area and Repeated Imprinting 172
A.2.2 Cookie-Cutter npAu Nanoparticles 173
A.2.3 Negative Results and Other Effects 174
A.3 Gray-Scale Electron Beam Lithography 179
A.3.1 Process Overview 179
A.3.2 dose64_jdi_ARB.m 181
A.3.3 Example Dose and Resist Profiles 182

B. ADDITIONAL Si-VO_2 MEASUREMENT NOTES AND FIGURES 184

B.1 Optical Measurement Set-Ups 184
B.1.1 Photothermal Pump-Probe Measurements 184

B.1.2 Nanosecond Pump-Probe Measurements 185

BIBLIOGRAPHY. 188

LIST OF FIGURES

1.1 Top view scanning electron microscope (SEM) images of various porous nanomaterials with unique morphologies, including: (a) npAu, (b) mesoporous silicon, (c) macroporous silicon, and (d) TiO_2-NTAs. 4
1.2 Effective Medium Approximation 5
1.3 Example pSi planar optical structures and corresponding reflectance spectra, including (a) single and (b) double layer films, (c) multilayer, and (d) microcavity. 6
1.4 Photonic characteristics and applications for selected porous nanomaterials, including (a) pAl_2O_3 SPR sensing, (b) pAl_2O_3 SERS templates, and (c) LSPR and (d) SPR resonances excited in npAu thin films. 8
1.5 Examples of patterned porous nanomaterial structures among three categories: (a-c) macro- to micro-scale, (d-f) microscale, (g-i) sub-micron and nanoscale. 10
1.6 (a) Ternary phase diagram showing a variety of chalcogen based PCNMs and related technological milestones. (b) Current-voltage trace showing typical switching behavior for a PCNM changing from an amorphous to crystalline state. 12
1.7 Threshold phase transition temperature for a variety of selected transition metal oxides. 14
1.8 VO_2 thin film hysteresis in (a) electrical resistivity and (b) optical reflectivity ($\lambda = 2\ \mu$m). 15
1.9 The structural phase transition (SPT) in VO_2. Coinciding with the SMT, a SPT occurs wherein the crystal structure is shifted from a monoclinic to rutile phase. 15
1.10 Real and imaginary parts of the refractive index $n_{VO_2} = n + ik$ for VO_2 in both the semiconducting and metallic states. 17
1.11 Some photonic applications of VO_2 selected from existing literature. 19
1.12 Q-factor vs. mode volume for a variety of selected optical cavity types including plasmonic, whispering gallery, micro-ring (used in Chapter 4), nanobeam (1D photonic crystal), and slotted nanobeam (introduced in Chapter 6). Solid points indicate experimentally measured devices and hollow points indicate calculated values. 23
1.13 SEM images of selected example optical cavities including both 1D (nanobeam) and 2D PhCs (scale bars 5 μm) and a micro-ring resonator (scale bar 10 μm). 24

2.1 Illustration of the DIPS process 27
2.2 Characterization of vertical featuring of DIPS on pSi. 30
2.3 AFM characterization of imprint depth with applied pressure. 31
2.4 Top view scanning electron microscope (SEM) images of porous nanomaterials patterned with DIPS. 34
2.5 SEM images of imprinted structures on porous TiO_2-NTAs and disordered pAl_2O_3 36

2.6 SEM images of curved features patterned by DIPS in (a,b) pSi and (c) npAu 36
2.7 Demonstration of selected device structures fabricated by DIPS. 38
2.8 SEM images depicting the overstamping regime on pSi 40
2.9 SEM images of various freestanding pSi microparticles removed either electrostatically with the stamp or by carbon tape 42
2.10 SEM images of stamps and imprinted structures after 1, 4, and 20 imprinting cycles. 43
2.11 Additional SEM and AFM images highlighting the durability of the stamp and fidelity of the imprinted pattern after 20 imprinting cycles. 44
2.12 SEM images of a Si stamp revealing the adsorption of porous debris from the porous substrate that was imprinted 44
2.13 SEM images of recent DIPS enabled device applications 45
2.14 Schematic of the pSi-DBB, AFM height image, visual response, and 3-APTES sensing. 48
2.15 Comparison between possible pSi-DBB configurations for sensing in solution. 53
2.16 Real-time pSi-DBB experimental configuration and sensing of various liquid analytes 55
2.17 Real-time sensing of sulfo-SMCC attachment to a pSi-DBB 56

3.1 Illustration of the gray-scale DIPS process 64
3.2 Patterning height, pore opening size, porosity and refractive index of pSi. . 66
3.3 Calculated variation in visible reflectance for pSi thin films as a function of imprint depth. 68
3.4 Tuning dielectric constant and plasmonic SERS enhancement of npAu. . . . 70
3.5 3D patterning of discrete, curved, and sharp features. 73
3.6 AFM height mappings of 3D patterned pSi and npAu, corresponding to the line scan profile data shown in Figure 3.5.k-m 74

4.1 Illustration of the gray-scale DIPS process 82
4.2 Schematic of the optical measurement set-up and passive spectral measurements. 84
4.3 Optical transmission of the 1.5 μm radius hybrid Si-VO_2 ring resonator as a function of wavelength, before and after triggering the SMT with a 532 nm pump laser. 87
4.4 Optical transmission of a 1.5 μm radius Si-only control ring resonator as a function of wavelength, before and after turning the 532 nm pump laser on pump laser. The lines are Lorentzian fits. 87
4.5 Optical transmission as a function of time at $\lambda = 1568.78$ nm, in the 1.5 μm radius hybrid Si-VO_2 device, when turning the 532 nm pump laser (a) ON and (b) OFF. 88
4.6 Resonance shifts and Q-factors for hybrid Si-VO_2 micro-ring resonators where the SMT is triggered photothermally 92

4.7 (a) Normalized transmission simulation of a Si-VO_2 hybrid MZI as a function of VO_2 coating refractive index at 1550 nm; (b) and (c) Electric field profiles, at 1550 nm, for the MZI in the 'ON' state ($n_{VO2} \sim 3.2$) and the 'OFF' state ($n_{VO2} \sim 1.8$) respectively. 95
4.8 (a) SEM image of an unbalanced Si based MZI, (b) Transmission spectra for MZIs with various arm length differences (vertically offset for clarity), (c) Fourier transformed transmission spectra with peaks corresponding to the optical path length nL, and (d) group index, n_g, determined from nL values obtained from the Fourier transforms. 97
4.9 (a) SEM image of an unbalanced Si-VO2 hybrid MZI, (b) Transmission spectra and model fits for VO_2 in the semiconducting (laser off) and metallic (laser on) states. 99
4.10 Modeling the effect of increased patch length and losses in a 100 μm unbalanced MZI with idealized 50:50 couplers and that the SMT induces both an absorption modulation, ~ 4 dB μm^{-1}, and effective index modulation, $\Delta n_{SMT} \approx -0.07$. 101

5.1 Overview of the Si-VO_2 hybrid photonic devices and all optical experimental setup 108
5.2 Normalized probe transmission through Si-VO_2 absorbers with (a) 1 μm and (b) $\sim$500 nm VO_2 patch lengths 111
5.3 (a) Typical resonance in the transmission spectra for a Si-VO_2 micro-ring resonator with radius $R = 1.5$ μm, and (b) Corresponding probe transmission where the probe wavelength is tuned to on-resonance ($\lambda = 1588.5$ nm). 112
5.4 Summary of pump-probe dynamics: pump dependence and relaxation times 113
5.5 Spectral reconfiguration of an ultra-compact Si-VO_2 micro-ring resonator . 116
5.6 Analysis of Si-VO_2 micro-ring resonator reconfiguration 118

6.1 Band structure and field plots of a pinch waveguide with $r = 0.42a$, $w = 1.2a$, and slot width $ws = 0.12a$ 126
6.2 Example electric field (instantaneous) and power distributions (time-averaged) for three waveguide structures. The pinch waveguide combines principles from both slot and periodic geometries to obtain extreme sub-wavelength confinement in a guided mode. Note that each field image is normalized to its own linear color scale (dark red + to dark blue -). 129
6.3 Analysis of $|E|^2$ enhancements provided by the pinch waveguide structure and comparison to traditional slot waveguides. 132
6.4 (a) Dispersion relation for the slotted PhC pinch waveguide, shown in the inset, with $w = 1.091a$, $r = 0.335a$, $ws = 0.093a$, and waveguide thickness $h = 0.379a$. (b) Field and power distributions for a single unit cell of the pinch waveguide structure calculated at the dielectric band edge. 135

6.5 (a) SEM images of a slotted photonic crystal single nanobeam cavity, showing the 52 nm slot width, air-clad waveguide coupled geometry, and input/output grating couplers. (b) Field and power distributions for the fundamental mode of the slotted photonic crystal single nanobeam cavity with Q-factor $\sim 3.5 \times 10^4$ and mode volume $\sim 0.01(\lambda/n)^3$. The plotted distributions are for a 2D slice through the center of the cavity, taken from 3D FDTD simulation. 137
6.6 (a) Transmission spectra for the slotted photonic crystal single nanobeam cavity, revealing the cavity resonance at 1513.9 nm and dielectric band edge at ~1548 nm. Inset reveals IR camera images (aligned to top SEM image) spanning the cavity and output grating coupler for different wavelengths of interest: on-resonance, in the PBG, and in the dielectric band. (b) Radiation spectra for the same device in (a), with the inset revealing a close up of the resonance at 1513.9 nm with a Lorenztian fit indicating an experimentally measured Q-factor, $Q_{meas} \approx 7.42 \times 10^3$. 141
6.7 Overview of the deterministic design approach. (a) Band structure for ellipsoidal pinch waveguides of varying ellipsoid parameters, i.e. $rb = 2a$ (blue) and $rb = 1.75a$ (red). (b) The cavity is formed by symmetrically tapering out from the cavity center, with a taper of length N, to the Bragg reflectors. (c) Mirror strength, γ, as a function of rb. 144
6.8 (a) Linear variation of mirror strength for selected taper lengths, N, and (b) the corresponding mapped variation of rb. (c) Electric field distribution, taken from 3D FDTD simulation, for a cavity with $N = 10$ and a high $Q = 5.7 \times 10^5$ and low $V = 0.028(\lambda/n)^3$. 146
6.9 Fourier transform of the electric field distributions for the original (Sec. 6.3.2) and deterministically designed slotted nanobeam cavities. 146
6.10 Simulated variation in (a) Q-factor, (b) mode volume, (c) resonant frequency, and (d) Q/V, for deterministically designed slotted nanobeam cavities of varying taper length, N. 148

A.1 Recommended tools for cleaving the stamps and mounting them on tape. . . 167
A.2 Image of various stamp patterns on a source wafer and a stamp after being cut out and properly mounted on scotch tape. 168
A.3 Configuring the Tinius Olsen with the proper metal adapter and metal base plates. 169
A.4 Images of the Tinius Olsen control panels 170
A.5 Images illustrating the DIPS process being performed on npAu with the Tinius Olsen testing machine, highlighting four key steps to consider before and after imprinting, including (a) positioning, (b) alignment, (c) peeling or removal of the stamp, and (d) inspection of the patterned porous substrate. 172
A.6 Photos of DIPS patterned npAu films after imprinting with the same stamp repeatedly. The uniformity of the imprints are readily visible by the naked eye. 173
A.7 SEM images of preliminary work relating to the fabrication of npAu nanoparticles through DIPS with a cookie-cutter approach. 174

A.8 (a) Optical microscope and (b-f) SEM images illustrating examples of negative results observed during the initial development and testing of DIPS. . 175
A.9 Example of unexpected "skewing" of an imprinted pattern. In this example, the circular patterns appear distorted or biased toward a common direction. 177
A.10 SEM images of other anomalous results obtained after performing DIPS. (a, b) Extreme skewing from a simple 2D grating patterned stamp produced bow-tie like structures in npAu with some structures exhibiting very small nanogaps ($<$ 10 nm). (c, d) Double imprinting observed in pSi and npAu patterns. 178
A.11 Example of unexpected "skewing" of an imprinted pattern. In this example, the circular patterns appear distorted or biased toward a common direction. 180
A.12 (a) Relative dose profiles mapped into the *.jdi* file, and corresponding resist profiles measured in (b) PMMA 950k, A4 and (c) PMMA 50k, A20 following exposure and development.. 183

B.1 Photograph of the measurement setup used to characterize hybrid Si/VO_2 devices under photothermal excitation. 185
B.2 Close up view of the beamsplitter, polarizer, tube system, and IR camera. . 186
B.3 Photograph of the measurement setup used to characterize hybrid Si/VO_2 devices under nanosecond pulsed optical pumping. 187
B.4 Example outcomes of using too high a pump fluence ($\sim$J cm^{-2}) with a 20x objective. 189

CHAPTER 1

INTRODUCTION

Advancing state-of-the art photonics, from communication systems, to sensing, solar energy harvesting, and beyond, requires drawing from a wide variety of disciplines and implementing new designs, material systems, and fabrication strategies. In this chapter, two important classes of nanomaterials are introduced, (1) porous nanomaterials and (2) phase change nanomaterials. This chapter further highlights the unique photonic properties of these nanomaterials and identifies some of the core challenges and opportunities associated with integrating them into a variety of emerging photonic applications. Finally, we introduce optical resonators and describe fundamental photonic concepts and design considerations that may be used to enhance light-matter interactions.

1.1 Porous Nanomaterials

1.1.1 Characteristics and Production

Porous nanomaterials such as porous silicon (pSi), porous alumina (pAl_2O_3), nanoporous gold (npAu), and titanium dioxide nanotube arrays (TiO_2-NTAs) are characterized by nanoscale voids and high specific surface area that give rise to their unique optical, electrical, chemical, and mechanical properties. The formation of such porous nanomaterials is self-organizing and elaborate fabrication techniques are not required [1–5]. This results in a class of nanomaterials that is cost-effective to produce and exhibits highly desirable

physical and chemical attributes over very large areas ($\sim$cm^2).

The self-organizing formation of porous nanomaterials can often be achieved by electrochemical methods. pSi for example, can be etched directly into a silicon wafer by utilizing a hydrofluoric acid (HF) electrolyte with an applied current density. For low potentials, a silicon dissolution reaction is initiated:

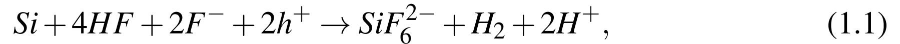

$$Si + 4HF + 2F^{-} + 2h^{+} \rightarrow SiF_6^{2-} + H_2 + 2H^{+}, \tag{1.1}$$

which leads to pore formation [6]. This process relies strongly on the availability of holes (h$^+$) to continue the reaction, which occurs primarily at surface irregularities, such as pore tips, where the electric field is most highly concentrated. As a result, pore formation proceeds preferentially into the silicon wafer along specific crystalline directions. By controlling parameters ranging from the substrate doping level, to the electrolyte concentration, wafer orientation, and applied current density, an incredible variety of porous morphologies can be produced. Indeed, with this approach, pore sizes ranging from less than 2 nm to greater than 100 nm can be achieved. For example, adjusting the current density is often used to control the pore dimensions and the porosity of a given layer. In this manner, simple modulation of the current density can be used to produce complex multilayers with unique properties.

Similar tunability and control over the desired porous morphology can be achieved with porous nanomaterials other than pSi, which rely on different electrolyte chemistries and formation mechanisms [1–3]. pAl_2O_3 for example, can be produced with interpore distances ranging from 50-420 nm by simply changing between oxalic, sulfuric, or phos-

phoric acid electrolytes of various concentrations [1]. npAu meanwhile, is readily produced by dissolving out the silver from a gold-silver alloy with nitric acid through the dissolution reaction:

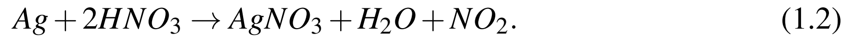

$$Ag + 2HNO_3 \rightarrow AgNO_3 + H_2O + NO_2. \tag{1.2}$$

Combined with the diffusion and clustering of Au adatoms, this process produces a spongelike bicontinuous structure of empty pores and Au ligaments. Adjusting the dealloying time can then be used to control the remaining pore and gold ligament sizes [2].

Fig. 1.1 illustrates a variety of porous nanomaterials ranging from metals, to semiconductors, and insulators with unique morphologies and a wide variety of pore dimensions. It should be noted that these porous nanomaterials are typically grown or etched as thin films, and can have thicknesses ranging from tens of nanometers to tens of microns or more.

Owing to their intricate internal morphology and nanoscale pores, porous nanomaterials commonly contain large surface areas, on the order of $\sim m^2/g$. This property is particularly useful in applications such as sensing, catalysts, or battery anodes, where chemical reactions or chemical binding is mediated at the surface. The enhanced surface area, provided by the nanoscale pores, can provide a means for enhancing analyte capture, sensor sensitivity, reaction kinetics, or chemical loading.

1.1.2 Photonic Properties and Applications

Porous nanomaterials offer a number of unique characteristics that make them particularly well suited for constructing advanced optical structures with potential applications in fields such as biosensing, drug delivery and imaging, and solar energy harvesting. Because the

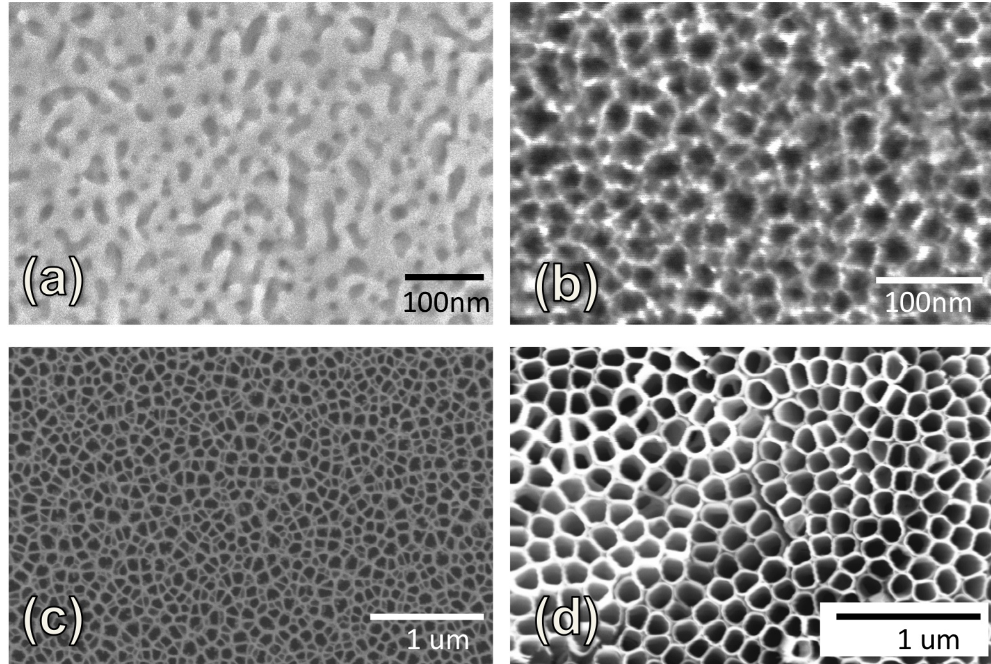

Figure 1.1: Top view scanning electron microscope (SEM) images of various porous nanomaterials with unique morphologies, including: (a) npAu, (b) mesoporous silicon, (c) macroporous silicon, and (d) TiO_2-NTAs.

pore dimension is often much smaller than the wavelength of light (i.e., d $<< \lambda$), incident electromagnetic radiation can no longer distinguish between the two or more materials which make up the composite structure. In such a case, the optical properties of a porous medium can be described by an effective medium approximation [7, 8]. Adjusting the material composition or porosity will thereby affect important optical properties, such as the refractive index or absorption coefficient. For example, given $n_{Si} = 3.5$ and $n_{air} = 1$ (near $\lambda = 1550$ nm), modulating the porosity of a pSi film from 0% - 100% (pure Si to pure air) enables a continuum of refractive indices, $n = 3.5 - 1.0$, to be realized. Note that porosity is defined volumetrically as the percentage of void space per unit volume, and in practice, the achievable porosity range will limit the maximum and minimum refractive indices that can be experimentally achieved. Alternatively, infiltration of chemicals or biomolecules

into the pores will also affect the optical properties of the porous medium. The large surface area and nanoscaled porous openings importantly allows a large number of analyte species to be immobilized inside the pores while simultaneously filtering out larger contaminants. With the proper design, porous structures can then be used as refractive index sensors capable of high-sensitivity and label-free detection of various analytes, including biomolecules [9–11].

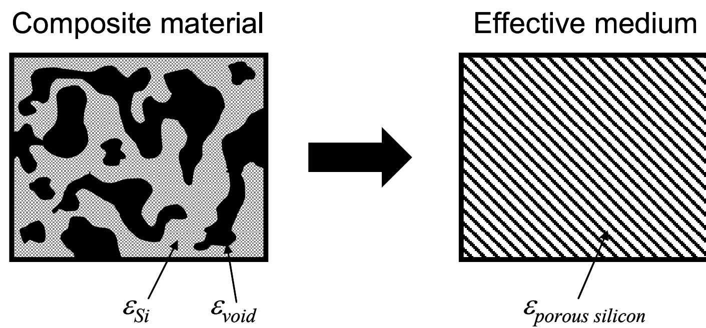

Figure 1.2: Example effective medium approach for porous silicon (adapted from [8]).

Planar Optical Structures

A wide variety of planar, thin-film optical structures, with advantageous characteristics, can be realized with porous nanomaterials. In pSi for example, by etching single or multiple layers with controlled current densities and times, thin-film optical structures can be produced with well controlled refractive indices and film thicknesses, respectively. A collection of example structures and their reflectance profiles are shown in Figure 1.3. For single layer films, reflectance spectra exhibit Fabry-Pérot interference fringes with periodic minima or maxima ordered by $m\lambda = 2nL$, where m is an integer, n is the refractive index, and L is the layer thickness. This effect arises from the interference of the light

reflected from the top and bottom interfaces of the thin-film. Because the fringe spacing is directly related to the optical thickness, nL, reflectance measurements can be used to track changes in a film's refractive index, n, (assuming L is unchanged) thus forming the basis for a refractive index sensor.

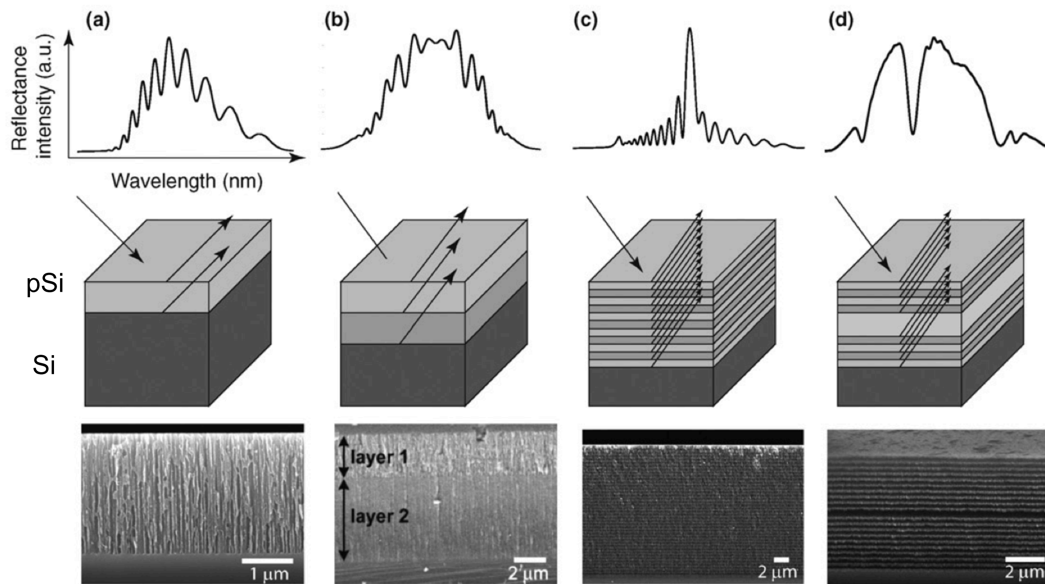

Figure 1.3: Example pSi planar optical structures and corresponding reflectance spectra, including (a) single and (b) double layer films, (c) multilayer, and (d) microcavity. (Figure adapted from [9]).

Alternatively, more complex optical structures can be developed by stacking two or more layers of pSi with differing refractive indices. Double layer films can be used to construct optical waveguides, where the bottom layer provides a lower refractive index necessary for total internal reflection, or double layer interferometers which exhibit reflectance spectra appearing as the superposition of two single layer films (Fig. 1.3.b). Multilayer films can also be constructed into 1D photonic crystals, or Bragg reflectors, (Fig. 1.3.c) that selectively reflect nearly 100% of light incident within the photonic band gap, which at normal incidence is centered at the design wavelength $\lambda = 4n_{hi}L_{hi} = 4n_{lo}L_{lo}$. This sort

of multilayer structure provides a distinct optical signature that may be distinguishable by eye, or easily discriminated when used as a filter with one or more lasers. As a sensor, this structure would be most sensitive to analyte species infiltrating deep throughout the porous network. The Bragg structure also provides a platform for exciting Bloch surface waves (BSW), a sort of optical mode in which light is confined to the multilayer-air interface. BSWs enable sensors to be constructed with particularly high sensitivity toward analytes located at or near the surface. Microcavity structures can also be constructed, wherein a defect layer introduces a resonance in the reflectance spectra. On resonance, light is locally confined within the defect region located between the top and bottom Bragg reflectors. In principle, this structure could be used to enhance light emission for lasers or LEDs, act as a narrow band optical filter, or operate as a refractive index sensor capable of detecting target analytes once immobilized within the defect region.

As shown in Figure 1.4, other porous nanomaterials such as pAl_2O_3 and npAu exhibit a variety of unique characteristics attractive for planar-type photonic applications. For example, pAl_2O_3 has been integrated onto planar metallic films to enhance the surface area and sensitivity of surface plasmon resonance (SPR) biosensors (Fig. 1.4.a) [12]. pAl_2O_3 thin films decorated with clusters of Au nanoparticles have also been used as surface enhanced Raman scattering (SERS) substrates capable of detecting TNT molecules down to the parts per trillion (ppt) level (Fig. 1.4.b) [13]. In these applications, the 3D porous matrix, provides the advantage of an increased surface area, thus immobilizing a larger number of target molecules or nanoparticle clusters than is achievable with a nonporous planar film. Moreover, the high transparency and additional waveguiding effects present in the pAl_2O_3 film are attributes that promote enhanced SERS intensity.

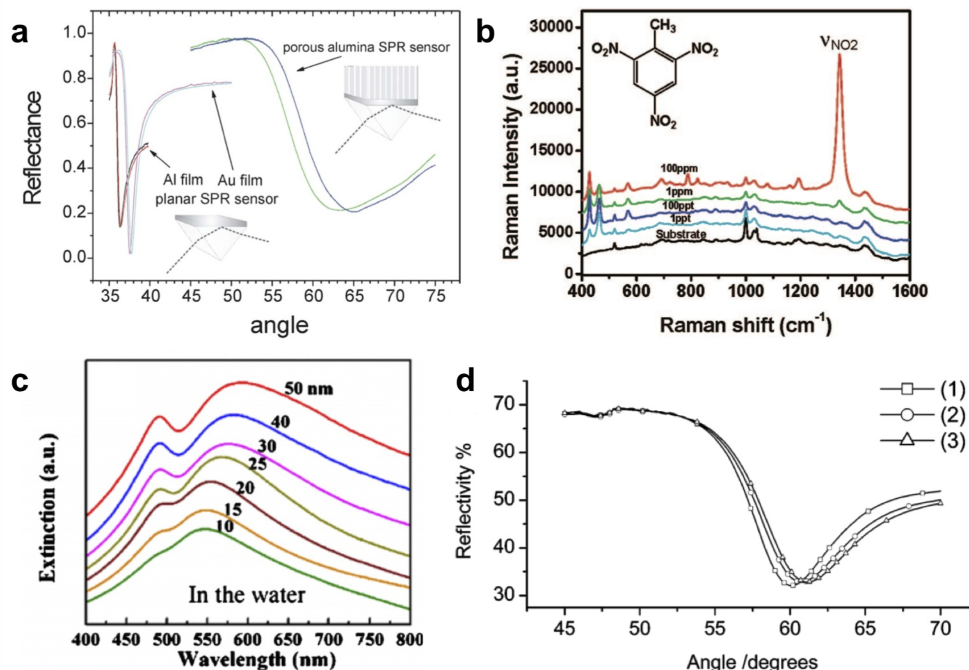

Figure 1.4: Photonic characteristics and applications for selected porous nanomaterials, including (a) pAl_2O_3 SPR sensing [12], (b) pAl_2O_3 SERS templates [13], and (c) LSPR [14] and (d) SPR resonances [15] excited in npAu thin films.

As a porous nanomaterial constructed entirely from the noble metal Au, which is commonly used in plasmonic devices, as-prepared npAu films are capable of supporting both localized surface plasmon resonances (LSPR, Fig. 1.4.c) [14] and SPR effects (Fig. 1.4.d) [15]. Notably, the LSPR effect arises specifically due to the nanoscaled morphology of npAu and is not present in planar Au films. On or near resonance, light is strongly confined within the pores, at the surface of the nanosized gold ligaments. Changing the pore size, or more specifically the pore to ligament size ratio, can be used to tune the LSPR resonance peak position in the range 550-600 nm. LSPR can be used to perform refractive index sensing or to enhance the local electromagnetic field intensity and contribute to enhancing signal intensity in SERS substrates. SPR excited on npAu films provides another route toward refractive index based sensing, and has been demonstrated for the detection

of various biomolecules, including sub-μM streptavidin and biotinylated IgG as shown in Fig. 1.4.d [15].

Patterning Porous Nanomaterials

A primary challenge in implementing porous materials for a variety of applications, including drug delivery and imaging [16–18], chemical and biological sensing [11, 19–21], catalysis [22–24], biomaterials [25, 26], battery anodes [27], plasmonics [28], integrated optoelectronics [29, 30], and solar energy conversion [31–33], is performing micro- and nanometer scale structuring. The structures and patterns that are required for these applications generally fall into one or more of the following three categories: (i) macro- to micro-scale structures and arrays (e.g. large area, multiplexed or replicated structures and sensors), (ii) microscale structures (e.g. microparticles, pixels, or gratings), and (iii) sub-micron to nanoscale elements (e.g. subwavelength optical components and nanoparticles). A variety of example structures, selected from literature, are displayed in Figure 1.5.

While many of these structures can be realized through the application of traditional lithography strategies (e.g. electron-beam lithography (EBL) and photolithography, followed or proceeded by etching), such techniques are expensive and limited by a trade-off between resolution and throughput. Many alternative patterning techniques exist, such as ion irradiation, UV ablation or photo-oxidation, but are not suitable for large scale use outside of a laboratory environment [35, 37]. The development of nanoimprint lithography (NIL) and soft lithography strategies has enabled high throughput fabrication of nano- to microscale features in planar media [40–43]. However, there remain several key challenges associated with applying any of the currently available fabrication techniques to

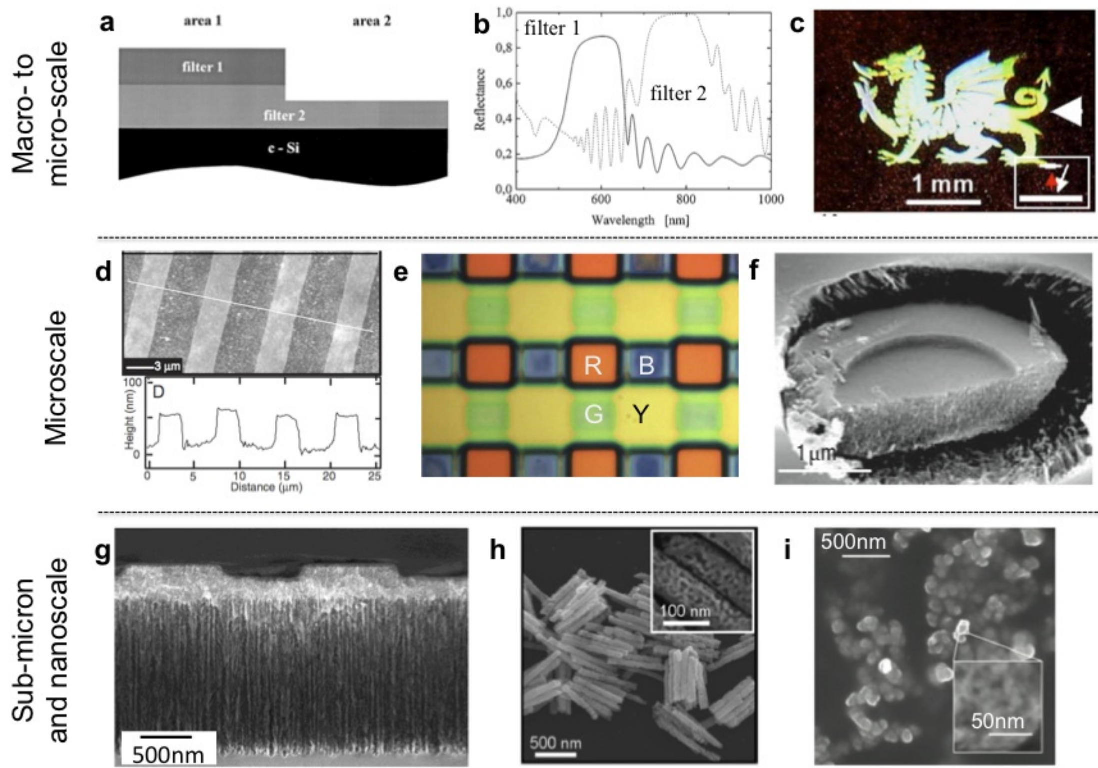

Figure 1.5: Examples of patterned porous nanomaterial structures among three categories: (a-c) macro- to micro-scale, (d-f) microscale, (g-i) sub-micron and nanoscale. Patterned pSi Bragg filters realized through (a, b) photolithography / RIE [34], and (c) ion irradiation [35]. (d) Microscale pSi diffraction grating patterned by dry removal soft lithography [36], (e) pSi distributed Bragg reflector (DBR) RGBY pixels [37], (f) pSi drug delivery / imaging microparticle [16]. (g) Grating coupled pSi waveguide [38], (h) npAu plasmonic nanorods [39], (i) pSi drug delivery / imaging nanoparticles [17].

porous nanomaterials. First, resists and thermoplastics are likely to infiltrate the pores, potentially modifying the internal porous structure and often proving very difficult to remove, especially in deep porous networks. Second, for porous materials, wet etching is not always an option due to chemical incompatibilities, and dry-etching techniques are expensive and require specific chemistries that must be appropriately characterized and tailored for each unique porous material. Additionally, resists and developers are costly, require complex and time consuming thermal processing, and generate large quantities of hazardous waste. The aforementioned challenges motivate a continued search for rapid, high-resolution patterning techniques which complement the straightforward and low-cost production of porous nanomaterials.

1.2 Phase Change Nanomaterials

1.2.1 Characteristics and Production

Phase change nanomaterials (PCNMs) are a particularly attractive class of "smart" materials which offer a wide variety of unique and switchable electrical, optical, or magnetic characteristics. Although the term 'phase change' may broadly apply to materials that undergo a change in their state of matter, e.g. a solid-to-liquid change at a critical transition temperature, materials exhibiting a solid-state phase change such as a semiconductor-to-metal transition (SMT) (also often historically referred to as a metal-to-insulator transition or MIT) are perhaps the most technologically relevant, especially for applications in memory and computing devices. A wide variety of phase change materials exist ranging from chalcogenides, to superconducting cuprates, and transition metal oxides [44–46].

Chalcogenide materials are formed as the combination of a more electropositive element (such as Ag, Ge, In, Si, etc.) with one or more chalcogens (e.g. S, Se, or Te). Some of the most relevant chalcogenide compounds and related phase change materials can be found in the ternary phase diagram shown in Figure 1.6.a [47]. Many of these PCNMs exhibit highly desirable traits required for memory applications, including: a rapid phase transition time, high thermal and chemical stability, large optical or resistive contrast between the two states, and extensive cycling lifetimes. Since the early 1990s, such PCNMs have been successfully developed into commercially available rewritable optical storage devices, including most prominently, CDs, DVDs, and Blu-ray disks [47]. In chalcogenide

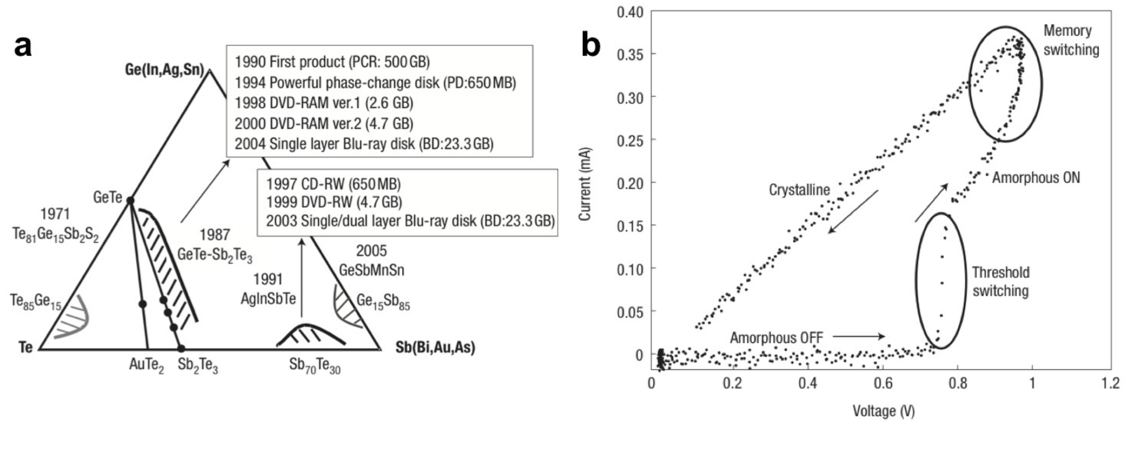

Figure 1.6: (a) Ternary phase diagram showing a variety of chalcogen based PCNMs and related technological milestones. (b) Current-voltage trace showing typical switching behavior for a PCNM changing from an amorphous to crystalline state. Figure adapted from Ref. [47]

based PCNMs the SMT is thermally triggered and coincides with a change between an amorphous (low reflectivity, high resistance) and crystalline (high reflectivity, low resistance) state. Since 1968 when it was first reported that a phase transition could be triggered by electrical stimuli using a short current pulse to heat the material past the critical

transition temperature [48], there has been growing research interest for using PCNMs in non-volatile and random access memory (RAM) devices. A typical current-voltage trace for switching a phase-change memory device from the amorphous to crystalline states is shown in Fig. 1.6.b [47]. Under low initial voltages, current flow is very minimal owing to the high resistivity of the amorphous state. At a certain voltage however, electronic threshold switching occurs wherein the resistivity is dramatically reduced although the material remains amorphous. In this lower resistance state, increased current flow leads the amorphous solid to recrystallize, thus writing a new memory state.

Transition metal oxides exhibiting a SMT are another important category of PCNMs. Since Morin's seminal paper in 1959 [49], these oxides have been at the center of intense research within the field of condensed matter physics. After decades of study, modern investigations continue to reveal the complex nature of the SMT (or MIT) occuring in correlated-electron systems. As shown in Figure 1.7 each specific metal oxide has a unique threshold temperature at which the SMT occurs. Among these materials, vanadium dioxide (VO_2) has received significant attention because of its large and reversible SMT which occurs near room temperature ($T \sim 67$ °C).

Across the SMT, the resistivity of VO_2 thin films changes by approximately four orders of magnitude (Figure 1.8.a), coinciding with a large change in near-infrared reflectivity (Figure 1.8.b). Hysteresis curves for bulk crystals generally show very narrow hysteresis widths, ~ 1 °C, while for thin films the hysteresis is slightly larger, $\sim 10-15$ °C. Nanostructured VO_2 generally exhibits the broadest hysteresis behaviors with hysteresis widths reported from $\sim 20-40$ °C [50]. The SMT also coincides with a change from a monoclinic to a tetragonal (or rutile) crystal structure [51, 52] (Figure 1.9). In the monoclinic

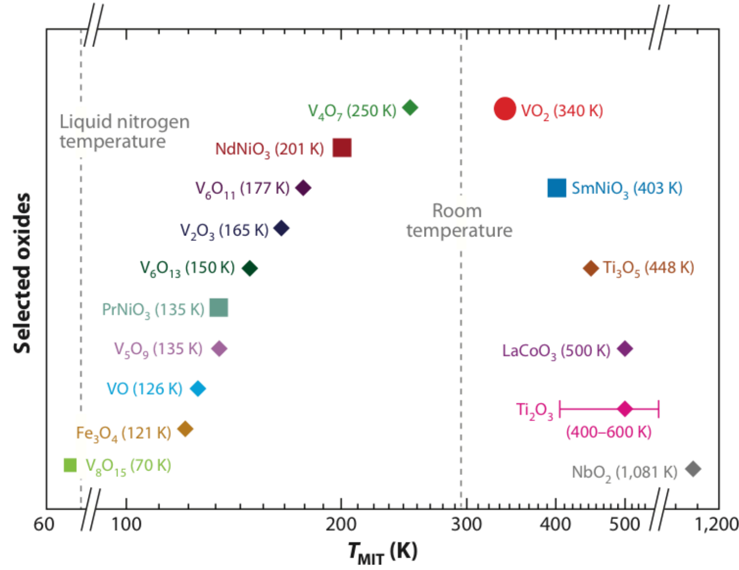

Figure 1.7: Threshold phase transition temperature for a variety of selected transition metal oxides. Figure adapted from Ref. [47].

phase, $V^{4+} - V^{4+}$ pairs alternate between shorter (0.265 nm) and longer (0.312 nm) separations along the a-axis, while in the higher symmetry rutile phase these ions are shifted to equidistant separations (0.288 nm) effectively halving the size of the unit cell. An exciting characteristic of VO_2 is that the phase transition can be triggered by a variety of stimuli, including: an applied pressure, strain, or electric field, and even optically in less than 100 fs by ultra-fast laser pulses [53, 54]. This opens the possibility to not only study the dynamics of the SMT from many perspectives, but to find unique applications for VO_2 in a variety of novel devices.

Synthesis of VO_2 bulk crystals and thin films is non-trivial owing to the many stable vanadium oxide phases that exist, such as VO, V_2O_3, V_2O_5, V_6O_{13}, etc. Thus, successful deposition or growth techniques generally include tested recipes which can finely control the stoichiometry of the VO_2 film. Indeed, a variety of techniques have been demonstrated

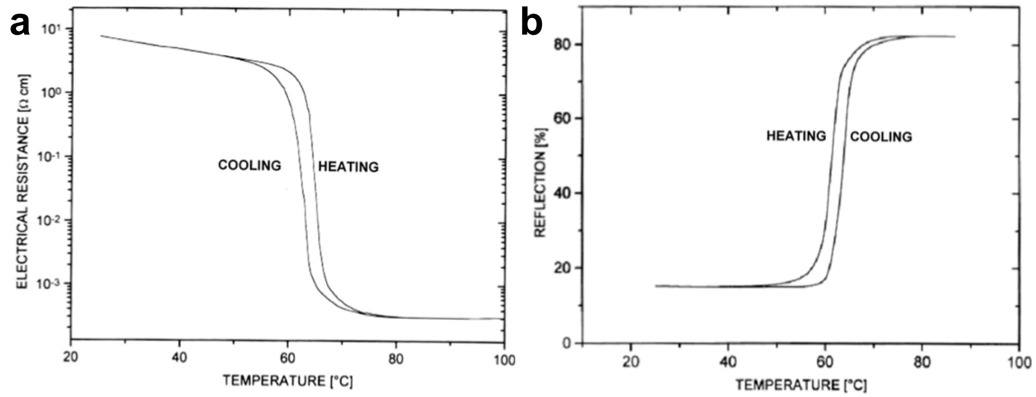

Figure 1.8: VO_2 thin film hysteresis in (a) electrical resistivity and (b) optical reflectivity ($\lambda = 2\ \mu$m). Figure adapted from Ref. [52].

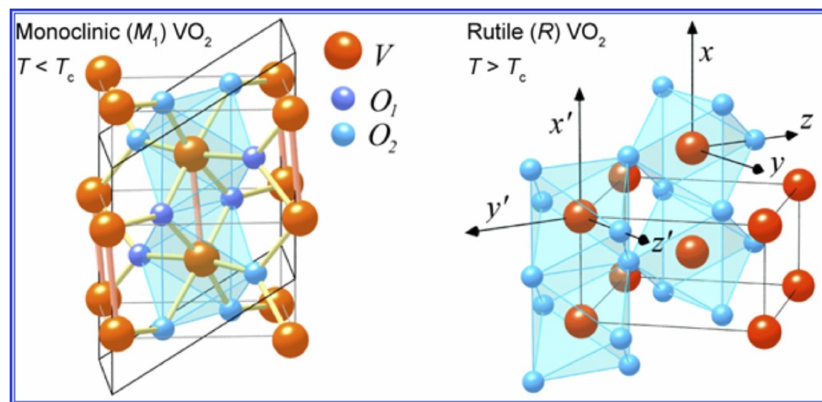

Figure 1.9: The structural phase transition (SPT) in VO_2. Coinciding with the SMT, a SPT occurs wherein the crystal structure is shifted from a monoclinic to rutile phase.

for synthesis of VO_2 thin-films, with the most common methods including sputtering, pulsed laser deposition (PLD), chemical vapor deposition (CVD), sol-gel, and evaporation. Most recently, atomic layer deposition (ALD) and molecular beam epitaxy (MBE) have also emerged as promising techniques for VO_2 synthesis [55], and show great promise for achieving ultra-thin and/or ultra-high quality films. Notably, ultra-thin films (< 40 nm) may exhibit significant strain (for example $VO_2(001)$ deposited/grown on $TiO_2(001)$), which can shift the SMT threshold temperature and produce unique electrical or optical characteristics [56]. Doping VO_2, for example with Au, Cr, Mo, Nb or W, is another area of growing interest, as this enables additional control and tailorability over the SMT threshold temperature and other properties. Among these dopants, W is commonly cited as one of the most effective, as it can reduce the transition temperature by 21-28 K/at. % [57]. Shifting the SMT threshold temperature can be used to optimize the thermo-optic or thermo-electric sensitivity of devices which operate at room temperature. This can promote lower switching energies or enable the hysteresis to be exploited for low energy memory devices operating at room-temperature.

1.2.2 Photonic Properties and Applications

As noted above and shown in Figure 1.8.b, triggering the phase transition in VO_2 results in dramatic changes in near infrared reflectivity and transmission. These effects are linked to the changing dielectric properties of VO_2 across the phase transition. Notably, switching from the low temperature semiconducting state to the high temperature metallic state results in a dramatic reduction in the real part of VO_2's refractive index (~ 3.21 to 1.9 in the near-IR) as shown in Figure 1.10.a. As VO_2 becomes metallic, its dielectric constant

becomes negative and the imaginary part of the refractive index increases substantially (Fig. 1.10.b). For bulk samples and many thin-films, this naturally results in increased optical reflectivity, a common characteristic of many metals. Compared to most materials with either fixed optical properties (i.e. n, k), or weakly tunable properties, the magnitude of Δn_{SMT} and Δk_{SMT} are remarkable characteristics that make VO_2 an attractive material for constructing *active*, *reconfigurable* photonic devices. Moreover, the contrast in VO_2's optical properties is maximized in the near- and mid-IR regions, making VO_2 especially attractive for telecommunications, IR imaging, and other applications found in this spectral range.

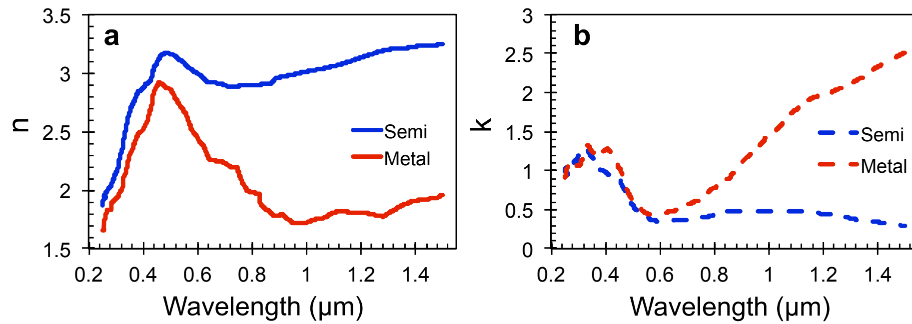

Figure 1.10: (a) Real and (b) imaginary parts of VO_2's refractive index, $n_{VO_2} = n + ik$, in both the semiconducting and metallic states.

VO_2 for Active, Reconfigurable Photonics

In recent years, the switchable optical characteristics of VO_2 have been harnessed in a wide variety of studies and devices. Figure 1.11 illustrates some of these applications and selected results. Owing to the thermally variable reflectivity of VO_2, a variety of works purposefully engineer devices or films with technologically useful thermo-chromic effects. For example, “smart” window coatings have been proposed and constructed, which limit

the flux of solar and thermal radiation through a glass window based on the temperature (Fig. 1.11.a) [58]. This passive technology is a promising and energy efficient solution to maintaining more stable room lighting or room temperature throughout the day or across different seasons. The use of VO_2 thin films has also been proposed for use in IR imaging systems, where the phase transition yields an optical shuttering effect that can be optimized for a specific wavelength regime by thin film design (i.e. near $\lambda = 4\ \mu$m, Fig. 1.11.b) [59]. VO_2 has also been integrated into core-shell Au/VO_2 nanoparticles, dubbed 'regulatrons', to provide self-regulating plasmonic functionality (Fig. 1.11.c) [60]. These particles exhibit a unique feedback between their heating and plasmonic properties that enables their temperature to be maintained in a specific range, an effect that could benefit certain applications in photothermal medical theraputics. Photoinducing the SMT in VO_2 nanoparticles also enables large, reversible changes to plasmonic absorption, $\Delta\alpha$, as shown in Fig. 1.11.d, an effect that can be triggered in an ultra-fast regime using pulsed laser light to trigger the SMT [54]. Aside from the aforementioned thin-films and plasmonic nanoparticles, VO_2 has also been integrated with metamaterial resonators [61] and photonic crystals [62] to provide unique, switchable characteristics and optical signatures.

One notable characteristic of the aforementioned devices is that the VO_2 is most commonly integrated with the structure through batch processing on the thin-film or colloidal solution level. These devices are also generally switched using thermal stimuli. Emerging and future devices, like the structures introduced in Chapters 4 and 5, will be developed with more complex nanostructures (via lithography) and switched by a variety of stimuli (i.e., thermal, optical, electrical). In this dissertation, we specifically investigate the application of VO_2 for constructing *active silicon photonic devices*.

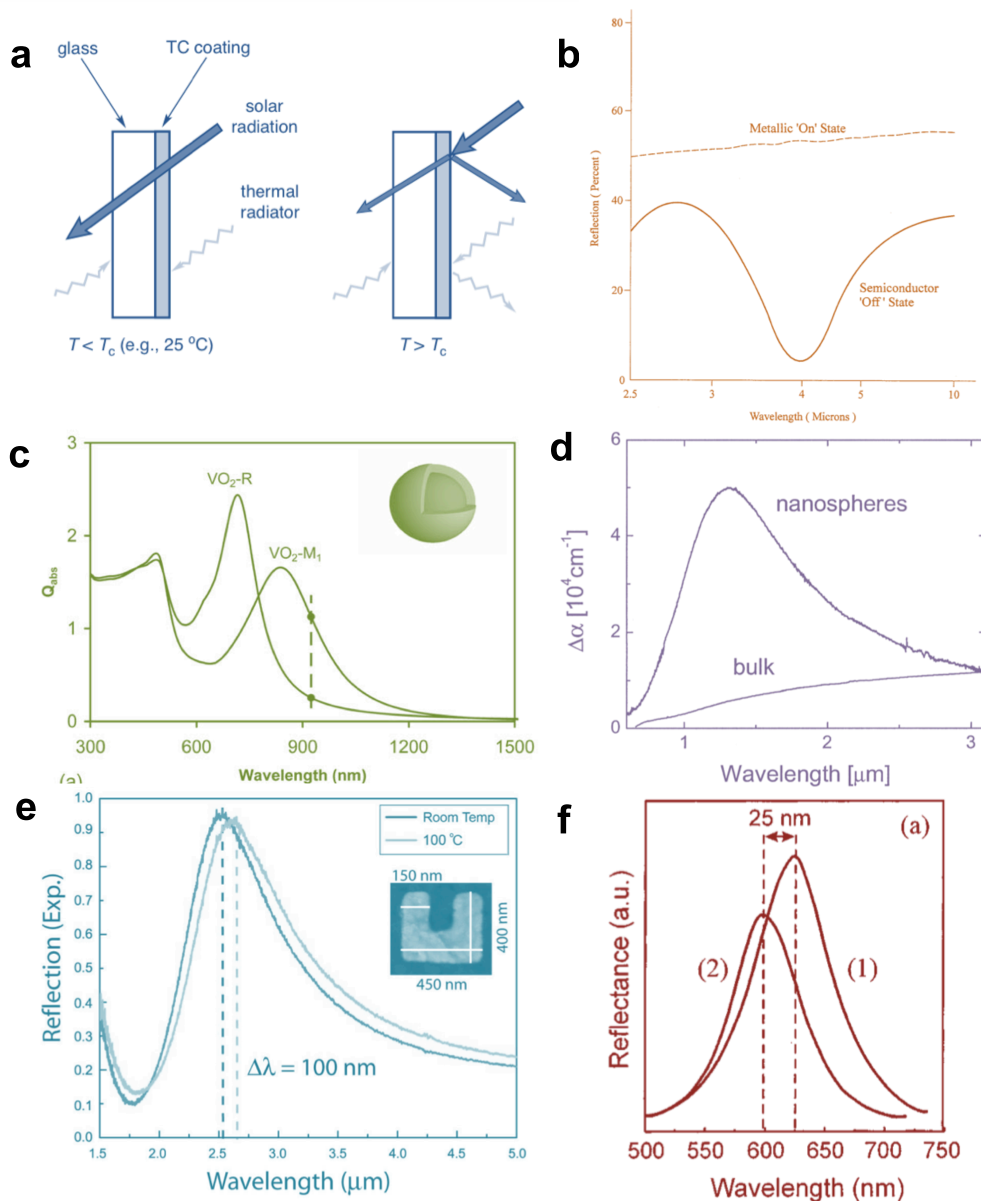

Figure 1.11: Some photonic applications of VO_2 selected from existing literature, including (a) "smart" window coatings [58], (b) IR imaging shutters for missile systems [59], (c) Au/VO_2 and (d) VO_2 plasmonic nanoparticles [54, 60], (e) metamaterial resonators [61], and (f) opal-based photonic crystals [62].

Active Silicon-Based Photonics

Over the past decade, great interest has been shown in developing silicon based photonic devices, such as modulators, which can be integrated alongside other photonic or electronic components on a single chip [63]. Notably, the silicon photonics platform provides excellent optical confinement and low-loss transmission at telecommunications frequencies, while also providing the opportunity to leverage modern CMOS processing techniques and existing fabrication facilities. One tactic often employed in all-silicon electro-optic modulators is to exploit the small variation in refractive index that occurs in response to a voltage modulated carrier concentration [63]. Various design schemes have been implemented to convert this change in refractive index to a change in optical transmission, including most prominently: (1) the ring resonator configuration [64], and (2) the Mach Zehnder interferometer (MZI) [65], both of which are capable of achieving fast, ~GHz speed, switching with modulation in excess of 15dB at a given wavelength. However, such all-silicon optical modulators still face a number of limitations with respect to speed and performance. Firstly, silicon's small electro-optic effect requires very narrow band, high quality factor (Q), resonators or very long, ~mm length, interferometers to be utilized. Notably, high-Q devices are difficult to implement, both in terms of required fabrication tolerances, and in terms of sensitivity to ambient conditions such as temperature fluctuations [63]. Indeed, high-Q silicon ring resonators are known to be highly temperature sensitive (30-80 pm K^{-1}) [66, 67], therefore requiring power consuming temperature compensation schemes to maintain temperature tolerances to less than ± 1 °C [68]. Moreover, the switching time of silicon based optical modulators are typically limited by carrier lifetimes for injection based devices

(e.g. $\sim$0.35 ns) [64], and RC constants in accumulation or depletion based devices (e.g. $\sim$0.014 ns) [63, 69].

The limitations posed by all-silicon active devices and optical modulators motivates the introduction of a secondary material, to form a hybrid device structure with the potential to improve overall device speed and performance [70–73]. In one recent example based on an MZI design, it has been demonstrated that intensity modulation with speeds up to 1 THz may be feasible with a hybrid polymer-silicon waveguide structure based on the all-optical Kerr effect [74]. Phase changing VO_2, meanwhile, has also recently been integrated onto a silicon waveguide to form an in-line absorption modulator [75]. Notably, the potential for ultra-low power consumption, combined with either electrical, thermal, or ultra-fast optical switching makes the Si-VO_2 hybrid platform very attractive for integration into next-generation photonic devices.

1.3 Optical Resonators and Light-Matter Interactions

Beyond studying and improving fabrication techniques and material platforms it is essential for the advancement of nearly all photonic applications to study and improve *photonic design* in order to enhance light-matter interactions. In other words, appropriate designs may achieve enhanced performance metrics spanning efficiency, sensitivity, compactness, cost, or other figures of merit. In modern nanophotonics and especially for sensing and communications, resonant optical devices such as the Si-VO_2 hybrid resonator motivated above (introduced in Chapter 4) have become increasingly important. In this section, we introduce and discuss some fundamental background relating to resonant devices, existing device configurations, and strategies for enhancing light-matter interactions.

Resonant optical devices have established a strong and growing presence in fields ranging from chemical and biological analysis to chip-scale optical communications, and they have begun transitioning from the academic laboratory into industrial production [76, 77]. The fundamental advantage offered by such resonant devices is their ability to spatially or temporally confine light, enabling enhanced light-matter interactions. Distinct optical signatures arising from these resonant phenomena can be harnessed in a diversity of devices spanning sensors [78], filters [79], modulators [80], and light-sources [81]. The enhancement of light-matter interactions, within or around the optical cavity, enables high sensitivity to small perturbations such as analyte capture or refractive index modulation, while also enabling significant amplification of typically weak processes such as non-linear effects or optical forces [82, 83]. Existing resonators achieve spatial and temporal confinement of light through various means. One common example is the micro-ring resonator, which is simply formed by making a waveguide into a loop to recirculate light, achieving resonance when the optical path length of the micro-ring is equal to an integer number of wavelengths. Micro-ring resonators provide a classic example of the typical trade-off between spatial confinement (V) and temporal confinement (Q) (Fig. 1.12). In these devices, V is primarily determined by the confinement provided by the waveguide structure and by the dimensions of the micro-ring. On the other hand, Q is directly linked to the photon cavity lifetime and is often limited by material absorption, scattering, or bending induced losses. Assuming minimal and fixed sidewall roughness and material absorption, achieving high Q-factors requires large ring radii to minimize bending losses, thus requiring an increase in V. Extremely high Q-factors surpassing 10^8 can be achieved in ultra low-loss whispering gallery devices with radii on the order of several tens of microns [84, 85]. While these

impressively high Q-factors enable large extinction ratios for very small resonance shifts, this comes at the cost of very large modal volumes, $> 6000(\lambda/n)^3$, and therefore a larger device footprint. This trade-off is illustrated in Figure 1.12 which plots the Q and V values for example devices from the literature alongside devices considered in this dissertation.

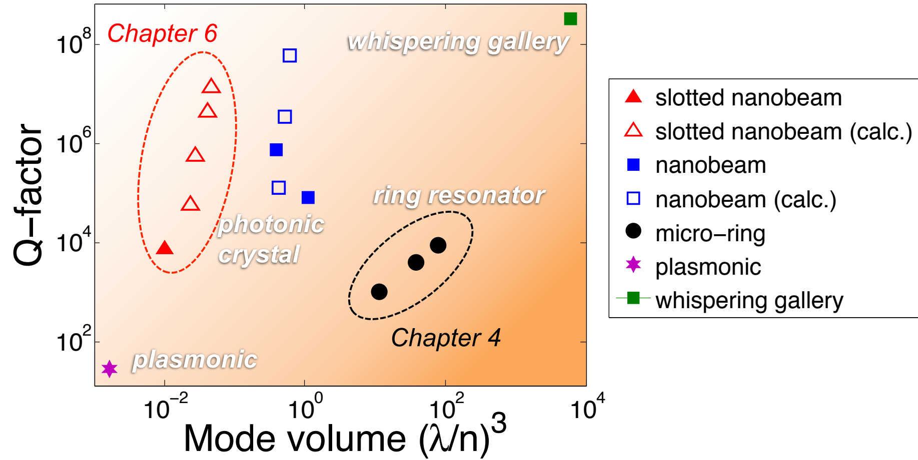

Figure 1.12: Q-factor vs. mode volume for a variety of selected optical cavities including plasmonic [86], whispering gallery [84], micro-ring (used in Chapter 4) [80], nanobeam (1D photonic crystal) [87, 88], and slotted nanobeam (introduced in Chapter 6) [89]. Solid points indicate experimentally measured devices and hollow points indicate calculated values.

Achieving ultra-low mode volumes $< 10^{-2}(\lambda/n)^3$ is possible in nanostructured metallic cavities through the excitation of plasmon resonance [86, 90]. Plasmon resonances arise from the excitation of collective electron oscillations in metallic nanostructures that are generally constructed with noble metals featuring large negative dielectric constants. Due to the required continuity of the displacement field ($\varepsilon_m E_m = \varepsilon_d E_d$) normal to the metal-dielectric interface, dramatic electric field enhancements can be achieved in the dielectric medium just outside the metallic surface. Mode volume is inversely related to the normal-

ized maximum field intensity $|E_{max}|^2$. Thus, the large localized field enhancements offered by plasmonic nanostructures promote very small mode volumes. However, Q in these plasmonic cavities is typically limited to the range 10-100 by metal induced losses [86, 90, 91]. Further, optimizing plasmonic cavities to achieve ultra-low V increases the losses induced by the metal, which limits many practical applications of these cavities. Consequently, while plasmonic cavities can achieve impressively low values of V, Q-factors are typically very low and cannot be tuned over a broad range.

Photonic crystal (PhC) cavities (Figure 1.13) can be viewed as bridging the gap between low-V, low-Q plasmonic cavities and high-Q, high-V whispering gallery and micro-ring resonators. PhCs provide a unique method of achieving strong spatial and temporal confinement of light by engineering allowed defect states into specific spectral regions, or photonic band gaps, where light propagation is forbidden. PhCs are formed from structures featuring a spatially varying, or periodic, dielectric function on a scale comparable to the wavelength of interest. Traditional PhC cavities can thus achieve low mode volumes $\sim (\lambda/n)^3$ while also offering high Q-factors (typically $\sim 10^4 - 10^6$) owing to their construction from low-loss dielectric materials.

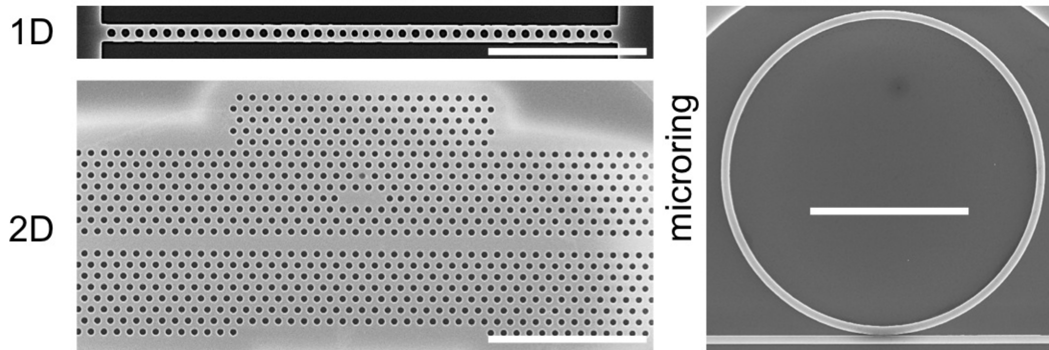

Figure 1.13: SEM images of selected example optical cavities including both 1D (nanobeam) and 2D PhCs (scale bars 5 μm) and a micro-ring resonator (scale bar 10 μm).

Notably, PhC cavities can be constructed in 1D, 2D, or 3D PhCs, although only 1D or 2D cavities can be readily realized with high reliability or quality through conventional fabrication techniques (Figure 1.13). While higher dimensional PhCs do offer increased control over light propagation, this does not necessarily translate to higher Q or lower V. Importantly, Q-factors are generally limited by radiation losses, which are not clearly linked to direct observables such as material absorption or bending radii as in other cavity systems. Minimizing radiation losses and achieving high Q PhC cavities has been an area of intense and continued research lasting more than a decade [92–94]. Only in the past few years have Q-factors near 10^6 been experimentally demonstrated and theoretical Q-factors realized beyond 10^8 for both 1D and 2D PhC cavities [88, 95–97]. Compared to their 2D counterparts, 1D PhC cavities offer advantages of a simpler geometry, reduced device footprint, and lower total mass.

Although 1D PhC cavities, or nanobeams, have seen substantial improvements to both experimental and theoretical Q-factors in recent years, they typically still feature $\sim (\lambda/n)^3$ mode volumes, almost unchanged in the past 15 years [98]. As illustrated in Fig 1.12 and introduced in detail in Chapter 6, integrating a nanoscale slot (or region of low refractive index), along side further design optimization, is a promising solution for significantly improving mode volume and Q-factor, and thus light-matter interactions within the ultra-compact 1D PhC platform.

CHAPTER 2

DIRECT IMPRINTING OF POROUS SUBSTRATES (DIPS)

2.1 Introduction

Modern micro- and nano-fabrication techniques enable an incredible diversity of photonic structures and devices to be realized. When utilizing porous nanomaterials, however, there are a number of challenges associated with using conventional or existing fabrication techniques, as summarized in Chapter 1. New technologies for direct patterning overcome many of the aforementioned challenges by eliminating the need for intermediate masking materials and etch recipes. For example, ultrafast liquefaction has been utilized to achieve direct imprinting of nanoscale features into Si substrates [99]. More recently, indentation lithography has been applied to directly produce topographic patterns on epoxy, Si, and SiO_2 [100]. Here, we demonstrate a direct patterning technique, coined ”direct imprinting of porous substrates” (DIPS), specifically motivated for structuring porous nanomaterials [101]. The process can be performed at room temperature in less than one minute. Our technique is based on the concept that a heterogeneous void network can accommodate volume changes in ways that would be impossible for a bulk solid. By applying a pre-mastered stamp to selectively compress or crush localized regions of the underlying porous nanomaterial, DIPS not only circumvents the challenges posed by traditional lithographic strategies, but it also allows local manipulation of the internal porous network (e.g., pore size and porosity) and the generation of complex three-dimensional topographies.

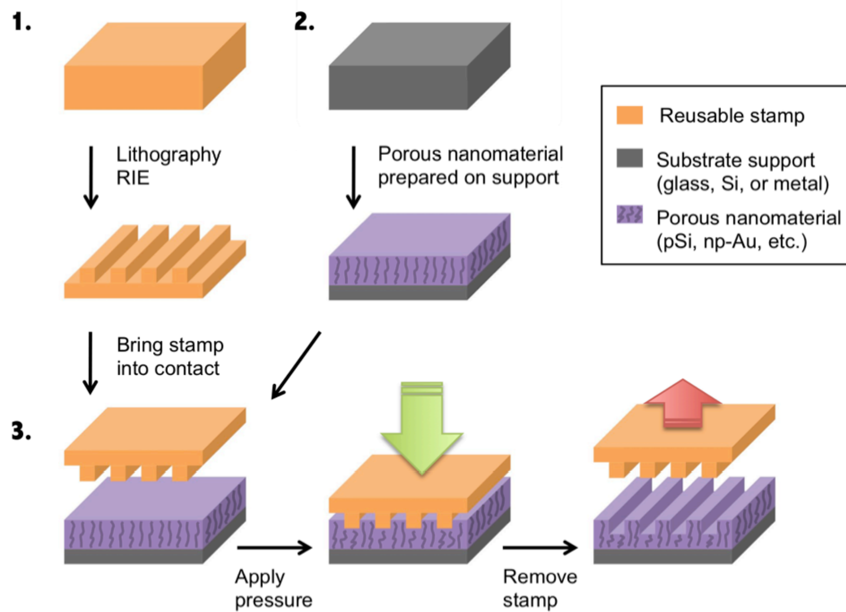

Figure 2.1: Illustration of the DIPS process [101].

Fig. 2.1 illustrates the DIPS process. A porous nanomaterial is prepared on a solid substrate support and is subsequently imprinted with a premastered and reusable stamp utilizing an applied pressure ∼100 N/mm^2 = 100 MPa (approx. 10^3 atm). The straightforward process can be performed in a matter of seconds at room temperature without the need for any curing, developing, baking, or etching processes. In our present investigations, we utilize silicon as the stamp material. Silicon stamps with a large variety of imprintable patterns can be readily fabricated through conventional lithographic techniques, and silicon has a desirably large material hardness (∼10 GPa). While silicon may not prove to be the optimal choice for a stamp material for all applications, our investigations have demonstrated its potential for extensive reusability and high fidelity imprinting of many porous materials.

2.2 Experimental Demonstrations and Capabilities of DIPS

2.2.1 Preparation of porous nanomaterials

pSi samples were prepared by electrochemical etching of a boron doped p+ type Si(100) wafer with a resistivity of 0.01-0.02 Ω cm and a thickness of 475-550 μm (University Wafer) in a mixture of 49% hydrofluoric acid (HF):ethanol mixture with a ratio of 3:7 (v/v). npAu samples were prepared from a $\sim$1.5$\times$1.5 cm sheet of one hundred nanometer thick Monarch 12 Karat white gold (fineartstore.com) that was dealloyed by floating on concentrated nitric acid for 15 minutes followed by mounting on substrate supports, as reported elsewhere [32]. Hexagonally ordered pAl_2O_3 was prepared by anodization of high purity 100 μm thick Al foil (99.99%, Sigma Aldrich), in 0.3 M oxalic acid electrolyte according to the literature [1]. The pores were subsequently opened in a bath of phosphoric acid (5% wt) for 90 min. TiO_2-NTAs were prepared from 0.25 mm thick Ti foil (99.7%, Sigma Aldrich), which were cut into 2$\times$2 cm squares that were first sonicated in isoproponal and then acetone, each for 10 min. Samples were then anodized at 80 V for 5-18 hrs in a two-electrode configuration utilizing an electrolyte solution of NH_4F (0.3% by weight) and water (0.1% by volume) in ethylene glycol, and subsequently annealed at 450 °C for 3 hrs with a 3.5 hr ramp up/down time.

2.2.2 Stamp preparation and imprinting

Silicon stamps were prepared from the same wafers used to prepare the pSi samples (described above). Standard photolithography and reactive ion etching were used to pattern the microscale (Λ = 5, 10 μm) grating stamps. All other stamp patterns were defined by

electron-beam lithography followed by: (i) electron-beam evaporation of a 10 nm Cr mask layer, (ii) lift-off in acetone, and (iii) subsequent reactive ion etching to a depth of approx. 0.5 μm (except for the sub-micrometer period gratings, which skipped steps i and ii). Imprinting was performed with a Tinius Olsen Super L 60K universal testing machine configured to apply a flat metallic plate onto the backside of the stamp, which was fixed face down on the porous nanomaterial with single sided Scotch Tape. After bringing the plate into contact with the backside of the stamp, a computer-controlled force was delivered and sustained for less than 1 s. For a more detailed step-by-step protocol, see Appendix A.1.

2.2.3 DIPS Fabricated Structures

As an example of DIPS, Figure 2.2.a shows the imprinting behavior of a $\approx$1 μm thick pSi film with pore diameters approximately 30-40 nm (prepared by electrochemical etching at 48 mA cm^{-2} for 35 s). After imprinting with a grating patterned stamp (area = 9mm^2; grating pitch, Λ = 5 μm) at a force of $\approx$2 kN as schematically illustrated in Figure 2.1, the imprinted regions are compressed to a thickness of approximately 615 nm while the other regions remain untouched. The mesoporous network accommodates the reduction in volume by bending and compressing pores together. In this case, the porous structure appears to be contiguous and unbroken. After imprinting, the sample was placed back in the electrochemical cell to determine if the densified porous network would prevent electrolyte infiltration and the etching of a second layer. SEM imaging (Fig. 2.2.a) reveals that the etching of a second porous layer (20 mA cm^{-2}, 30 s) proceeded uniformly in both the printed and unprinted regions; the ethanolic HF etching solution readily infiltrated the entire imprinted pSi layer, and reinitiated etching where the pores were previously

terminated. This opens the possibility of fabricating devices through a multistep approach, where further electrochemical etching can be performed following DIPS.

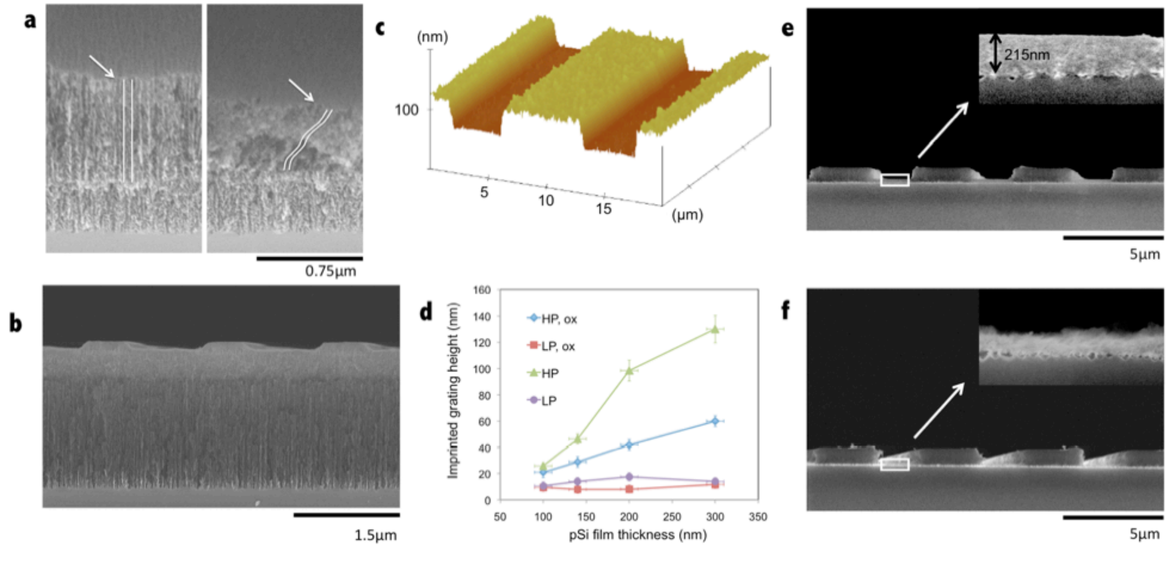

Figure 2.2: Characterization of vertical featuring of DIPS on pSi. (a) Cross-sectional SEM images (45 degree tilt), of unstamped and stamped regions of a 1 μm thick pSi film (the white arrows indicate highlighted typical pores). Following DIPS, a second layer could be uniformly etched in both regions. (b) SEM image of a grating coupled pSi waveguide fabricated with DIPS in a multistep process. (c) AFM height image of a typical pSi thin film after performing DIPS. (d) Variation of imprinted grating height for pSi thin films for various film thicknesses and preparation conditions. High-porosity (HP) and low-porosity (LP) films were electrochemically prepared at current densities of 80 mA cm^{-2} and 5 mA cm^{-2} respectively. Oxidation was performed at 500 °C for 5 min in air ambient. (e) SEM image of a pSi grating fabricated by imprinting a 1 μm thick HP film to a depth of 785 nm (the inset reveals a crushed pSi film remaining in the imprinted regions). (f) SEM image of a similarly prepared pSi grating where the crushed pSi region has been removed by ultrasonication (the inset reveals only the silicon substrate remains in the imprinted region). Adapted from Ref. [101].

As an example of a device structure that would benefit from a multistep process, we have fabricated a grating-coupled porous silicon waveguide sensor (Fig. 2.2.b). Grating coupled pSi waveguides function by coupling diffracted light into a waveguide mode where light is confined in a high refractive index layer through total internal reflection [10]. A pSi structure can readily achieve the refractive index contrast necessary for waveguiding by

modulating the porosity (and thus the effective refractive index). The structure of Fig. 2.2.b was fabricated by first etching a thin ∼200 nm high-porosity cladding layer followed by a low porosity ∼300 nm waveguiding core layer. DIPS was then performed with a silicon-grating stamp (Λ = 1.7 μm), and followed by further electrochemical etching of a 1.5 μm thick high-porosity cladding layer.

Tuning Imprint Depth

From prior work on nanoindentation, it is expected that the imprint depth depends primarily on the pressure applied to the stamp, the hardness of the material being imprinted, and the stamp geometry. Not surprisingly, AFM measurements of both npAu and pSi films

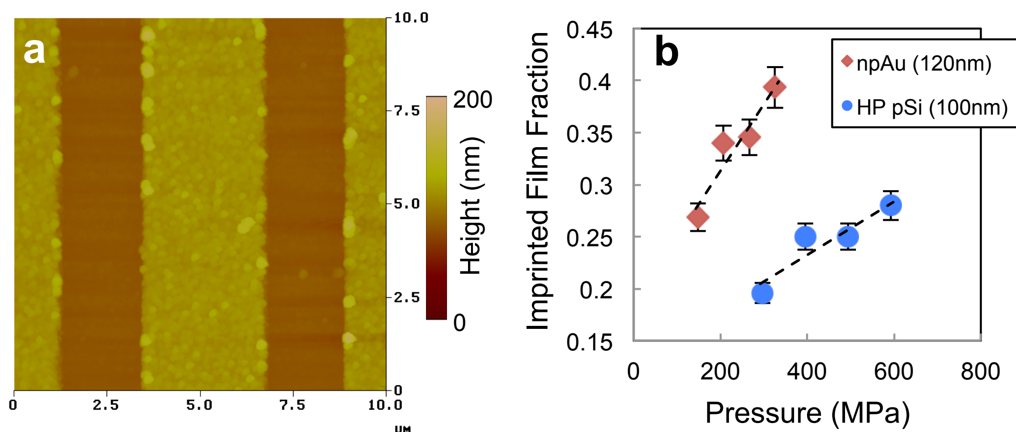

Figure 2.3: AFM characterization of imprint depth with applied pressure. (a) AFM scan for a ∼100 nm HP pSi film imprinted with a grating patterned stamp to a depth of ∼29 nm. (b) Imprint film fraction vs. applied pressure for example npAu and HP pSi thin films with initial film thicknesses of 120 nm and 100 nm respectively. Note: this pressure is calculated from the applied force divided by the estimated stamp contact area (total area × duty cycle).

indicate that the stamping imprint depth scales with the applied pressure (Fig. 2.3). Aside from the material type, porous nanomaterial properties such as porosity, thickness, or con-

ditioning methods (for example, oxidation in the case of pSi) were also found to affect the imprint depth through variations of material hardness. Atomic force microscopy (AFM) (Fig. 2.2.c,d) reveals how the imprint depth depends on all of these parameters. These points were examined through a standardized DIPS process utilizing a grating patterned stamp (area = 9 mm^2, Λ = 10 μm) applied to porous substrates at a fixed force ($\sim$2 kN). By varying the electrochemical preparation conditions, we fabricated high porosity (HP) and low porosity (LP) films, estimated at $\sim$80% and $\sim$55%, respectively, at a number of different film thicknesses. Duplicate samples were also prepared and treated with oxidation in air ambient at 500 °C for 5 min to examine the influence of conditioning effects. Atomic force microscopy (AFM) measurements (Fig. 2c,d) revealed that oxidized and as-etched LP films exhibited imprint depths that were approximately constant with film thickness, whereas oxidized and as-etched HP films exhibited a trend of increasing imprint depth with increasing film thickness. The observed variation of imprint depth on HP films is attributed to changes in effective hardness that arises when the imprint depth is greater than 10% of the film thickness [102]. The underlying silicon substrate contributes more to the effective hardness of HP pSi as the film thickness is reduced [103]. In other words, thinner HP films have a larger hardness that is manifested in the form of smaller imprint depths, while LP films exhibit a nearly constant hardness, and the fractional imprint depth is not greater than 10% of the pSi film thickness. In all cases, oxidized samples imprinted to shallower depths than their un-oxidized counterparts. This behaviour is likely attributed to oxide growth simultaneously reducing porosity and strengthening the interconnected mesoporous network [104]. Thus, by tuning the applied pressure and the film preparation conditions, precise nanometer scale control over the imprint depth can be achieved.

Imprinting porous structures to a depth that is a significant fraction of the original film thickness has also been investigated. This is particularly relevant for applications where a large aspect ratio is required. Under the assumption that volume reduction is accommodated primarily by a compression of the pores and a reduction of the void fraction, then the theoretical limit of the maximum imprintable film fraction should equal the original porosity of the film. Experimentally it is possible to come very close to this limit by imprinting a 1 μm thick pSi film, with an initial porosity estimated at $\sim$80%, using an increased pressure (approx. 400 N/mm^2). Figure 2.2.e shows that the porous silicon grating can be imprinted to a depth of 785 nm, very close to the theoretical limit of 800 nm. In this case, the imprinted region no longer resembles the compressed porous structure of Fig. 2.2.a, but rather resembles a crushed and densified film of broken silicon crystallites. The broken nature of the crushed film suggests that there no longer exists robust adhesion to the substrate, and indeed with ultrasonication the crushed region of pSi can be removed (Fig. 2.2.f). In this manner, imprinted structures can be produced with micro-scale vertical features and aspect ratios that exceed those of the stamp itself.

Patterns and Variety of Porous Substrates

Figure 2.4 illustrates the range of patterns that can be imprinted into various porous nanomaterials. Figure 2.4.a, c reveal pSi and np-Au, respectively, after performing DIPS with a grating patterned stamp (area = 9 mm^2, Λ = 750 nm), which demonstrates the ability to pattern submicrometer features over large areas. The observed sidewall roughness confirms that the dimension of the pore diameter fundamentally limits the resolution of pattern transfer, as expected. DIPS is capable of patterning subwavelength optical structures of arbitrary

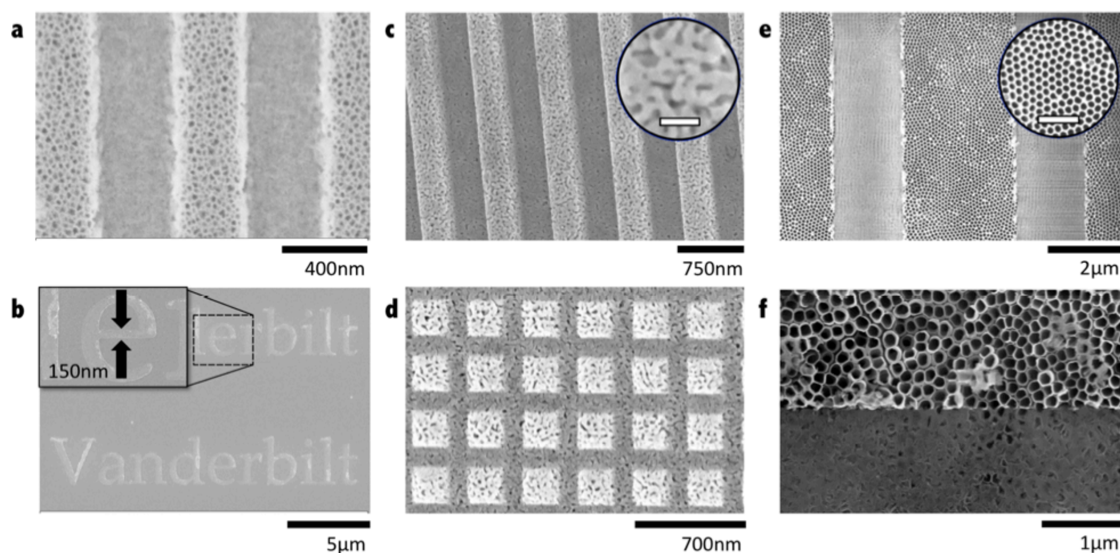

Figure 2.4: Top view scanning electron microscope (SEM) images of porous nanomaterials patterned with DIPS. (a) pSi grating (Λ = 750 nm) with submicrometer sized features. The mean pore diameter is approximately 20-30 nm. (b) pSi imprinted with 3 μm font Vanderbilt text. (c) np-Au grating (Λ = 750 nm). Inset reveals the original pore morphology (scale bar = 100 nm). (d) npAu square mesh produced by imprinting with a silicon grating (Λ = 350 nm), rotating 90 degrees and imprinting again. (e) Imprinted pAl_2O_3 grating (Λ = 5 μm). Inset reveals the original pore morphology (scale bar = 500 nm). (f) Imprinted and non-imprinted regions of a TiO_2-NTA. Adapted from Ref. [101].

nanoscale shapes, limited only by this resolution. This is demonstrated with the imprinting of text into pSi (in 3 μm size font) that contains curved features and details smaller than 100 nm (Fig. 2.4.b). Alternatively, patterns can be easily scaled to produce larger, micron scale features and patterned arrays.

Figure 2.4.d shows npAu after imprinting with a grating patterned stamp (area = 9 mm^2, Λ = 350 nm), rotating 90 degrees, and imprinting again. This demonstrates that step and print structures can be constructed, where a stamp is shifted or rotated multiple times between imprints in order to achieve structures more complex than that of the stamp itself (although in this example a 2D grating patterned stamp could achieve similar results). The resulting structure here is a nanoscale square mesh of npAu. To our knowledge, this demonstrates a patterning resolution never before achieved on npAu. Based on these results, we expect that DIPS could be employed to realize a new class of low-cost plasmonic devices employing np-Au [28, 105].

DIPS has also been successfully used to imprint hexagonally ordered pAl_2O_3 (Fig. 2.4.e) as well as disordered pAl_2O_3 (Fig. 2.5). Figure 2.4.f shows the imprinted and non-imprinted regions of a TiO_2-NTA, and reveals results similar to those obtained with other porous nanomaterials (also see Fig. 2.5). These results indicate that a host of porous materials can be imprinted using DIPS, with excellent pattern reproduction and large area uniformity. We further show in Figure 2.6 examples of curved features imprinted into pSi and npAu. These results confirm that arbitrary stamp shapes and curves can be patterned in porous substrates with high fidelity.

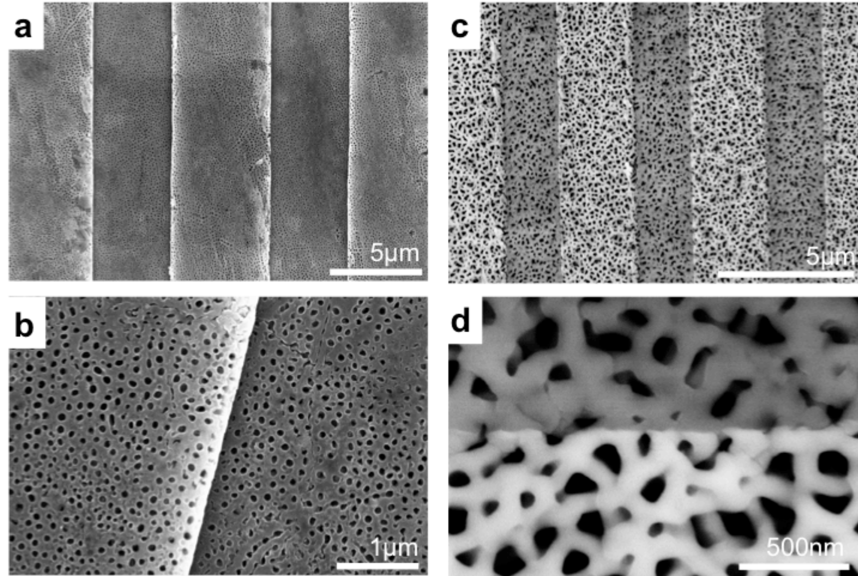

Figure 2.5: (a,b) SEM images of porous TiO_2-NTAs imprinted with a silicon grating patterned stamp (Λ= 5 μm, area = 9 mm^2). This sample was prepared by anodization at 65 V for 5 hrs (as opposed to the 80 V sample reported in Fig. 2.4.f). (c,d) SEM images of imprinted structures on disordered pAl_2O_3. Disordered pAl_2O_3 was prepared by following previously reported methods and starting from a $\sim$1 μm thick Al film sputtered onto a Si substrate, followed by anodization at 80 V in 10% wt phosphoric acid solution, and a short 15 min pore opening step in 5% wt phosphoric acid solution. Imprinting was performed with Si grating patterned stamp (Λ= 5 μm, area = 9 mm^2) applied at a force of approximately 4kN. Adapted from Ref. [101].

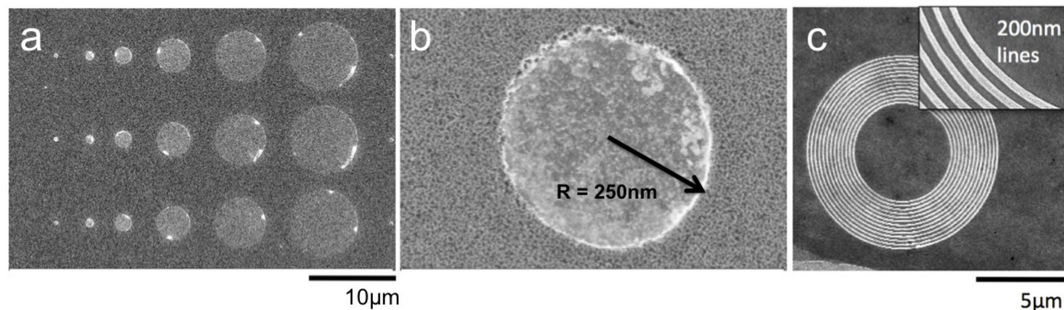

Figure 2.6: SEM images of curved features patterned by in (a,b) pSi and (c) npAu.

Example Device Structures

To suggest the variety of applications that could be enabled by DIPS, we have fabricated several sample structures (Fig. 2.7). First, we show that appropriately patterned DIPS structures can be readily used as optical diffraction gratings. Figure 2.7.a reveals a square diffraction grating fabricated on npAu on a glass substrate. A clear and distinct diffraction pattern appears due to the large spatial uniformity of the imprinted micro-scale pattern. This demonstrates that DIPS is capable of patterning macro- to microscale arrays, an important class of structures on porous nanomaterials. The fabrication of diffraction gratings in porous materials is particularly relevant to sensing applications, where the presence of analytes in the porous matrix modifies the effective refractive index of the grating, leading to significant changes in the diffraction signature. We have recently demonstrated this phenomenon for label-free sensing of small molecules using a micron-scale one-dimensional porous dielectric grating (see Section 2.4), and for significantly enhanced SERS sensing using a submicron-scale two-dimensional porous metal grating [105]. Porous diffraction gratings could also be utilized to couple light into dielectric waveguides (as in Fig. 2.2.b)) or launch surface plasmons in metallic films. Furthermore, grating structures are of particular interest in photovoltaic applications, owing to their ability to couple light into guided modes of thin-film devices for light harvesting [106].

As a second example, we report the ability to fabricate rib waveguides (Fig. 2.7.b) utilizing DIPS on pSi in a multistep process similar to that previously described for the grating coupled 2D waveguide (Fig. 2.2.b). Horizontal confinement of light (coplanar direction) is achieved by imprinting trenches into a $\sim$450 nm thickness medium porosity ($\sim$67%) pSi

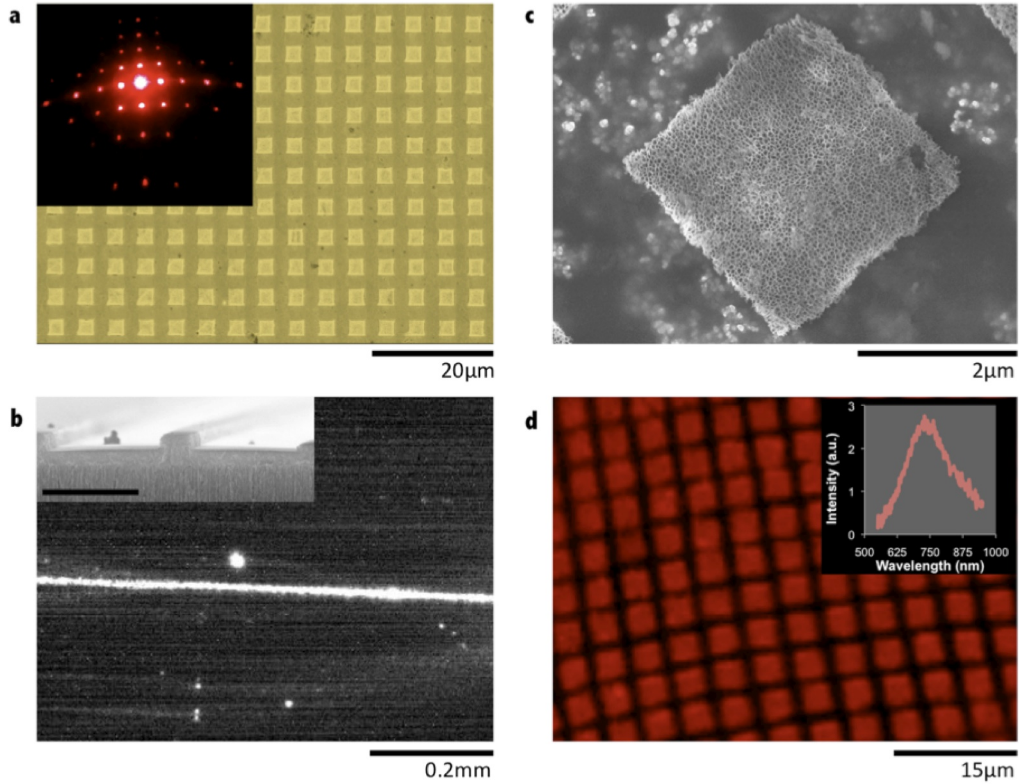

Figure 2.7: Demonstration of selected device structures fabricated by DIPS. (a) SEM image of a np-Au square diffraction grating (Λ= 5 μm), produced in the same manner as in Fig. 2.4.d). Inset reveals the optical diffraction pattern (λ = 647 nm) at approximately 15 $^\circ$ from normal incidence. (b) Camera image (top view) of a DIPS patterned pSi structure waveguiding near-infrared (λ = 1200-1700 nm) light (the inset reveals a waveguide SEM cross-section, scale bar is 1 μm). (c) SEM image of a free standing square pSi microparticle. (d) Confocal fluorescence micrograph of freestanding pSi microparticles on carbon tape (inset shows the photoluminescence spectra of an as-anodized pSi film, excitation λ = 488 nm). Adapted from Ref. [101].

film prepared at a current density of 20 mA cm^{-2}. Subsequent etching of a 1.8 μm thick high porosity (~80%) pSi cladding layer (80 mA cm^{-2}) produces the vertical confinement required for waveguiding. An advantage of utilizing photonic structures constructed from porous nanomaterials is the ability to infiltrate various species into the porous network that can then be used in switching, sensing, or light emission applications. Note that with this pSi waveguide example we demonstrate that DIPS is well equipped for patterning submicron and nanoscale structures.

2.2.4 Free Standing Microparticle Fabrication and Overstamping

In Figure 2.7.c, d we present the ability to fabricate microscale structures, in particular freestanding pSi microparticles, using DIPS. The fabrication follows a procedure similar to that described above (Fig. 2.4.d), with some modifications. When a stamp is imprinted all the way into pSi, with the entire stamp surface brought into contact with the substrate, a new and interesting stamping regime occurs. We refer to it as overstamping, to distinguish it from the previous examples we have presented. Overstamping affords the ability to selectively weaken the base of the porous nanostructure (Fig. 2.8). In this manner, patterned structures can be easily detached from the substrate. This can be done by using the combination of frictional and electrostatic forces that exist between the stamp and the imprinted structure (Fig. 2.9.a, b), by performing ultrasonication in an aqueous solution, or by simply applying and removing an adhesive such as carbon tape (Fig. 2.7.c, d and Fig. 2.9.c-e). These pSi microparticles exhibit excellent size uniformity, and can be readily placed in solution. Other particle geometries could also be realized, on both the micro- and nanoscale, by simply changing the geometry of the applied stamp. Selected particles

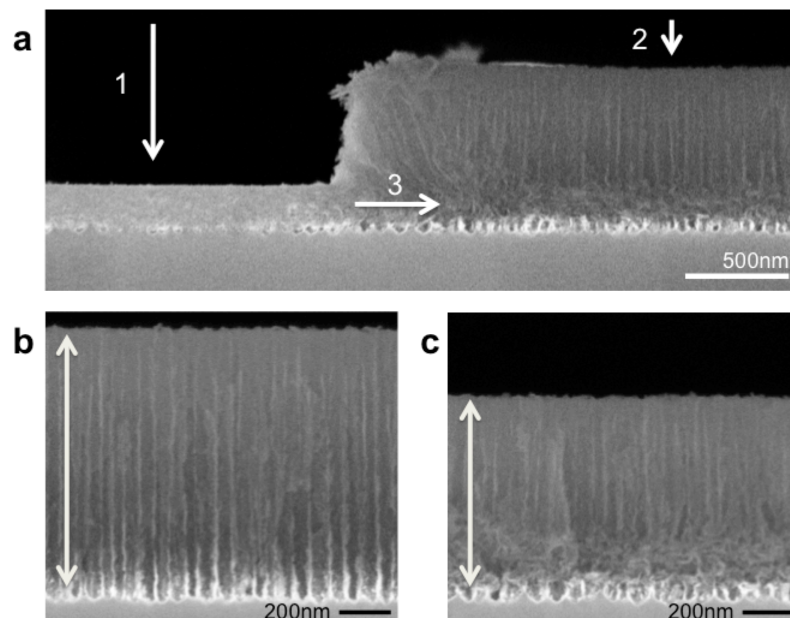

Figure 2.8: SEM images depicting the overstamping regime on pSi. (a) Imprinting in the overstamping regime requires that the stamp makes contact and applies a pressure in regions 1 & 2. As a result of extreme densification and vertical compression in region 1, some horizontal expansion occurs through region 3, leading to weakening and collapsing of the pore bottoms as they are compressed in region 2, (b) the original 1 μm thick 80% porosity film, and (c) the overstamped pSi film with a selectively weakened bottom interface. Adapted from Ref. [101].

can exhibit highly desirable traits for use in vivo that include efficient loading of therapeutics or imaging contrast agents, distinctive photoluminescence or other signatures, and biodegradability [16–18]. In Figure 2.7.d we further demonstrate that these pSi microparticles maintain their intrinsic photoluminescence properties. pSi Bragg reflecting particles, composed of alternating layers of high and low refractive index, can also be fabricated as shown in Figure 2.9.d, e. In addition to particular interest for in vivo applications, we note that the design of isolated porous particles is also of growing interest for Si-based Li-ion battery anodes, which are particularly attractive for their large specific capacity, low volume, light weight, and potentially low cost [27]. It should also be noted, that while these pSi particles are fabricated with a grating patterned stamp, in a two-step imprint and rotate technique, a wide variety of micro- and nano-particles, of varying shapes and sizes, could be realized simply by changing the stamp pattern. Also, as examined in Chapter 3 further design adjustments can facilitate >90% areal particle packing densities and improved particle liftoff.

2.3 Stamp Reusability

We examined the durability and fidelity of both Si stamps and imprinted porous samples as a function of imprinting cycles. Grating patterned Si stamps with a pitch of 5 microns were repeatedly imprinted into porous silicon samples. After imprinting 1, 4, and 20 times, SEM images were taken (see Fig. 2.10). No systematic degradation of the stamp quality or the imprint fidelity are observed.

Additional SEM and AFM images in Fig. 2.11 highlight the excellent durability of the stamp and quality of the imprinted features after twenty imprinting cycles. In some

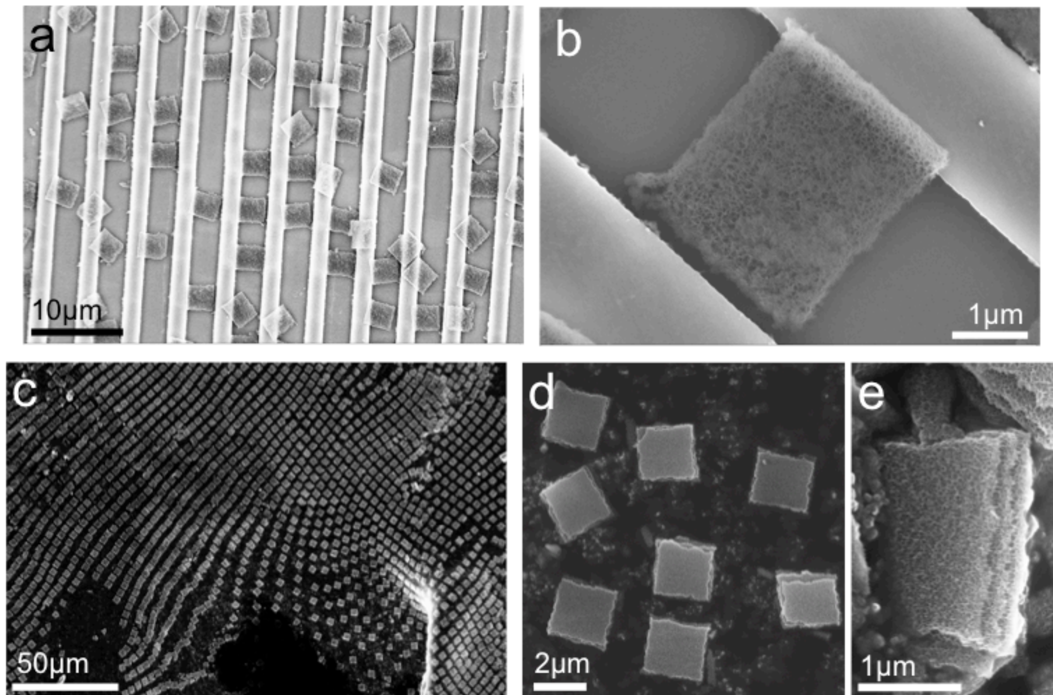

Figure 2.9: (a,b) SEM images of freestanding pSi microparticles on the Si stamp used to pattern them. After an initial stamping with a silicon grating (Λ = 5 μm, area = 9 mm^2 on a 1 μm thick 80% porosity pSi film, the stamp was rotated 90degrees and imprinted again with a force of approximately 3 kN [101]. As a result of overstamping weakening the bottom interface of the pores, some particles are removed by the frictional and electrostatic forces that exist between the pSi and Si stamp. (c) SEM image of pSi particles removed from the substrate with carbon tape [101]. (d) pSi Bragg reflector particles on carbon tape, and (e) pSi Bragg reflector particle seen on its side, showing its multiple high and low porosity layers.

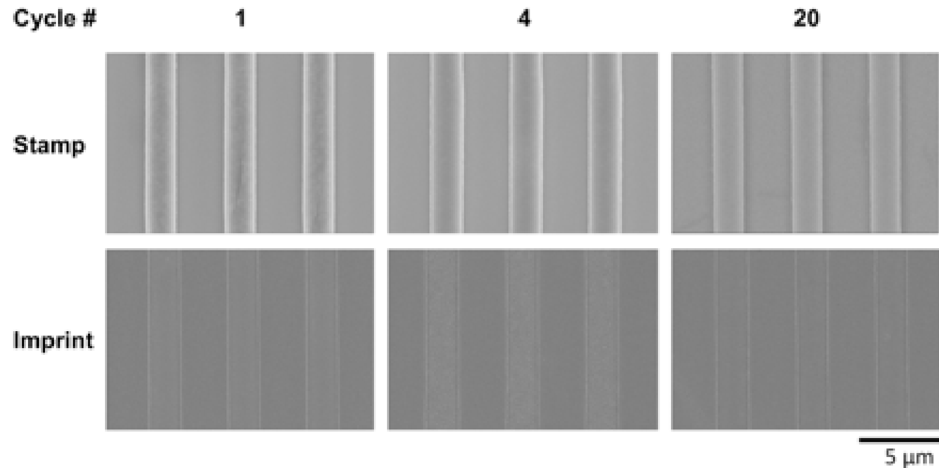

Figure 2.10: SEM images of stamps and imprinted structures after 1, 4, and 20 imprinting cycles [101]. Stamps consist of 5 μm period gratings with a height of ~500 nm, the imprinted porous substrate used is ~80% porosity pSi with a film thickness ~300 nm, that is imprinted to a depth of ~200 nm. No significant systematic reduction in the imprint fidelity or degradation of the Si stamp is observed. This result highlights the reusability of stamps used in DIPS.

cases, debris has been observed on stamp surfaces, as illustrated by the SEM in Fig. 2.12. Nevertheless, imprints made using these stamps retained high fidelity and any roughness introduced into the imprinted features could not be resolved by AFM (Fig. 2.11). Note that the quantity of porous debris adsorbed on a DIPS stamp depends on the particular material being imprinted and any preconditioning performed. Systematic cleaning of the stamp, which was not performed in this work, may help to minimize the build-up of porous debris. Additional examples of DIPS being applied for repeated patterning with the same stamp, and over large areas, can be found in the Appendix A.2.1

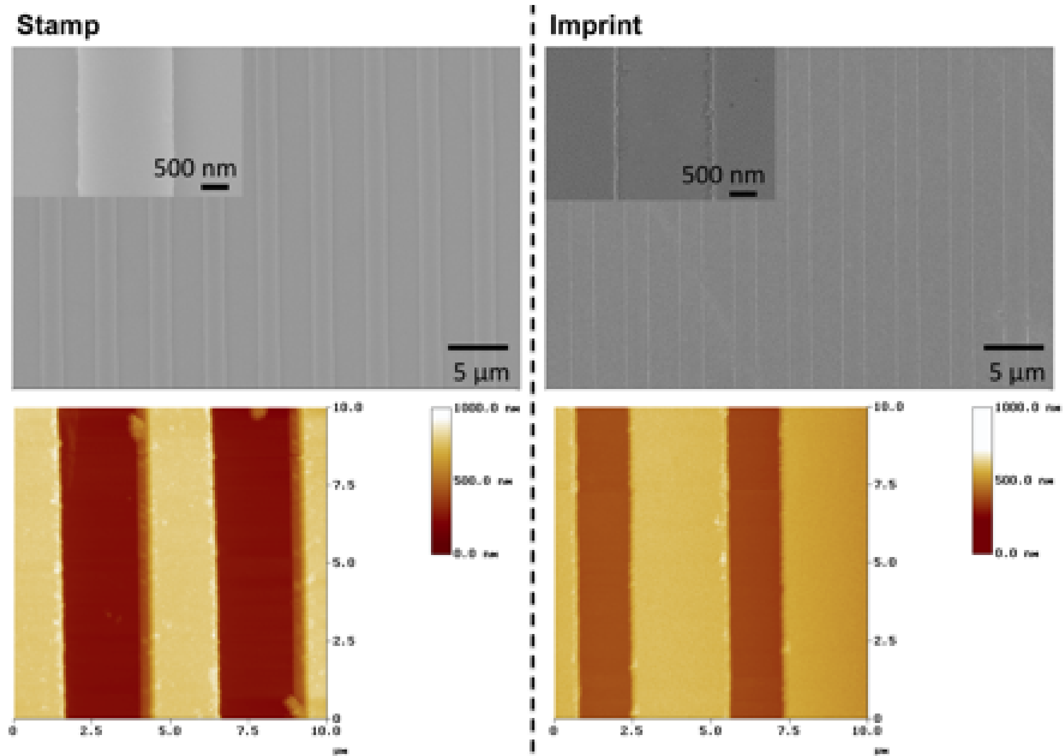

Figure 2.11: Additional SEM and AFM images highlighting the durability of the stamp and fidelity of the imprinted pattern after 20 imprinting cycles [101]. AFM does reveal some accumulation of debris on the stamp, which was not cleaned between imprinting and imaging. Despite this accumulation, the fidelity of the imprinted pattern remains very high.

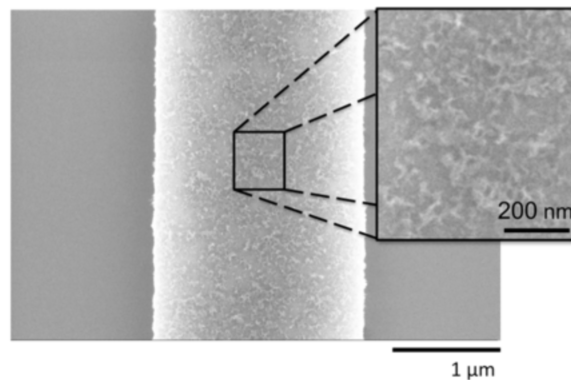

Figure 2.12: SEM images of a Si stamp revealing the adsorption of porous debris from the porous substrate that was imprinted. The imprinted substrate in this case was a 300 nm thick, high porosity ($\sim$80%) pSi sample (DIPS pressure $\sim$140 N/mm^2). Note that debris is not found on all stamps and accumulation of debris depends strongly on the material being imprinted as well as any preconditioning. Adapted from Ref. [101].

2.4 Application: Diffraction-Based Biosensing

Several recent works have adapted the DIPS technique for applications which require structuring porous nanomaterials on the micro and nanoscale. In one example, seen in Fig. 2.13.a, DIPS has been applied to pattern np-Au films for use as surface enhanced Raman scattering (SERS) substrates [105]. DIPS has also been demonstrated for producing micron scale grating couplers on porous silicon waveguides for use as optical biosensors (Fig. 2.13.b) [107]. Research efforts are also underway which seek to adapt the DIPS technique for producing pSi nanoparticles which can then be loaded with therapeutic agents and used as drug delivery vehicles (Fig. 2.13.c). Here, we demonstrate and discuss in detail how DIPS also enables the low-cost fabrication of pSi diffraction gratings, which can be utilized as diffraction based biosensors [11].

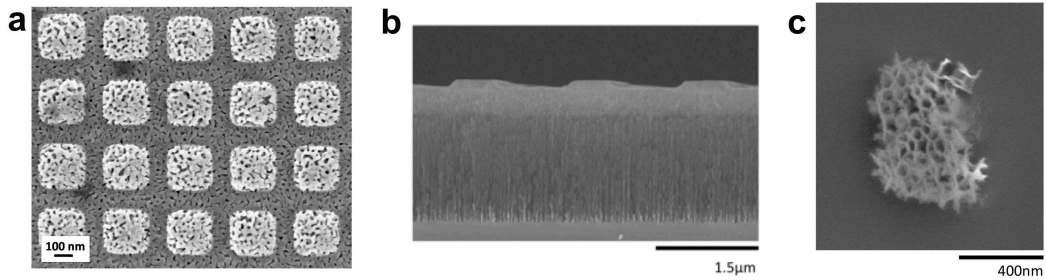

Figure 2.13: SEM images of recent DIPS enabled device applications including: (a) patterned np-Au as an effective SERS template, (b) grating coupled pSi waveguide for optical biosensing, and (c) pSi nanoparticles for drug delivery.

2.4.1 Principles of Diffraction-Based Biosensing (DBB)

A growing number of optical biosensing systems rely on expensive and bulky equipment for the high resolution determination of the angle or wavelength of optical interrogation [108].

This limits the portability of such systems, and may restrict their usefulness in sensing applications outside of a controlled laboratory environment. Diffraction-based biosensors (DBB), on the other hand, operate at a fixed wavelength and detection angle; they exploit the variation of diffraction efficiency that occurs due to the presence of a chemical or biological species on a diffraction grating [109–111]. The diffraction efficiency, taken as the ratio of the output power for a selected diffraction order to the input power, is unaffected by fluctuations in the power of the probe laser [112]. In traditional DBBs, biochemical species are selectively adsorbed onto the top surface of a diffraction grating, giving rise to an increase of the diffraction efficiency proportional to the change in the grating thickness. Similar to other traditional biosensors, the limited surface area available for biochemical attachment on the gratings ultimately limits the device performance.

The use of porous materials with large internal surface area is a promising strategy for constructing biosensing devices [10, 12, 19, 113–115]. Compared to many traditional sensors with limited surface area, porous sensors offer large improvements in device sensitivity, especially for small molecule detection. For example, the sensitivity and size-selectivity of traditional surface plasmon and waveguide sensors have been increased by the use of porous alumina [12] and porous silicon, respectively [10, 114]. Further, porous materials can be robust, and there is often great flexibility in the design of their physical and optical properties [115].

Here, we present a porous silicon diffraction-based biosensor (pSi-DBB) that combines the benefits of both diffraction-based biosensing and large surface area porous materials. Our pSi-DBB is a porous diffraction grating fabricated at low-cost and at high throughput by a stamping process on a pSi film. For a diffraction grating of thickness h much smaller

than the wavelength λ of the incident beam, the diffraction efficiency is [116]

$$\eta = \alpha(f, \Lambda, \lambda, ...)(h\Delta n)^2, \tag{2.1}$$

where Δn is the grating refractive index contrast with respect to the cladding index, and α is a coefficient that depends on the incident wavelength, the grating period Λ, the air filling fraction f, and the optical properties of the cladding and substrate. In traditional DBBs, analytes give rise to an increase (h+δh)Δn-hΔn in the optical thickness through an increase δh in the grating height. In a pSi-DBB, analytes infiltrate the pores and lead to a change h(Δn+δΔn)-hΔn in the optical thickness through a change δΔn in the refractive index contrast. These perturbations of the optical thickness lead to changes $\Delta\eta$ of diffraction efficiency. We demonstrate the feasibility of the pSi-DBB and its potential to enhance the response of traditional DBBs, while using a simpler sample preparation protocol.

2.4.2 pSi-DBB Experiments

Device Fabrication and Characterization

Porous silicon substrates were prepared through electrochemical etching of boron doped p+ silicon wafers (0.01-0.02 Ωcm) in a 15% ethanoic hydrofluoric acid electrolyte. A current density of 80 mA/cm^2 was applied for 3.5 s. From earlier work, we estimate that these conditions lead to a 140 nm thick film with ∼81% porosity [10]. Standard contact lithography and reactive-ion etching techniques were used to fabricate silicon grating stamps (9 mm^2) composed of a 5 μm pitch grating, 500 nm in depth. DIPS was then applied, using a force of ≈2000 N, which imprinted a silicon stamp grating pattern into the pSi as shown in the

AFM image in Fig. 2.14.b. The pSi-DBB used in this work has a 5 μm pitch, 29 nm grating height, and an effective refractive index $n_{pSi} = 1.205$ after oxidation in ambient conditions at 500 °C for 5 min. Partial oxidation of the pSi grating provides a suitable silica surface for attachment of biochemical species [117].

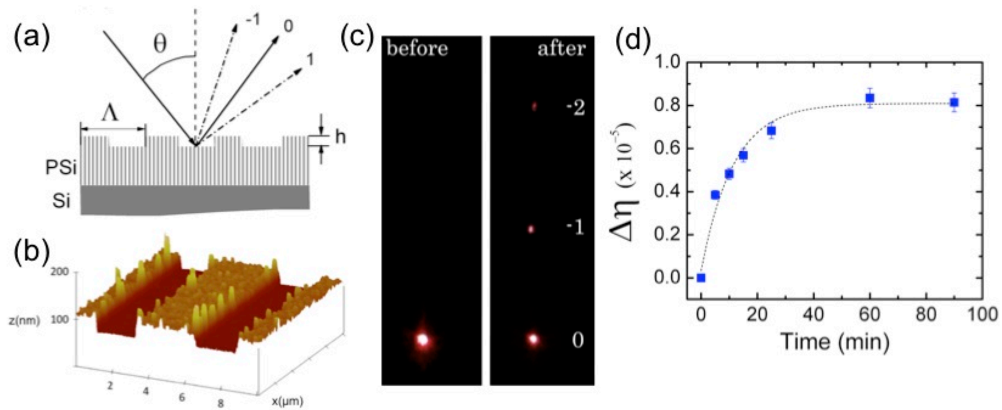

Figure 2.14: (a) Schematic of the pSi-DBB, (b) AFM height image of the pSi-DBB, (c) camera image of reflected and diffracted beams before and after water vapor condensation, and (d) change in diffraction efficiency during a 3-APTES silane attachment experiment. Adapted from Ref. [11].

Diffraction experiments were performed with the 647 nm line from an Ar/Kr laser at an incident angle of 67°. A silicon photodetector was used to monitor the input and diffracted beam powers. An input beam power on the order of 1 mW was used in all experiments. To avoid as much scattered light as possible from the 0th order beam, the diffracted intensity of the back diffracted $m = -3$ diffraction order was monitored.

Visual Response to Water Vapor

A visual demonstration of the performance of the pSi-DBB is achieved by simply condensing water vapor onto the sample. Before applying water vapor to the sample surface,

diffraction is too weak to be observed with the camera (Fig. 2.14.c, before). Once water vapor is applied to the sample, it condenses inside the pores and produces a large increase in the effective refractive index of the grating due to water ($n_{water} \approx 1.33$) displacing air ($n_{air} \approx 1$). This increase in refractive index results in a large increase in the diffraction efficiency and the visible appearance of diffracted orders (Fig. 2.14.c, after). Within a few seconds after water vapor condensation, the water evaporates from the sample and the initial diffraction intensities are restored.

Sensor Response to Small Molecules

To demonstrate the pSi-DBB performance in response to small molecules, we study the infiltration of 3-aminopropyltriethoxysilane (3-APTES), which is a commonly used and well-studied molecule for promoting adhesion between silica surfaces and organic materials [117]. pSi-DBBs are exposed to various concentrations of 3-APTES, diluted in a H_2O:methanol (1:1) mixture, at varied time intervals up to 90 min. Before each measurement, the sample is rinsed vigorously in deionized water and dried under nitrogen flow to remove unbound species. Figure 2.14.d shows the time-dependent change in diffraction efficiency $\Delta\eta$ of the $m = -3$ back diffracted beam over the course of the experiment for a 0.25% 3-APTES solution; the change saturates in approximately 50 minutes. For a 1% 3-APTES and higher concentration solutions, the diffraction efficiency saturated in less than 15 minutes. The trend shown in Fig. 2.14.d indicates binding of 3-APTES that is consistent with monolayer formation. Our observed saturation time for 3% 3-APTES is comparable to that observed in studies of mesoporous microcavity biosensors [118]. However, in the microcavity study, exposure to 0.25% 3-APTES solution led to only ~8% of a monolayer

after 20 minutes, whereas for our structure the same exposure led to $\sim$70% of a monolayer in the same time. The distinctly faster response of our pSi-DBB is attributed to the $\sim$30 nm of porous grating that must be infiltrated to produce a measurable response, compared to the nearly 2 μm that must be infiltrated in the microcavity sensor. Thus, the shallow geometry of our pSi-DBB favors very rapid small molecule detection.

The nominal diffraction efficiency η of $m = -3$ diffraction order for the 29 nm PSi grating was $\sim 1.7 \times 10^{-5}$ before silanization, and $\sim 2.5 \times 10^{-5}$ after silanization, with light collected over $\sim 1/300$ steradians. To produce a theoretical estimate of the diffraction efficiencies, we first performed reflectance measurements of uniform pSi films before and after silanization. After measuring the film thickness with SEM, transfer matrix calculations were used to fit the reflectance spectra and estimate the film's refractive index. The indices we extracted were $n_{pSi} = 1.2054$ and $n_{pSi+APTES} = 1.2454$. With the nominal grating height of 29 nm and air fill fraction 0.4, a scattering matrix calculation predicts a diffraction efficiency of $\sim 1.5 \times 10^{-5}$ before silanization and an efficiency of $\sim 2.3 \times 10^{-5}$ after silanization [119]. There would be both positive and negative corrections of these ideal calculations to compare with experiment: the first because some scattered light from the specularly reflected beam arrives within the collection window, and the second because some diffracted light that would arrive within the collection window for an ideal structure is scattered out of it. Including these corrections will require further study, but even at this stage we note the good qualitative agreement between theory and experiment. Furthermore, there is good quantitative agreement between theory and experiment for the change in diffraction efficiency with silanization. Importantly, the observed $\sim$80% increase to diffraction efficiency for the pSi-DBB is found to be more than an order of magnitude

greater than the simulated response of a comparable 30 nm grating height non-porous silicon DBB where a monolayer of 3-APTES is attached only to the top surface.

2.4.3 Real-time Sensing and Fluidic Considerations

The pSi-DBB platform offers a number of important advantages over other label-free biosensors. First, because the measured signal is simply the diffraction efficiency (i.e. a ratio of two beam powers), operation of the pSi-DBB occurs at a fixed angle and wavelength. Most other label-free biosensors, however, require interrogating a sample (i.e. performing reflectance, absorption, etc.) over a range of wavelengths or angles. Therefore, the detection limit of the sensor is generally limited by the spectral or angular resolution of the measurement system. In such systems performing a single scan can take on the order of several seconds to minutes, or longer. Furthermore, their portability is limited by the bulky and expensive equipment required to make such measurements. By comparison, the pSi-DBB is a particularly attractive technology with the potential for low-cost, and portable operation, while also offering the possibility for performing high-resolution real-time sensing measurements.

The demonstration of the pSi-DBB in Fig. 2.14.d showed ‘step-wise’ sensing, where measurements were performed after individual molecule attachment steps. In many situations, real-time sensing of fluidic analyte solutions is prefered, as this approach enables molecular infiltration and attachment kinetics to be directly monitored or compared. This method also provides immediate quantitative information, which could be vital for rapid point-of-care diagnostics or other time-sensitive scenarios. To detect analytes in liquid environments and in real-time, several design considerations must be taken into account:

i.) The influence of ambient refractive index on device sensitivity

The refractive index contrast Δn between the porous diffraction grating and the surrounding medium is expected to directly affect the device sensitivy. Theoretically, the relative change in diffraction efficiency varies as

$$\frac{\Delta\eta}{\eta} = \frac{2\,\delta(\Delta n)}{\Delta n}. \tag{2.2}$$

Therefore, it is desirable to maintain a low refractive index contrast, Δn, between the porous grating and the ambient cladding to ensure a large relative change in the diffraction efficiency during sensing. This is naturally easier to achieve in a liquid environment, where the refractive index of the surrounding medium is higher (i.e., $n \sim 1.33$ vs. $n = 1$). However, a liquid environment also tends to reduce the change in refractive index contrast, δ(Δn), that occurs due to analyte infiltration or attachment, because the refractive index of most biomolecules (e.g., $n = 1.5$) is closer to that of the liquid medium rather than air ambient. This challenge is universal to all refractive index based optical sensors, and is mostly unavoidable. Fortunately, the large surface area of the pSi assists in offsetting this effect. To further enhance sensitivity in liquid media, one possible approach is to utilize dielectric labels. For example, target molecules might first be tagged with semiconductor quantum dots, which typically have a higher refractive index than most biomolecules (i.e., $n_{QD} \sim 2.5$ vs. $n_{bio} \sim 1.5$) [120]. The larger refractive index of the dielectric label would produce a larger change in refractive index contrast, δ(Δn), per target molecule attached, thus yielding improved sensitivity.

ii.) Choosing the laser/detection configuration to avoid signal distortion in liquid cell

As shown in Fig. 2.15, there are a number of potential pSi-DBB configurations for performing real-time sensing in solution. However, care must be taken to ensure that the incident and diffracted laser light is not scattered or attenuated due to introduction of liquid environment. Perhaps the best choice is to use a backside interrogation scheme (Fig. 2.15.c), where the liquid environment does not directly interfere with the measurement. Also, adding a prism to the configuration shown in Fig. 2.15.c would improve collection of the diffracted signal and promote a better signal-to-noise ratio [111].

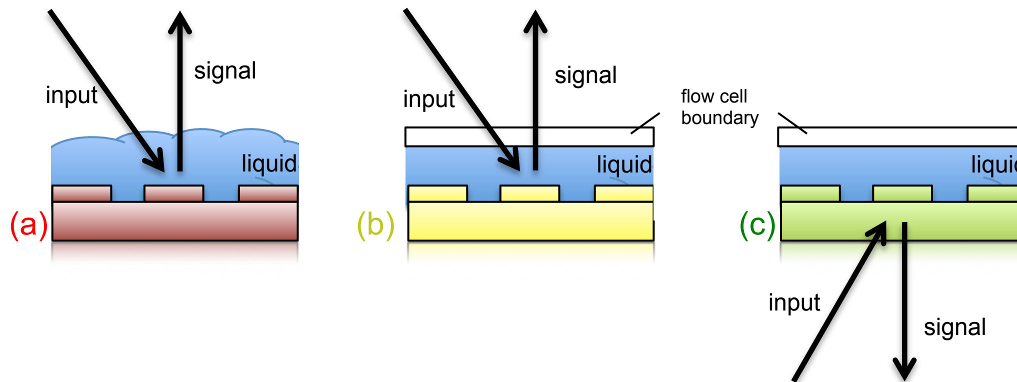

Figure 2.15: Comparison between possible pSi-DBB configurations for sensing in solution. (a) "Poor": with scattering at liquid/air interface and possible scattering or absorption in solution, (b) "OK": controlled boundary removes scattering but light attenuation in solution still possible, and (c) "Best": backside interrogation removes both issues but requires a transparent substrate.

iii.) The influence of pore size and device thickness on sensor response time

The sensor response time is an important consideration in any real-time sensing platform. In a porous material system, a number of parameters can strongly influence the response time including: (1) analyte/molecule size, (2) pore size, and (3) active porous layer thickness. While points (1) and (2) can be freely tuned depending on the particu-

lar application (and investigated in more fundamental studies [121]), point (3), the layer thickness, depends most strongly on the intrinsic design and configuration of the sensor. Importantly, the pSi-DBB requires only very thin porous gratings, with thicknesses on the order of 10 nm, to be fabricated. This promotes a fast sensor response time, especially when compared to thicker multilayer structures [11].

Real-Time Sensing Experiments

To facilitate real-time sensing, pSi-DBBs were fabricated on transparent glass substrates by DIPS in a modified multi-step process and integrated with polydimethylsiloxane (PDMS) fluidic channels. First, $\sim$100-200 nm thick pSi films were electrochemically etched at a current density of 48mA/cm^2 following the protocol from Sec. 2.2.1. DIPS was then performed with a grating patterned stamp (Λ = 5 μm, area = 9 mm^2) with an applied force of $\approx$2 kN, yielding grating heights ranging from $\sim$30-90 nm. Samples were then reinserted into the etch cell, where a $\sim$2 μm thick porous silicon mechanical support layer was etched at a current density of 48 mA/cm^2. Lift-off of the pSi film was then performed by applying between four to twelve 1.5 second long pulses of high current density (250 mA/cm^2), until detachment of the film was evident. pSi-DBB membranes were then gently rinsed and diluted in ethanol (EtOH) solution and mounted onto glass slides. After drying, thermal oxidation was performed performed at 500 $^\circ$C for 5 min in air ambient. This simultaneously anchored the pSi-DBB membranes to the glass slides and promoted growth of a surface oxide layer required for subsequent attachment of biomolecules. PDMS flow cells were then bonded to the glass slides after a brief O_2 plasma treatment. This protocol produces pSi-DBBs which can be tested in the geometry illustrated in Fig. 2.15.c.

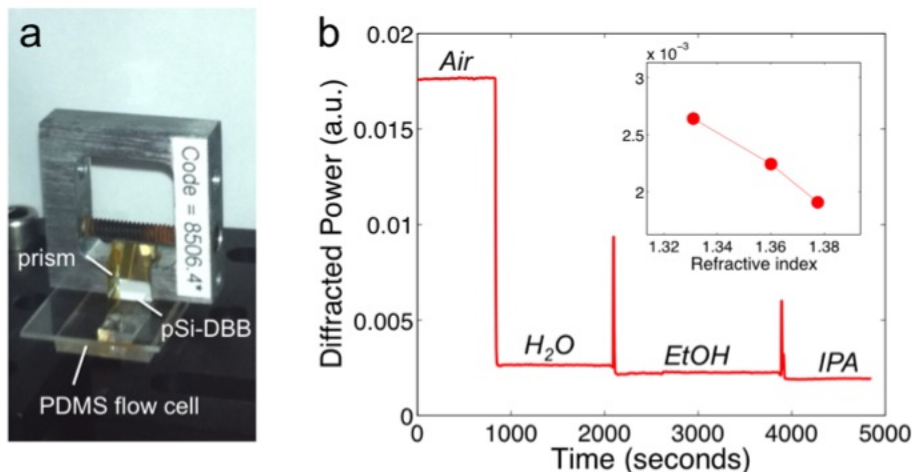

Figure 2.16: (a) Real-time pSi-DBB experimental configuration and (b) sensing of various liquid analytes. Observed spikes are due to air-bubbles during injection. The inset shows the average diffracted power vs. the liquid analyte refractive index (corresponding to the three liquids tested: water, ethanol and isopropyl alcohol). This demonstrates successful real-time refractive index based sensing with the pSi-DBB.

Measurements were performed, as illustrated in Fig. 2.15.c and shown in Fig. 2.16.a, using a Schott K5 glass prism and index matching silicone oil on the backside of the glass slide. Liquids were flowed through the PDMS flow cell using flow tubes and a manual syringe injector. The 647 nm line from an Ar/Kr laser was illuminated onto the pSi-DBB, through the prism, oil, and glass slide, and the $m = -3$ diffracted order was monitored with a silicon photodiode and power meter.

Fig. 2.16.b shows the pSi-DBB sensor response following injection of various liquid analytes with known refractive indicies including: water ($n_{H_2O} \approx 1.3310$), ethanol ($n_{EtOH} \approx 1.3601$), and isopropyl alcohol ($n_{IPA} \approx 1.3776$). As expected from Equations 2.1 and 2.2, increased refractive index of the liquid analytes results in a lower diffracted power, owing to a reduction in the refractive index contrast Δn. For small changes in Δn, the quadratic variation in diffraction efficiency, η, with refractive index contrast (Eq. 2.1)

can be reduced to a linear variation according to h(Δn+δΔn)-hΔn. The expected linear variation is experimentally confirmed, as shown in the inset to Fig. 2.16.b.

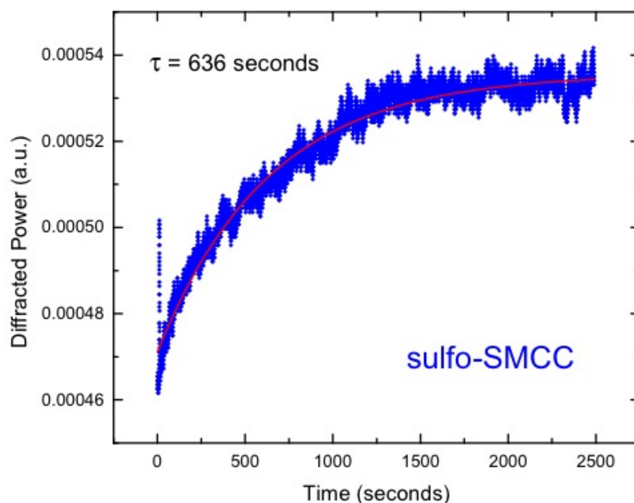

Figure 2.17: Real-time sensing of sulfo-SMCC attachment to a pSi-DBB. Red curve shows a single exponential fit, with a time constant $\tau = 636$ seconds.

To demonstrate real-time sensing of small molecules, pSi-DBB samples were exposed to small molecules, 3-APTES and Sulfosuccinimidyl 4-[N-maleimidomethyl] cyclo-hexane-1-carboxylate (sulfo-SMCC, Pierce, 2.5 mg L^{-1}). The pSi-DBB was first exposed to a 4% 3-APTES solution in water/methanol (50:50) for 20 min, to provide amine surface termination. After flushing with water, the pSi-DBB was exposed to sulfo-SMCC for approximately 40 min, and the power from the $m = -3$ diffracted order was monitored in real-time as shown in Figure 2.17. A clear increase in diffracted power is observed in response to exposure to the sulfo-SMCC. The observed trend is consistent with the expected molecular diffusion and attachment inside the pores. Unlike bulk liquid sensing (Fig. 2.16) where higher refractive index analytes reduce the refractive index contrast, Δn, the attachment of small molecules inside the pores increases Δn, thus increasing the diffracted power. Fitting

the data to a single exponential function yields a time constant $\tau = 636$ s. This time scale is consistent with monolayer formation inside the pores, and is comparable to what has previously been observed in grating coupled porous silicon waveguides [122]. Importantly, this measurement is performed with only a laser and photodetector, and circumvents the need for bulky or expensive equipment to interrogate angle or wavelength. This opens the possibility for constructing light-weight, low-cost, portable systems capable of real-time sensing using the pSi-DBB.

2.4.4 Conclusion

In summary, we have demonstrated the fabrication and highly sensitive response of a porous silicon diffraction-based biosensor (pSi-DBB). A wide range of structures of this type can be constructed. For example, our diffraction technique could be employed in a more complicated geometry where the light-matter interaction can be enhanced through a light-confinement mechanism. Further optimization of the grating material, such as the incorporation of porous alumina or porous silica could be used to reduce the refractive index contrast and increase the relative change $\Delta\eta/\eta$ in diffraction efficiency that arises in response to analyte infiltration. Our experiments and modeling suggest that the porous nature of the pSi-DBB leads to significant sensitivity improvements over traditional DBBs while maintaining the important advantages that traditional DBBs have over other detection systems: (1) operation without the need for expensive and bulky equipment to perform angular or wavelength resolved measurements and (2) self-referencing. Moreover, pSi-DBBs can be fabricated in a straightforward, low-cost, and high throughput stamping process on highly tunable porous substrates.

2.5 Summary

As illustrated in this chapter, DIPS offers an exciting and straightforward approach for realizing a large variety of important structures based on a wide class of porous nanomaterials. While our implementation of the DIPS process currently utilizes only a normal force (i.e., perpendicular to the plane of the stamp), a lateral or shear force component could also be added to produce an even wider variety of interesting imprinted topographies. We have demonstrated using DIPS for the fabrication of three classes of structures particularly relevant to porous nanomaterials including: (i) macro- to micro-scale arrays, (ii) microscale structures, and (iii) submicron to nanoscale elements. We have also examined in detail the application of DIPS toward realizing a highly sensitive, low-cost porous biosensor, the pSi-DBB. The DIPS process enables the fabrication of these structures with an unprecedented combination of fast throughput, low-cost, and high resolution. As a result, DIPS enhances both the commercialization potential and accessibility of nanostructured materials and devices. Moreover, we have demonstrated the use of DIPS on insulating, semiconducting, and metallic porous materials. DIPS circumvents the need for lithography, or masking materials and etch chemistries, that form the usual paradigms for the fabrication of structures from porous media. Thus DIPS may open a new class of low-cost technologies utilizing porous materials. In Chapter 3, we will further explore the DIPS process and demonstrate how it can be adapted to enable three-dimensional patterning and morphological control over porous nanomaterials.

CHAPTER 3

GRAY-SCALE DIPS

3.1 Introduction

In Chapter 2 we presented the direct imprinting of porous substrates (DIPS) process, which directly patterns porous nanomaterials through the application of a *binary* stamp. In this Chapter we present a method for direct three-dimensional (3D) patterning of porous nanomaterials through the application of a premastered and reusable *gray-scale* stamp – a process herein referred to as gray-scale DIPS. Four classes of 3D nanostructures are demonstrated for the first time in porous media: gradient profiles, digital patterns, curves and lens shapes, and sharp features including v-grooves, nano-pits, and cookie-cutter particles. Further, we demonstrate this technique enables morphological tuning and direct tailoring of nanomaterial properties, including porosity, average pore size, dielectric constant, and plasmonic response. This work opens a rapid and low-cost route for fabricating novel nanostructures and devices utilizing porous nanomaterials, with promising applications spanning diffractive and plasmonic sensing, holography, micro- and transformation optics, and drug delivery and imaging.

3.1.1 Introduction to Three-Dimensional Surface Patterning

Three-dimensional (3D) patterning technologies enable complex micro- and nano-structures to be realized that are otherwise unachievable by conventional two-dimensional (2D) pat-

terning routes. Gray-scale lithography (GSL) is one category of 3D patterning wherein both lateral and vertical dimensions can be precisely and arbitrarily tailored at the surface of a chip. Primary examples of GSL include gray-scale variants of electron-beam lithography (EBL), laser direct write and masked photolithography, and focused ion-beam milling [123–125]. When applied to materials ranging from semiconductors, to metals and polymers, 3D patterning technologies enable applications in diffractive and micro-optics [126–128], holography [129], plasmonics and transformation optics [130, 131], and micro-electro-mechanics (MEMS) [132]. Compared to most bulk and thin-film solids, porous nanomaterials offer a large internal surface area and distinct optical, electrical, and mechanical properties that can be controlled over a wide range by adjusting the pore morphology (i.e. porosity, pore size, and shape). Extending GSL techniques to porous nanomaterials is an especially attractive, yet unexplored, combination that would enable their unique nanoscaled properties to be exploited in many of the aforementioned applications. In addition to the fabrication of 3D structures, the ability to arbitrarily manipulate the internal porous network and achieve tailored material properties across the surface of a chip, such as laterally tuning the nanoscaled morphology or effective optical properties, could open new possibilities for many existing applications of porous nanomaterials, for example in: biomaterials [25, 26], label-free chemical or biological sensing [10, 11, 19, 133], drug delivery and imaging [16, 17], and surface enhanced Raman spectroscopy (SERS) [105].

By directly patterning porous nanomaterials through the use of a reusable pre-patterned stamp, DIPS eliminates the need for repeated application of masking materials, exposures, development, and etching chemistries. In Chapter 2, DIPS was only demonstrated using binary patterns, where a 2D stamp pattern is transferred to the porous substrate at a uniform

depth across the sample. However, there is no fundamental limitation in extending DIPS to 3D pattern replication by using a premastered 3D stamp. 3D imprinting and molding have been demonstrated in a variety of techniques on solid substrates including replica molding using elastomeric masters [134], step-and-flash imprint lithography using multi-level patterned stamps [135, 136], nanotransfer printing using conformal ink layers [137], and electrochemical nanoimprinting using solid-state superionic stamps [138].

3.2 Experimental Methods

3.2.1 Porous substrate preparation

As in Section 2.2.1, pSi films were prepared by electrochemically etching p-type Si(100) wafers (0.01-0.02 Ω cm) in a 3:7 (v/v) mixture of 49% hydrofluoric acid (HF) and ethanol. Etching was performed at a current density of 80 mA cm^{-2} with the time adjusted to control the film thickness. Reflectance measurements and optical modeling were used to approximate the initial pSi porosity at ∼80%. The underlying ∼475-550 μm thick Si wafer supported the pSi films. npAu films were prepared by a method described in a previous work [32]. Briefly, ∼1.5×1.5 cm sheets of ∼120-160 nm thick Monarch 12 karat white gold (fineartstore.com) are dealloyed by floating on concentrated nitric acid for 15 min. npAu films are mounted on ∼475-550 μm thick Si wafers coated with a >100 nm layer of Au, which is surface-modified with 1,6-hexanedithiol for robust anchoring.

3.2.2 Stamps and imprinting

Silicon stamps were prepared from $\sim$475-550 μm thick Si(100) wafers by gray-scale electron-beam lithography (EBL) followed by anisotropic reactive ion etching (RIE), unless otherwise noted. Two different PMMA resists, 950k A4 (spun at 6,000 rpm and baked at 180 °C for 10 min) and 50k A20 (spun at 2,000 rpm and baked at 180 °C for 5min) are employed to realize either shallow ($\sim$200nm) or deep ($\sim$1.5μm) structures, respectively. Gray-scale EBL (JEOL JBX-9300100kV) is performed with a 2 nA beam current, pattern shot pitch of 5nm, and a base dose of 375 μC cm^{-2}, with the relative dose modulated from -33% to 0%. Development is performed in a 1:2 (v/v) mixture of de-ionized water and IPA for 30 s, followed immediately by drying under nitrogen. Thermal reflow of the resist was performed in some cases to smooth the resist profile and remove roughness by baking at 115 °C for 10 min to 1 hr, with intermittent evaluation under dark-field optical microscopy [139]. Further detail and discussion of the gray-scale EBL process can be found in the Appendix A.3. Anisotropic reactive-ion etching was then performed (Oxford PlasmaLab 100) using C_4F_8/SF_6/Ar process gases to transfer the resist pattern into the Si substrate. For sharply pointed stamps, conventional EBL and isotropic etching in SF_6 were employed. The duration of the isotropic etch is tuned to achieve sharp features at the intersection of neighboring etch fronts. Imprinting was performed in accordance to prior work. Briefly, we use a Tinius Olsen Super L 60k universal testing machine to press a flat metallic plate onto the backside of the stamp, which is covered with single-sided Scotch tape. A computer-monitored force was then delivered and sustained for less than 1s.

3.2.3 Surface Enhanced Raman Spectroscopy Mapping

Surface enhanced Raman spectroscopy (SERS) measurements were performed using a DXR Raman microscope (Thermo Scientific) with a 780 nm diode laser at 0.9 mW power. A 10x objective (N = 0.25) was employed, resulting in a $\sim$3.1 μm spot size. Raman spectra were collected in a line-scanning mode with a 5 μm step-size, 1 s integration time and averaging of 2 scans. Prior to SERS measurements, the gradient patterned npAu sample was immersed in 10 mM benzenethiol in ethanol for 1 hour to attach a monolayer of benzenethiol to the internal gold surface. The sample was then rinsed thoroughly with ethanol and dried under nitrogen flow.

3.3 Experimental Results

Figure 3.1 illustrates the gray-scale DIPS technique. First, a pre-patterned silicon stamp with a gray-scale pattern, for example a blazed diffraction grating, is brought into contact with a porous substrate, which is prepared on a solid substrate support. Imprinting is then performed by applying a pressure on the order of 100 N/mm^2 (100 MPa), resulting in local densification of the porous network and direct patterning of the porous substrate. No thermal processing is required. The stamp can then be removed and reused many times (Sec. 2.3). To demonstrate the basic function of gray scale DIPS, we imprinted a $\sim$200 nm high, 10 μm period blazed grating silicon stamp into a 500nm thick, high-porosity pSi thin-film with a pressure of $\sim$220 N/mm^2. Atomic force microscopy (AFM) images, shown in Fig. 3.1, reveal the high fidelity 1:1 pattern transfer of the gray-scale pattern that resulted in a $\sim$200 nm height blazed pSi diffraction grating. The realization of such a grating is

technologically important for enhancing diffraction efficiency, and could be implemented to improve coupling efficiency in grating-coupled pSi waveguide biosensors or improve the diffraction efficiency in porous diffraction based biosensors [11, 38]. More advanced grating designs could enable porous nanomaterials to be cheaply implemented in a variety of diffractive optics applications, spanning from diffractive-lenses to holography, while offering a wider range of refractive indices compared to most plastics/polymers [128, 129, 134].

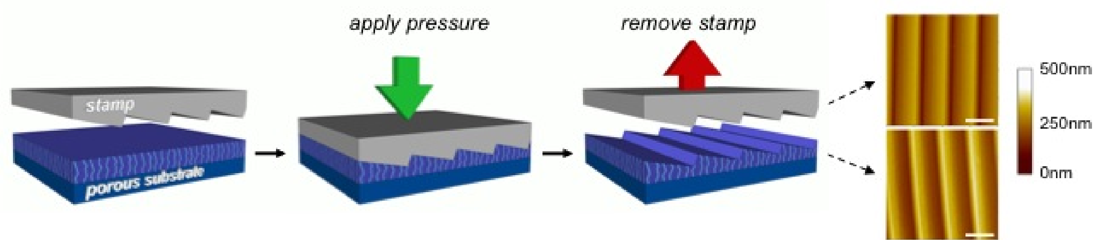

Figure 3.1: Illustration of the gray-scale DIPS process. A prepatterned and reusable stamp with a 3D gray-scale profile is imprinted into the porous substrate. The underlying porous nanomaterial is restructured, forming the desired 3D pattern. Example AFM scans of a blazed grating stamp and the subsequently patterned pSi substrate are shown on the right. White scale bars indicate 10 μm. Figure adapted from Ref. [140].

The fabrication of a blazed grating, as shown in Fig. 3.1, illustrates the basic concept of the gray-scale DIPS technique. In general, this process can be applied to realize a much wider variety of 3D patterns while further offering the unique ability to modify morphology and nanomaterial properties. In the following sections, we step through a number of relevant 3D patterns including (i) gradient profiles, (ii) digital patterns, (iii) curvilinear elements and lens shapes, and (iv) sharp features including v-grooves, nano-pits, and cookie-cutter particles. As we demonstrate these 3D patterns, we also highlight the morphological control that can be achieved over key nanomaterial properties including pore dimensions, porosity, dielectric constant or refractive index, and plasmonic response.

These novel capabilities are further examined in the context of existing technologies and potential device applications.

3.3.1 Gradient Profiles and Morphologies

Figure 3.2 shows scanning electron microscope (SEM) and optical microscope images of a $\sim$2 μm thick high porosity pSi film after applying gray-scale DIPS with a $\sim$1.5 μm height contoured silicon grating stamp. By imprinting deep gradient features into a pSi film of microscale thickness, a wide range of tailored properties can simultaneously be patterned and readily examined through standard SEM and optical imaging techniques. Cross-sectional SEM (Fig. 3.2.a, b) reveals a smoothly varying microscale height profile in the patterned pSi layer. Notably, the gray-scale profile is achieved by imparting a gray-scale densification to the porous layer. SEM reveals that the interior nano-structured porous matrix is continuously restructured, resulting in a gradient of porosities ranging from the initial $\sim$80% high porosity to a very low, nearly 0%, porosity. Throughout most of the pattern, the local nanostructure and porosity appear to be very uniform within vertical slices (z-direction) of the pSi layer. Some buckling of the pores occurs along the lowest portion of the thicker regions in the patterned film, similar to the over-stamping effect noted in our earlier work [101]. This effect can be enhanced or removed by changing the stamp height relative to the porous layer thickness, or by changing the applied pressure to adjust the imprinted film fraction.

Examining this structure with top view SEM (Fig. 3.2.c) reveals a gradient in the average pore opening size, ranging from approximately 30 nm to $<$5 nm, which coincides with the gradient in height and porosity observed from cross-sectional imaging. Optical

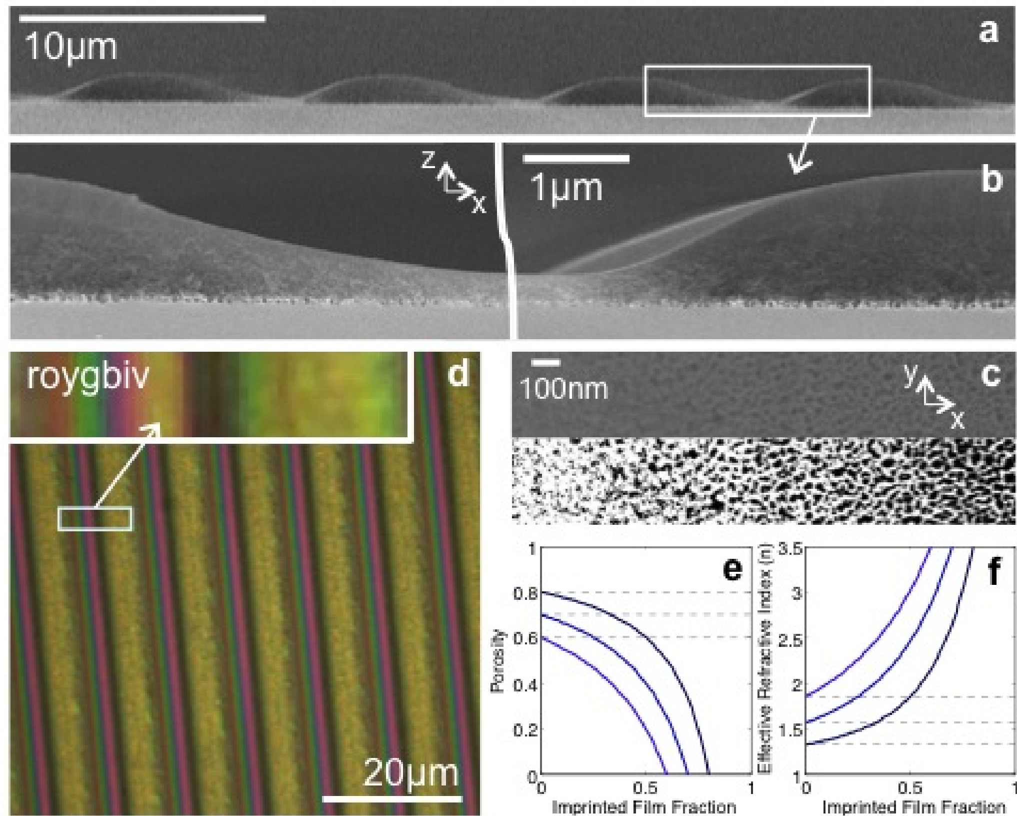

Figure 3.2: Patterning height, pore opening size, porosity and refractive index of pSi. (a,b) Cross sectional SEM images of a gray-scale patterned pSi film with a microscale height profile. (c) Top down SEM image and binary image revealing the gradient patterned pore opening; the estimated pore sizes are tuned from ∼30 nm to <5 nm in diameter. (d) Top down optical microscope image of the same pSi film under white-light illumination, revealing a strongly modulated Fabry-Pérot color response. (e) Calculated variation in porosity and (f) refractive index for pSi thin films as a function of imprinted film fraction. Figure adapted from Ref. [140].

microscopy (Fig. 3.2.d) reveals that this gray-scale patterned pSi film exhibits strong variations in white light reflectivity. The observed color gradients, which span the entire visible spectrum, result from the strongly modulated optical thickness (product of index and thickness, nL) directly affecting the Fabry-Pérot interference of the single layer thin-film. In Figures 3.2.e, f we present calculations that provide a guide illustrating how adjusting the imprint depth tunes film porosity and effective refractive index. These calculations assume uniform densification, achieved solely through a reduction of the void fraction, and an isotropic refractive index determined from a Bruggeman effective medium approximation. Based on these primary assumptions, the maximum imprintable film fraction is therefore equal to the initial porosity. Gray-scale imprinting on a high porosity, low refractive index pSi film would thus enable a wide range of refractive indices, from $\sim$1.3 to 3.5, to be realized with almost any arbitrarly designed lateral index gradient. Transfer-matrix calculations (Figure 3.3) confirm a dramatic blue-shifting color change occurs in response to imprinting.

Combined with well-established etch tuning of out-of-plane parameters (i.e., porosity and refractive index) [9, 10, 19, 38], gray-scale DIPS tunes in-plane parameters to provide a new dimension of control, and enables a new class of 3D structures to be realized. The gray-scale DIPS patterned pSi sample shown in Figure 3.2 demonstrates, for the first time, a method for manipulating the internal porous network and continuously and controllably patterning height, porosity, and pore opening size on the surface of a chip. Such a technology is expected to enable or enhance variety of device capabilities using porous nanomaterials. For example, patterning the pore opening size could be exploited for size-selective filtration or sensing applications [121], where integrating an array of different pore sizes into a compact area, on a single chip, could enable rapid and multiplexed screening

of target analytes with a specific size. Gray-scale patterning of porosity, meanwhile, could be exploited to locally control the effective refractive index and realize compact gradient index optical structures based on porous nanomaterials.

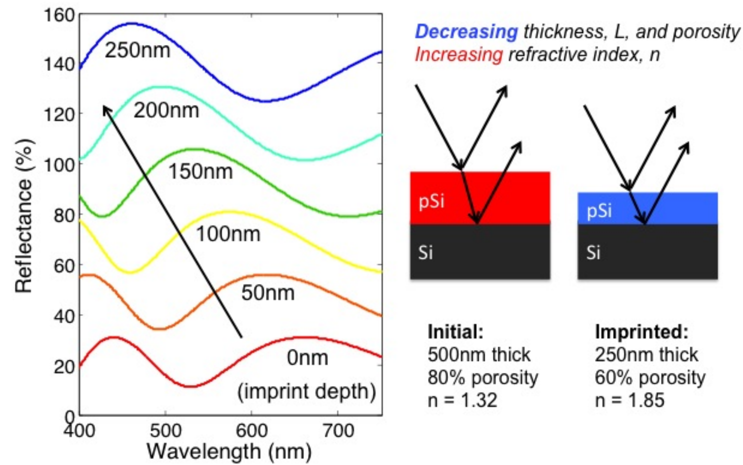

Figure 3.3: Calculated variation in visible reflectance for pSi thin films as a function of imprint depth. This example assumes an initial ∼80% porosity, 500 nm thick film of pSi. Imprinting up to 250 nm is shown to blueshift the reflectance spectra owing to the net reduction in optical thickness, *nL*. Figure adapted from Ref. [140].

3.3.2 Morphological Control Over Dielectric Constant and Plasmonic Response

Nanoporous gold (npAu) is a unique, metallic porous nanomaterial which can support both propagating and localized surface plasmonic effects [14, 15, 141, 142]. Each of these effects are particularly sensitive to the effective dielectric constant and pore dimensions, respectively. Controlling the pore dimensions and porosity of npAu is typically achieved during fabrication by adjusting the dealloying parameters [2], or by post process annealing or electroplating steps [143, 144]. To our knowledge, no method has ever previously demonstrated tunable and localized patterning of the pore size, porosity, or dielectric function in a planar metallic film.

Figures 3.4a, b reveal the complex dielectric function of npAu, as determined by ellipsometry, after uniformly imprinting npAu films to depths ranging from $0-68$ nm. Compared to bulk gold, as prepared npAu features a less negative real part of the dielectric constant, owing to its heterogeneous composition and reduced metallic-like character. After imprinting, however, the porosity is reduced and the real part of the dielectric constant is significantly decreased, i.e., from $Re(\varepsilon_r) = -4.15$ to $Re(\varepsilon_r) = -9.72$ at $\lambda = 800$ nm. Imprinting similarly tunes the imaginary part of the dielectric constant, $Im(\varepsilon_r)$, to approach that found for bulk Au. Consistent with other reports for as prepared npAu, $Im(\varepsilon_r)$ is generally 2-3 times smaller than for bulk Au in the ultra-violet and near-infrared regions, while $Im(\varepsilon_r)$ is up to twice as large compared to bulk Au at visible wavelengths [142]. We note that the observed changes in dielectric constant do not follow a direct linear relationship with imprint depth. Instead, the dielectric constant is increasingly modified at deeper imprint depths, which is expected given that porosity is also increasingly modified as shown in Fig. 3.2.e. These results confirm that gray-scale DIPS can be used to arbitrarily tune porosity and dielectric constant over a wide range by simply adjusting the imprint depth. This new capability for locally tuning the dielectric constant could be used, for example, to locally control the dispersion of propagating plasmons on npAu and enable the straightforward fabrication of plasmonic meta-devices [142, 145].

In addition to tailoring the effective dielectric constant, gray-scale tuning of the pore size of npAu also directly affects the activation of localized surface plasmons (LSP) arising from the nanoscaled morphology of npAu [144, 146]. To demonstrate this capability, we used gray-scale DIPS to pattern a 200 μm long gradient height profile in npAu, and used surface enhanced Raman spectroscopy (SERS) to probe for localized electric field enhance-

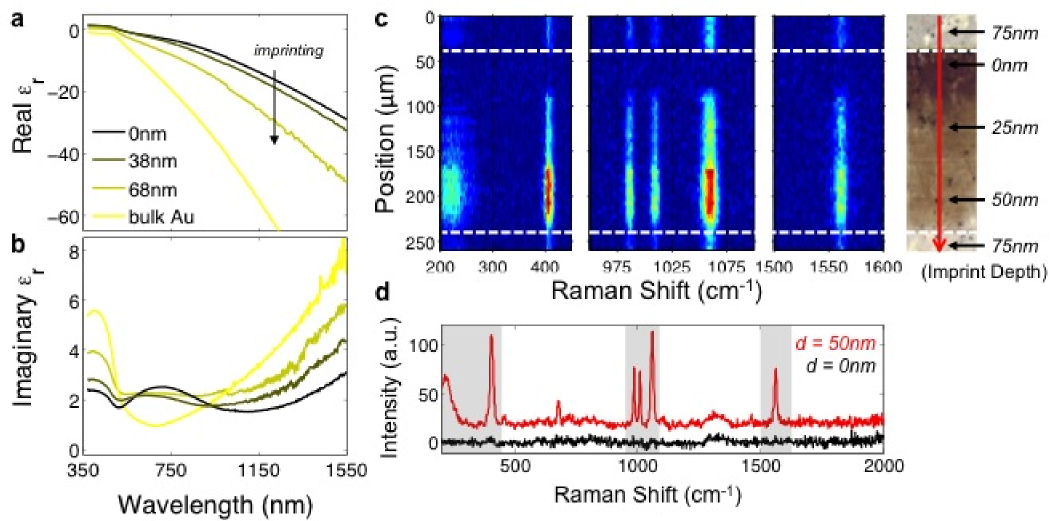

Figure 3.4: Tuning dielectric constant and plasmonic SERS enhancement of npAu. (a) The real part and (b) imaginary part of the dielectric constant of npAu, initially ∼120 nm thick, imprinted at different depths. (c) Line scanned SERS mapping of benzenethiol on gradient densified npAu. The 200 μm long gradient pattern, shown in the rightmost optical microscope image, varies in imprint depth from 0 nm to 75 nm. (d) Full SERS spectrum for benzenethiol on npAu at selected imprint depths, d = 0 nm and 50 nm. Figure adapted from Ref. [140].

ments arising from LSP (Fig. 3.4.c). Because gold itself is not Raman active, we attached a monolayer of benzenethiol which has a well-known Raman spectrum and is commonly used as a test molecule for SERS substrates [105]. Profilometry was performed to estimate a maximum imprint depth of $\sim$75 nm. The gradient densification is readily observed by optical microscopy in the form of a strong color gradient from dark to light (Fig. 3.4.c). SERS spectra were recorded in a line-scan mapping (red arrow) along the entire 200 μm gradient pattern. The non-imprinted region of the pattern ($d = 0$ nm), where the pore size is the largest, shows no detectable SERS signal (Fig. 3.4.d). As npAu is densified however, a clear enhancement of the SERS signal is observed for all the spectral bands of benzenethiol up to an imprint depth $d \approx 50$ nm. The broadband SERS enhancement is indicative of the broadband localized plasmon resonance in npAu [146], and we attribute the observed SERS enhancement to LSP activation and an increasing localized field enhancement with reducing pore size [143, 144, 146]. From prior work, the maximum SERS enhancement factor is conservatively estimated to be at least 10^6 and at least one order of magnitude greater than as-prepared npAu [105]. Beyond $\sim$50 nm imprint depth, the SERS signal is slightly reduced, although it remains detectable. The reduction in SERS enhancement beyond $\sim$50 nm imprint depth, is likely due to the average pore size reducing to the point where many of the pores have become closed. If it were possible to continue imprinting until all of the pores were closed, we expect that the SERS signal would disappear entirely, resembling planar Au films. This experiment demonstrates that gray-scale DIPS enables not only the patterning of pore size, but also tailoring of the plasmonic and SERS response.

3.3.3 Digital Patterns

In Figure 3.5 we demonstrate porous nanomaterials patterned using gray-scale DIPS with three additional types of stamp patterns: (1) digital structures, (2) curvilinear dome shapes, and (3) sharp edges and tips. Digital patterns are formed by creating a stamp with multiple discrete height values, such as the Mario test pattern shown in Figure 3.5.a. This particular pattern is encoded with four different height values, representative of the different colors contained in the Mario source image. Imprinting into a ~1.5 μm pSi film enables direct digital patterning of the pSi substrate. Optical microscopy, under white-light illumination (Fig. 3.5.f), reveals a multi-colored image that results from digitizing both the height and refractive index of the pSi layer. A cross-sectional AFM scan (Fig. 3.5.k), taken vertically across the center of the pattern, confirms high-fidelity patterning of four discrete height values in the porous substrate. A full AFM mapping of this structure, and subsequent examples, can be found in Figure 3.6. Based on this height profile, our calculations (Fig. 3.2.f) indicate that the porosity and refractive indices have been digitized to values: ~80%, 78%, 75%, 62% and ~1.32, 1.37, 1.43, 1.78, respectively. This example suggests that gray-scale DIPS could be used to realize a wide variety of digital patterns in porous nanomaterials, which is especially attractive for holographic applications where arbitrary refractive index tailoring is required to increase the number of phase levels that can simultaneously be achieved. Recent hologram designs utilize lithographic approaches to artificially tailor the refractive index through either an effective medium [147], or metamaterial approach [148], but are limited in the number of achievable values or the operational wavelength range, respectively, by the patterning resolution. Gray-scale imprinting of porous

nanomaterials, on the other hand, provides a route toward locally controlling the effective refractive index solely by the imprint depth. This promotes a broad range of accessible refractive indices while not being limited in the number of achievable index values by the lateral patterning resolution.

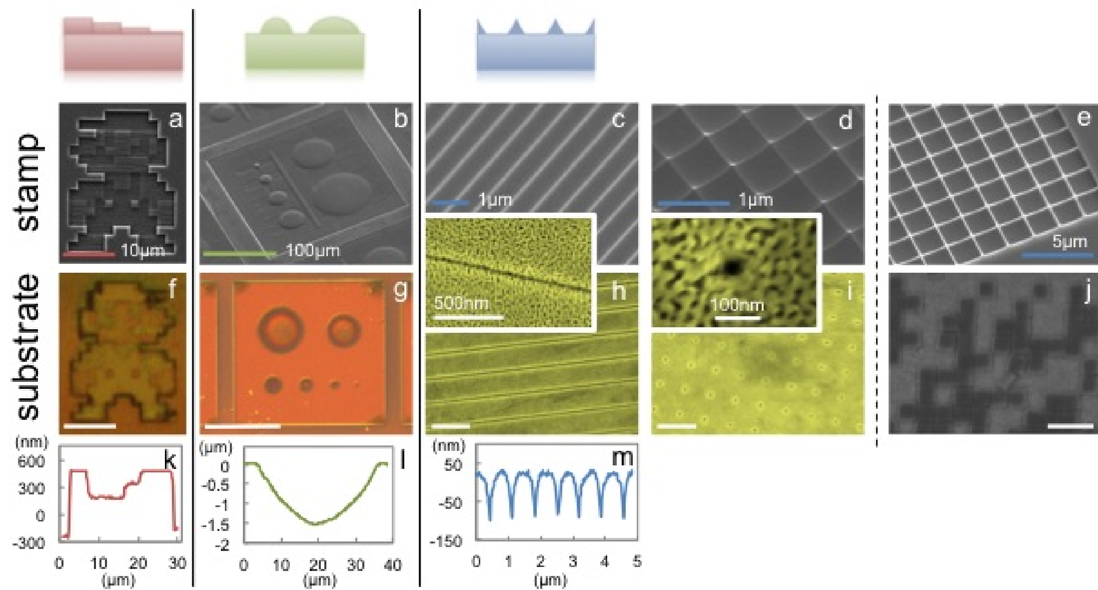

Figure 3.5: 3D patterning of discrete, curved, and sharp features. Top row (a-e) SEM images of the silicon stamps used to pattern the corresponding porous nanomaterials shown in rows two and three. (f, k) Optical miscroscope images and AFM line scans of the digitally patterned pSi Mario, and (g, l) gradient index bowl/lens shapes realized in pSi, respectively. (h) SEM images of v-grooves and (i) nano-pits realized in npAu, and (m) the corresponding AFM height profile. (j) SEM image of monodisperse cookie-cutter pSi microparticles (dimensions $2 \times 2 \times 0.5$ μm), fabricated with >90% packing density and shown loosely adhered to the original substrate. Note: substrate scale bars match their respective stamp images. Figure adapted from Ref. [140].

3.3.4 Curvilinear Elements and Lens Shapes

Figure 3.5.b shows tilt view SEM of a silicon stamp patterned with dome shaped, 3D curved, structures. Performing gray-scale DIPS with such a stamp enables the replication of bowl shaped gradient index structures in pSi. The gradient optical thickness and

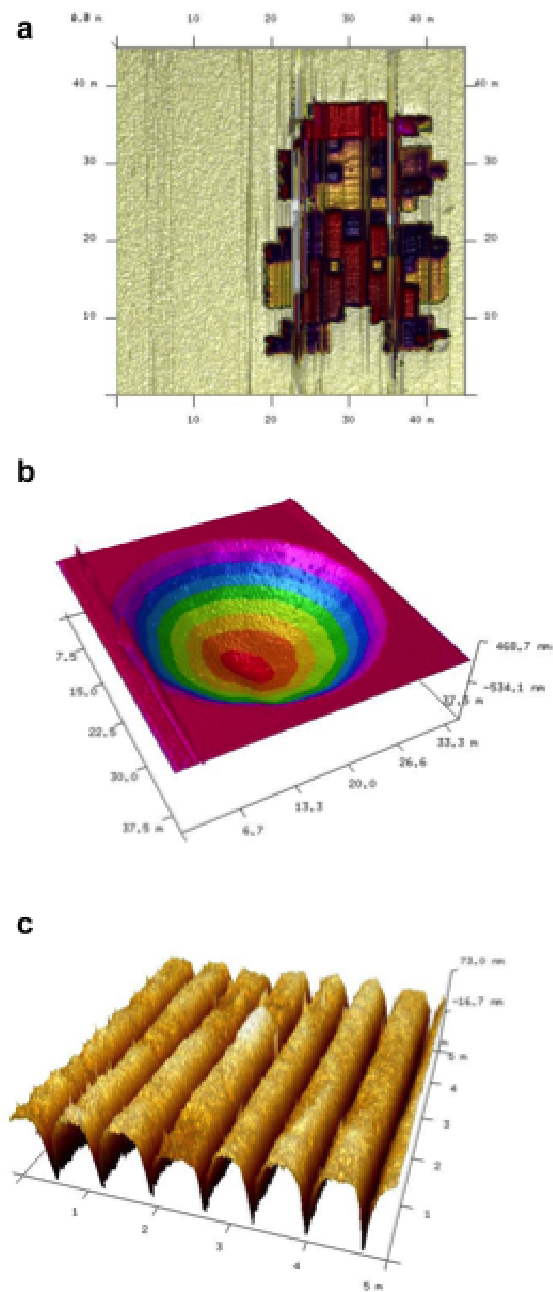

Figure 3.6: AFM height mappings of 3D patterned (a,b) pSi and (c) npAu, corresponding to the line scan profile data shown in Figure 3.5.k-m. Figure adapted from Ref. [140].

smoothly curved pSi profile are readily observable under optical microscopy (Fig. 3.5.g) and AFM (Figs. 3.5.l and 3.6.b). Based on AFM measurements and an initial $\sim 2\ \mu$m film thickness, our calculations (Fig. 3.2.f) indicate that this particular structure contains porosities and refractive indices which smoothly vary from $\sim$ 80% to 17% and $\sim$1.32 to 3.1, respectively. The low cost fabrication of devices with well-defined optical properties and 3D curvature is technologically important for realizing novel micro-optic devices. We note that it would be possible to utilize gradient index pSi waveguides to rapidly and cheaply construct in-plane transformation optic devices such as multi-functional metadevices and optical cloaks [149–151].

3.3.5 Fabrication of Nano-Grooves and Nano-Pits

The low-cost fabrication of nanoscaled metallic features, such as tips, grooves, or pits, is desireable for enabling applications spanning plasmonics, SERS, and label-free sensing. Thus, we investigate the application of gray-scale DIPS using a stamp containing sharp edge and tip patterns. SEM images of the fabricated stamps are shown in Figs. 3.5.c-e. Unlike stamps discussed previously, these sharply pointed stamps are fabricated by conventional EBL followed by isotropic RIE. The sharp vertical features are formed at the intersection of neighboring lateral etch fronts. Imprinting into a $\sim$160 nm thick npAu film enables the replication of sharp 1D v-groove and 2D nano-pit arrays, as shown in Figs. 3.5.h, i. Notably, these patterns represent the smallest features ever patterned into npAu. AFM reveals that the v-grooves and pits are $\sim$109 nm deep (Figs. 3.5.m and 3.6.c). The imprinted film fraction, $\sim$0.68, is comparable to the initial porosity, indicating that npAu can be locally densified into a nearly non-porous state. The ability to pattern sharp nanoscaled features,

with <100 nm resolution, combined with the ability to dramatically and locally tune the effective dielectric function (Fig. 3.4.a, b), enables the plasmonic properties of npAu to be tailored with improved freedom [152, 153]. Furthermore, as a direct-to-device technique, gray-scale DIPS enables these nanoscaled features to be replicated without the need for repeated lithography or etching steps.

3.3.6 Fabrication of Well Defined Cookie-Cutter Microparticles

In Figs. 3.5.e, j we show that performing gray-scale DIPS with a sharp-edged stamp pattern enables cookie-cutter pSi microparticles to be fabricated. In this example, the ∼80% porosity pSi substrate is ∼500 nm thick, resulting in pSi microparticles precisely tailored in size (e.g., $2 \times 2 \times 0.5$ μm). Although the 'overstamping' effect, discussed previously in Sec. 2.2.4, is absent in this situation because the stamp depth is deeper than the film thickness, these high porosity particles are still relatively weakly attached to the underlying substrate and many are visibly removed with the stamp after imprinting. The remaining particles can be removed using an adhesive, an electrochemical lift-off step, or by brief sonication in liquid. Notably, with this particular stamp design, we demonstrate that >90% areal packing density of highly monodisperse pSi microparticles can be achieved in a single step process. Such particles are particularly attractive for drug delivery and imaging applications [16, 17]. More advanced stamp designs could be used to tailor not only the size and shape of the particles, but also pattern the pore opening size or porosity within a given particle, enabling their optical and mechanical properties or drug loading and release kinetics to be altered. Aside from providing a high areal packing density of particles, the stamp design demonstrated here is advantageous as it reduces the total contact area between

the stamp and the substrate, enabling a clean, deep cutting imprint to be performed with a lower applied force. Moreover, the isotropically etched stamp, used here, should promote easier release of particles attached to the stamp during rinsing or sonication, owing to its smoothly curved internal surface and the lack of straight sidewalls or corners. Preliminary testing also indicates that npAu nanoparticles may be produced using the 'cookie-cutter' approach. For SEM images and a brief discussion of these results, see Appendix A.2.2.

3.4 Summary

In summary, we have demonstrated the ability to three-dimensionally pattern porous nanomaterials through a rapid and low-cost imprinting technique. Four classes of 3D structures are demonstrated: continuous sloped profiles, digital patterns, curves and lens shapes, and sharp features including v-grooves, nano-pits, and cookie-cutter particles. Importantly, beyond patterning 3D geometries, gray-scale DIPS enables nanomaterial properties to be arbitrarily tailored including porosity, average pore size, dielectric constant, and plasmonic response. Gray-scale DIPS thus opens the possibility to construct a new class of structures and devices utilizing porous nanomaterials with promising applications spanning diffractive and plasmonic sensing, holography, micro- and transformation optics, and drug delivery and imaging.

CHAPTER 4

ULTRA-COMPACT, HYBRID Si-VO_2 PLATFORM

In this Chapter, we introduce the Si-VO_2 hybrid platform and demonstrate photothermally induced optical switching of hybrid Si-VO_2 ring resonators. The devices consist of a sub-micron length $\sim$70 nm thick patch of phase-changing VO_2 integrated onto silicon ring resonators as small as 1.5 μm in radius [80]. The semiconductor-to-metal transition (SMT) of VO_2 is triggered using a 532 nm pump heating laser, while optical transmission is probed using a tunable cw laser near 1550 nm. We observe optical modulation greater than 10 dB from modest quality-factor ($\sim 10^3$) resonances, as well as a large -1.26 nm change in resonant wavelength $\Delta\lambda$, resulting from the large change in the dielectric function of VO_2 in the insulator-to-metal transition achieved by laser heating.

4.1 Motivation

Silicon-based photonics has rapidly emerged as the leading candidate platform from which to revolutionize modern computing and communications. By replacing electrical components, such as copper interconnects, with optical devices and architectures, dramatic improvements to a variety of metrics including bandwidth, speed, loss, cross-talk, and power consumption can be achieved [63]. For the realization of integrated silicon photonics, it is vital to develop compact silicon-based optical modulators that exceed the performance metrics of comparable electronic devices. Micro-ring resonant cavities have already been used to realize compact optical modulators, capable of operating at $\sim$ GHz speeds, based

on the electro-optic effect in silicon [64]. The micro-ring platform has also been used to demonstrate compact all-optical switching and logic operations on Si [154, 155], and offers a convenient architecture for performing wavelength division multiplexing (WDM) [156]. While the resonator geometry offers substantial reductions in size and energy requirements for optical switching compared to millimeter-scale interferometer approaches [65], such compact all-Si optical modulators still face a number of limitations with respect to speed and performance. The small plasma dispersion effect in silicon requires very narrow band, high Q-factor devices to be utilized. But high Q-factor devices are difficult to implement, both in terms of required fabrication tolerances and in terms of sensitivity to ambient conditions such as temperature fluctuations [63]. Indeed, high Q-factor silicon ring resonators are known to be highly temperature sensitive (30-80 pm/K) [66, 67], therefore requiring power hungry temperature compensation schemes to maintain temperature tolerances to less than ± 1 °C [68]. Additionally, the switching times of silicon based optical modulators are typically limited by carrier lifetimes for injection based devices (e.g. ~ 0.35 ns) [64], and RC constants in accumulation or depletion based devices (e.g. ~ 0.014 ns) [63, 69].

The limitations of Si modulators motivate a search for hybrid material combinations that could satisfy device requirements by incorporating a second material on the silicon platform to control modulation [70–72, 74, 75]. In one recent example, it has been proposed that intensity modulation with speeds up to 1 THz may be feasible with a hybrid polymer-silicon waveguide structure based on the all-optical Kerr effect [74]. Graphene has also recently been integrated onto silicon waveguides and used to demonstrate a high-speed electroabsorption based broadband optical modulator [157]. Similarly, VO_2 has been integrated onto silicon waveguides to function as an in-line broadband absorption modulator [75].

Phase-changing VO_2 is a particularly attractive candidate hybrid material that is well known for its reversible semiconductor-to-metal transition (SMT) occurring near 67 °C, accompanied by a structural change from monoclinic to tetragonal crystal structure [51]. The SMT results in large changes to resistivity, near-infrared transmission, and refractive index (∼1.96 to 3.25) [49]. Importantly, the phase transition in VO_2 can be triggered by a variety of stimuli aside from temperature including: strain [158], electric field [159, 160], or optical excitation [161]. In the case of pulsed optical excitation, the SMT has been shown to occur on time-scales less than 100 fs [53, 162], perhaps offering the possibility for achieving optical modulation at THz speeds.

Here we report on a silicon-based hybrid optical modulator incorporating VO_2 as the optical switching element on an ultra-compact silicon micro-ring resonator. By combining a very small, ∼0.28 μm^2, active area of VO_2 on a low-mode volume, ∼1 μm^3, resonator, large changes to resonant wavelength, and thus optical transmission, can be induced by triggering the SMT. This hybrid Si-VO_2 resonator lays the foundation for a new class of electro-optic or all-optical modulators utilizing VO_2 on Si.

4.2 Device Fabrication

The Si-VO_2 hybrid micro-ring resonator structure was fabricated on a silicon-on-insulator (SOI) substrate with a 220 nm p-type, 14-22 Ω cm resistivity, Si(100) layer and 1 μm buried oxide layer (SOITEC). Electron-beam lithography (JEOL JBX-9300100kV) was performed using ZEP 520A e-beam resist spun at 6,000 rpm (∼300 nm thick). After pattern exposure and development in xylenes for 30s followed by an IPA rinse and N_2 drying, anisotropic reactive-ion etching was performed (Oxford PlasmaLab 100) using

$C_4F_8/SF_6/Ar$ process gases to completely etch the exposed portion of the 220 nm Si layer. A second stage of electron-beam lithography (Raith eLine) was performed to open windows for VO_2 deposition, using ZEP 520A spun at 2,000 rpm ($\sim$500 nm thick) to better facilitate VO_2 lift-off. Amorphous VO_x was then deposited by electron-beam vaporization of VO_2 powder (100 mesh, 99.5% purity) in an Ångstrom Engineering deposition system. After deposition, lift-off in acetone under ultra-sonication was performed, leaving behind amorphous VO_x patches across the silicon rings. Samples were then annealed in a vacuum chamber with 250 mTorr of oxygen at 450 °C for five minutes.

The fabricated device structure is shown in the scanning electron microscopy (SEM) image in Fig. 4.1.a. The radius of the ring, measured to the center of the ring waveguide, is 1.5 μm. The ring waveguide width is $\sim$500 nm while the bus waveguide width is slightly reduced to $\sim$400 nm to promote better phase matching [163]. A coupling gap of $\sim$75 nm is employed to achieve near-critical coupling. Note that a top air cladding is used in this structure and all subsequent measurements. A $\sim$560 nm long patch of nanocrystalline VO_2 with a low-apparent roughness coats a small portion of the ring. Profilometry measurements revealed the VO_2 film thickness to be $\sim$70 nm. The quality of the VO_2 film was evaluated by temperature-dependent reflectance measurements on witness samples that consisted of VO_2 films deposited on Si(100) substrates at the same time and under the same conditions as the device structures. Figure 4.1.b reveals the hysteresis behavior in optical reflectivity, measured using a white-light source and silicon photo-detector. As the film temperature is increased beyond a critical temperature, $\sim$63 °C, a dramatic increase in reflectivity is observed, indicating initiation of the transition between semiconducting and metallic phases. The steep slope, high contrast, and relatively narrow hysteresis ex-

hibited by these reflectivity measurements indicate the high quality of the deposited VO_2 films [164]. Independent X-ray photoelectron spectroscopy (XPS) measurements on similar electron-beam deposited films further confirm the near perfect stoichiometry of the as deposited film, measured to be $V_{1.01}O_2$ [165]. The high quality VO_2, smooth surface structure of the VO_2 patch, and the corresponding optical performance are attributed to the short duration annealing conditions, known from a previous work [166].

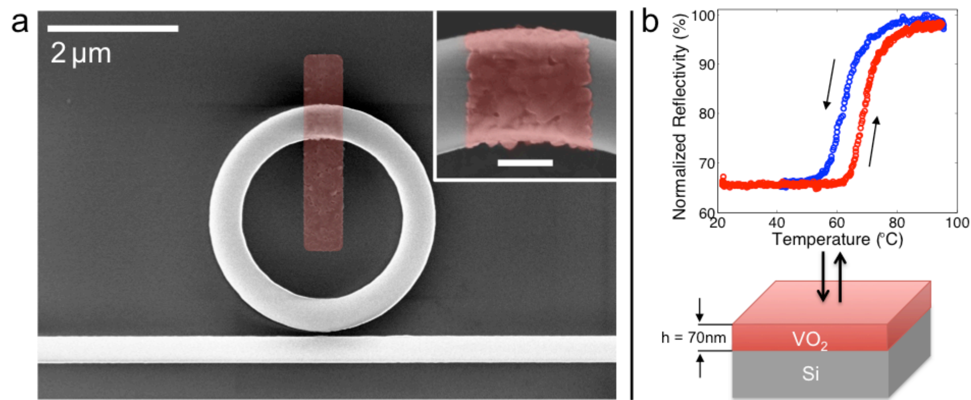

Figure 4.1: (a) SEM image of a hybrid Si-VO_2 micro-ring resonator with 1.5 μm radius. The lithographically placed VO_2 patch is highlighted in false-color. (Inset scale bar is 250 nm). (b) White-light reflectivity versus temperature on a thin film VO_2 control sample deposited on a Si(100) substrate. Adapted from Ref. [80].

4.3 Experiment and Analysis

4.3.1 Measurement Set-Up and Passive Spectral Measurements

In preparation for optical measurements, samples were cleaved across each end of the bus waveguide, several millimeters away from the central device, and mounted on an XY positioning stage. Piezo-controled XYZ stages were used to position and couple light to/from polarization maintaining lensed fibers (OZ Optics Ltd.) as shown in Fig. 4.2.a. A tunable

cw laser (Santec TSL-510) was used to perform passive transmission measurements, utilizing quasi-TE polarization, over the wavelength range 1500 – 1630 nm. Additional images and description of this optical setup can be found in Appendix B.1.1.

In Fig. 4.2.b, the transmission of two 1.5 μm radius ring-resonators with and without integration of VO_2 are compared. Both devices exhibit a very large free-spectral range (FSR) near 60 nm, which is highly desirable for enabling multiplexed photonic architectures [156, 167]. Taking the average FSR values and resonance positions, we estimate group indices of $\sim$4.385 and $\sim$4.415 for the all-Si and hybrid Si-VO_2 resonators, respectively. Note that in the case of the hybrid resonator, the measured group index comprises contributions from both the bare-Si and VO_2-coated sections. Thus, when taking into account the $\sim$6% VO_2 coverage on the ring, we approximate a group index closer to $\sim$4.9 for the VO_2 coated section of the ring waveguide. Further, we find that the Si-VO_2 hybrid resonator has deeper resonances, which suggest near-critical coupling. This result is deliberately achieved by initially over-coupling the all-Si resonator by the use of the small $\sim$75 nm air gap. Introduction of the small VO_2 patch increases the round trip loss, primarily due to the modal mismatch between the bare-Si ring waveguide and hybrid VO_2-coated waveguide sections. A more detailed discussion can be found in Section 4.3.3 where we further analyze the device Q-factors.

4.3.2 Photothermally Induced Optical Modulation

To characterize the optical response of the hybrid Si-VO_2 micro-ring resonator in both states of the SMT, a 532 nm cw pump laser (New Focus 3951-20) is focused onto the device with a 20x objective as shown in Fig. 4.2.a. An infrared (IR) camera was used for alignment

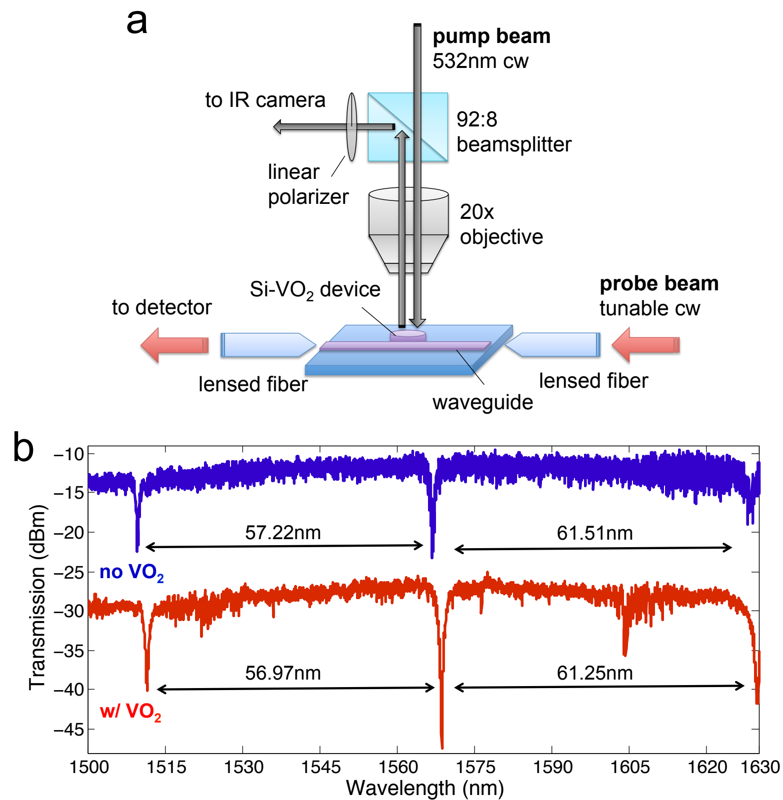

Figure 4.2: (a) Schematic of the optical measurement set-up. (b) Passive spectral measurements of optical transmission on 1.5 μm radius micro-ring resonators with (bottom) and without (top) an integrated VO_2 patch. For clarity, the top all-Si curve has been offset by +20 dBm. Adapted from Ref. [80].

purposes. IR imaging at maximum exposure and contrast settings was used to determine an upper bound for the Gaussian beam size, $w_0 \approx 90$ μm. Given that nearly 100% of the total power (P_{total}) is contained within the radius $2w_0$, we estimate the average intensity to be approximately 15 W/cm^2. The peak on-axis intensity is therefore $\sim$30 W/cm^2. In our experiments we found that precise positioning of the pump beam, to within approximately 10 microns, was required to trigger the SMT, suggesting that the peak on-axis intensity may be a more reasonable indicator of the laser intensity near the Si-VO_2 micro-ring. We note that photothermal VO_2 switching has previously been demonstrated with threshold intensities below 10 W/cm^2 for thin-films on glass substrates while under continuous optical pumping at 532 nm [168]. However, the threshold intensity and switching dynamics depend strongly on the VO_2 film thickness, and will further vary strongly with the properties of the substrate (e.g., thermal conductivity and diffusivity) and the particular geometry employed.

In Figure 4.3, we present the optical transmission of the 1.5 μm radius hybrid Si-VO_2 ring resonator as measured before and after triggering the SMT with the 532 nm pump laser. After unblocking the 532 nm laser, the system is given a few minutes to reach thermal equilibrium before again measuring the optical transmission with the tunable laser. These measurements reveal a sizeable shift $\Delta\lambda = -1.26$ nm in the resonance wavelength, coinciding with an optical modulation greater than 10 dB at the initial resonance position, $\lambda = 1568.78$nm. Because VO_2 exhibits a dramatically reduced refractive index in the metallic state, a blue-shift in resonance frequency is naturally expected to arise from triggering the SMT. However, additional effects are also expected to be present during this experiment, including dependence on: (1) the thermo-optic (TO) effect in silicon, $\Delta n/\Delta T = +1.86 \times 10^{-4}$ K [169], and (2) the free-carrier index (FCI) [170]. These two

effects are weaker than the much larger optical response of the VO_2 and, in this experiment, also carry opposite signs. Thus, the photothermal approach for triggering VO_2s SMT enables silicons TO and FCI refractive index contributions to be used against each other so that the optical signature of VO_2 can be more readily distinguished. We verified that the dominant contribution to this resonance shift was indeed coming from the VO_2 by performing a control experiment on a 1.5 μm radius Si-only ring resonator, revealing a $\Delta\lambda = +0.938$ nm net red-shift in resonance wavelength as shown in Fig. 4.4. This indicates that in the absence of TO or FCI effects, the achievable resonance blue-shift arising solely from the SMT of VO_2 is even larger than the $\Delta\lambda = -1.26$ nm value reported from this experiment. A further analysis of the interplay betwen these effects can be found in Section 4.3.3.

Figure 4.5 illustrates the time-dependent optical response at the fixed probe wavelength $\lambda = 1568.78$ nm. When VO_2 is in the semiconducting state, this wavelength corresponds to being 'on-resonance', and thus the initial optical transmission is very low. Illuminating the device with the 532 nm pump laser results in an immediate increase in the optical transmission followed by a $\sim$15 s decay toward low transmission and then an increase toward high transmission lasting about 3 min (Fig. 4.5.a). This time-dependent optical response can be explained entirely in the context of laser-induced heating. The initial spike to high transmission results from rapid heating of the silicon ring and a thermo-optic dominated shift to longer resonance wavelength; this was confirmed by repeating the experiment at slightly red-shifted probe wavelength. However, once the SMT threshold temperature is approached, the resonance immediately begins to blue-shift back toward its original position and beyond, effectively sweeping across the resonance and producing a

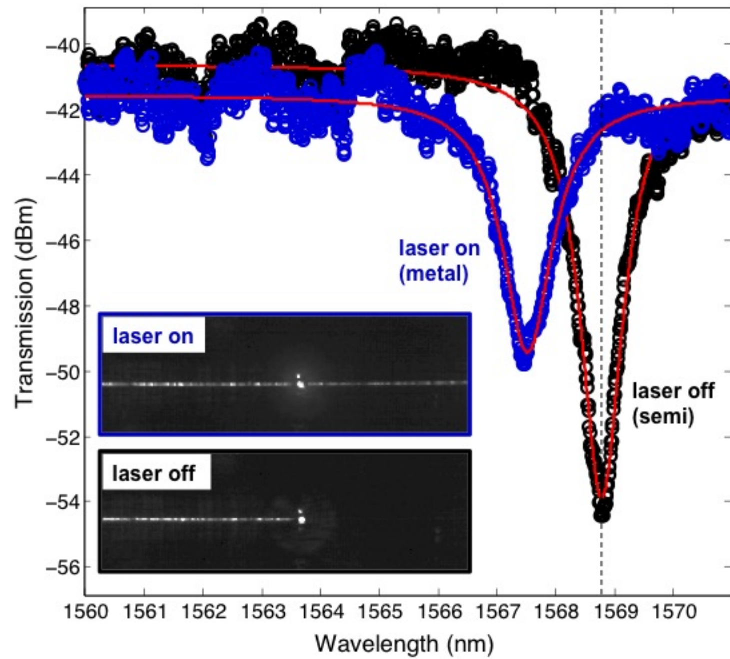

Figure 4.3: Optical transmission of the 1.5 μm radius hybrid Si-VO_2 ring resonator as a function of wavelength, before and after triggering the SMT with a 532 nm pump laser. The lines are Lorentzian fits. Inset: IR camera images revealing vertical radiation at a fixed probe wavelength, $\lambda = 1568.78$ nm (dashed line). Adapted from Ref. [80].

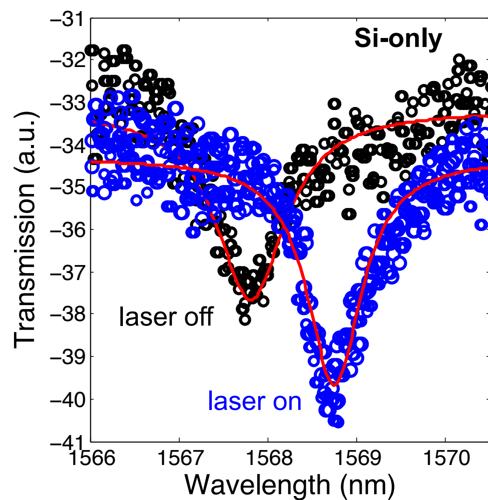

Figure 4.4: Optical transmission of a 1.5 μm radius Si-only control ring resonator as a function of wavelength, before and after turning the 532 nm pump laser on pump laser. The lines are Lorentzian fits.

dip and rise in transmission. Here we emphasize that the photothermal approach for triggering the SMT, taken in this experiment (Fig. 4.2.a), can be tuned to reduce response time by over three orders of magnitude by increasing the pump intensity [168]. Further, the photothermal technique is very robust, especially when compared to substrate heating methods. Substrate heating/cooling is relatively slow and also leads to unwanted thermal expansion or contraction of the substrate and heating stage, making it very difficult to maintain consistent coupling on- and off-chip. Localized photothermal excitation overcomes these problems and further exhibits an optical configuration in which future nanosecond and even ultrafast all-optical switching measurements could be carried out. In Chapter 5 we experimentally demonstrate and further discuss nanosecond optical switching with the hybrid Si-VO_2 platform.

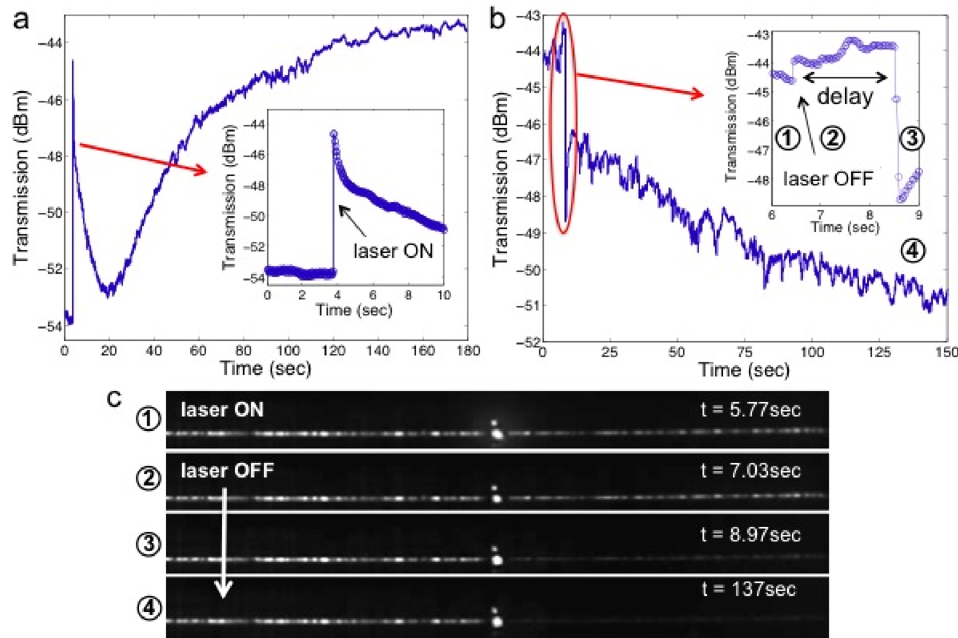

Figure 4.5: Optical transmission as a function of time at $\lambda = 1568.78$ nm, in the 1.5 μm radius hybrid Si-VO_2 device, when turning the 532 nm pump laser (a) ON and (b) OFF. (c) Single-frame images from the IR camera, highlighting the delayed probe response observed in (b). Adapted from Ref. [80].

In Figs. 4.5.b ,c we examine the optical response, again at $\lambda = 1568.78$ nm, after turning off (i.e. blocking) the 532 nm pump laser. When this occurs, the device immediately begins cooling off, ultimately resulting in a return to the VO_2 semiconducting state and an 'on-resonance' level of low transmission. However, an immediate drop in transmission is not observed; rather, turning off the laser coincides with a very small ($\sim$0.5 dB) increase in transmission followed by a $\sim$2 s delay before a dramatic, $\sim$2-5 dB, drop in transmission. The initial increase, which is repeatably observed during multiple experiments, might possibly be attributed to either a small TO shift from the cooling silicon ring waveguide or to the recombination of photo-generated carriers in the silicon, which would eliminate free-carrier absorption effects. Most importantly however, we attribute the $\sim$2 s delay to device cooling at temperatures above the threshold SMT temperature. Once the threshold temperature is reached, the transition between metallic and semiconducting states is triggered. The $\sim$2 s delay between the pump shut-off and large probe response is similarly observed using the IR camera (Fig. 4.5.c), and is strong evidence that a complete SMT indeed takes place prior to blocking the pump laser beam. After crossing the metal-to-semiconductor threshold temperature, the device requires several more minutes to cool completely back to room temperature. We note that this cooling time-scale is not fundamental to the phase-transition, but is rather a function of our experimental configuration and the absence of well-designed heat dissipation components in this proof-of-concept experiment.

4.3.3 Influence of Ring-Size and VO_2 Fractional Coverage

In addition to the 1.5 μm radius hybrid Si-VO_2 resonator, we also fabricated and tested devices with larger radii of 5 μm and 10 μm. For comparison purposes, these devices were

made with VO_2 patches of the same dimensions as the 1.5 μm radius structure ($\sim$560 nm long). In Fig. 4.6 we plot the observed resonance shift, $\Delta\lambda$, normalized to the initial resonance position, after photothermally triggering the SMT. Interestingly, these results show a trend of decreasing blue-shift with increasing ring radius. As mentioned in Section 4.3.3, there are a number of effects contributing to the net resonance shift, primarily including: the SMT in the VO_2, and the TO and FCI effects in silicon. The net contribution of these effects to the effective index change N_{eff} of the hybrid micro-ring can be approximated by

$$\Delta N_{eff} = \Delta N_{SMT}\left(\frac{L_{VO2}}{2\pi R}\right) + \Gamma_{Si}(\Delta n_{TO} + \Delta n_{FCI}), \tag{4.1}$$

where ΔN_{SMT} represents the change in effective index of the VO_2 coated waveguide section, which has a length L_{VO2}, R is the ring radius, Γ_{Si} the field confinement factor within the Si portion of the waveguide [171] and Δn_{TO} and Δn_{FCI} are the refractive index changes arising from the TO and FCI effects in silicon, respectively. Here the effective index N is distinguished from the real refractive index n by capitalization. Although this model is somewhat simplified, the fractional VO_2 coverage on the hybrid micro-ring is taken into account with the term $L_{VO2}/2\pi R$. Three-dimensional, finite-difference time-domain (FDTD) mode calculations for a 220 nm$\times$500 nm SOI waveguide coated with $\sim$70 nm of VO_2 on top reveal $N_{semi} = 2.49$ and $N_{metal} = 2.42$ near a wavelength of 1568 nm, resulting in $\Delta N_{SMT} = 0.07$. Experimentally, we estimate $\Delta N_{SMT} = 0.105$ after applying Eq. 4.1, where the measured resonant response is related to the change in effective index by $\Delta\lambda/\lambda = \Delta N_{eff}/N_g$ where N_g is $\sim$4.4 for the ring waveguide. The change in effective index due to the TO and FCI effects is estimated to be $\Delta N_{Si} = +4.95 \times 10^{-4}$ in the control experiment on the ultra-

compact 1.5 μm radius ring resonator. Overall, there is good agreement between simulation and experiment for the change of effective index, ΔN_{SMT}, induced by the SMT of VO_2. The experimentally determined value of $\Delta N_{SMT} = 0.105$ is very large, especially when compared to conventional silicon based modulators where ΔN_{Si} is typically on the order of 10^{-4} [63], enabling significant changes to the overall effective index of the ring resonator, N_{eff}, to be realized.

Reducing the fractional coverage of VO_2 on the ring (e.g., by increasing R or decreasing L_{VO2}) diminishes the effect of the SMT on the overall effective index change. This results in a corresponding reduction in resonant response, as observed in Fig. 4.6.a. This sort of behavior would be present even in the absence of TO or FCI effects. Further the observed change of sign in the resonant response (from blue-shift to red-shift) for the largest ring radii is an expected result occurring when the TO effect in Si dominates the overall effective index change. When adapting this device structure for operation under different conditions (e.g., triggering the SMT by electrical or all-optical excitation) it is important to recognize that the achievable resonance shift can be precisely tuned by varying the fractional VO_2 coverage on the resonator and probably by the volume of the VO_2 patch. Furthermore, the resonant response could be adjusted by employing alternate waveguide geometries, such as the slot waveguide or pinch waveguide [171, 172], which could simultaneously maximize ΔN_{SMT} and minimize Γ_{Si}. In considering alternate waveguide geometries, however, it will be important to take account of the trade-off between increased resonant response, $\Delta\lambda/\lambda$, and the potential for increased losses, or reduced Q-factor.

Figure 4.6.b shows the Q-factor of the different radii hybrid resonators, both before and after photothermally triggering the SMT, as determined by fitting the resonances to

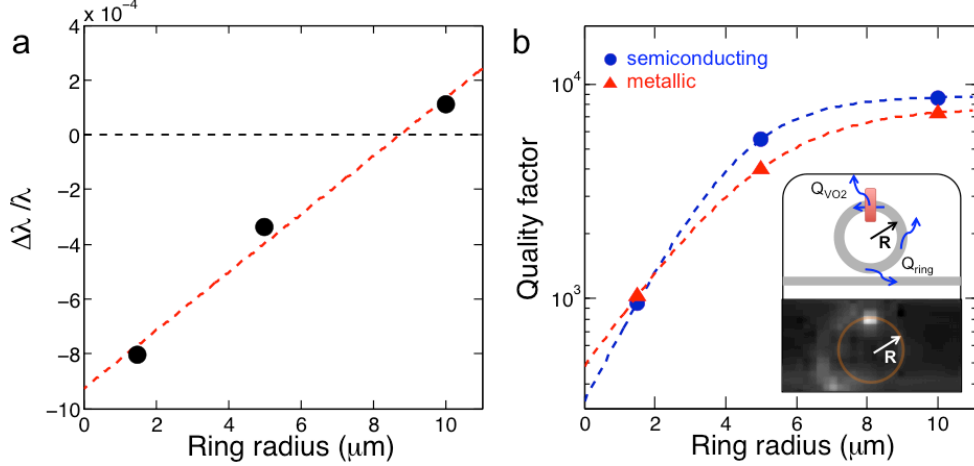

Figure 4.6: (a) Normalized resonance shift after photothermally triggering the SMT for hybrid Si-VO_2 micro-ring resonators of different radii and the same VO_2 patch length L_{VO2} = 560 nm. (b) Corresponding Q-factor for these devices before and after triggering the SMT. Inset illustrates the various decay channels affecting total Q-factor and an IR camera image showing vertical radiation from a 10 μm radius hybrid resonator when 'on-resonance' in the semiconducting state. Adapted from Ref. [80].

a Lorentzian lineshape. In both cases, we observe a trend of increasing Q-factor with increasing ring radius. An exponential increase in Q-factor is generally expected to occur with increasing ring radius, owing to a corresponding exponential reduction in bending losses [163]. While we do observe an exponential increase in Q-factor when increasing the radius from 1.5 μm to 5 μm, this increase appears to plateau at larger ring radii. This result can be explained by decomposing the total Q-factor, Q_{tot}, into the primary decay channels of coupling loss and propagation loss through the relation:

$$\frac{1}{Q_{tot}} = \frac{1}{Q_{coup}} + \frac{1}{Q_{prop}}. \tag{4.2}$$

We can further isolate the sources of propagation loss, as coming from the Si ring or the VO_2 patch [75], by:

$$\frac{1}{Q_{prop}} = \frac{1}{Q_{ring}} + \frac{1}{Q_{VO2}}. \tag{4.3}$$

The dashed trendlines shown in Fig. 4.6.b were obtained by combining Eqs. 4.2 and 4.3 and assuming Q_{ring} to have an exponential dependence on ring radius. The trends show that for low ring radii the Q-factor is primarily limited by bending loss, while for larger ring radii the Q-factor is limited by loss induced from the presence of the VO_2 patch. IR camera imaging of the 10 μm radius hybrid resonator (inset 4.6.b) further confirms that vertical radiation losses are primarily coming from the location of the VO_2 patch. Furthermore, we note that transitioning from the semiconducting to metallic state is expected to result in a decrease of Q_{VO2} owing to the increased absorption of the metallic VO_2 film. However, because we have employed a short $\sim$560 nm long patch of VO_2, the added round trip losses due to absorption in the metallic state are expected to be very low [75], and the change in Q_{VO2} should be relatively small. This matches our observations, as we find a decrease of Q_{VO2} from $\sim$8,800 to $\sim$7,800. The SMT would yield a more dramatic change to the Q-factor if a larger VO_2 fractional coverage were utilized. Photogenerated carriers in the Si, under $\sim$15 W/cm^2 532 nm illumination, are another potential source of increased losses within the ring, and in the present experiment may be generated at significant rate, $\sim 10^{23}$ cm$^{-3}s^{-1}$. However, past work has shown that while carrier concentrations on the order of $\sim 10^{17}$ cm^{-3} (which could be achieved in the present experiment assuming a $\sim$1 μs effective carrier lifetime) are large enough to produce large, nm scale, resonance blueshifts, the added losses are still several times smaller than the intrinsic scattering losses of a conventional ring resonator with a 5 μm radius [154]. Therefore, the absorption loss induced

from photogenerated carriers is not expected to account for a significant fraction of the total losses, especially when compared to the bending losses at low ring radii or radiation losses induced from the VO_2 patch. We emphasize the experiments reported here demonstrate that a small fractional coverage of VO_2 ($\sim$6%) on a silicon ring is sufficient to produce a large resonant response and almost no effect to the total Q-factor in the case of the ultra-compact 1.5 μm radius device. Further, the modest Q-factor ($\sim 10^3$) results in a very short cavity lifetime ($<$ 1ps), opening the possibility for future ultrafast operation.

4.4 Si-VO_2 Mach-Zehnder Interferometer

4.4.1 Concept and Simulation

In addition to the ultra-compact Si-VO_2 ring resonator, we also consider the Mach-Zehnder interferometer (MZI) geometry. In principle, the SMT of VO_2 can be harnessed to induce a phase shift in an optical signal and thus achieve modulation through interference with a reference signal. 2D FDTD simulations shown in Figure 4.7 demonstrate the operation of a Si-VO_2 hybrid MZI for the modulation of an optical signal at 1550 nm. This device (non-optimized design) utilizes a 20 μm active length coating of VO_2 (80 nm thickness) on the sides of a 600 nm wide silicon waveguide. In the 'ON' state, the VO_2 coating on each arm is free from external stimuli and thus the VO_2 on both arms have the same refractive index ($n_{VO2} \sim 3.2$), producing no relative phase shift (Fig. 4.7.b). However, when the VO_2 of one arm is modulated toward the metallic state ($n_{VO2} \sim 1.8$) the modal index of that arm is significantly reduced ($\Delta N \sim 0.12$) and a relative phase difference is produced. This relative phase difference between the two arms leads to destructive interference and a dramatic

reduction in transmitted intensity (Fig. 4.7.c). The dynamic refractive index variation of VO_2 favors the construction of highly functional MZIs with an active lengths on the micrometer scale - a significant advance compared to purely Si-based devices (∼mm scale). Importantly however, this simulation does not consider the losses induced in the metallic state. For micro-scale patch lengths of VO_2 the increased losses will lead to significantly reduced fringe contrast since the intensity in each arm of the MZI will no longer be equal. These effects are examined in the photothermal experiment described below.

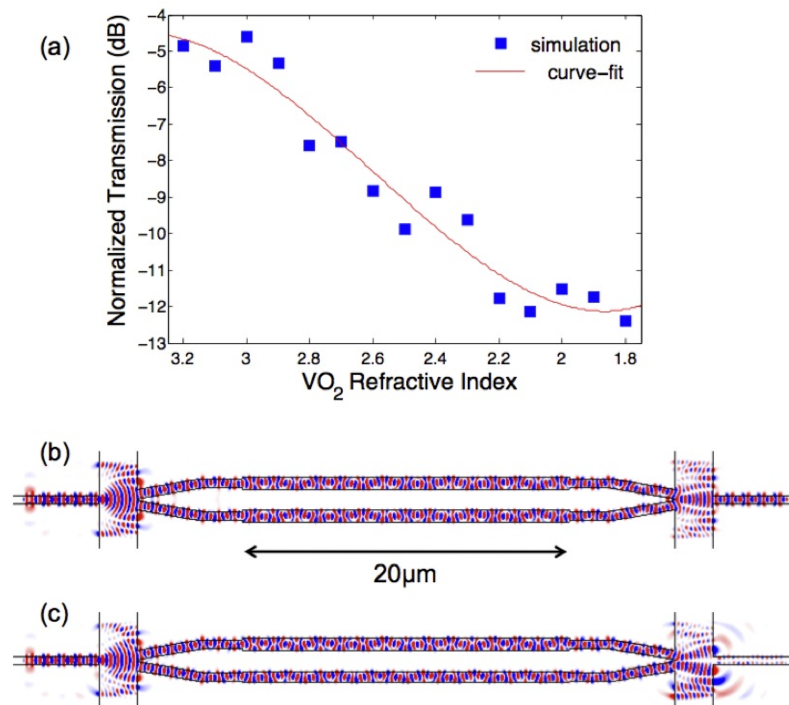

Figure 4.7: (a) Normalized transmission simulation of a Si-VO_2 hybrid MZI as a function of VO_2 coating refractive index at 1550 nm; (b) and (c) Electric field profiles, at 1550 nm, for the MZI in the 'ON' state ($n_{VO2} \sim 3.2$) and the 'OFF' state ($n_{VO2} \sim 1.8$) respectively.

4.4.2 Photothermal Experiments

Unbalanced MZI Characterization

MZI devices were fabricated using an unbalanced geometry (Fig. 4.8.a) adapted from Ref. [173]. Although it is less compact than a balanced geometry, the unbalanced structure features a 'built in' optical path length difference, producing interference fringes and sharp spectral features which are favorable for performing sensitive measurements of phase or refractive index with an improved signal-to-noise ratio. Prior to VO_2 deposition and active measurements, a chip containing unbalanced MZIs with varying path length differences, L, was characterized. The measured transmission curves (Fig. 4.8.b) confirm that the fringe spacing, $\Delta\lambda$, is inversely related to the optical path length difference L, as predicted from the relation $\Delta\lambda = \lambda_0^2/(2\ n_g\ L)$ where n_g is the group index of the silicon waveguide. By performing a Fourier transform of the transmission spectra (which can be interpolated to an x-axis of wavenumber (nm^{-1}) instead of wavelength (nm)), the nL components can be extracted as shown in Fig. 4.8.c. This analysis technique is similar to methods commonly used in reflective interferometric Fourier transform spectroscopy (RIFTS) and optical backscatter reflectometry (OBR) [174, 175] and enables experimental determination of the group index. The measured group index of the Si ridge waveguides, $n_g \approx 4.36$, is close to the group index previously determined with the ultra-compact ring resonator in Sec. 4.3.1. Note: the varying FFT peak heights (Fig. 4.8.c) arise due to the varying losses induced by unbalanced phase shifter and the imperfect performance of the 50:50 splitter and combiner.

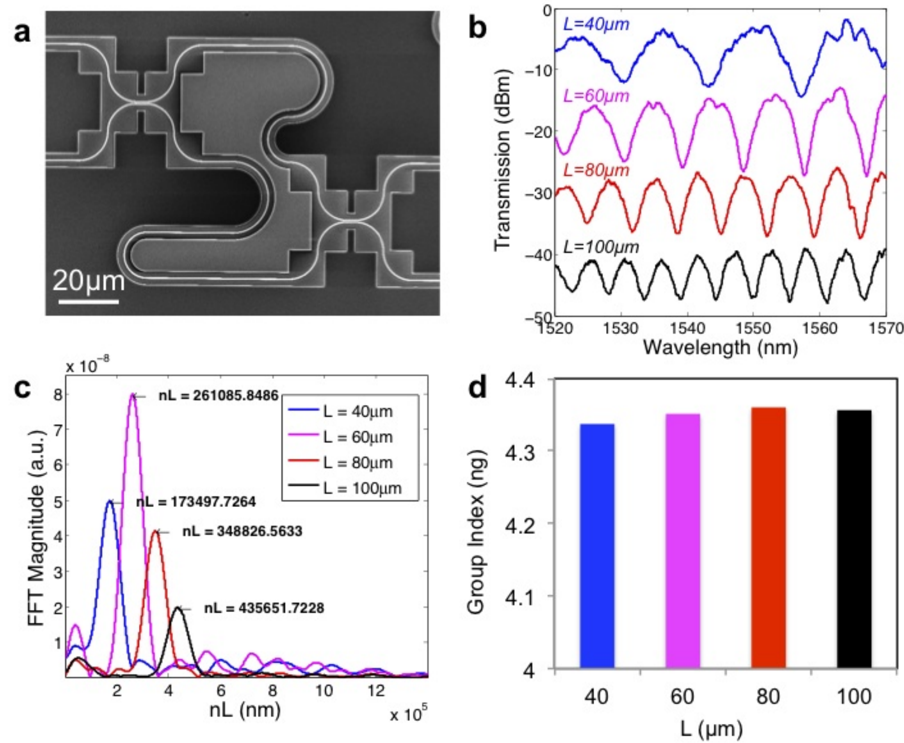

Figure 4.8: (a) SEM image of an unbalanced Si based MZI, (b) Transmission spectra for MZIs with various arm length differences (vertically offset for clarity), (c) Fourier transformed transmission spectra with peaks corresponding to the optical path length nL, and (d) group index, n_g, determined from nL values obtained from the Fourier transforms.

Si-VO_2 MZI Switching

Figure 4.9 shows the experimental results for photothermally switching a hybrid MZI with a $L_0 = 100\ \mu$m path length offset and a VO_2 patch length $L_{VO2} = 2\ \mu$m. Photothermal SMT triggering was performed under the same pump geometry and conditions used for the hybrid ring resonators (Sec. 4.3.2). The transmission spectra shows a clear blueshift of the interference fringes, as well as a reduced fringe amplitude. The transmitted intensity was modeled using the equation

$$I(\lambda) = I_{ref} + I_{VO2} + 2\sqrt{I_{ref}\, I_{VO2}}\ \cos\left(\frac{2\pi\, n_g\, L_0}{\lambda} + \phi_c + \Delta\Phi\right), \tag{4.4}$$

where I_{ref} and I_{VO2} are the intensities in the reference and active VO_2 arms, ϕ_c is a fixed fit parameter that accounts for any phase shift arising from the two couplers, and $\Delta\Phi$ is the phase shift induced by the photothermal stimuli. This simplistic model assumes the intensity in each arm does not vary with wavelength and similarly assumes the phase shift is independent of wavelength. The shifted spectra, corresponding to 'laser on', is fitted to a phase shift $\Delta\Phi \approx -0.584$ rad. The negative value indicates that the SMT dominates the phase shift with a decreasing effective index. As with the ring resonator experiment, TO and EO effects in the silicon waveguide also contribute to the phase shift. Although similar values for Δn_{TO} and Δn_{EO} should be expected, isolating each effect's relative contribution to the overall phase shift $\Delta\Phi$ is challenging because the path length over which each effect occurs, i.e. L_{TO} or L_{EO}, is not a fixed parameter as it is in the ultra-compact ring resonator (where we assume $L_{TO} = L_{EO} = 2\pi R$). We can simplify the situation by assuming the TO and EO effects approximately balance each other out ($-\Delta n_{TO} L_{TO} \approx \Delta n_{EO} L_{EO}$). The

effective index change, Δn_{SMT}, induced by the photothermal stimuli can then be approximated by $\Delta\,\Phi\ \approx\ 2\pi\ \Delta n_{SMT} L_{VO2}/\lambda$, yielding $\Delta n_{SMT} \approx -0.07$. Although the EO and TO effects would produce small positive or negative corrections to this value, we note that this approximation is in good agreement with values obtained on the hybrid Si-VO_2 ring resonators. FFT analysis was also performed on the data to estimate the group index for the hybrid Si-VO_2 waveguide, resulting in $n_{g,\ semi} \sim 5.21$ and $n_{g,\ metal} \sim 6.01$. The group indices are notably larger than conventional Si ridge waveguides. This effect confirms the strong optical confinement present in the Si-VO_2 hybrid waveguides and arises primarily from a stronger wavelength dependence on the mode profile and effective index, as well as increased material dispersion in the VO_2.

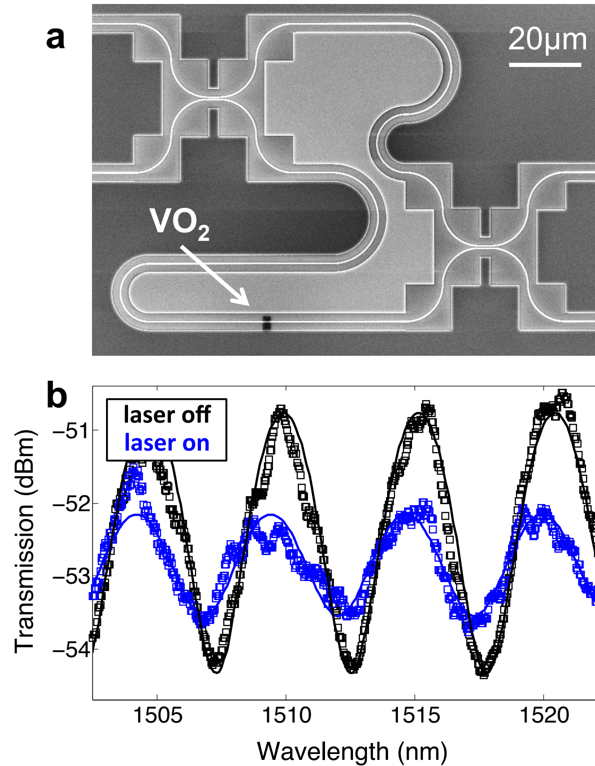

Figure 4.9: (a) SEM image of an unbalanced Si-VO2 hybrid MZI, (b) Transmission spectra and model fits for VO_2 in the semiconducting (laser off) and metallic (laser on) states.

The reduced amplitude of the spectral fringe pattern, observed after turning the laser on, was fit with intensity in each arm reduced to 0.9 I_{ref} and 0.14 I_{VO2}. Although ideally I_{ref} should remain unchanged, the reduction factor of ~0.9 was found to be necessary in order to achieve a good fit. This indicates either that the fiber-to-chip coupling was not constant over the course of the experiment or that the experiment induces some additional loss in the references arm (which may be reasonable considering the large spot size of the laser). By normalizing the intensity change in the VO_2 arm to the change in the reference arm we can estimate the modulation induced by the SMT as $0.14/0.9 \sim 0.156$.

Considering the 2 μm VO_2 patch length, this change in transmission corresponds to a large absorption modulation value ~ 4 dB μm^{-1}. For micro-scale VO_2 patch lengths (required to achieve $> \pi/4$ phase shifts) the significant losses indicate that the Si-VO_2 hybrid MZI would most likely be impractical for performing optical modulation. The effect of increasing insertion losses in the metallic state with increasing VO_2 patch length are modeled using Eq. 4.4 and plotted in Figure 4.10. These calculations assume a 100 μm unbalanced MZI with idealized 50:50 couplers and that the SMT induces both an absorption modulation, ~ 4 dB μm^{-1}, and effective index modulation, $\Delta n_{SMT} \approx -0.07$. Although increasing L_{VO2} to microscale patch lengths enables large extinction ratios (> 35 dB) this comes at the cost of a large insertion loss limited by the 50:50 couplers to 6 dB. At wavelengths where the maximum insertion loss to less than 6 dB, the total extinction ratio lower than a simple in-line absorption modulator. To make practical use of a Si-VO_2 hybrid MZI for optical modulation, the potential benefits of size, speed, or energy must outweigh the cost of high insertion losses. Finally, exploring alternative designs could be advantageous, for example a push-pull MZI would enable twice the phase modulation with about half the total loss.

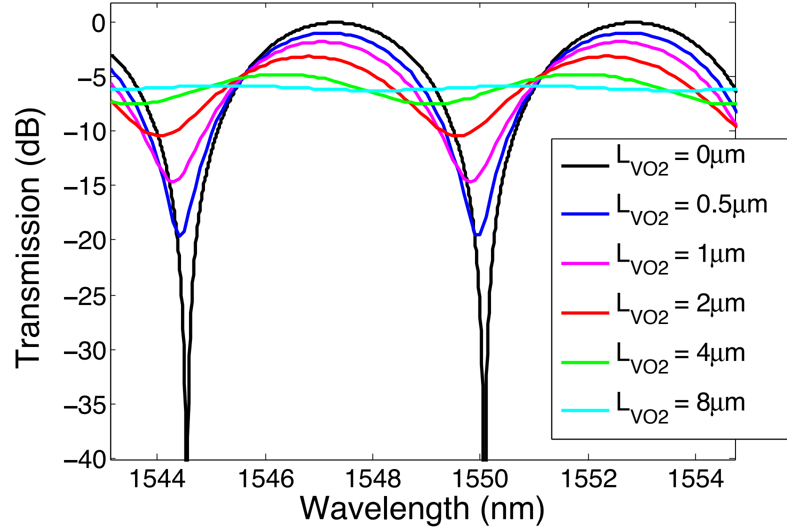

Figure 4.10: Modeling the effect of increased patch length and losses in a 100 μm unbalanced MZI with idealized 50:50 couplers and that the SMT induces both an absorption modulation, ~ 4 dB μm^{-1}, and effective index modulation, $\Delta n_{SMT} \approx -0.07$.

4.5 Discussion

From prior estimates on the energy density required to thermally switch thin-film VO_2, $\sim 10^2$ J cm^{-3} [75], the minimum energy required to thermally switch our hybrid device is expected to be $\sim 3 \times 10^{-12}$ J. For faster and lower threshold switching, either electric-field assisted switching or all-optical excitation should be employed. Given the measured threshold laser fluence of $\sim$0.25 mJ cm^{-2} for nanoscale VO_2 pumped at 1550 nm, and an active area $\sim$0.3 μm^2 of VO_2 [54] for the hybrid Si-VO_2 ring resonator, the minimum energy required for ultra-fast all-optical switching is predicted to be of order $\sim$190 fJ/bit ($\sim$750 fJ$\times$1/4; accounting for the likelihood of a 0-1 transition in a random signal) [176]. A hybrid Si-VO_2 MZI with a micro-scale patch length would require nearly 1 pJ/bit to achieve $\pi/2$ phase modulation. Similar switching energies are expected for electrically

driven devices, although the SMT would occur on slower timescales, on the order of 10^{-8} s compared to 10^{-13} s for all-optical excitation [75]. For comparison, forward biased electro-optic ring-resonator modulators with switching times below 10^{-9} s have been shown to use ~300 fJ/bit after accounting for temperature stabilization [63, 177]. Notably, the low mode-volume resonator geometry employed in this work enables >10 dB optical modulation to be achieved with approximately 1/10th the active area of VO_2 that would be required to achieve similar modulation depths in a single-pass broadband absorption modulator [75], thereby promoting reduced power requirements as well as a compact device footprint.

4.6 Summary

We have demonstrated photothermally induced optical switching of hybrid Si-VO_2 micro-ring resonators and MZIs. Triggering the SMT in VO_2 results in a large reduction in refractive index and a correspondingly large blue-shift in resonant frequency. Optical modulation greater than 10 dB from a low mode volume ($\sim 1\ \mu m^3$) silicon-based micro-ring device is found to require only a very small ($\sim 0.28\ \mu m^2$) active area of VO_2. Combined with a large FSR, modest Q-factor, short cavity lifetime, and the potential for ultrafast operation, the hybrid Si-VO_2 micro-ring platform presents a robust framework for next-generation optical switching. In the hybrid MZI configuration, photothermally induced phase shifting was successfully demonstrated, with an experimental effective index change comparable to that found for the hybrid ring-resonator. However, increased absorption from the longer micro-scale VO_2 patch adversely impacts optical contrast and increases insertion loss.

While there are still a number of challenges and opportunities associated with the details of the SMT of VO_2, these experiments demonstrate that the hybrid Si-VO_2 platform offers

an attractive candidate platform for optical modulation and reconfigurable optical routing. Further, this platform may form the basis for future electro-optic or all-optical modulators utilizing a hybrid Si-VO_2 geometry. Many of the above items will be further examined and discussed in Chapter 5, as we study the optically induced, nanosecond reconfiguration of hybrid Si-VO_2 absorbers and resonators. Further studies, presented in Chapter 6, investigate scaling devices to super-ultra-compact and ultra-low power configurations through nanophotonic designs featuring enhanced light-matter interaction.

CHAPTER 5

OPTICALLY INDUCED, NANOSECOND RECONFIGURATION OF HYBRID Si-VO_2 DEVICES

In Chapter 4 we introduced the hybrid Si-VO_2 ring resonator platform and demonstrated optical modulation by photothermally triggering the semiconductor-to-metal phase transition (SMT) of VO_2. In this chapter, we investigate more generally the ability to reconfigure silicon photonic devices, in both resonant and non-resonant configurations, by optically inducing the SMT with a nanosecond pulsed laser. With this approach, it is possible to achieve not only faster switching speeds, but to avoid localized system heating and thermo-optic effects which may slow or mitigate the optical response derived from the SMT of VO_2. This work further illuminates and strengthens the capabilities of the hybrid Si-VO_2 platform, and serves as an important stepping stone toward realizing dynamic on-chip networks and ultrafast optical shutters and modulators.

5.1 Introduction

Active photonic devices featuring compact size and a large, rapid, and energy efficient optical response are essential to nanophotonic technologies serving as reconfigurable filters, lasers, photonic networks, optical memories, and optical modulators. While silicon remains the preferred platform for large-scale manufacturing and provides natural advantages for optoelectronic integration, silicon suffers from limited dynamic optical functionality owing to its indirect band gap, and its modest electro-optic and nonlinear responses.

Although electro-optic or nonlinear effects in silicon can be used in modulators or optical logic components, for example, this typically requires lengthy interferometers [178] (mm scale) or very narrow band resonators [64, 155] (less than 15 GHz), which are extremely sensitive to thermal or ambient fluctuations and fabrication errors.

Circumventing these challenges and realizing devices with improved functionality continues to be a central aim of nanophotonics research. One option is to construct active optical devices through optomechanics [179]. Utilizing silicon's robust mechanical properties and large refractive index, it is possible to construct devices whose optical properties are exquisitely sensitive to mechanical actuation or reconfiguration. Although modest optomechanical response times ($\sim\mu$s) may limit their use in optical modulation, robust active devices capable of all-optical operation, ranging from reconfigurable filters [79] to optical memories [180], have been demonstrated. A second option is to harness the electro-optic or nonlinear properties of secondary materials integrated onto silicon, such as germanium, graphene, or organics. Electro-absorption effects in germanium [181] and graphene [73] have in fact been used to construct broadband optical modulators operating above GHz speeds; however, these devices are still tens of microns in length, and not suitable for on-demand optical routing, filtering, or all-optical switching. Silicon-organic hybrid geometries can provide all-optical and ultrafast operation capabilities [182, 183], but require very long (100 μm to several mm) interaction lengths even in waveguides with very high nonlinear waveguide parameters ($\gamma > 10^5$ W^{-1}km^{-1}) or slow-light effects [83].

The challenges highlighted by these examples motivate a continued search for alternative materials that can be integrated with silicon photonics to provide a large, rapid, and energy-efficient optical response while promoting wavelength-scale device dimensions and

the capability for all optical operation. Vanadium dioxide (VO_2) is a promising active optical material owing to its semiconductor-to-metal phase transition (SMT), which provides orders of magnitude change in resistivity, as well as large changes to absorption and refractive index [52]. The SMT alters the optical properties of VO_2 from the near- to far-infrared. The most substantial optical contrast between the semiconducting and metallic states occurs near 1.5 μm, making VO_2 particularly attractive for applications in optical communications [184]. The first-order SMT is nearly congruent with a structural transition from a monoclinic to rutile crystal structure and occurs above a critical temperature Tc $\sim$ 67 °C (340 K). Importantly, it has been shown that the SMT of VO_2 can be triggered by strain [158], electric current or bias [56, 160], terahertz electric-field [185], hydrogenation [186], hot-electron injection [187], and all-optical pumping [161]. In the case of all-optical pumping, the transition has been shown to occur on timescales comparable to the pump pulse duration, down to ~75 fs [188]. The SMT is fully reversible and has recently been demonstrated in concept for use in a variety of reconfigurable or active metamaterial [61, 189], plasmonic [54], and photonic [75, 80] devices generally relying on either global or local system heating (such as the photothermal stimuli demonstrated in Chapter 4).

Here we report the first demonstration of all-optical switching and reconfiguration of silicon photonic devices driven by a nanosecond photo-induced SMT in VO_2. Aside from triggering devices much faster than conventional thermal excitation, all-optical operation eliminates unwanted thermo-optic effects in the silicon waveguides, enabling large and robust reconfiguration. In the Si-VO_2 hybrid devices, we demonstrate record values of optically induced broadband in-line absorption modulation (~4 dB μm^{-1}) and intracavity phase modulation ($\sim \pi/5$ rad μm^{-1}). By optically controlling attenuation or phase in

both non-resonant and resonant structures, a variety of compact, highly reconfigurable and active photonic devices can be realized including filters, routers, shutters, and modulators. This work further sets the stage for SMT-driven optical limiters, semiconductor saturable absorbers, optical logic gates, and optical memories compatible with the current silicon architecture.

5.2 Si-VO_2 Absorbers and Resonators

Figure 5.1.a, b illustrates the two device geometries utilized in this work. By integrating VO_2 onto single-mode silicon waveguides, the SMT can be harnessed to introduce a significant change in absorption, $\Delta\alpha$, as shown in Fig. 1a. This non-resonant configuration utilizes the large contrast in the imaginary part of VO_2's refractive index, $\Delta Im(n_{VO_2}) = Im(n_M) - Im(n_S)$, on the order of $+2.6i$ at 1550 nm [75]. The absorption induced in the waveguide can be engineered by controlling the evanescent field overlap with the VO_2 patch (i.e., waveguide dimensions and patch thickness) and by tuning the VO_2 patch length. Because the optical properties of VO_2 and the waveguide optical confinement are relatively uniform (slowly varying) near telecommunications frequencies, device operation is considered to be broadband; however, high optical contrast requires substantial volumes of VO_2 that may be detrimental to overall system performance.

Alternatively, the large contrast in the real part of VO_2's refractive index, $\Delta Re(n_{VO_2}) = Re(n_M) - Re(n_S)$, approximately -1.06 at 1550 nm, can be used to introduce a significant change in effective index, or phase $\Delta\phi$. When placed inside an optical cavity, such as an ultra-compact micro-ring resonator (R = 1.5 μm, Fig. 5.1.b), a short $\sim$0.5 μm-long patch is sufficient to promote large changes in resonant wavelength without significantly affect-

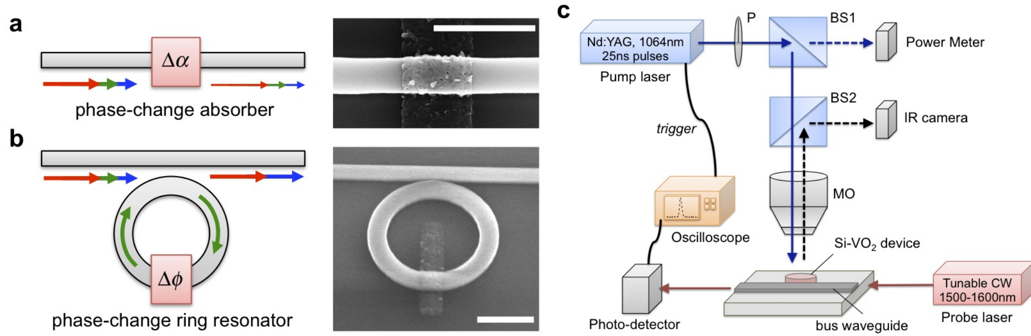

Figure 5.1: (a) Illustration of a phase-change absorber where the SMT induces a broadband change in absorption $\Delta\alpha$. SEM image of a typical ultra-compact Si-VO_2 absorber with a 1 μm VO_2 patch length. (c) Illustration of a phase-change ring resonator where the SMT induces an intracavity phase modulation $\Delta\phi$. SEM image of an ultra-compact Si-VO_2 micro-ring resonator with radius $R = 1.5$ μm and a $\sim$500 nm VO_2 patch length. Scale bars in both SEM images correspond to 1.5 μm, approximately the probe wavelength in free space. (c) Schematic of the experimental pump probe configuration utilized in this work. Tunable probe laser transmission is monitored with a photo-detector and oscilloscope, while nanosecond-pulsed pump light is delivered to the device through a microscope objective (MO) and two beam-splitters (B1 and B2) with power controlled by a linear polarizer (P).

ing Q-factor (Sec. 4.3.3) [61]. In principle, this configuration could serve as a wavelength-selective reconfigurable filter or modulator, or combined with a drop port for use as a router. With longer patch lengths, intracavity absorption modulation could also effectively extinguish resonances [190]; however, given the evident disadvantages of this approach in realistic device structures, in this work we will emphasize resonant frequency reconfiguration.

5.3 Experimental Methods

5.3.1 Device Fabrication

The Si-VO_2 hybrid structures were made from silicon-on-insulator (SOI) wafers with a 220 nm p-type Si(100) device layer and a 1 μm buried oxide (SOITEC) as described in Sec. 4.2. Briefly, two stages of electron beam lithography (EBL) were first used to pattern

the silicon photonic structures and VO_2 patches. After the first stage of EBL (JEOL JBX-9300-100kV), the Si device layer was created by anisotropic reactive ion etching (Oxford PlasmaLab 100) with $C_4F_8/SF_6/Ar$ process gases. After the second stage of EBL (Raith eLine), amorphous sub-stoichiometric VO_x was deposited by electron-beam vaporization of VO_2 powder (100mesh, 99.5% purity). Lift-off in acetone was performed prior to final annealing. The VO_x patches were annealed in a vacuum chamber under 250 mTorr of oxygen at 450 °C for ten minutes to form stoichiometric and polycrystalline VO_2 in accordance to prior work [165]. This process temperature is within the regime required for CMOS-compatible processing ($T < 450$ °C).

5.3.2 All-Optical Pump-Probe Experiments

Devices were tested in a pump-probe configuration as illustrated in Fig.5.1.c. Probe light from a tunable cw laser (Santec TSL-510) was coupled to and from mm length bus waveguides using polarization maintaining lensed fibers (OZ Optics Ltd.) mounted on piezo-controlled XYZ stages. Photo-detection of the transmitted probe light was performed using a fiber coupled avalanche photodiode photoreceiver (Newport 1647), with differential outputs monitored by an oscilloscope (Tektronix TDS 2024C). The oscilloscope was triggered directly from the nanosecond pump laser, which consisted of a Q-switched Nd:YAG laser operating at 1064 nm with a low 10 Hz repetition rate (Continuum Minilite). Pump intensity was controlled by a polarizer (P) and delivered to the sample through two beam-splitters (BS1 and BS2) and a 5x long working distance microscope objective (MO). Use of a power meter (Newport 2936 C) and IR camera (Sensors Unlimited 320M) enabled the calibration and measurement of pump fluence and precise positioning of the pump beam

onto the device of interest. Additional image(s) and descriptions of this measurement setup can be found in the Appendix B.1.2.

5.4 Pump-Probe Experiments

5.4.1 Si-VO_2 Absorbers

Figure 5.2.a shows the time-dependent optical transmission of the SOI waveguide with Si-VO_2 in-line absorbers for varying pump fluence and patch lengths ($L_{VO_2} \sim 1$ μm and 500 nm). Both devices exhibit an abrupt reduction in optical transmission in response to optical pumping. This drop occurs on a time-scale comparable to the pump pulse FWHM (~25 ns), consistent with reports using $\sim 10^{-8} - 10^{-14}$ s laser pulses to optically trigger the SMT in VO_2 thin films [188]. In the devices tested here, the modulation depth increases approximately linearly with pump intensity and saturates near a threshold fluence of ~1.27 mJ cm^{-2} (Fig.5.4.a). This saturation is indicative of a completed SMT occurring throughout the VO_2 patch and is a hallmark of the structural phase transition (SPT) [191]. The observed threshold of ~1.27 mJ cm^{-2} is comparable to other reports spanning both nanosecond and femtosecond measurements [192, 193]. At threshold, we estimate the modulation depth of the Si-VO_2 in-line absorbers to be 4 ± 0.3 dB μm^{-1}, which is approximately 40 times larger than monolayer graphene-on-Si absorbers (~0.1 dB μm^{-1}) [73] and more than three orders of magnitude larger than silicon-based two-photon cross-absorption modulation (~0.001 dB μm^{-1}) [194]. The insertion loss of the 1 μm Si-VO_2 device was within fiber-to-chip coupling variations, estimated at ~0.5-2 dB. Broadband device operation was verified over a wide wavelength range, 1500-1600 nm, as shown in Fig. 5.2.c.

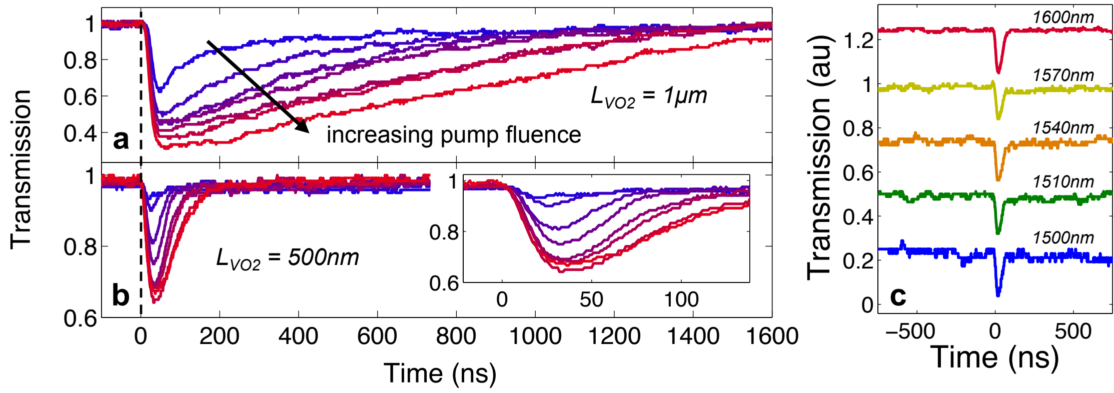

Figure 5.2: Normalized probe transmission through Si-VO_2 absorbers with (a) 1 μm and (b) ~500 nm VO_2 patch lengths. The pump fluence is incrementally increased in the range ~0.5-8 mJ cm^{-2}. (c) Transmission through a ~500 nm Si-VO_2 absorber for probe wavelengths ranging from 1500-1600 nm, demonstrating that the SMT of VO_2 can be used to realize broadband absorption modulation. Pump fluence was above threshold, ~5 mJ cm^{-2}. Plots are vertically stacked (0.25 offset) for clarity.

5.4.2 Si-VO_2 Ring Resonators

In addition to the Si-VO_2 in-line absorbers (Fig. 5.1.a), we also tested the dynamic reconfigurability of Si-VO_2 hybrid micro-ring resonators (Fig. 5.1.b). Figure 5.3.a shows the transmission spectra for an ultra-compact device, $R = 1.5$ μm, with an integrated ~500 nm long and ~70 nm thick VO_2 patch coating a portion of the ring waveguide. Owing primarily to bending losses at this ultra-compact ring radius, this device shows a modest $Q \sim 10^3$, resulting in an optical bandwidth exceeding 100 GHz (as discussed in Sec. 4.3.3). The time-dependent optical transmission for the pump-probe experiment is shown in Fig. 5.3.b, where probe wavelength is tuned to match the resonance minimum ($\lambda = 1588.5$ nm). Optically inducing the SMT results in an abrupt increase in transmission, estimated in this case to be ~7.2 dB, followed by a slower relaxation to the low initial value. The observed modulation depth is several times larger than what can be achieved for the in-line absorber

with the same active VO_2 area. The large increase in transmission observed for this modest Q-factor device suggests that the resonance wavelength is significantly modified by the photoinduced SMT. This is in stark contrast to conventional Si-only devices, where relatively weak electro-optic or nonlinear effects necessitate the use of high Q-factor, very narrow band (less than 5 GHz) resonators to observe significant modulation [64].

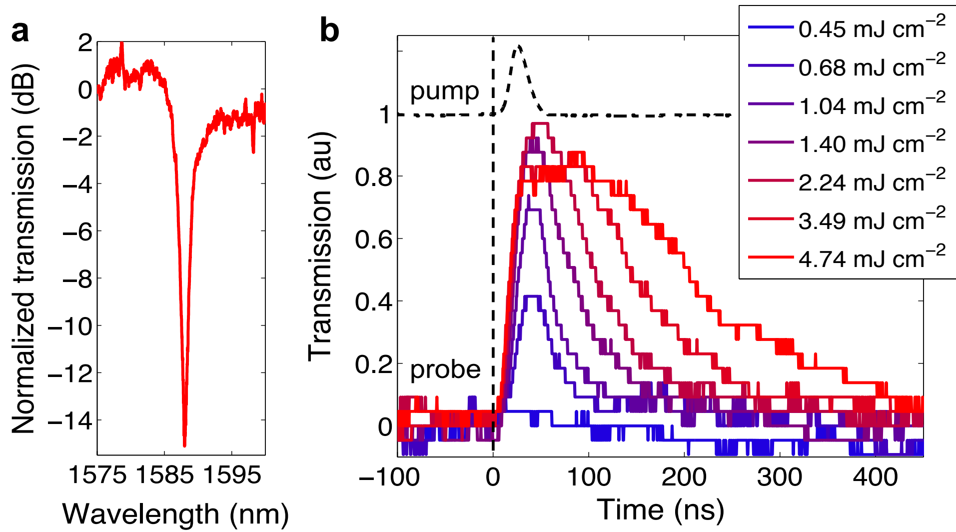

Figure 5.3: (a) Typical resonance in the transmission spectra for a Si-VO_2 micro-ring resonator with radius $R = 1.5\ \mu$m. (b) Corresponding probe transmission where the probe wavelength is tuned to on-resonance ($\lambda = 1588.5$ nm).

5.4.3 Relaxation Time and Dependence on VO_2 Patch Length

As shown in Figure 5.2.a and 5.4.b, the temporal dynamics of the reverse transition to the semiconducting phase of VO_2 can be significantly slower than the SMT, and depend strongly on both pump fluence and VO_2 patch length. The photoinduced SMT is an abrupt and potentially ultrafast athermal process, driven by photogeneration of electron-hole pairs and an electronically controlled lattice transformation into the higher symmetry rutile struc-

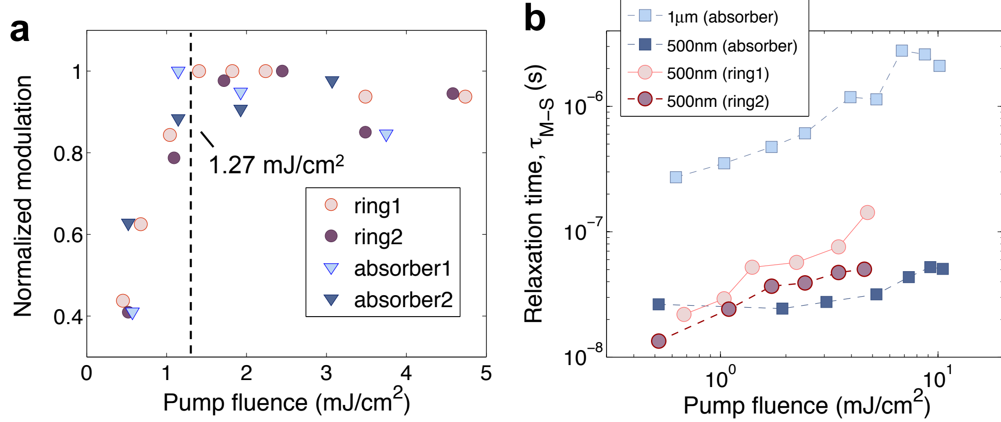

Figure 5.4: (a) Saturation in the modulated probe signal is observed beyond a critical threshold fluence $\sim$1.27 mJ cm^{-2}. (b) Relaxation time, τ_{M-S}, for the transition from the metallic state to the initial semiconducting state as a function of pump fluence plotted for Si-VO_2 absorbers and micro-ring resonators with 500 nm or 1 μm VO_2 patch lengths.

ture [161, 192]. In our experiment, the ensuing thermalization transiently increases the internal temperature of the VO_2 patch [188]. Undoing the SPT is a thermally mediated relaxation process dependent on thermal diffusion and nucleation of the monoclinic phase [191, 195]. It is important to emphasize that all-optical switching does not generate a localized heating effect, as the underlying silicon ring structure experiences virtually no temperature change during the SMT (see analysis/discussion of Fig. 4a). Structural relaxation of the VO_2 patch depends strongly on the thermal interface to the underlying heat sink, in this case the Si waveguide. Because the Si waveguide remains at room temperature during the SMT, and has a much larger thermal conductivity than VO_2 ($\sim$149 W m^{-1}K^{-1} vs. $\sim$6.5 W m^{-1}K^{-1}), the transient thermal relaxation of the VO_2 patch to the semiconducting state can still be relatively fast ($\sim$10^{-9} s) [196, 197]. Dramatic improvements in relaxation time, τ_{M-S}, to less than 10^{-9} s may be possible through various schemes, such as triggering the SMT without driving a complete SPT [162, 192].

Our experiments (Figs. 5.2.a and 5.4.b) show that in the case where the SPT is complete, simply changing the VO_2 patch length on a SOI waveguide to sub micron dimensions, from 1 μm to 500 nm, reduces the relaxation decay time τ_{M-S} by approximately an order of magnitude. A thermal boundary-resistance model would predict a faster relaxation time when film thickness (d) is reduced ($\tau \propto d$) [196], but it cannot account for our observed effect when the VO_2 volume and thermal interface area are changed in the same proportion (classically, $\tau \propto V/A$). This faster relaxation time with shorter VO_2 patches likely arises partially from the quasi-one-dimensional geometry of the SOI waveguide (for 1D, $\tau \propto L^2$) since the waveguide dimensions are comparable to the phonon mean free path in silicon, $\sim$250 nm, or perhaps some other size-dependent effect in the nanocrystalline VO_2 patch. The Si-VO_2 hybrid ring resonators utilizing the shorter $\sim$500 nm VO_2 patch length also show similarly reduced relaxation times, with some sample to sample variation (Fig. 5.4.b). We take this as further evidence that the thermal properties of the nanostructured interface play a significant role in the dynamics of the reverse SPT and can therefore be optimized.

5.5 Si-VO_2 Spectral Reconfiguration

5.5.1 Multi-Wavelength Pump-Probe Characterization

We carried out time dependent measurements at varying probe wavelengths to examine the spectral characteristics of resonator response to the SMT. The response of an ultra-compact, $R = 1.5$ μm, Si-VO_2 hybrid ring resonator with $L_{VO_2} \sim 500$ nm is shown in Figure 5.5 and further analyzed in Figure 5.6. This device is pumped at 1.9 mJ cm^{-2}, above the threshold required to complete the SMT by forming the rutile crystalline phase in VO_2.

Optically triggering the SMT results in a rapid shift in resonant wavelength estimated to be $\Delta\lambda_{SMT} = -3.07$ nm (Figure 5.6.a), extracted by fitting the data to a Lorentzian lineshape. Performing this experiment on a control Si-only resonator, pumped at the same fluence, reveals a wavelength shift estimated to be $\Delta\lambda_{Si} = -0.057$ nm, nearly sixty times smaller (Figure 5.5). Whereas the large $\Delta\lambda_{SMT}$ reduction in resonant wavelength for the Si-VO_2 hybrid device arises from the substantial modification of VO_2 refractive index, $\Delta Re(n_{VO_2}) = 1.06$, the small $\Delta\lambda_{Si}$ reduction arises from weak dependence of the silicon refractive index on free carrier concentration, estimated in this case to change by $\Delta Re(n_{Si}) = 1.6 \times 10^{-4}$. The Si only device was also tested under a pump fluence about six times higher, 11.5 mJ cm^{-2}, and showed a wavelength shift about six times larger than before, $\Delta\lambda_{Si} = -0.325$ nm (Figure 5.5). At this high fluence, in addition to the free-carrier effect, phonon excitations in the Si lattice produce a residual thermo optic redshift as high as $\Delta\lambda_{Si} = +0.13$ nm, visible in Fig. 5.6.a beyond $\sim$30 ns. This corresponds to a transient temperature increase of the Si waveguide estimated between $1-2\,^{\circ}$C [198]. No such effect is observed at 1.9 mJ cm^{-2} fluence, indicating that the Si waveguide temperature is not affected by the pump pulse near but just above threshold. By eliminating the thermo-optic contribution of the Si waveguide at the low pump fluence, the optical response of the device is entirely controlled by the SMT in the VO_2 patch. This greatly simplifies device operation and maximizes the achievable optical response, as the SMT in VO_2 and the thermo-optic effect in Si generally provide opposing contributions to refractive index. Furthermore, we can also assume the timescale for device operation is dictated solely by the switching time of the VO_2.

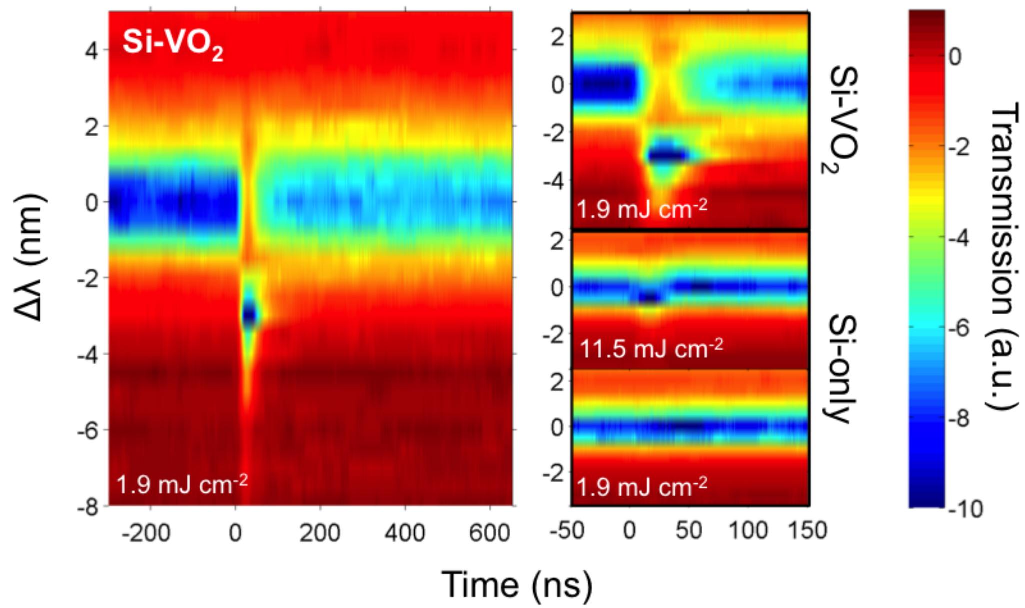

Figure 5.5: Mapped optical transmission for variable wavelength pump-probe measurements performed on a Si-VO_2 micro-ring resonator ($R = 1.5$ μm) at a pump fluence above threshold (1.9 mJ cm^{-2}). Right column reveals a zoomed in mapping for the same device as well as results from a Si only control device pumped at 1.9 mJ cm^{-2} and 11.5 mJ cm^{-2}. Colorbar indicates a logarithmic scale.

5.5.2 Analysis

As shown in Figure 5.6.a, the SMT-induced resonance shift and the SPT completed in $\sim 25-30$ns. At threshold, this timescale is primarily controlled by the FWHM of the pump pulse. Based on the reported response times of VO_2 thin films optically excited with shorter pulses [53, 161, 188], it should be possible to extend device operation to ultra-fast all-optical switching (less than 100 fs). Following optically driven reconfiguration of the resonator, the reverse SMT returns the VO_2 to its higher-index semiconducting state, bringing the resonant wavelength back to its initial value in $\sim 50-70$ ns. As mentioned earlier, this $\sim 10^{-8}$ s relaxation time scale is not intrinsic to the phase-transition of VO_2 and can be controlled by a variety of factors. In the regime where the SMT coincides with a complete SPT from monoclinic to rutile structure, improving the timescale for the reverse transition could be achieved through more sophisticated thermal design, such as reducing the VO_2 thickness, depositing a top-cladding (e.g., SiO_2), or tailoring the SOI substrate geometry. Alternatively, recent THz conductivity experiments indicate lattice-relaxation times less than 2-3 ps are possible when the fluence for ultra-fast, $\sim$15 fs, pump pulses is maintained below threshold [162]. In this regime, it has been hypothesized that photo-generated carriers may rapidly excite the electronic transition and rapidly decay through a fast trapping or relaxation pathways without cooperatively driving a complete SPT. There is additional evidence for the existence of a monoclinic metallic phase during both thermal and ultrafast excitation of VO_2 that suggests an operating window just above threshold where fast relaxation of the metallic phase is possible [195, 199, 200]. It may also be possible to enhance relaxation times using an applied bias to rapidly sweep out photo-

generated carriers [201]. Thus, there are several design strategies through which Si-VO_2 hybrids could be a practical basis for ultrafast all-optical devices, such as modulators or logic gates, in silicon platforms.

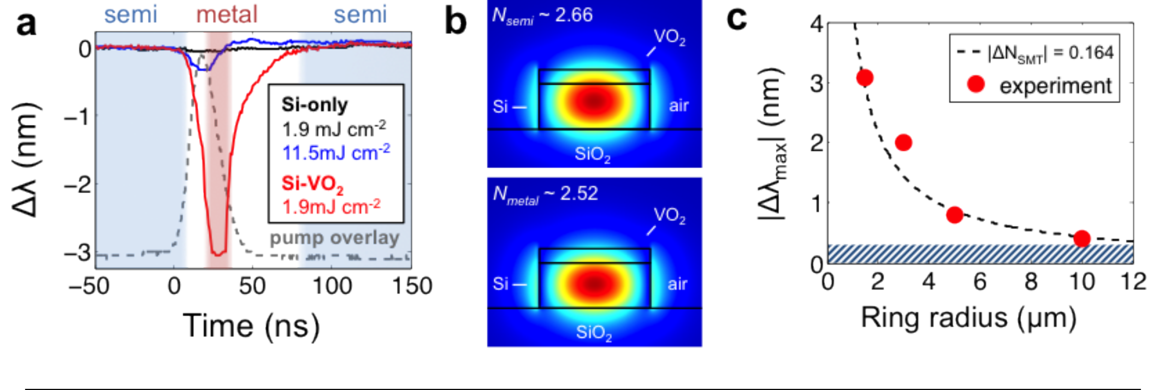

Figure 5.6: (a) Resonant wavelength as a function of time, extracted from the variable wavelength pump-probe measurements shown in Fig. 5.5 The pump signal is overlaid for comparison purposes. (b) FDTD mode simulation for a hybrid Si-VO_2 waveguide, with Si dimensions 220×500 nm and a 70 nm thick VO_2 patch on top. (c) Magnitude of the resonance wavelength blue-shift $\Delta\lambda_{max}$, occurring in response to photo-inducing the SMT on Si-VO_2 micro-ring resonators with varying ring radii and a fixed $\sim$500 nm VO_2 patch length. Shaded region indicates the regime where $\Delta\lambda < 0.3$ nm, corresponding to typical thermo-optic variability of Si resonators under temperature variations $\pm 3\,^{\circ}$C, also equivalent to $\sim$2 linewidths for a high Q ($\sim 10^4$) resonator.

The observed $\Delta\lambda_{SMT} = -3.07$ nm for the ultra-compact, R = 1.5 μm, Si-VO_2 hybrid ring resonator corresponds to a resonant frequency reconfiguration of $\sim$360 GHz. This large reconfiguration is achieved utilizing a very small $\sim 0.275\ \mu\text{m}^2$ active area of $\sim$70 nm thick VO_2, corresponding to a $\sim$5.3% surface coverage on the micro-ring. By controlling the surface coverage, VO_2 thickness, or modal overlap, the resonant reconfiguration induced by the SMT could be tuned and optimized. For a hybrid Si VO_2 waveguide, with Si dimensions 220×500 nm and a 70 nm thick VO_2 layer, the SMT is expected to produce a large change in effective index $\Delta N_{SMT} \sim -0.14$, as indicated by finite difference

time domain (FDTD) modal calculations shown in Figure 4b. To demonstrate that the response derived from this effect is both large and highly tunable, we fabricated devices with the same $\sim 0.275\ \mu\text{m}^2$ VO_2 patch area, but varying ring radii ranging from $1.5 - 10\ \mu$m. The maximum wavelength shift, $\Delta\lambda_{max}$, for each ring radius R was then determined by performing variable wavelength pump-probe measurements. As shown in Figure 4c, the magnitude of the resonant response, $|\Delta\lambda_{max}|$, follows an R^{-1} dependence. This agrees with calculations where the average effective index change in the ring resonator can be modeled as $\Delta N_{eff} = \Delta N_{SMT} L_{VO_2}(2\pi R)^{-1}$. We experimentally estimate $\Delta N_{SMT} \sim 0.164 \pm 0.033$, from the relation $\Delta\lambda_{max}/\lambda_0 = \Delta N_{eff}/N_g$, where N_g is the group index of the ring waveguide (~ 4.4) and λ_0 is the initial resonant wavelength ($\sim 1550 - 1590$ nm), which is close to, but slightly larger than, the value calculated in FDTD simulations. The intracavity phase modulation $\Delta\phi_{SMT}/L_{VO_2} = 2\pi/\lambda_0\ \Delta N_{SMT}$ induced by the SMT is then estimated at $\sim \pi/5$ rad μm^{-1}, while that of the Si-only device is estimated to be three orders of magnitude lower, $\sim \pi/5000$ rad μm^{-1}. It is for this reason that the small ($\sim 0.275\ \mu\text{m}^2$) active area of VO_2, equivalent to 5.3% surface coverage on the ring, can still provide $\sim$60 times larger resonant response than the Si-only device.

5.6 Discussion

A notable advantage of a large resonant response is that devices can operate outside the regime where ambient effects, such as thermal fluctuations, can play a significant role. The shaded gray region in Fig. 5.6.c covers the region where $\Delta\lambda < 0.3$ nm, and corresponds to a temperature tolerance of ± 3 °C for silicon resonators with a typical thermo-optic sensitivity of $\sim$0.1 nm/°C. This region also corresponds to roughly two linewidths for a cavity with

$Q \sim 10^4$. High-Q silicon photonic devices that operate in this regime are highly susceptible to noise or error and thus require added complexity or energy consumption for active thermal compensation. The longer cavity lifetime of these high-Q resonators also limits the speed at which they can operate. Thus, constructing ultrafast reconfigurable photonic devices, capable of speeds exceeding 100 GHz, will ultimately require either non-resonant effects (e.g., interferometers, absorbers), or modest $Q \leq 10^3$ resonators with a large optical response. By providing larger enhancements for larger fractional VO_2 surface coverage, the Si-VO_2 platform further favors ultra-compact device geometries. This can be clearly seen in Fig. 5.6.c, where the smallest micro-ring resonator exhibits the largest resonant response. Given the fixed VO_2 volume, this is equivalent to a wavelength sensitivity inversely related to the cavity mode volume, V. While the $R = 1.5$ μm micro-ring has a low mode volume, $\sim 11.5(\lambda/n)^3$, further reducing the cavity mode volume would be attractive for realizing super-ultra-compact, ultra-low-power devices.

5.7 Summary

In summary, we have demonstrated all-optical operation of Si-VO_2 broadband in line absorbers and micro-ring resonators. Laser induction of the SMT of VO_2 yielded record values of modulation (∼4 dB μm^{-1}) and intracavity phase modulation ($\sim \pi/5$ rad μm^{-1}) for all-optical silicon photonic devices. For resonant devices, the large optical response enables larger bandwidth, reduced ambient sensitivity, ultra-compact geometries, and reduced power requirements. With this platform, a wide variety of reconfigurable active photonic devices can be reduced to practice, including filters, routers, shutters, and modulators. Given the potential to trigger the SMT in less than 100 fs both optically and electro-

optically, and with a plausible strategy for reducing the switch-off time below 3 ps, the $Si-VO_2$ platform could lead to a new class of ultrafast silicon photonic devices ranging from optical limiters to optical logic gates and ultrafast optical memories.

CHAPTER 6

DESIGNING FOR ENHANCED LIGHT-MATTER INTERACTION

In the previous Chapters we have shown how novel approaches to fabrication and material integration can benefit photonic applications ranging from sensing to communications. In this Chapter, we focus on *photonic design* – and how improved designs, utilizing existing fabrication and material platforms, might provide significant enhancements to light-matter interactions. Specifically, we first introduce a periodic slot waveguide, aka. the "pinch waveguide", that provides significant localized field and power density enhancements over traditional slot waveguides. The basic structure is based on a slot waveguide with 1D periodic holes. The slot effect provides strong field enhancement and subwavelength confinement, and the periodicity of the structure is exploited to locally magnify or "pinch" the electric field distribution, resulting in additional enhancements. Characteristics of the modes presented by this structure are examined by finite-difference time-domain (FDTD) modeling. We then experimentally demonstrate using the pinch waveguide to form a 1D photonic crystal (slotted nanobeam) cavity with a record low mode-volume. A design approach for further enhancing Q and Q/V values is also introduced and demonstrated through FDTD simulations. Potential applications of the periodic slot waveguide structure to fields including optical manipulation, sensing, and nonlinear or active material integration, are also discussed.

6.1 Introduction

The slot waveguide is formed when a low refractive index discontinuity is embedded within a conventional high index waveguide structure. This simple design concept has emerged as a useful tool within the growing suite of photonic components for achieving enhanced light-matter interactions as it offers strong sub-wavelength confinement, enhanced field-intensity, low effective index, and large field overlap with void/cladding materials [202]. The distinct properties of the slot waveguide have led to advances in a wide variety of applications including sensing [75, 171, 203, 204], nano-optomechanics [205, 206], non-linear effects [183, 207–211], optical modulation [210–212], and optical manipulation [213–215]. Similarly, photonic crystals (introduced in Chapter 1.3) have gained significant attention across a breadth of applications due to their ability to enhance light-matter interactions by manipulating light in one, two, and three-dimensions [216].

There is great potential in combining the photonic crystal and slot platforms to obtain superior characteristics within a single device structure. Indeed, recent works have theoretically investigated embedding a slot into 1D photonic crystals, such as in a nanocavity to achieve ultralow mode volumes [217, 218], or in a coupled resonator configuration to obtain slow light effects [219]. In addition, several studies have investigated incorporating slots into the high-Q cavities of 2D photonic crystal slab structures [75, 205, 211, 220, 221]. All of these demonstrations have sought to enhance the local field intensity and improve light-matter interaction by either trapping light in a slotted cavity or slowing-light down in a slotted photonic crystal waveguide (where field enhancement is inversely related to the group velocity v_g). However, few of these works specifically investigate the strong

field confinement and localized enhancements that can be achieved in the slotted photonic crystal platform.

Here, we demonstrate that incorporating 1D periodicity into the slot waveguide structure can be exploited to significantly redistribute the fields of both guided and defect modes, resulting in distinct optical gradients and localized field enhancements that exceed those of traditional slot or photonic crystal structures. The basic structure is highly tunable and can be readily integrated into the suite of existing nanophotonic components. We refer to this novel waveguide structure as the "pinch waveguide".

6.2 Theoretical Background

6.2.1 Bands and Field Properties

The pinch waveguide structure consists of a traditional slot waveguide superimposed with air (or low index) holes periodically arranged at every interval a along the length of the waveguide. For an appropriate range of parameters, this structure exhibits a photonic band gap (PBG), which prevents a set of frequencies $\{\omega_1, \omega_2\}$ from guiding. Outside of the PBG there are various distinct bands, or eigenmodes, where guiding is possible.

To examine the modal characteristics of the pinch waveguide structure, simulations were performed using the 2D finite-difference time-domain (FDTD) method [222], combined with harmonic analysis techniques [223], in a freely available software package [224]. Unless otherwise noted, all simulations are performed using normalized units with a grid resolution of $a/144$ and sub-pixel averaging enabled to improve accuracy [225].

Figure 6.1 presents the proposed waveguide geometry and the band structure for an

example design with a high dielectric contrast: $\varepsilon_1 = 13$, $\varepsilon_2 = 1$ (e.g., InGaAs or Si in the near IR). The air-hole structure was selected because its connectivity promotes large PBGs for TE polarization [226], and TE polarization is required to observe the slot-effect [202]. Compared to a periodic air-hole waveguide, the addition of the slot effectively reduces the dielectric contrast of the 1D periodic structure. Despite this reduced contrast, large PBGs are observed, with gap-to-midgap ratios $\Delta\omega/\omega_0 = 2(\omega_2 - \omega_1)/(\omega_2 + \omega_1)$ typically around 0.15. As shown in the inset to Fig. 6.1.a, adjusting the slot-width, ws, or the hole-radius, r, influences the gap-to-midgap ratio. For moderate values of ws, such as those examined in Fig. 6.1.a, the gap-to-midgap ratio tends to increase with hole-radius. Here, we note that a mode-gap cavity could theoretically be implemented in a manner similar to other slotted 2D photonic crystal slab structures where a local modification in the hole size and/or positioning, or alternatively the slot width, give rise to a cavity mode. Recent work has demonstrated the possibility of achieving ultra-high Q-factors, up to $\sim 7.2 - 7.5 \times 10^5$, in 1D mode gap cavities based on non-slotted air-hole waveguides [88, 96, 97]; similar Q-factors can be expected for pinch waveguides with proper design optimization. We further discuss and analyze such defect modes in Section 6.3.

Immediately above and below the PBG are the air and dielectric bands, respectively. The air band is characterized by the electric fields concentrating primarily in the vicinity of the air-holes (or low index). The fields are also highly evanescent, suggesting that such modes have a very low modal index, n_{eff}. If we consider a pinch waveguide operating at 1550 nm, for example, with $r = 0.45a$, $ws = 0.24a$, $w = 1.2a$, and $a = 600$ nm, we find a very low modal index of $n_{eff} \approx 1.16$. Given these characteristics, we expect that such a structure would be particularly well suited for optical sensing in gas or liquid environments,

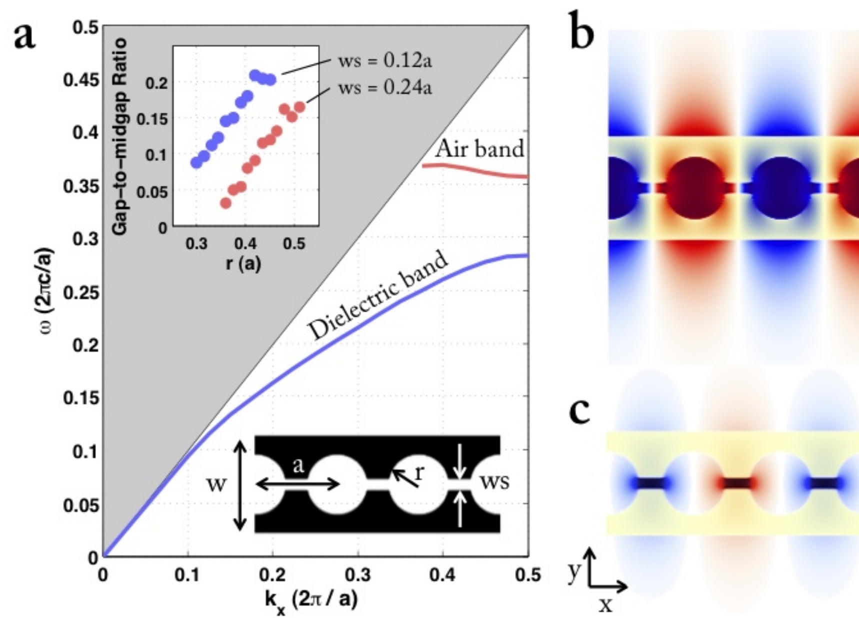

Figure 6.1: (a) Band structure of a pinch waveguide with $r = 0.42a$, $w = 1.2a$, and slot width $ws = 0.12a$. Inset reveals the gap-to-midgap ratio as a function of hole radius size. Note: the gray shaded region represents the light cone above which radiation modes exist with a continuous spectrum. (b) Ey field distribution for a guided mode in the air band. (c) Ey field distribution for a guided mode in the dielectric band. Figure adapted from [172].

where significant field overlap with cladding materials provides enhanced sensitivity [203]. Furthermore, we predict that this structure could provide substantial enhancements to surface sensing, for example, the detection of biomolecular monolayers, owing to the increase in surface area compared to the traditional slot waveguide [227].

The dielectric band, which will serve as our primary focus for the remainder of this Chapter, is characterized by the electric field being very tightly confined to the slot region between air-holes, as shown in the field distribution in Fig. 6.1.c. This local confinement is a direct result of combining two important effects resulting from Maxwells equations. The first effect provides strong optical confinement in the y-direction, and is the well-known slot-effect resulting from the continuity of the displacement field normal to an interface [202]. For high dielectric contrast structures, this leads to a distinct discontinuity in the electric field in the form of an enhancement in the region of low dielectric constant, as described by Eq. 6.1, where the slot has dielectric constant ε_2 and is oriented such that the y-direction is normal to the dielectric interface. Thus, for a large dielectric contrast structure, such as $\varepsilon_1 = 13,\ \varepsilon_2 = 1$, the electric field immediately inside the slot can be enhanced approximately one order of magnitude:

$$D_{y,\ \varepsilon_1} = D_{y,\ \varepsilon_2} \rightarrow \frac{\varepsilon_1}{\varepsilon_2} E_{y,\ \varepsilon_1} = E_{y,\ \varepsilon_2}. \tag{6.1}$$

The second effect arises from the periodicity of the structure, resulting in a redistribution of the fields in the x-direction, and locally enhances the fields in the regions between holes where the effective dielectric constant is the highest. The tendency for electric fields to concentrate in regions of higher effective dielectric constant can be considered as

a property of the electromagnetic variational theorem [216], which states that the lowest-frequency mode corresponds to a field distribution that minimizes the electromagnetic energy functional,

$$U_f(\mathbf{H}) = \frac{\int d^3\mathbf{r} |\nabla \times \mathbf{E}(\mathbf{r})|^2}{\int d^3\mathbf{r}\, \varepsilon(\mathbf{r}) |\mathbf{E}(\mathbf{r})|^2}. \tag{6.2}$$

In this expression, $\mathbf{H}$ represents the magnetic-field eigenmode that minimizes the electromagnetic energy functional U_f, ε is the dielectric function, and $\mathbf{E}$ is the corresponding electric field distribution, subject to $\nabla \cdot \varepsilon E = 0$. Note that concentrating the electric field to regions of higher dielectric constant helps to minimize U_f by maximizing the denominator of Eq. 6.2. Due to the dielectric band containing the lowest frequency modes, the resulting field distributions for this band are most tightly confined to the higher ε regions between air-holes (Fig. 6.1.c) [216].

In Fig. 6.2, we compare the modal characteristics of the pinch waveguide to those of the traditional slot waveguide and 1D periodic air-hole waveguide. Individually, the field distributions of the slot waveguide and air-hole waveguide directly illustrate the two primary effects, discussed above, which respectively contribute to the strong field confinement observed in the pinch waveguide structure. As expected, the slot waveguide is characterized by strong field confinement in the y-direction. However, we note that the time-averaged power density shows a significant fraction of the total power is distributed in the high dielectric region, which is also true for traditional slot waveguides. Typically, a traditional slot waveguide cannot confine more than $\sim$30% of the optical power inside of the slot region [202]. The air-hole waveguide, by comparison, shows relatively poor confinement in the y-direction, but strong field localization along the x-direction in the region between

air-holes, which is especially apparent in the time-average power distribution. This is a primary example of the sort of behavior that is expected from the electromagnetic variational theorem and Eq. 6.2. The combination of the slot effect and the periodic field concentration in the pinch waveguide locally compresses the electric field in space, resulting in a very strong sub-wavelength confinement and strong localized field enhancements.

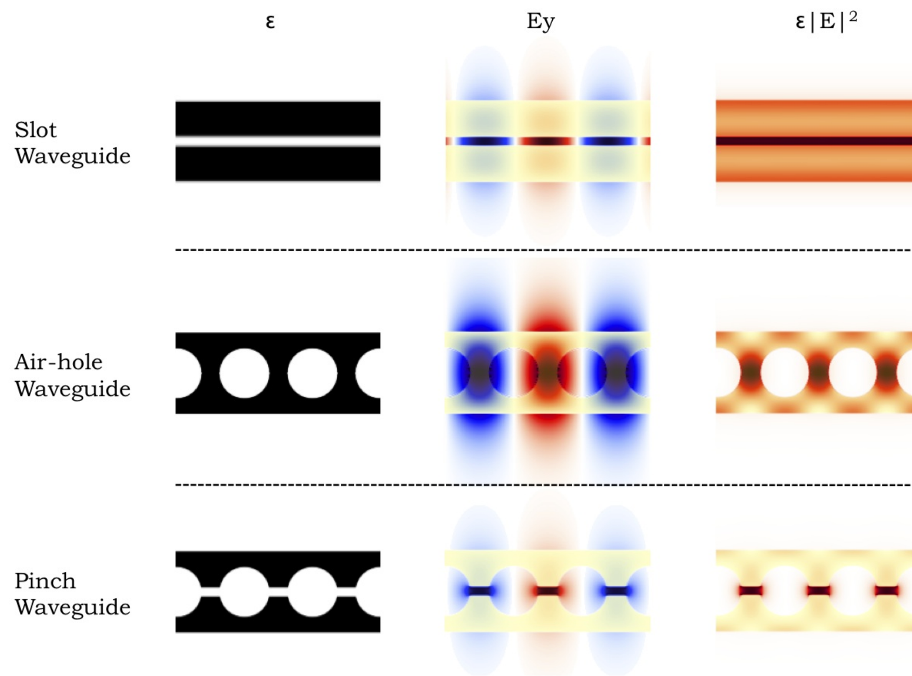

Figure 6.2: Example electric field (instantaneous) and power distributions (time-averaged) for three waveguide structures. The pinch waveguide combines principles from both slot and periodic geometries to obtain extreme sub-wavelength confinement in a guided mode. Note that each field image is normalized to its own linear color scale (dark red + to dark blue -). Figure adapted from [172].

6.2.2 Field Enhancements and Power Confinement

For a more detailed examination, we compare example slot and pinch waveguides with a high dielectric contrast ($\varepsilon_1 = 13,\ \varepsilon_2 = 1$), designed to operate at $\lambda = 1550$ nm. Choosing $a = 387.5$ nm places the nominal operating range well into the dielectric band, and away

from the band edge where group velocity theoretically slows to zero. This design choice allows us to demonstrate that the fundamental field enhancement of the pinch waveguide is not a slow-light effect, while we note that designing the pinch waveguide to operate in the slow-light regime would only further enhance the local field intensities. Now let us consider a slot width, $ws = 0.12a$, of approximately 45 nm. This relatively small slot width is chosen, firstly, because for a traditional slot waveguide the field-enhancement within the slot always increases with reducing slot width [202], and secondly, it is close to the low-end of the scale of what can be reliably produced by conventional electron-beam lithography. In other words, this choice of ws represents a case where the field-intensity in the traditional slot waveguide is very high. We note that for some applications, for example when maximum field enhancement is desired, the optimal design choice may be dictated by technological limitations.

In Fig. 6.3, we compare the electric field enhancement and power confinement provided by the pinch waveguide to that of the traditional slot waveguide. In order to make this comparison, all intensities are normalized to the total optical power in the respective waveguide, and then weighed relative to the traditional slot waveguide. As observed in Fig. 6.2, the time average of $|E|^2$ is non-zero and, for the traditional slot waveguide, constant as a function of x-position. This is also clear in Fig. 6.3.b when examining the field in the middle of the waveguide as a function of x-position for the case $r = 0$ (traditional slot waveguide), where we find a uniform $|E|^2$. The pinch waveguide however, shows significant $|E|^2$ enhancements, up to $\sim 4-5$ times greater than the slot waveguide, which are maximized periodically in x at locations directly between holes.

Importantly, we find that both the nominal peak enhancement and the general shape

of the spatial enhancement can be tuned by varying the hole radius. As the hole radius is increased, the length of the high index region between holes is reduced. This further compresses the field in the x-direction and results in additional field enhancement (Fig. 6.3.b-d). The trend for field enhancement as a function of hole radius is shown as the inset to Fig. 6.3.c. If we assumed that all of the electromagnetic energy was uniformly confined between holes, then the field enhancement would continue to increase with r, eventually approaching infinity as the hole radius approached $0.5a$. However, this is clearly not the case, as we do not observe an asymptotic increase in the field enhancement. Instead, we find that the field enhancement increases monotonically and plateaus to a maximum value near $r = 0.5a$.

Here we would like to emphasize that by achieving such strong field enhancements over the traditional slot waveguide, the pinch waveguide achieves normalized field intensities that are superior to any dielectric-based guided mode structure that is not operating in the slow light regime. Also, these field enhancements coincide with a reduced total interaction volume, similar to the trade-off posed by the traditional slot-waveguide, where the largest enhancements occur for the smallest slot widths.

As shown in Fig. 6.3.e we have also investigated the power confinement within particular regions of the pinch waveguide as a function of hole size (again considering $a = 387.5$ nm, $\lambda = 1550$ nm). For this analysis, we define two regions from the unit cell, regions I and II, each with width $ws = 0.12a$ (Fig. 6.3.a). We also define a third region, region III, as the intersection of regions I and II, containing a small area $ws \times ws$. The equivalent regions on the traditional slot waveguide are denoted in lower case (i, ii, iii).

Examining the power distribution in the x-direction, we find that up to $\sim$28% of the

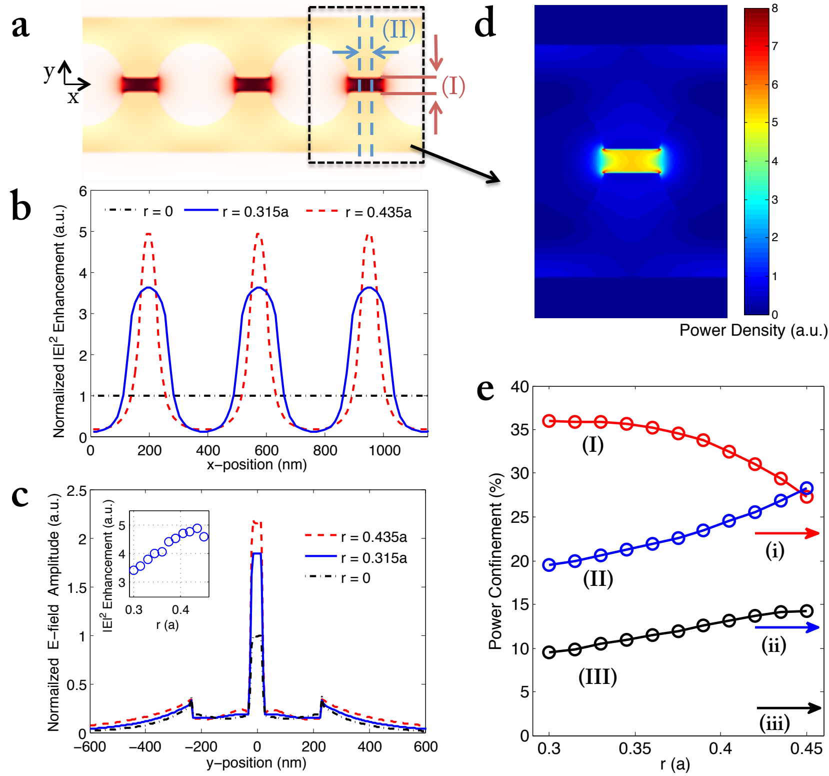

Figure 6.3: (a) Example, pinch waveguide power distribution and illustration of regions (I, II), where power confinement is analyzed in (e). (b) Time-averaged $|E|^2$ enhancement relative to a traditional slot waveguide operating at $\lambda = 1.55\ \mu$m, with $a = 387.5$ nm (slice centered at $y = 0$). (c) Time-averaged E-field amplitude (slice centered between holes), inset circles: simulated peak $|E|^2$ enhancement, along $y = 0$, as a function of hole radius. (d) Snap shot for r = 0.36a of an animation showing the power density variation with hole-size (available for download at http://ieeexplore.ieee.org, or see Ref. [172]). (e) Percentage of total power confined to selected regions of the pinch waveguide with $ws = 0.12a$, $w = 1.2a$, and frequency = 0.25. Region III is defined as the intersection of regions I and II. Lower case arrows, labeled i-iii, indicate the power confinement of a traditional slot waveguide with the same dimensions. Figure adapted from [172].

optical power can be found in region II (centered between air-holes). This is a significant increase over the 12% of power that would be found in the same region ii for any traditional waveguide (slot or otherwise) that has continuous translational symmetry. We find that up to ∼35% of the optical power is confined in the y-direction to region I. This value is also larger than the ∼23% power confinement that can be achieved in a traditional slot waveguide of the same dimensions. Owing to the behavior observed in Fig. 3d, we refer to region III as the pinch region. The power confined in this region is as high as ∼15%, a significant increase over what is found in the traditional slot waveguide, which shows only ∼3% power confinement. In other words, the typical power confined within the "pinch" region of the pinch waveguide is up to 400% enhanced compared to a traditional slot waveguide of the same dimensions.

6.3 Experimental Demonstration

In this Section we present the design and experimental demonstration of a slotted ultra-small mode volume single nanobeam cavity in silicon (or "pinch" cavity), achieving a mode volume $V \approx 0.01(\lambda/n)^3$ and experimental $Q = 7.42 \times 10^3$. The concept of introducing a slot into a 1D PhC cavity was originally proposed by Robinson et al. [217], where it was shown that the effective mode volume can theoretically be reduced by a factor of $(n_{hi}/n_{lo})^5$ for an infinitesimal slot width. Unfortunately, introducing a finite slot, without any further design tailoring, can reduce the theoretical Q-factor by over three orders of magnitude, thereby limiting the Q-factor to be on the order of $\sim 10^2$ [218]. Such low Q-factors are almost entirely a result of increased radiation losses, which occur because the introduction of a finite slot causes a large perturbation to the optical mode and introduces

spatial frequencies inside the light cone [92, 228]. In order to reduce leakage to radiation modes, and improve the radiation quality factor Q_{rad}, we have incorporated two important design choices into the present work: (1) the use of a common five-hole taper design [75, 96, 229] and (2) the use of a continuous slot which is unterminated in the principle direction of the photonic band gap (PBG) [172]. Both of these design choices present a gentler way of breaking the translational symmetry of the PhC mirror and serve to reduce the typically large mismatch between the effective index of the defect and evanescent Bloch mode in the mirror. Moreover, the continuous slot geometry promotes efficient input/output coupling to slot waveguides.

6.3.1 3D Design and Calculations

Fig. 6.4.a shows the dispersion relation for the slotted photonic crystal waveguide structure used in this work. This waveguide structure, which we refer to as the pinch waveguide [172], exhibits guided modes that lie outside the air (n = 1) light line and shows a sizeable $\Delta\omega \approx 0.063$ mode-gap. The dispersion relation is obtained from a 3D band structure calculation for quasi-TE polarization and a periodic unit cell of length a, with waveguide width $w = 1.091a$, hole radius $r = 0.335a$, slot width $ws = 0.093a$, and waveguide thickness $h = 0.379a$ (corresponding to the mirror dimensions of the device shown and tested in Figs. 6.5 & 6.6). A refractive index $n_{Si} = 3.46$ is used for silicon in all simulations. These dimensions were selected to balance three primary constraints: (1) the predefined SOI device layer thickness ∼212 nm, (2) a minimum reproducible slot width ∼50nm, and (3) the ability to place the dielectric band edge near ∼1550 nm. The connected nature of the basic holey waveguide structure promotes the largest photonic band gaps for quasi-

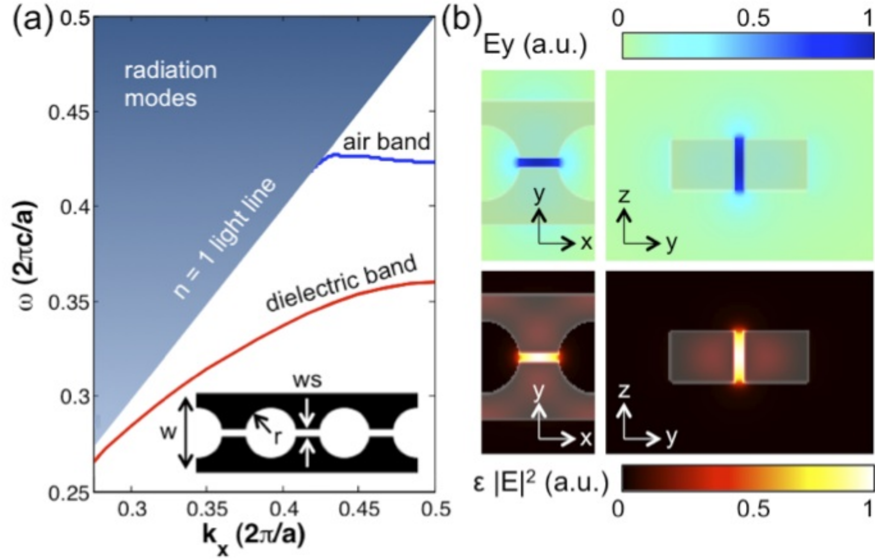

Figure 6.4: (a) Dispersion relation for the slotted PhC pinch waveguide, shown in the inset, with $w = 1.091a$, $r = 0.335a$, $ws = 0.093a$, and waveguide thickness $h = 0.379a$. (b) Field and power distributions for a single unit cell of the pinch waveguide structure calculated at the dielectric band edge. Figure adapted from Ref. [89].

TE polarization [230]. Moreover, quasi-TE polarization, where the dominant electric field component, E_y, is oriented in the plane, gives rise to a strong slot-type field enhancement [202]. Fig. 6.4.b reveals the field and power distribution for a mode on the dielectric band at the edge of the first Brillouin zone. The dielectric band is characterized by strong field confinement and localized field enhancement within the slot, located in the "pinch" region between neighboring air holes. These favorable field characteristics are conducive to low mode volume cavities. As reported previously, the pinch waveguide is capable of providing a normalized $|E_{max}|^2$ enhancement up to ∼4-5 times greater than that of a traditional slot waveguide of the same nominal dimensions [172]. Thus, according to the definition of the effective mode volume [217], with $V_{eff} \propto 1/|E_{max}|^2$, the mode volume of a pinch waveguide can be up to ∼4-5 times smaller than that of a comparable standard slot waveguide.

6.3.2 Fabrication, SEM, and Simulation

Our devices were fabricated from silicon-on-insulator (SOI) wafers with a $\sim$212 nm thick Si device layer and $\sim$1 μm thick buried oxide. Electron beam lithography (JEOL JBX-9300-100kV) was performed using ZEP 520A resist spun at 6,000 rpm ($\sim$300 nm thick). Reactive ion etching of the exposed Si regions was performed with C_4F_8, SF_6, and Ar process gases. Photolithography was then carried out using Shipley 1813 photoresist to facilitate selective undercutting of the nanobeam while not affecting the input/output bus waveguides and grating couplers. A standard 10:1 buffered oxide etchant (BOE) was applied in two ten-minute intervals with deionized (DI) water rinsing and nitrogen drying performed in between and after the BOE steps. This approach was sufficient to release the $\sim$30 μm length nanobeams without the need for vapor etching or critical point drying. Finally, samples were soaked and agitated in acetone for 5 min to remove the photoresist, and immediately rinsed in DI water and dried under nitrogen flow.

Our slotted single nanobeam cavity, shown in Fig. 6.5, is formed utilizing a pair of Bragg mirrors, consisting of $N = 9$ mirror segments, with lattice constant $a = 559$ nm. This choice of a places the dielectric band edge near 1550 nm. Toward the center of the cavity five-hole tapers are used, wherein the hole spacing is linearly tapered from 559 nm to a defect spacing of 450 nm between the central most air-holes. At the same time, the hole radii are tapered from approximately 187.5 nm to 150 nm. On either side of the Bragg mirrors, input/output tapers are used to promote more efficient coupling to slot waveguides [96]. These tapers utilize the same linear reduction in hole spacing as the central cavity tapers, but with a linear reduction in hole size from 187.5 nm radius to 110 nm to better

match the effective index of the slot waveguide. Across the entire device length, a slot width of 52 nm and waveguide width of 610 nm are used. Lastly, the slot waveguides are efficiently coupled to input/output bus ridge waveguides through compact mode converters [231] that are routed to input/output grating couplers oriented at 90° to facilitate cross-polarized optical characterization.

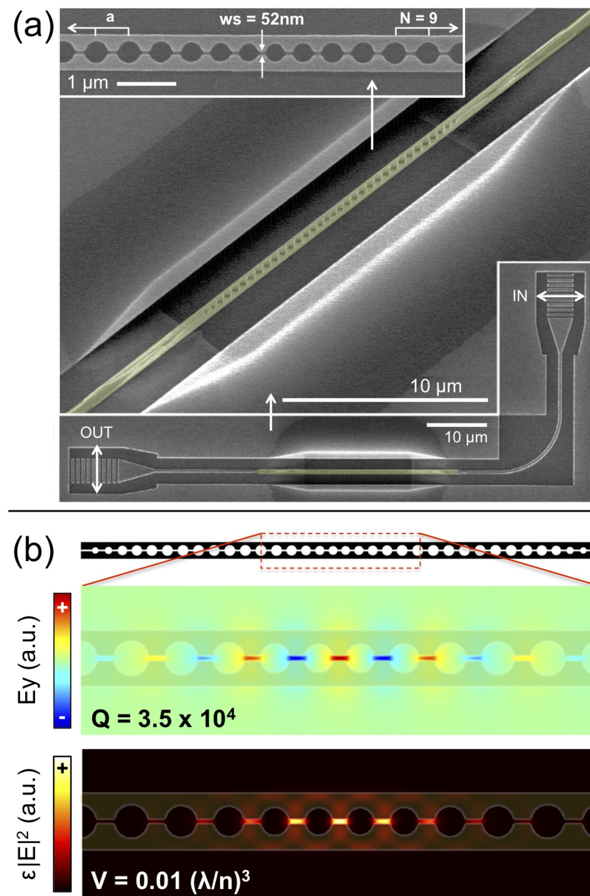

Figure 6.5: (a) SEM images of a slotted photonic crystal single nanobeam cavity, showing the 52 nm slot width, air-clad waveguide coupled geometry, and input/output grating couplers. (b) Field and power distributions for the fundamental mode of the slotted photonic crystal single nanobeam cavity with Q-factor $\sim 3.5\times10^4$ and mode volume $\sim 0.01(\lambda/n)^3$. The plotted distributions are for a 2D slice through the center of the cavity, taken from 3D FDTD simulation. Figure adapted from Ref. [89].

As shown in Fig. 6.5.b the slotted PhC single nanobeam cavity structure supports a fundamental mode with a high Q-factor $\sim 3.5 \times 10^4$ and ultra-small mode volume $\sim 0.01(\lambda/n)^3$, determined from 3D finite difference time domain (FDTD) simulation. In our simulations, we found that the device Q-factor was very sensitive to the exact defect spacing and taper geometry, similar to reports for non-slotted nanobeam cavities [75, 87]. The Q-factor reported here is more than one order of magnitude higher than a recently proposed design with the same slot width [232]. By using an even smaller slot width, a simultaneous increase in Q-factor and reduction in mode volume could be achieved. However, due to fabrication feature-size limitations, it may be desirable to realize higher Q-factors by instead employing a more gradual tapering strategy or a deterministic design approach [87, 94, 233]. We anticipate that the theoretical cavity Q-factor of a slotted PhC single nanobeam cavity can be increased to match the recently reported ultrahigh $> 10^6$ Q-factors reported for other 1D PhC cavities. However, any substantial increase in Q-factor will likely come at the cost of an increased modal volume. These issues will be examined in greater detail in Section 6.4.1 as we explore ultra-high Q/V designs.

6.3.3 Measurement and Analysis

Slotted PhC single nanobeam cavities were measured using a cross-polarized optical configuration, which was found to be a rapid and straightforward method that enabled the measurement of many devices within a compact area, thus eliminating the need for $\sim$mm length input/output waveguides and precisely aligned lensed fibers. Light from a tunable laser (Santec TSL-510) is sent through a beam splitter and focused onto the input grating coupler, Fig. 6.5.a, through a long working distance 20x objective. From infrared imag-

ing, the spot size was estimated to be $\sim 30\ \mu$m in diameter. With the same objective and beamsplitter, light from the sample surface is simultaneously collected, passed through a linear polarizer oriented 90° relative to the input polarization, and analyzed by an InGaAs photodetector camera.

Fig. 6.6.a shows the optical transmission of the slotted photonic crystal single nanobeam cavity normalized by the peak optical transmission near the band edge. Similar to other recently demonstrated nanobeam cavities, simulations suggest approximately unity optical transmission near the band edge [87, 234]. The measurement shown in Fig. 6.6.a reveals the dielectric band edge at $\sim$1548 nm, in close agreement with simulations (Fig. 6.4.a), and the presence of a single high Q-factor resonance, at 1513.9 nm, with a peak normalized optical transmission of $\sim$0.12. This relatively low resonance transmission level, which can be described by $T = (Q_{meas}/Q_{wvg})$ [216, 229] suggests that the cavity Q-factor is not limited by the waveguide Q-factor, Q_{wvg}, but rather the radiation Q-factor, Q_{rad}. Note that $1/Q_{meas} = 1/Q_{rad} + 1/Q_{wvg}$. In other words, the lifetime for a photon to be scattered out of the cavity is shorter than the lifetime for a photon to decay into the waveguide. This is further apparent when examining the IR camera image of the cavity on resonance [inset; Fig. 6.6.a], as we observe a larger intensity for vertical radiation coming from the nanobeam than we do for light coming from the output grating coupler. As shown in Fig. 6.6.b, our optical interrogation technique also enables us to measure vertical radiation spectra for light radiating out of the cavity. Whereas other configurations might isolate the collected signal using a pinhole and photodiode [235], our scheme relies on the position sensitive detection capability of the photodetector camera, similar to what has been reported for measurements on multiple ring resonator systems [236]. The vertical radiation spectra similarly reveals

the single high Q-factor resonance at 1513.9nm, but with an even higher signal-to-noise ratio, confirming that both the measured Q-factor and ~0.12 transmission level are limited by the radiation losses. Lorentzian fitting of both resonance measurements reveals a measured quality factor, $Q_{meas} \approx 7.42 \times 10^3$. Combined with the ~0.12 on-resonance optical transmission, we estimate an intrinsic radiation Q-factor, $Q_{rad} \approx 1.14 \times 10^4$. Although this quality factor is smaller than the record high Q-factors reported for non-slotted 1D PhC cavities [75, 97], our experimentally achieved $\sim 10^4$ Q-factor is already sufficient to enable applications ranging from optical modulation to sensing, where the ultra-small $\sim 0.01(\lambda/n)^3$ mode volume should offer substantial improvements to device sensitivity.

6.4 Ultra-High Q and Q/V

6.4.1 Introduction

Obtaining a high resonance Q-factor is another important consideration for achieving enhanced light-matter interaction. While mode-volume, V, relates to the *spatial confinement* of an optical mode, the Q-factor is directly related to the cavity lifetime and can be considered a measure of *temporal confinement*. With ultra-high Q-factors, the resonant light coupled into a cavity can build up to very high field intensities. For example, a whispering gallery resonator with a $Q \sim 10^8$ may confine up to approximately 10W of optical power when a coupling fiber is injected with only 1 mW input power.

In the original slotted nanobeam design introduced in Section 6.3.2, theoretical Q-factors $> 10^4$ were achieved with an ultra low $V \sim 0.01(\lambda/n)^3$ by incorporating two important design choices: (1) the use of a common five-hole taper design and (2) the use of

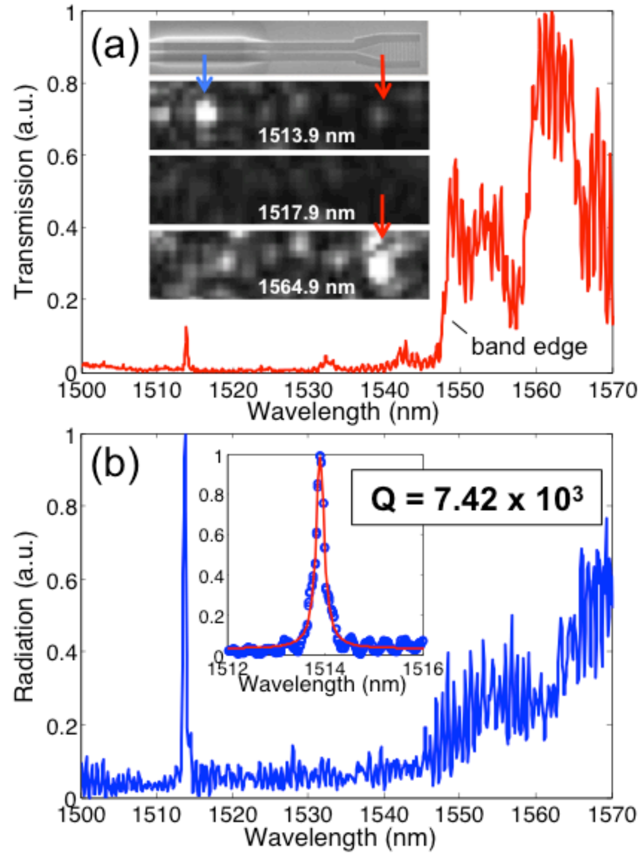

Figure 6.6: (a) Transmission spectra for the slotted photonic crystal single nanobeam cavity, revealing the cavity resonance at 1513.9 nm and dielectric band edge at ∼1548 nm. Inset reveals IR camera images (aligned to top SEM image) spanning the cavity and output grating coupler for different wavelengths of interest: on-resonance, in the PBG, and in the dielectric band. (b) Radiation spectra for the same device in (a), with the inset revealing a close up of the resonance at 1513.9 nm with a Lorenztian fit indicating an experimentally measured Q-factor, $Q_{meas} \approx 7.42 \times 10^3$. Figure adapted from Ref. [89].

a continuous slot, which is unterminated along the length of the nanobeam. Both of these design choices suppress radiation losses by reducing the typically large effective index mismatch between the defect and Bloch mode in the PhC mirror. However, these initial designs were developed through a parameter search and do not globally maximize Q or Q/V. In principle, significantly improved Q-factors, potentially $> 10^6$, should be achievable with proper design considerations. In this Section, we will adapt a deterministic design approach to investigate the possibility of achieving ultra-high Q-factors ($> 10^6$) alongside low mode volumes using the slotted nanobeam cavity platform.

6.4.2 Deterministic Design

The deterministic design approach, taken here, is a recently established method for achieving record high Q-factors without the need for a trial-and-error parameter search [87]. The principle of this method is to establish a Gaussian field distribution by specifically tapering the PhC to provide linearly changing mirror strength γ. This method has demonstrated that an arbitrarily high Q, greater than 10^9, can theoretically be realized provided an arbitrarily long and gradually tapered PhC is employed.

In this analysis we adapt the slotted nanobeam structure to utilize a periodic arrangement of ellipsoids instead of circles. This structure is more generalized than the circular case, and also provides a larger dynamic range of tunable band structures. This enables the air and dielectric bands to be shifted slightly further away from the light cone, and is a strategy that has previously been implemented to realize high-Q, low index contrast nanobeam cavities [237]. Although high theoretical Q-factors can be realized with the circular hole slotted nanobeam cavity, we note here that the ellipsoidal geometry may be preferred for

future implementations of the slotted nanobeam in reduced index contrast configurations (e.g., involving oxide or liquid claddings) owing to its larger photonic band gap and larger effective index. The following simulations will strictly examine the ellipsoidal hole slotted nanobeam in a suspended all-air cladding configuration.

Figure 6.7 illustrates the fundamental components of the deterministic design approach. To create the cavity resonance, the band structure will be spatially modulated by fixing the periodicity, a, and tapering the ellipsoid dimensions. For simplicity, we will fix the slot width ws, waveguide width w, and the ellipse minor axis dimension ra, thus restricting our taper to utilizing only a spatially varying ellipse major axis dimension rb. The appropriate taper design will be the one which provides a linearly varying mirror strength defined as:

$$\gamma = \sqrt{(\omega_2 - \omega_1)^2/(\omega_2 + \omega_1)^2 - (\omega_{res} - \omega_{mid})^2/\omega_{mid}^2}, \tag{6.3}$$

where ω_2 and ω_1 are the frequencies corresponding to the air and dielectric band edges, ω_{res} is the resonant frequency (equivalent to the local dielectric band edge in the center of the cavity), and ω_{mid} is the mid-gap frequency $(\omega_2 + \omega_1)/2$. At the center of the cavity, the ellipse dimension rb will be largest (blue, Fig. 6.7) and then taper to a smaller value out into the Bragg reflectors (red, Fig. 6.7). The taper slowly shifts the bands downward (toward lower frequencies), thus placing ω_{res} inside the mode gap. 3D band structure calculations are used to determine the dispersion and band edge frequencies as in Fig. 6.7.a. This calculation also assumes an ellipse minor axis $ra = 0.84a$, slot width $ws = 0.125a$, waveguide width $w = 2.16a$, and height $h = 0.455a$. These parameters were pre-selected in order to meet a design criteria for the minimum achievable slot width dimension, $\sim 50-60$ nm, and

a 220 nm waveguide height set by the SOI wafer. With $rb = 2.0a$ at the center of the cavity, this combination of parameters produces a normalized $\omega_{res} \approx 0.32$, enabling the resonant wavelength to be set to near 1550 nm by choosing $a = 500$ nm ($500/0.32 = 1562.5$). We then use 3D band structure calculations to determine γ as a function of rb, varying between $1a$ and $2a$, as shown in Fig. 6.7.c. As rb initially decreases from $2a$, γ increases, levels out near a maximum value, and then decreases back to zero. The maximum mirror strength is obtained when the resonance frequency is centered within the mode gap. We then choose to narrow our design parameter space to utilize rb in the range from $2a$ to $1.75a$.

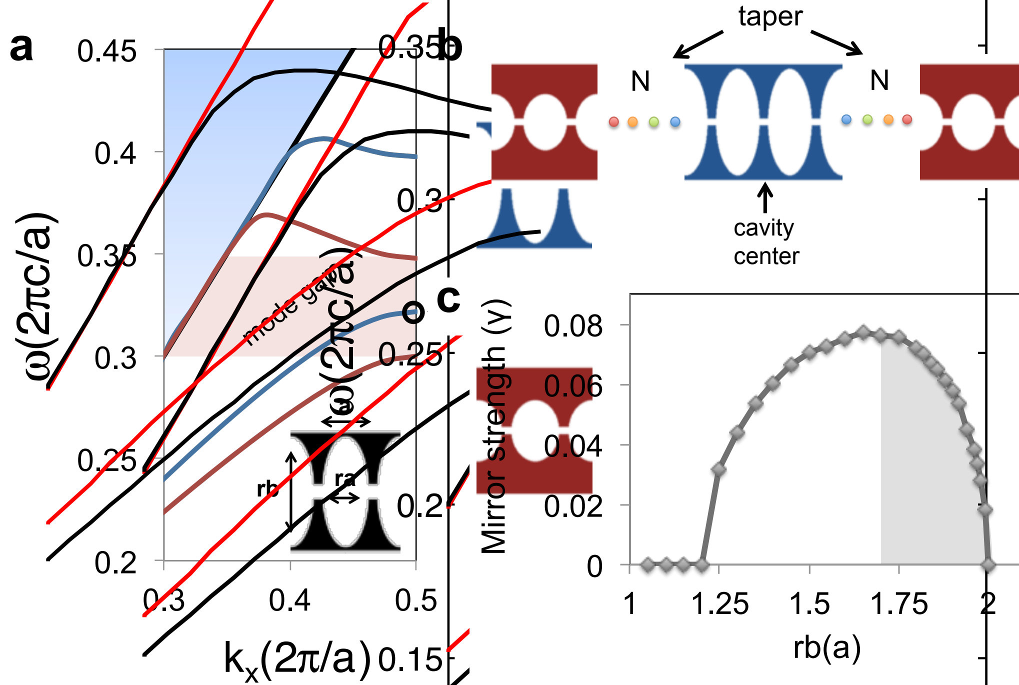

Figure 6.7: Overview of the deterministic design approach. (a) Band structure for ellipsoidal pinch waveguides of varying ellipsoid parameters, i.e. $rb = 2a$ (blue) and $rb = 1.75a$ (red). (b) The cavity is formed by symmetrically tapering out from the cavity center, with a taper of length N, to the Bragg reflectors. (c) Mirror strength, γ, as a function of rb. The taper should be designed to provide a linearly changing mirror strength.

6.4.3 Simulation Results

After determining the mirror strength γ as a function of the design parameters (in this case varying just rb), we can linearize the mirror strengths and map out rb as a function of mirror segment number. Linearized mirror strengths and the corresponding mappings are shown in Figures 6.8.a, b for varying taper lengths $N = 5,\ 10,\ 20,\ 40$. With these parameters, the tapers and optical cavities can be constructed and simulated. Figure 6.8.c shows 3D FDTD simulation of an example slotted nanobeam designed with a taper length $N = 10$. This structure and all subsequent simulated cavities also include Bragg reflectors of length $N+1$, with design parameters equivalent to the final mirror segment in the taper ($rb = 1.75a$). As with the original slotted nanobeam design, this structure exhibits strong localized field enhancements within the nanoscaled slot. For this structure, 3D FDTD simulation yields a high $Q = 5.7 \times 10^5$ and low $V = 0.028(\lambda/n)^3$, with a resonance wavelength of $\sim$1533 nm, thus verifying the validity of the deterministic design approach.

A comparison of the Fourier transformed field distribution for the original and deterministically designed slotted nanobeam cavities is shown in Figure 6.9. The original design clearly has a broader distribution of field components, including overlap near the origin and within the light cone. These field components couple to radiation modes and thus limit the cavity Q-factor. In the deterministic case however, the field components are better localized to $+\pi/a$ and $-\pi/a$, with minimal overlap near the origin. This demonstrates that the deterministic design approach achieves high Q-factors by suppressing field components within the light cone and minimizing radiation losses.

To investigate the influence of the taper length N on the theoretical Q and V values,

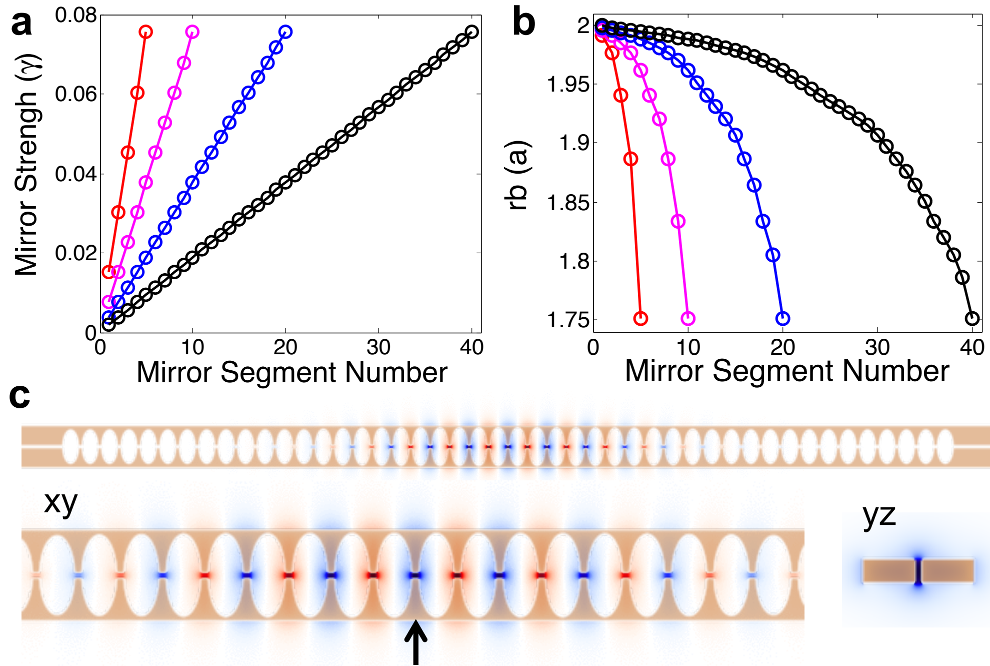

Figure 6.8: (a) Linear variation of mirror strength for selected taper lengths, N, and (b) the corresponding mapped variation of rb. (c) Electric field distribution, taken from 3D FDTD simulation, for a cavity with $N = 10$ and a high $Q = 5.7 \times 10^5$ and low $V = 0.028(\lambda/n)^3$.

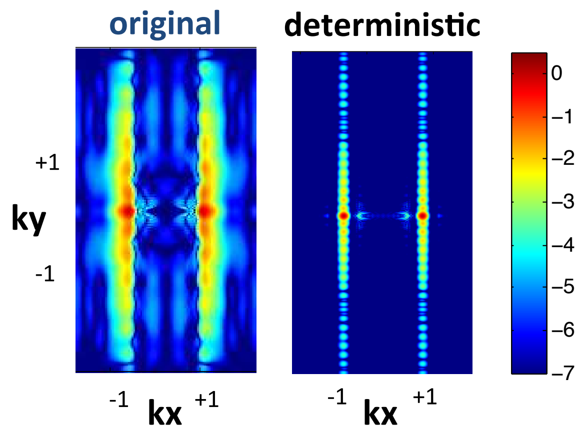

Figure 6.9: Fourier transform of the electric field distributions for the original (Sec. 6.3.2) and deterministically designed slotted nanobeam cavities.

we also performed 3D FDTD simulations on deterministically designed slotted nanobeam cavities with taper lengths ranging from $N = 1$ to 20. The results are summarized in Figure 6.10. As expected, increasing N also significantly increases Q, as longer tapers provide a more graduate change in effective index, and a better approximation of a linearly varying mirror strength. For $N = 20$ a record high $Q = 1.3 \times 10^7$, is found for the slotted nanobeam cavity. Changing N also affects the mode volume V and resonance frequency ω. For most cases of practical interest, a larger N corresponds to a larger mode volume. We do observe an exception at $N = 1$, as this taper design does not produce a cavity with good optical confinement. Unlike Q-factor, which changes by several orders of magnitude with varying values of N, the mode volume only varies over a relatively small range, from $\approx 0.02(\lambda/n)^3$ to $0.047(\lambda/n)^3$. Thus, by sacrificing a small increase in mode volume, several orders of magnitude enhancements to Q and Q/V (Fig. 6.10.c) can be obtained. For these design parameters, ultra-high Q/V values, $> 10^8(\lambda/n)^{-3}$, can be obtained. Therefore, the deterministic design approach can be utilized to provide greater than two orders of magnitude improvement to Q or Q/V when compared to the original slotted nanobeam design (Sec. 6.3.2). It is also likely that additional design improvements, or optimization of the starting waveguide dimensions, could yield even higher values of Q and Q/V for a given taper length N.

6.5 Summary

In this Chapter we have introduced a novel photonic platform, the “pinch waveguide” (or slotted nanobeam), which is based on a slot waveguide with 1D periodic holes. The structure exhibits significant localized field enhancements in both guided and defect modes that

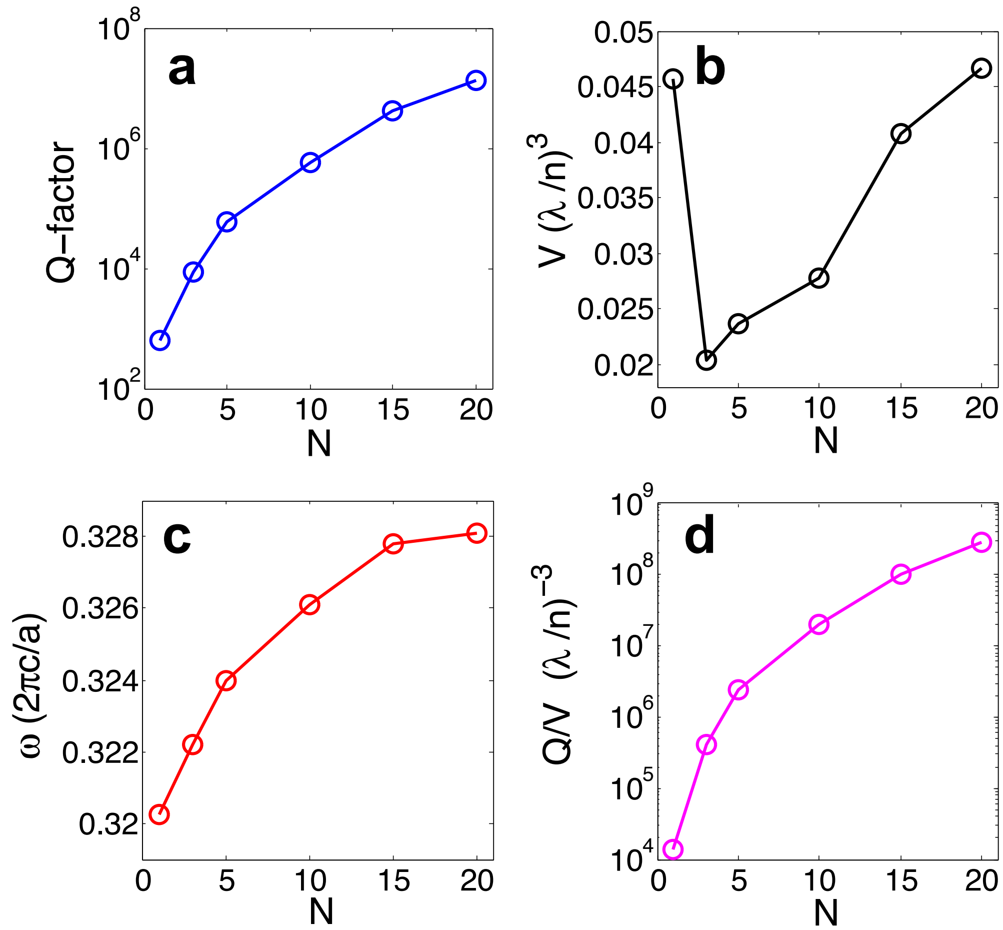

Figure 6.10: Simulated variation in (a) Q-factor, (b) mode volume, (c) resonant frequency, and (d) Q/V for deterministically designed slotted nanobeam cavities of varying taper length, N.

are stronger than what can be achieved by using either the conventional slot or 1D periodic hole structures alone. Distinct and tunable optical gradients as well as localized $|E|^2$ and power confinement enhancements, up to $\sim$4-5 times and $\sim$250-400% enhanced respectively, over comparable slot waveguides can be achieved. Notably, the guided mode field enhancements of the pinch waveguide are fundamentally not linked to slow-light effects, as are other previous combinations of slotted and photonic crystal geometries. Therefore, extension into the slow-light regime would only produce further enhancements owing to the reduction in v_g. The pinched field phenomenon arises from the combination of two important results of Maxwells equations: (1) the slot effect and (2) the electromagnetic variational principle. Many potential applications related to sensing, optical manipulation, and non-linear or active material integration could benefit from utilizing the pinch waveguide design.

We have also reported the experimental demonstration of a slotted photonic crystal single nanobeam cavity in silicon. The slot geometry is exploited to provide strong confinement and localized field enhancements, resulting in an ultra-small mode volume $\sim 0.01(\lambda/n)^3$. This represents the smallest mode volume ever achieved in an all-dielectric 1D PhC cavity while still maintaining a Q-factor $> 10^3$. The high Q-factor is achieved by combining a common five-hole taper design with the continuously slotted pinch waveguide platform. Through additional design tailoring, such as the application of a deterministic design approach, ultra-high theoretical Q-factors $> 10^7$ can be realized in this low mode volume platform. Importantly, the slotted nanobeam platform could be used to benefit a variety of applications including non-linear optics, cavity QED, sensing, optical modulation, and nano-optomechanics.

CHAPTER 7

CONCLUSION

7.1 Summary

In this dissertation, we opened with an introduction to two important classes of nanomaterials: (1) porous nanomaterials and (2) phase-change nanomaterials. These material platforms offer unique and attractive characteristics rendering them appropriate for a variety of photonic applications, particularly in sensing and communications. Prior to this work, unsolved challenges and questions remained pertaining to the fabrication, integration, and characteristics of photonic devices constructed from these materials. Further, the study of phase-change materials integrated with optical resonators revealed unanswered questions regarding light-matter interactions, and motivated more general investigation in photonic design.

An important focus of this dissertation pertaining to porous nanomaterials has been the development of a novel fabrication technique – direct imprinting of porous substrates (DIPS). DIPS is the first lithographic technique applied to porous nanomaterials capable of directly patterning porous device layers without the need for resists, thermoplastics, or etching processes. The combination of high resolution pattern transfer (< 100 nm) and rapid processing (< 1 min) is unique to DIPS, and technologically advantageous for advancing both the research and commercial potential of porous nanomaterials. In this work, DIPS was utilized to pattern a wide variety of porous nanomaterials, spanning insulators,

semiconductors, and metals. DIPS has further been utilized to pattern nanoporous gold (npAu) on the sub-micron scale for the first time. This has led to the development of surface enhanced Raman scattering (SERS) substrates with the desirable combination of low-cost and high enhancement factor, as described in another dissertation [238]. In porous silicon (pSi), we utilized DIPS to demonstrate the first porous diffraction based biosensor. The diffractive sensing technique was demonstrated for the highly sensitive detection of the small molecule 3-APTES, and was shown to offer the advantage of fixed wavelength and fixed angle interrogation, as well as the advantage of an enhanced surface area when compared to non-porous diffraction gratings. The porous diffraction grating was also integrated with micro-fluidics for real-time monitoring of small molecule attachment. The successful proof-of-concept experiments demonstrate that porous diffractive sensors are attractive for performing low-cost, high sensitivity, and real-time label-free biosensing.

The introduced DIPS technique achieves patterning by imprinting porous nanomaterials and locally densifying selected regions. This unique ability, which does not exist in any previously demonstrated technique, was further investigated and utilized in gray-scale DIPS, which enables 3D surface patterning and morphological control over porous nanomaterial properties. These studies required the refinement of gray-scale electron beam lithography techniques in order to fabricate the silicon stamps. Four classes of 3D structures were demonstrated in porous nanomaterials for the first time, including: (1) continuous sloped profiles (i.e., blazed diffraction gratings), (2) digital patterns, (3) curves and lens shapes, and (4) sharp nanoscaled features including v-grooves, nano-pits, and cookie-cutter particles. Gray-scale DIPS was further employed and demonstrated for tailoring nanomaterial properties including porosity, pore size, dielectric constant, and plasmonic response. These

new capabilities open the possibility of constructing a wide range of novel nano- and micro-optic devices with porous nanomaterials, spanning applications in diffraction or plasmonic sensing, holography, micro- and transformation optics, and drug delivery and imaging.

Regarding the photonic application of phase-change nanomaterials (PCNMs), a primary focus of this dissertation studied the integration of the well known PCNM vanadium dioxide, VO_2, with the silicon photonics platform. Unlike the challenges addressed by DIPS, these investigations utilized existing fabrication techniques and focused on exploring the characteristics and advantages of an integrated hybrid Si-VO_2 platform. Through a combination of lithography, etching, deposition, and lift-off processes, which were individually refined, ultra-compact hybrid Si-VO_2 micro-ring resonators were fabricated and characterized. We demonstrated that the phase transition could be successfully triggered in the hybrid Si-VO_2 platform by utilizing photothermal stimuli to locally heat devices beyond the phase transition threshold temperature. This approach was found to be a convenient alternative to using large heating stages, and facilitated measurement and characterization of individual devices with minimal thermal expansion or fiber-to-chip coupling issues. The ultra-compact hybrid Si-VO_2 resonator was demonstrated to provide greater than 10 dB optical modulation while requiring only a very small ($\sim 0.28\ \mu m^2$) active area of integrated VO_2. Compared to previous works, typically studying the optical response of VO_2 thin-films or large-area arrays, this work demonstrates a significant reduction in the total size of an individually probed photonic structure incorporating VO_2. Aside from its potential for use in communications and computing applications, the hybrid Si-VO_2 platform may be attractive for fundamentally studying the phase transition of VO_2 or other potentially integrate-able PCNMs owing to the resonant device geometry and small active dimensions

required to observe a response.

The photothermal approach for switching hybrid Si-VO_2 devices was experimentally found to suffer from two primary limitations: (1) the local heating effect can be slow (switching occurred over many seconds or minutes under our pump conditions), and (2) heating of the Si produces small, but measurable thermo-optic effects which reduce the overall resonant response provided by the SMT of the VO_2. To explore overcoming these issues and to further develop and characterize the hybrid Si-VO_2 platform, we developed a new set of experiments, wherein the SMT was triggered by a nanosecond pulsed laser. With this new approach, we achieved nearly 9-orders of magnitude enhancement in switching speed, demonstrating optically induced reconfiguration of hybrid Si-VO_2 resonators and absorbers on a time scale comparable to the pump pulse duration ($\sim 25-30$ ns). We also confirmed our expectation, that the "off" time (or time to reverse the SMT), typically tens to hundreds of nanoseconds, was longer than the rapid "on" time. Unexpectedly however, we discovered that the "off" time could be substantially reduced, by nearly an order of magnitude, by changing the length of the VO_2 patch to sub-micron dimensions.

With these experiments we also introduced the hybrid Si-VO_2 platform as a more generalized approach for performing either absorption modulation or intracavity phase modulation. We discovered that the nanosecond pulsed laser can optically induce the SMT without global device heating, thereby eliminating unwanted thermo-optic effects in the Si. This enables the hybrid Si-VO_2 platform to perform optical reconfiguration dictated solely by the optical response of the integrated VO_2. Importantly, we experimentally demonstrated record values of optically induced in-line absorption modulation (~ 4 dB μm^{-1}) and intracavity phase modulation ($\sim \pi/5$ rad μm^{-1}). The in-line absorption modulation

effect was also demonstrated to be very broadband, effective across a broad spectral range ($\sim 1500-1600$ nm). The resonant response of the ultra-compact, 1.5 μm radius, Si-VO_2 micro-ring resonator was ~ 60 times larger than control Si-only devices, and enables resonant reconfiguration to be performed very effectively with lower Q-factor devices. This importantly promotes the ability to operate outside the regime where thermal fluctuations can play a significant role. Further, we experimentally demonstrated that the resonant response is maximized for the smallest devices, following a R^{-1} dependence. This result demonstrates the technological importance of reducing the mode volume of an optical resonator as it enables a simultaneous improvement to device performance and reduction in device footprint.

The final focus of this dissertation, regarding the enhancement of light-matter interactions, led to the development of a novel photonic platform referred to as the "pinch" waveguide (or slotted 1D PhC nanobeam). This work was motivated largely by the clear importance of mode volume and device footprint revealed in the hybrid Si-VO_2 experiments. The "pinch" waveguide was conceptually introduced through finite difference time domain (FDTD) simulations, where it was demonstrated to provide distinct and tunable optical gradients as well as localized $|E|^2$ and power confinement enhancements, up to $\sim 4-5$ times and $\sim 250-400\%$ enhanced, respectively, when compared to traditional slot waveguides. With the slotted nanobeam platform, a record low-mode volume 1D PhC cavity maintaining a high Q-factor was proposed and then experimentally demonstrated. Experiments revealed that the Q-factor (nearly 10^4) was limited primarily by radiation losses, and it was proposed that more advanced designs could be implemented to surpress radiation losses and increase Q-factor.

Fabricating the slotted nanobeam required refinement of the electron beam lithography and reactive ion etching processes in order to realize a nanoscaled slot dimension close to ~ 50 nm. We found that $\sim 30\ \mu$m length nanobeams were stiff enough to be suspended, without collapsing, through standard buffered oxide etching without the need for HF vapor etching or critical point drying procedures. The mechanical stability of this length slotted nanobeam is attractive for potential integration into microfluidic sensing. In these experiments, we also developed a custom technique for measuring vertical transmission or radiation spectra using input/output grating couplers oriented at 90 $^{\circ}$C in a cross-polarized configuration using an InGaAs photodetector camera. This measurement technique could be employed to rapidly measure many devices on the same chip, eliminating the need for $\sim$mm length bus waveguides, as well as input/output fibers or opto-mechanic accessories to position or rotate such fibers.

Lastly, we investigated the possibility of developing slotted nanobeam cavities with ultra-high Q and Q/V values. This was explored and achieved in 3D FDTD simulations after adopting a recently developed deterministic design approach. With appropriate taper designs, theoretical Q-factors $> 10^7$ were identified, representing nearly 3 orders of magnitude enhancement over the original slotted nanobeam. Importantly, it was demonstrated that these deterministically designed cavities also maintained low mode volumes, $< 0.05(\lambda/n)^3$, up to an order of magnitude smaller than conventional 1D PhC cavities. The successful experimental demonstration of the slotted nanobeam, in combination with these simulated design improvements, indicates that the slotted nanobeam platform could be used to realize nanophotonic devices with record values of Q/V.

7.2 Future Work

7.2.1 DIPS for Sensing and Drug Delivery

In this dissertation, DIPS was demonstrated for the rapid and high resolution patterning of porous nanomaterials. While this has already led to the fabrication of low-cost diffraction based biosensors, SERS substrates, and porous micro-particles, there are a variety of avenues for continued exploration and improvement.

First, opportunities exist for further improving the porous diffraction based sensor. This may include adjusting the refractive index contrast, i.e., tuning porosity or changing to another porous nanomaterial, to tune the change in diffraction efficiency that occurs in response to analyte exposure. Initial attempts using pAl_2O_3 have successfully verified a significant diffractive response to water vapor exposure, indicating that the concept can be readily extended to other porous nanomaterial platforms. As with other porous sensors, the pore size may also be optimized for a particular target analyze size. Further enhancements to sensitivity may be achieved by incorporating a light-confinement mechanism to enhance the diffraction efficiency and thus increase sensor response. One way to achieve this is to combine the diffraction grating with a Bloch surface wave. This approach has already been successfully reported in planar, non-porous configurations. Alternatively, it should be possible to enhance the diffractive response using surface plasmon effects launched in npAu films.

In principle, these sensors could be mass produced and integrated with low cost lasers, photodiodes, and microfluidics to create a complete sensing package. However, DIPS has thus far only been applied for uniform imprinting of patterns generally $< 20\ mm^2$ in area.

One approach for larger scale production, would be to automate the DIPS process, using a step-and-repeat method. This approach is particularly promising because each imprinting step can be rapidly performed in less than a few seconds. This would require careful attention to ensuring constant fidelity and cleanliness of the stamp and/or substrates. Processes could be incorporated to automatically wash or monitor the stamps to ensure high quality patterning. Alternative stamping geometries, such as a 'roller stamp' could provide an elegant solution to rapidly replicating patterns over large areas. This is challenging in practice, however, because fabrication of the stamps is generally limited to planar fabrication techniques. Ideally, DIPS could be extended to large area patterning on the wafer scale. However, uniformly imprinting patterns over such large areas is very challenging owing to a number of factors. First, very uniform leveling of the sample holder and imprinting plate must be ensured. Further, the applied force must be uniformly distributed across the wafer and applied normal to the wafer surface. Another challenge at large areas is the potential for microscale flexing of the wafer and potential non-uniformity of device layer thicknesses or porous substrate properties. However, flexing of the stamp wafer could potentially be used as an advantage in alternative stamping configurations (i.e., where the pressure is purposely non-uniformly applied to imprint different regions to different depths, or to perform imprinting in multiple steps). DIPS may also be difficult at the wafer scale, owing to the large forces that may be required to achieve the appropriate pressures required for imprinting. This could be circumvented somewhat, through appropriately designing the stamps to minimize unnecessary surface contact area with the porous substrates. There is further room to explore other stamp materials which may provide more robust mechanical properties. These challenges motivate continued study and improvement, and would benefit not

only sensing applications, but nearly all potential applications of the DIPS process.

Drug delivery and imaging are particularly attractive potential applications of the DIPS process because DIPS can be applied to fabricate large area arrays of nanoparticles with well defined shapes and sizes. Obtaining the desired nanoparticle size and shape is relatively straightforward, requiring only the appropriate stamp pattern to be fabricated. In practice, two primary challenges which merit continued investigation are: (1) improving nanoparticle yields and quantities, and (2) improving/optimizing nanoparticle lift-off or detachment. The yield/quantity problem is partially tied to the challenge of large area imprinting as discussed above. However, it is possible to improve particle quantities by appropriately designing the stamp to maximize the packing density of particles. This has been initially demonstrated for micro-particle fabrication and could be extended to nanoparticles with appropriate optimization of the stamp fabrication processes. Large packing densities provide a further advantage of reducing the total force required to reach imprinting pressures. This 'cookie-cutter' process also minimizes the total area of pore densification and reduces the total area of discarded or wasted porous substrate. The 'step-and-repeat' technique is promising for large area patterning, but is complicated in the case of micro- and nano-particle fabrication because of the tendency for particles to lift-off with the stamp. Thus, the lift-off problem is particularly important, but must be optimized for each specific porous substrate. Ideally, DIPS could be applied repeatedly with the same stamp without lifting-off the particles directly. Subsequent removal of the particles should then be optimized to ensure high yield, without particle loss or damage. Potential candidate techniques include the use of dissolvable adhesives, or the application of brief sonication and washing steps. With pSi, thin lift-off layers of high porosity can be purposefully etched

beneath the patterned device layer, either before or after imprinting, to better control lift-off. Finally, more advanced micro- and nano-particles can be envisioned which incorporate specific optical signatures or controlled mechanical properties. Preliminary investigations have verified the ability to fabricate Bragg reflecting micro-particles from pSi multilayers. These particles, which exhibit distinct colors and reflectance properties, would be attractive for imaging applications or monitoring of drug delivery. Gray-scale DIPS could also be applied to pattern the mechanical or optical properties within a given micro-particle, thus enabling greater control over particle degradation, drug loading or release, and colorimetric properties.

7.2.2 Hybrid Si-VO_2 Photonics

Opportunities exist for exploring and studying the hybrid Si-VO_2 platform and other potential PCNM platforms in new device configurations, which may improve speed, energy consumption, reconfigurablity, or other perfomance metrics.

A primary objective of ongoing and future work, should include achieving ultra-fast device operation. These experiments would require the use of femtosecond pulsed lasers in a slightly modified pump-probe configuration. Studies of ultra-fast SMT switching on the sub-pico second timescale should also be accompanied by exploration of ways to reduce the relaxation time. Unlike the athermal and ultrafast $\sim 10^{-13}$ s optically driven SMT of VO_2, the structural phase transition (SPT) from the tetragonal, metallic crystal structure back into the monoclinic, semiconducting state relies on carrier-phonon interactions taking place on longer $\sim 10^{-9}$ s timescales. Improving the relaxation time is currently a topic of significant research interest. A number of factors are known or expected to influence

this relaxation time, including the active VO_2 volume, crystallite domain size, doping, and excitation fluence. For example, measurements of the THz signal show that up to a threshold of about 3 mJ cm^{-2} in a thin VO_2 film pumped by a femtosecond 800 nm pulse, the recovery from the metallic state takes only about 1 ps [162]. For the nanoscale VO_2 patches needed for the ring resonator, the fluence needed to reach the threshold should be much lower for near band-edge pump wavelengths. As we have already identified, patch size is an important factor influencing relaxation of the SPT, and further studies should investigate this effect over a wider range of geometries. It may also be possible to speed up the relaxation time by incorporating an electrical bias or diode configuration to rapidly sweep away excess carriers. Such experiments further motivate the development of electro-optic Si-VO_2 devices. Future work should also include measurements of the time-dependent dielectric function as a function of fluence, and measurements of the SMT threshold and SPT relaxation for near band-edge pump wavelengths.

The successful demonstration of the optically triggered Si-VO_2 photonic platform opens the door to new investigations wherein the phase transition is triggered by alternative stimuli. For example, by incorporating an applied bias, and using electrical contacts, it should be possible to achieve electro-optic device operation. Such investigations could also be performed in other nanophotonic configurations, for example using plasmonic devices. Importantly, questions remain about how rapidly or efficiently such hybrid electro-optic devices can be switched. Studies should include the goal of determining the relative influence of voltage or current on the SMT to reveal the relative contributions from electric-field or Joule heating effects. Alternative devices can also now be envisioned which might harness doping, strain, or exothermic reactions to trigger the phase transition. These devices could

form ultra-compact sensors capable of monitoring a diversity of environmental parameters.

The hybrid Si-VO_2 photonic platform, and other potential hybrid PCNM combinations, are also attractive for developing optical memories. The hysteresis of VO_2 provides a method for efficiently storing memory states. The semiconducting and metallic states are analogs of polycrystalline and amorphous states of electronic phase-change memories, commonly made from chalcogenide glasses. Based on this principle, reconfigurable VO_2 memory metamaterials have recently been proposed and demonstrated [189]. The memory state can be written electrically using an applied current pulse, which transiently heats the VO_2 through Joule heating (perhaps assisted by electric-field switching). Multiple memory states can be realized with properties varying anywhere in-between the semiconducting and metallic states by applying smaller electrical current pulses. Although memory operation of pure VO_2 would require elevated operating temperatures, near 67 $^{\circ}$C, doping should be used to bring the hysteresis to room temperature, which would enable non-volatile memories to be realized.

Hybrid photonic memory elements could provide several unique advantages over electronic memories. First, the read time is intrinsically ultrafast as it only requires optically probing transmission or reflection. Optical read-out also guarantees minimal power dissipation and immunity from electromagnetic interference. With the Si-VO_2 hybrid platform, we expect that the memory state could be written using short current pulses $\sim 10^{-9}$ s or ultrafast optical pulses $\sim 10^{-12} - 10^{-13}$ s, significantly faster than those of optomechanical memories (10^{-6} s) for example. Moreover, the memory effect can, in principle, be built into any photonic device structure, including optical cavities (e.g., ring resonator, photonic crystals) and waveguides (dielectric or plasmonic). Non-volatile memory op-

eration is also especially attractive for reconfigurable photonics applications where rapid modulation times are not necessarily required. For example, a photonic network could be adaptively reconfigured to route optical signals or to transform between different types of optical logic gates.

7.2.3 Slotted PhC Nanobeam Applications

The primary features of the slotted PhC nanobeam, including its ultra-compact footprint, ultra-small V, and potential for ultra-high Q, make it an attractive photonic platform for a wide variety of applications ranging from nano-optomechanics, to sensing, and communications.

The slotted PhC nanobeam cavity is attractive for nano-optomechanics applications, partially due to its stronger field confinement and a lower total mass ($<$ 10pg) than previously demonstrated nanobeam cavity configurations (typically $\sim$10-50pg) [235, 239]. Because the slot mechanically separates each half of the nanobeam, we anticipate that optical forces could be exploited to manipulate the slot width and tune the cavity, or achieve strong opto-mechanical coupling, similar to what has been reported for dual nanobeam implementations [79, 235, 240, 241]. Given the lower mode volume of the slotted nanobeam cavity and its increased sensitivity to the exact slot dimensions, we anticipate that the optical response will be much more sensitive to mechanical displacements. This should enable enhanced tunability for electrically programmable nanobeam cavities [242] and all-optically reconfigurable optomechanical filters [242].

Another prospective application of the slotted nanobeam is for optical manipulation, where small matter, such as nanoparticles or biomolecules, are confined and transported

by optical command. One problem faced by conventional optical manipulation techniques, such as optical tweezers or evanescent trapping, is that small particles only interact with a very small fraction of the optical field. This ultimately makes it difficult to achieve sufficiently strong optical forces to manipulate very small particles. Recent advancements have demonstrated increased optical control by using slot waveguides [213], microring resonators [243], and nanocavities [244]. These approaches increase light-matter interaction and correspondingly increase the optical forces experienced by small particles, resulting in unparalleled trapping stiffness [245]. In a similar manner, we expect that the field enhancements and sharp optical gradients of the pinch waveguide could be exploited for optical manipulation. In a guided mode structure, for example, nanoparticles will experience significantly enhanced optical forces owing to the distinct power and electric field concentration in the "pinch" regions. Thus, the structure could be considered as a nanoarray of strong point traps where optical confinement and radiation pressure are distinctly enhanced. Naturally, a slotted nanobeam cavity, could also be employed to further improve the optical confinement and enable stronger stationary trapping.

The strong power confinement of the pinch waveguide further opens the possibility for increasing the effectiveness of integrated active materials. A wide variety of non-linear [178, 207–211], phase changing [75, 80], electroluminescent [246], or otherwise active materials are being explored for achieving optical amplification, modulation, and detection in nanophotonic devices. Integrating these materials into the "pinch" region of the slotted nanobeam, where power confinement is enhanced $\sim 250-400\%$ over a conventional slot waveguide, could enable more effective and/or compact devices with reduced power requirements. For example, by integrating VO_2 with a slotted nanobeam cavity, where V is

on the order of $\sim 0.01(\lambda/n)^3$, we anticipate that large, $\sim$ nm scale, $\Delta\lambda$ resonant reconfiguration could be achieved at sub-fJ switching energies using single nanoparticles of VO_2.

The excellent optical confinement, compact size, and tunable properties of the slotted nanobeam provide a promising platform for studying and enhancing optofluidic interactions and developing next generation biosensors. For example, microfluidic channels may be integrated on-chip for controlled analyte delivery of low molecular weight molecules and nanoparticles of varying size (< 100 nm). Importantly, previous work in the Weiss group has demonstrated that sensing of small molecules and DNA $\sim 1-10$ nm in length is readily achieved in nanoporous sensors or multi-hole defect PhC cavities featuring pore openings on the order of $\sim 10-60$ nm [121, 122, 227]. These results suggest that slotted nanobeams with comparable slot dimensions should perform well in immobilizing and detecting small molecules. Monitoring the real-time optical response (i.e., resonant wavelength shift) will enable reaction kinetics and monolayer formation to be tracked. Notably, molecular kinetics in high aspect ratio porous silicon pores have previously been found to be significantly modified compared to binding kinetics on flat surfaces [122, 247]. Thus, it would also be valuable to examine the influence of nanostructure, such as slot width or aspect ratio, on sensor performance. Another notable advantage of the slotted nanobeam, especially when compared to whispering gallery or 2D PhC cavities, is its compact size and record low mode volume, which favors not only high sensitivity but also reduced analyte volume requirements. In particular, the active sensing volume of the slotted nanobeam, estimated from a 50 nm slot width and 30 μm beam length, is less than 1 fL. Assuming each nanobeam is submerged in a liquid cladding extending ~ 3 μm in all directions, a typical ~ 30 μm long device encompasses a total volume on the order of a few pL.

The ultra-low analyte volume regime is important for the detection of analyte species in trace quantities and for enabling multiplexed or redundant sample analysis. Ultra-compact slotted nanobeams may also be integrated with multiple fluidic channels and arrayed for performing multiplexed detection.

APPENDIX A

DIPS PROTOCOLS, ADDITIONAL FIGURES, AND RESULTS

A.1 Stamp Preparation and Imprinting

In this section, we will illustrate the steps required to perform DIPS with the Tinius Olsen Super L 60K universal testing machine, at Vanderbilt, using stamps lithographically prepared according to Section 2.2.2.

A.1.1 Cutting Out Stamps and Mounting on Tape

Before imprinting can be performed, the stamps must first be separated from their parent wafer and properly mounted onto Scotch tape. The items required for performing this task are shown in Figure A.1 below. Using the diamond scribe, the stamp should be cut from the silicon wafer. This can be accomplished by scratching and snapping (cleaving) the wafer multiple times. If the stamp is deep within the chip or wafer, cut around the stamp to make a chip with a more manageable size. This way, subsequent cleaves will be more precisely positioned near the edge of the stamp. For patterns with large area arrays, if you leave a blank space around the edge of the pattern, try to do so evenly on all four sides. Do not hesitate to practice cleaving blank silicon samples before cleaving your actual stamp. Although scratching in the appropriate place is relatively straightforward, mistakes can be made when actually snapping (cleaving). Two techniques are highly recommended: (1) grab the chip on either side of the scratch with two flat edge tweezers (Note: grab very close to the edge and very near to the scratch) and snap, or (2) a faster technique is to place the scribe tip underneath the chip where the scratch was made; then, using this as a fulcrum,

one half of the chip can be held down to the table (wearing gloves) while the raised side is then pressed down to snap the chip (Note: if this approach is made, be sure not to touch the patterned area, as residue can be deposited onto the chip even while wearing gloves. Note: the two tweezer method is recommended for the final cleave to minimize contact with the stamp surface).

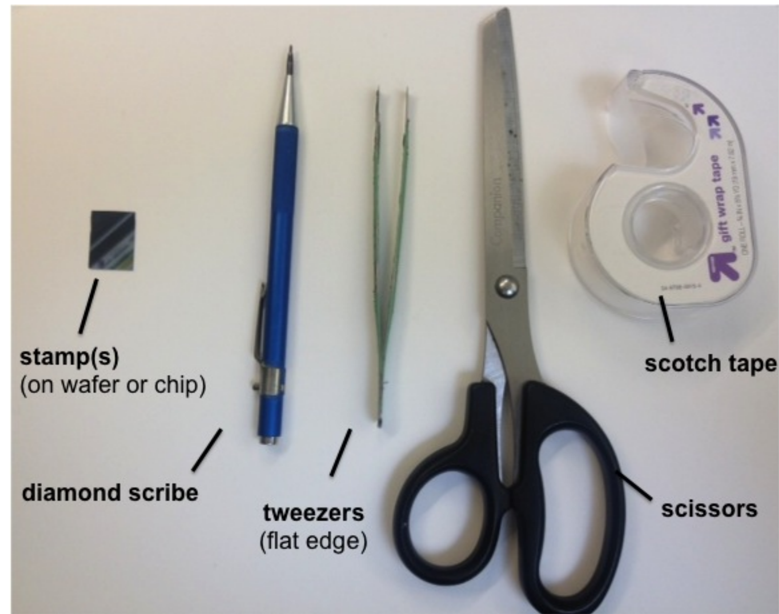

Figure A.1: Recommended tools for cleaving the stamps and mounting them on tape.

After the stamp is cut out from the parent chip or wafer, cut out small piece of scotch tape on which to mount the stamp. A long piece, slightly wider than the stamp is recommended. Long pieces of tape can then be folded over (sticky-side to sticky-side) to obtain the proper dimensions. This also promotes easy labeling and handling of the stamps, as your hands or tweezers can readily pick up the non-sticky ends of the tape. A successfully tape-mounted stamp may look like the one pictured in Figure A.2. At this point you can handle your stamp and measure its dimensions with the micrometer, so you can record its size (area). Recording this value will be valuable for calculating your applied pressure or target force later on.

Figure A.2: Image of various stamp patterns on a source wafer and a stamp after being cut out and properly mounted on scotch tape.

A.1.2 Configuring the Tinius Olsen Super L 60K

WARNING: The following steps assume that you are already trained to use the Tinius Olsen and have received proper authorization and access to the testing lab. Serious injury (or worse) may occur if you are not careful with this machine!

The Tinius Olsen (TO) should be configured to press a flat metallic adapter (found in lab) down against your sample, which is placed on steel base plates (from Weiss lab). The flat metallic adapter, pictured in Figure A.3 should be tightly secured with a large circular washer, rectangular top plate, and bolt. The two base plates should be centered and stacked on each other. Range limitations of the machine require both plates to be used, as well as the circular washer to secure the top plate. Updated adapters or plate re-polishing may be available through the testing lab or machine shop. Proper centering and flatness of these pieces is important for achieving a uniform imprint, so be sure to inspect these pieces for any non uniformity or bends that may have been caused by other users.

The TO will also need to be powered on by unlocking the power box and flipping the power switch. After the system initializes, press the *PUMP ON* button on the top right

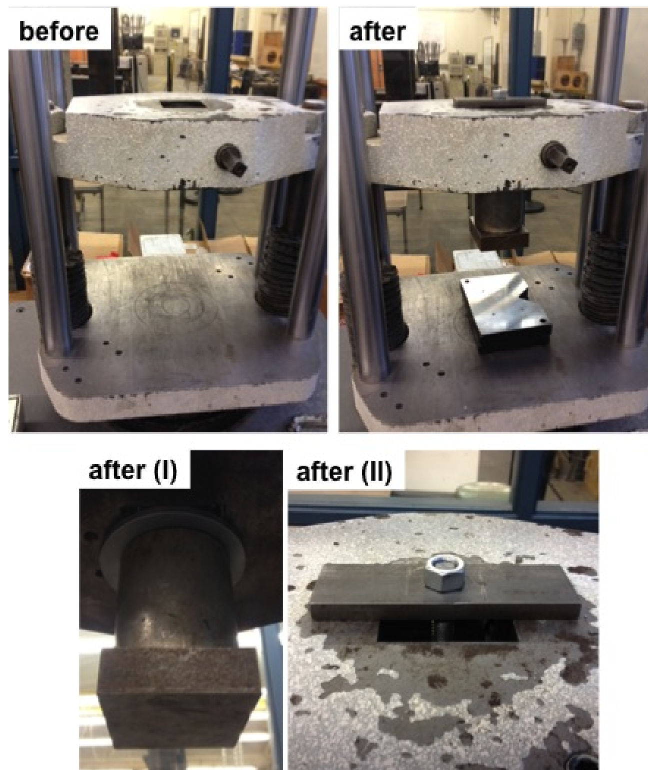

Figure A.3: Configuring the Tinius Olsen with the proper metal adapter and metal base plates.

of the panel shown in Figure A.4. The next step is to press *HOME* (first make sure the base plates/specimen and imprinting plates are very far apart, as the HOME function will change the y-positioning and could damage the set-up or samples if not done properly). After waiting for 10s, press the *HOME* button a second time. This time the *HOME* light should go *green* indicating the TO has been properly *homed*. After everything has been initialized, you can zero the sensors on the left panel by pressing buttons 7,4, and 1 sequentially (Fig. A.4).

Figure A.4: Images of the Tinius Olsen control panels.

A.1.3 Sample Positioning and Imprinting

After the TO has been configured and is ready for testing, place your sample on the base metal plate(s) with the stamp-pattern face down as shown in Figure A.5.a. Be sure to place the stamp where you want the pattern to be imprinted. Also, this is an opportunity to remove any air bubbles trapped by the tape on the back side of the stamp. Use a pair of flat edge tweezers to gently remove any air bubbles from the tape. Next, center the specimen and backside of the stamp in the center of the metal plate adapter. It is best to lower the plate down and inspect the alignment from the front and sides. After the plate is brought within a few centimeters of the sample, manually lower the plate toward the sample with the crank.

If imprinting is going to be performed with the computer, simply use the crank to lower the plate until it is almost touching the tape. Then follow the appropriate steps to configure your test (i.e., load *Ryckman test samples* or another approved configuration and change your pressing rate or applied force accordingly).

If imprinting is going to be performed manually with the crank, lower the plate down until it is almost touching the tape. At that point, begin watching the force meter shown in Figure A.4.a as you gently continue cranking. Once full contact is made, the force will rise rapidly. Continue to crank evenly toward your target load. Never stop or let the force drop during an imprint as the sample may shift, resulting in undesired results, such as a double-imprint. As you approach your target force, slow the cranking down, almost to a stop and watch the force sensor closely. Once the target force is reached, you can immediately un-crank to raise the metal plate off of the stamp and return the applied force to 0. After removing the crank handle, it is safe to raise the adapter up with the automatic controls.

After imprinting has been performed, remove the stamp from the sample with a peeling motion (note: sometimes the stamp will electrostatically adhere to the top metal plate and you may have to grab it with tweezers). Finally, you can inspect your DIPS patterned sample, which may look like the specimen shown in Fig. A.4.d. In most cases, the stamp may immediately be repositioned on the porous sample and used again. Visually inspect the stamp to ensure that no porous debris has accumulated to the stamp, and that no accidental cracking has occurred. If the stamp appears dirty, there is a strong likelihood that porous material came off with the stamp. In such a case, the stamp should be thoroughly cleaned before reuse. If the stamp has cracked, it may be reusable depending on where the crack occured. Cracking of the stamp or substrate maybe an indication that: (1) your setup was not level, (2) the pressure applied was much too high, (3) the stamp was not well centered under the top plate, (4) the stamp had unusually rough edges after cleaving, or (5) dust or

other grain like particles got in between the stamp and substrate.

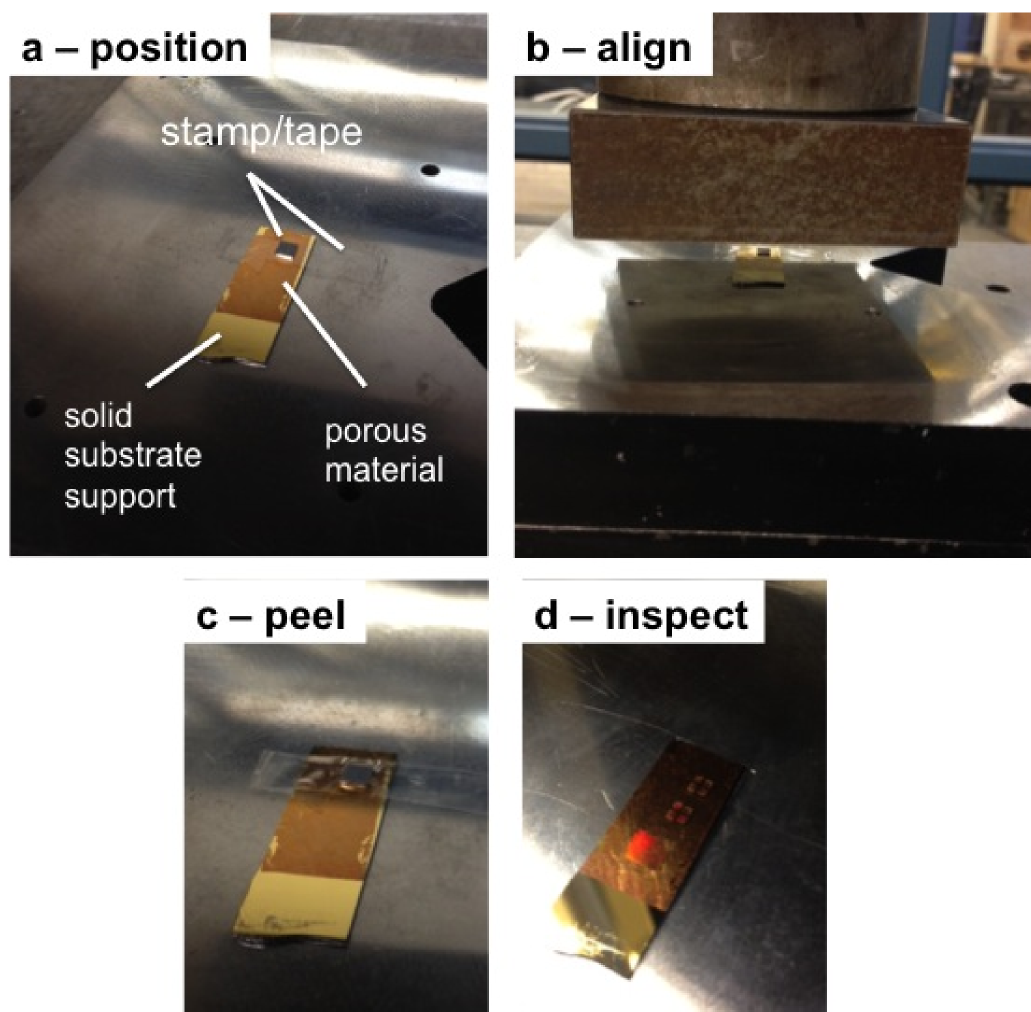

Figure A.5: Images illustrating the DIPS process being performed on npAu with the Tinius Olsen testing machine, highlighting four key steps to consider before and after imprinting, including (a) positioning, (b) alignment, (c) peeling or removal of the stamp, and (d) inspection of the patterned porous substrate.

A.2 Additional Figures

A.2.1 Large Area and Repeated Imprinting

Figure A.6 shows additional photos of DIPS being successfully applied for repeated imprinting with the same stamp. Both images reveal patterning of npAu SERS substrates.

Fig. A.6 highlights imprinting with a large, $\sim$16mm^2, area stamp

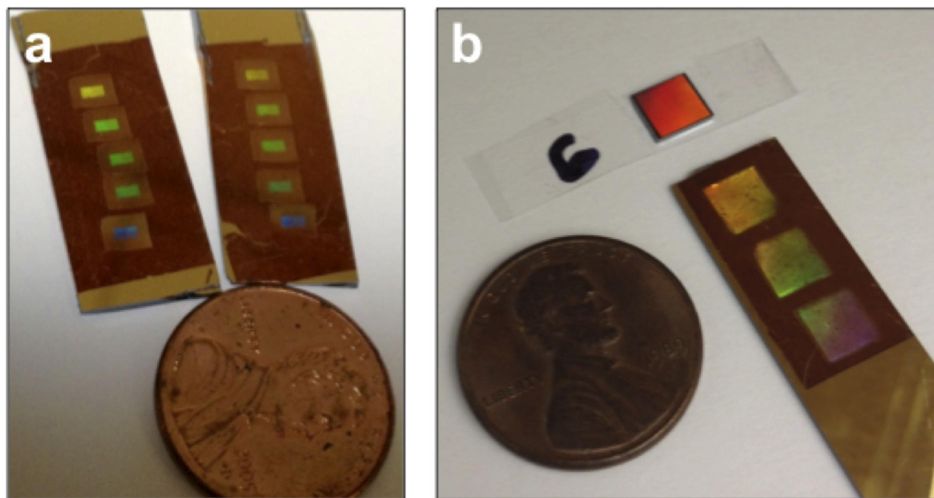

Figure A.6: Photos of DIPS patterned npAu films after imprinting with the same stamp repeatedly. The uniformity of the imprints are readily visible by the naked eye.

A.2.2 Cookie-Cutter npAu Nanoparticles

Similar to the demonstration of cookie-cutter pSi microparticles in Chapter 3 (Figure 3.5.j), preliminary testing, shown in Figure A.7, also suggests that this method maybe suitable for the fabrication of npAu nanoparticles. In this experiment, imprinting was performed at an elevated pressure, close to $\sim$ 1000 N/mm^2. After imprinting, both the porous substrate and stamp were examined with SEM. The particles were cleanly patterned over a large area, but lifted-off inconsistently in different regions. In some areas, the underlying Au film also came off of the substrate (Fig. A.7.a). This is partially due to the fact that at this elevated pressure the Au film itself was imprinted, as shown in Fig. A.7.b. In some areas, individual npAu nanoparticles can be seen loosely adhering to original substrate (Fig. A.7.c.). Many of npAu nanoparticles were also found embedded within the Si stamp (Fig. A.7.d.). Overall, these results suggest that mass production of npAu nanoparticles should be possible using DIPS. However, as Au is generally softer and less brittle than

Si, complete separation of individual nanoparticles through the cookie-cutter approach is more difficult and requires higher pressures. These npAu nanoparticles could potentially be very attractive for applications in catalysis and plasmonics. Thus, further studies which optimize npAu nanoparticle fabrication using DIPS should be considered in future work.

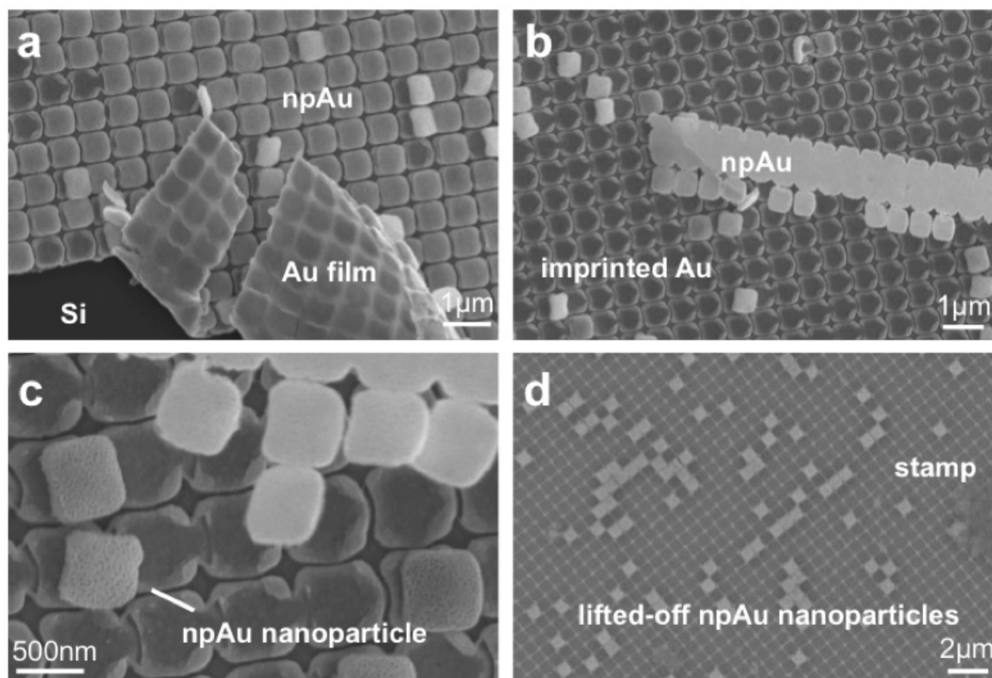

Figure A.7: SEM images of preliminary work relating to the fabrication of npAu nanoparticles through DIPS with a cookie-cutter type stamp.

A.2.3 Negative Results and Other Effects

Negative Results

Figure A.8 illustrates some of the negative results that were obtained during the initial development of the DIPS process. Some of first trial imprints were performed using a simple vice grip, which was found to not provide sufficient leveling required for a uniform imprint. As a result, imprinted pSi films often cracked and exhibited highly non-uniform patterns as shown in the optical microscope image Fig. A.8.a. Other early attempts were

performed on old or discarded pSi multilayer films. However these films were generally too thick to pattern with high fidelity, resulting only in crushing deep into the film and significant residual debris as shown in Figs. A.8.b, c.

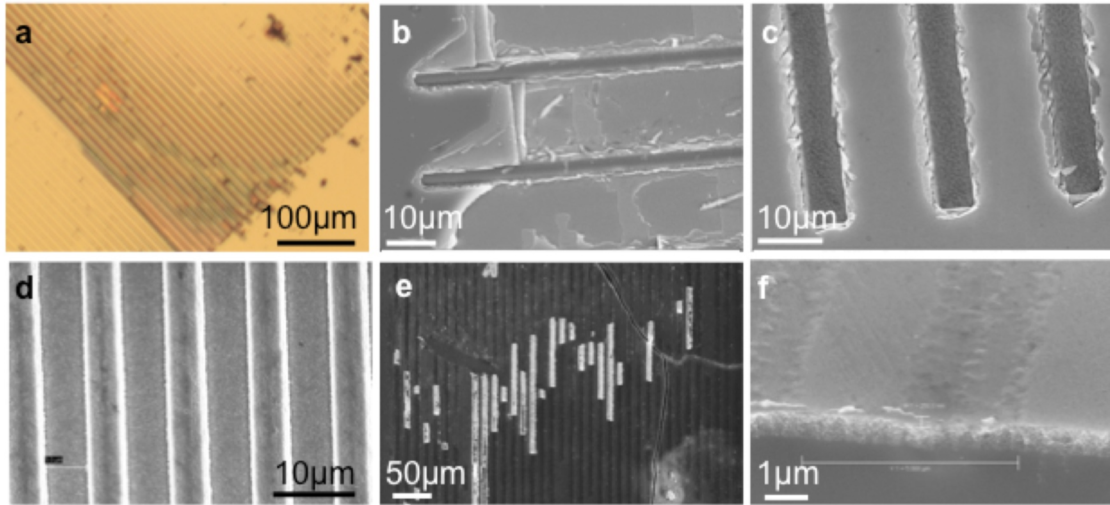

Figure A.8: (a) Optical microscope and (b-f) SEM images illustrating examples of negative results observed during the initial development and testing of DIPS.

Figures A.8.d-e shows SEMs from early DIPS attempts where the stamp was comprised of sputtered aluminum diffraction gratings. An example Al grating is shown in Fig. A.8.d. These stamps were convenient to fabricate, but did not produce good results on pSi thin films. In a number of cases, the Al ridges would break off and adhere to the porous substrate after imprinting as shown in Fig. A.8.e. SEM further revealed that although some imprinting did occur, it was generally not uniform and could not be replicated with high fidelity (Fig. A.8.f). Although some of the non-uniformity could be attributed to the intrinsic surface roughness of the sputtered Al films, the primary challenge limiting the application of Al as a stamp material is its very low hardness ($\sim$167MPa).

Other Effects

Even with the appropriate stamp material and appropriate imprinting apparatus, other effects and unexpected results have also been observed. For example, under certain conditions "skewed" patterns have been observed as shown in Figure A.9. The exact cause for such skewing effects is not entirely clear, however in some cases it is likely a result of poor leveling of the imprinting apparatus. In other cases, such as in the example shown in Figure A.9, the stamp which produced the "skewed" pattern may not have been cleaved properly. Compared to the stamp which produced the "good" pattern, the improperly cleaved stamp left a large open area of unpatterned Si asymmetrically on one side of the stamp. In this example, it is possible that the asymmetry of the stamp lead to a non-uniform imprinting pressure which produced the slight skewing of the pattern. However, with further study it may be possible to better understand and control such skewing effects. Incorporating a controlled lateral shear force would be advantageous for producing a variety of new structures not achievable with traditional DIPS.

In some rare cases, extreme skewing has produced structures far different than the intended pattern. One such example is shown in Figures A.10.a, b, where a simple square grating pattern resulted in the production of gold nanostructures resembling "bowties". This odd result may have been caused by a combination of shear force components, or slight rotation or flexing of the stamp during imprinting. These results were not reproducible and may likely have been assisted by poor leveling of the imprinting apparatus. Interestingly however, some of the "bowties" exhibited very small nanogaps (< 10 nm) as shown in Fig. A.10.b. As mentioned above, the ability to controllably and purposefully create such structures could be attractive for a variety of applications in nanoscience. Notably, achieving small nanogaps and feature sizes, < 10 nm, is generally very diffi-

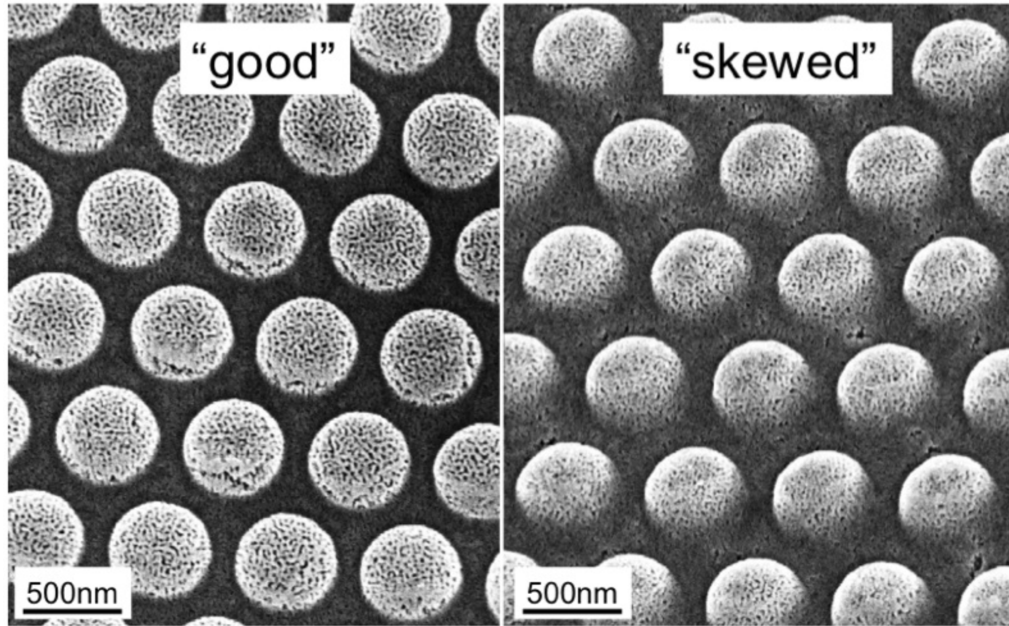

Figure A.9: Example of unexpected "skewing" of an imprinted pattern. In this example, the circular patterns appear distorted or biased toward a common direction.

cult to achieve with any lithographic process. Another effect which has been observed is "double-imprinting", shown in Figures A.10.c and d. As the term implies, these patterns are achieved by accidentally imprinting twice. This may occur due to poor manual control over the imprinting pressure (i.e., accidentally imprinting during the alignment process), or through a computer error. Occasionally the Tinius Olsen testing machine has been found to 'glitch' in this manner, when controlled through the computer (i.e., another short duration force is applied when the imprinting head is removed). For this reason, it may be preferable to apply the force manually using the crank.

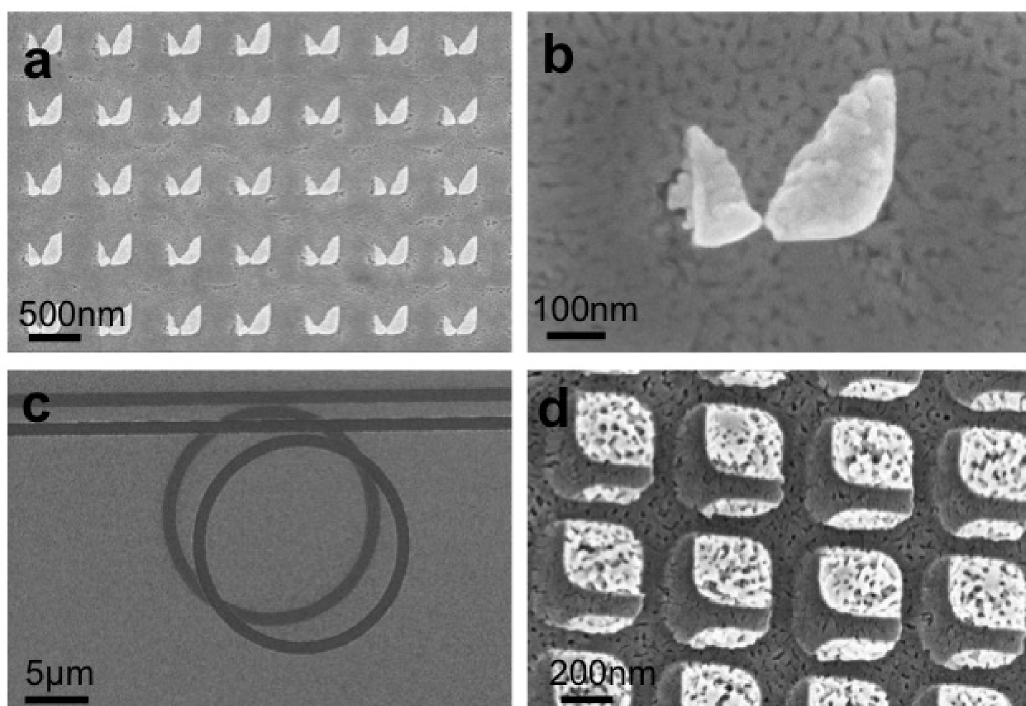

Figure A.10: SEM images of other anomalous results obtained after performing DIPS. (a, b) Extreme skewing from a simple 2D grating patterned stamp produced bow-tie like structures in npAu with some structures exhibiting very small nanogaps (< 10 nm). (c, d) Double imprinting observed in pSi and npAu patterns.

A.3 Gray-Scale Electron Beam Lithography

This section includes additional descriptions, figures, and Matlab code regarding the gray-scale EBL process described in Section 3.2.2.

A.3.1 Process Overview

Gray-scale EBL was performed using the JEOL JBX-9300100kV located in the Center for Nanophase Materials Science (CNMS) at Oak Ridge National Laboratory. In order to realize a gray-scale resist profile, the dosage must be properly modulated and the appropriate resist and development process should be used. In this work, two different PMMA resists, 950k A4 (spun at 6,000 rpm and baked at 180 °C for 10 min) and 50k A20 (spun at 2,000 rpm and baked at 180°C for 5 min) are used to realize either shallow (~200 nm) or deep (~1.5 μm) structures, respectively. EBL is performed with a 2 nA beam current, pattern shot pitch of 5 nm, and a base dose of 375 μC cm^{-2}, with the relative dose modulated from -33% to 0%. Development is performed in a 1:2 (v/v) mixture of de-ionized water and IPA for 30 s, followed immediately by drying under nitrogen.

In order to spatially modulate the relative dose that is delivered to the resist, the pattern file must be prepared using multiple data types. Generally, *.gdsii* patterns are prepared and subsequently converted to *.v30* files for use with the JEOL JBX-9300100kV. The *.v30* files should also be accompanied with a *.jdi* file which contains the information which assigns each data type (or layer) to a particular dose. The *.jdi* is ultimately copied into the job deck file (JDF) that will be executed. This approach is similar to how proximity correction is performed, except the pattern is purposefully prepared with multiple data types using predetermined relative dose values. Example *.gdsii* patterns are shown in Figure A.11.

Although it is often convenient to utilize multiple layers, which often have unique and

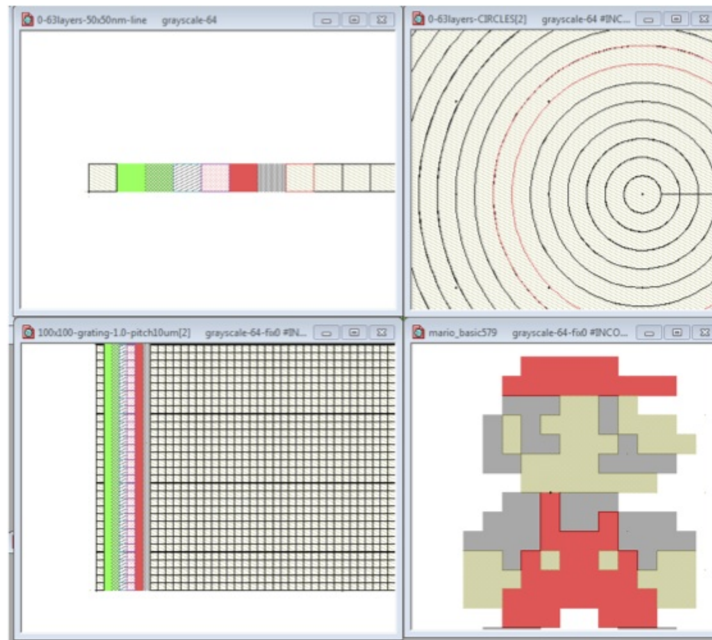

Figure A.11: Example *.gdsii* patterns used for gray-scale EBL. Each polygon is assigned a specific GDSII data type which is later used to assign the appropriate dose.

identifiable textures or colors, it is the GDSII data type and not the layer number which is used to assign dosage. Thus, if multiple layers are used, it is important to assign each layer to a unique GDSII data type. For most of the patterns used in this dissertation 64 separate data types are used (0-63). Patterns are prepared by changing the data type of individual polygons. For example, a simple cell might include 64 pixels (measuring 50×50 nm) arranged in a line, or concentric rings of a fixed thickness. More advanced structures can be realized by arraying elements or cells and using the appropriate dose profile. For example, a blazed grating with a particular period can be made by stretching and arraying the cell containing the line of 64 pixels and assigning a linearly varying dose profile. When saving or exporting the pattern as a *.gds* file with L-Edit, it is especially important to uncheck the box *'Overwrite object data type with layer data type'*, as this will ensure that the locally defined data type (i.e., for each individual polygon) is used.

A.3.2 dose64_jdi_ARB.m

The *.jdi* files are prepared using the Matlab code `dose64_jdi_ARB.m` found below. This code enables mapping of an arbitrary function to a dose profile with a variable number of layers (in this case 64). The code outputs text which can then be copied into a text editor and then saved as a *.jdi* file or simply copied into the final JDF.

```
%Initial Settings
numLayers = 64; %number of layers i.e. 0-63
minDose = 0.67; %0.67 equals a Rel. Dose of -33
maxDose = 1; %1 equals a Rel. Dose of 0

%Convert to Rel. Dose
minD = (minDose-1)*100;
maxD = (maxDose-1)*100;
dDose = (maxD - minD)/64;
Doses = minD:dDose:minD+(63)*dDose;

%Define Dose Function
xx=0:63;
exponent=1;%i.e. 0.25, 0.5, 1, 2, 3, 4
yy=(sqrt(2-(xx/63).^exponent)).^exponent; %or choose your own function!

%Convert Function to Doses
Doses=yy;
Doses = (1-Doses)/min(1-Doses)*minD;

%Output text for .jdi file, begining with first line
qstart = sprintf(['SHOT01: MODULAT (( 0, %s ) , ( 1, %s ) , ( 2, '...
  '%s ) , ( 3, %s ) , ( 4, %s ) , ( 5, %s )\n'],num2str(Doses(1)),...
num2str(Doses(2)),num2str(Doses(3)),num2str(Doses(4)),...
num2str(Doses(5)),num2str(Doses(6)));

%Continue with middle lines
qq = qstart;
for ii = 6:3:62
    qtemp = sprintf(['-      , ( %s,  %s ) , ( %s,  %s ) , ( %s,  '...
       '%s )\n'],num2str(ii), num2str(Doses(ii+1)),num2str(ii+1), ...
       num2str(Doses(ii+2)),num2str(ii+2), num2str(Doses(ii+3)));
    qq = sprintf([qq qtemp]);
end

%Clean up last line
for ii = 63
qtemp = sprintf('-      , ( %s,  %s ))',num2str(ii),num2str(Doses(ii+1)))
    qq = sprintf([qq qtemp]);
end
```

```
%Print text to screen for copying to text editor
qq

%Plot dose profile (optional)
% figure(1);
% hold on
% plot(wrev(100-Doses))
```

A.3.3 Example Dose and Resist Profiles

Control over the resist profile can be achieved, in part, by adjusting the dose profile defined in the *.jdi* file. To verify this capability, a simple 200 μm wide gradient pattern composed of 64 stripes was used. The relative dose profile was assigned using the function found in `dose64_jdi_ARB.m` with exponent values of 0.25, 0.5, 1, 2, 3, and 4 as shown in Figure A.12.a. The pattern was exposed with a base dose of 375 μC cm^{-2} at a beam current of 2 nA. Under these conditions, the minimum dwell time on the EBL tool does not allow doses below 250 μC cm^{-2}. This is why a minimum relative dose of -33 is utilized (375*(1-0.33)=251). Changing to a lower beam current would allow a larger dose range to be realized, however this would come at the cost of a longer exposure time.

The dose profile test patterns were exposed on two different PMMA resists on Si wafers: (1) 950k A4 (spun at 6,000 rpm and baked at 180°C for 10 min) and (2) 50k A20 (spun at 2,000 rpm and baked at 180°C for 5 min). Both resists are developed a 1:2 (v/v) mixture of de-ionized water and IPA for 30s, followed immediately by drying under nitrogen. Profilometry was then performed to measure the resist profiles (Figs. A.12.b, c). Under these conditions, a height contrast of up to $\sim$ 200 nm and $\sim$ 600 nm is achieved in the 950k A4 and 50k A20 PMMA resists, respectively. Overall, the exposed profiles match very well with the dose profile (Fig. A.12.a), indicating that the resist exposure and development is very linear for this particular dose range and development recipe. Proximity effects are noticeable and distort the profile slightly at both ends of the test pattern.

The developed resist profiles can then be transferred into the Si substrate using anisotropic RIE. Typically an existing recipe on the Oxford PlasmaLab 100 is used consisting of C_4F_8/SF_6/Ar process gases. With these processes the Si:PMMA etch selectivity can be as high as $\sim$2.5:1, although recipes can be made to reduce this closer to 1:1. The specific etch rate and selectivity depend strongly on

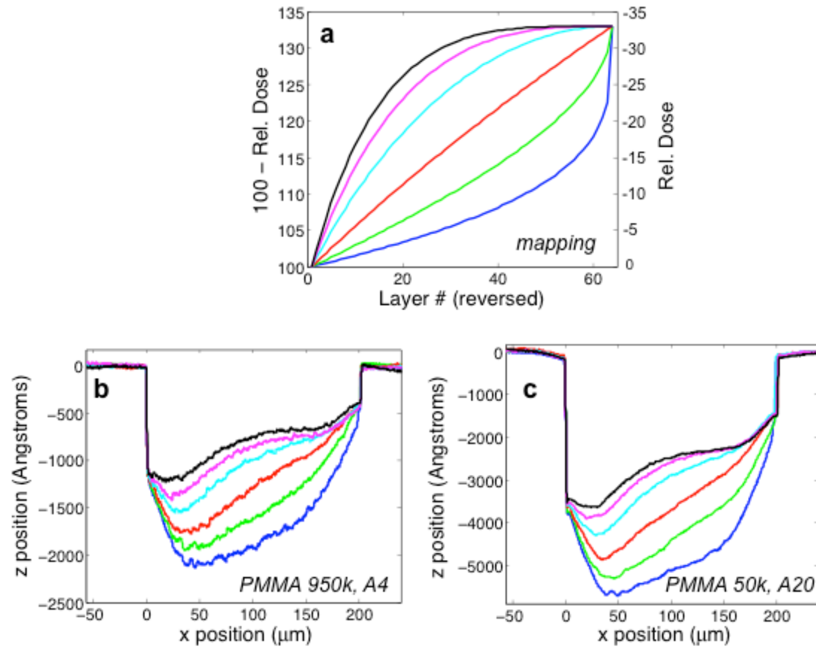

Figure A.12: (a) Relative dose profiles mapped into the *.jdi* file, and corresponding resist profiles measured in (b) PMMA 950k, A4 and (c) PMMA 50k, A20 following exposure and development.

the particular tool, etch recipe, and resist, as well as any potential loading effects (i.e., total area of open Si vs. resist). For most gray-scale stamps, the resist is usually slightly over-etched (etched all the way through) to ensure that the entire resist profile is transferred to the Si substrate. A clear indicator of 'over-etching' is the resist no longer being visible by the naked eye (the unexposed Si substrate returns to its original mirror-like appearance).

APPENDIX B

ADDITIONAL Si-VO_2 MEASUREMENT NOTES AND FIGURES

B.1 Optical Measurement Set-Ups

The following sections includes additional images and descriptions of the optical measurement setup used to characterize the hybrid Si/VO_2 devices under, (1) photothermal excitation as described in Sec. 4.3.1 and (2) nanosecond pulsed excitation as described in Sec. 5.3.2.

B.1.1 Photothermal Pump-Probe Measurements

Figure B.1 shows a photograph of the optical setup illustrated in Fig. 4.2.a. A 532 nm cw pump laser (New Focus 3951-20) is focused onto the device with a 20x objective, and an IR camera (Sensors Unlimited 320M) is used to focus the pump beam and position it directly on the device under test. For the probe, a tunable cw laser (Santec TSL-510) is used to perform passive transmission measurements, utilizing quasi-TE polarization, over the wavelength range 1500 – 1630 nm. Probe light is delivered to/from the cleaved facets of the bus waveguides using tapered lensed fibers (OZ Optics Ltd), which are mounted on xyz piezo controlled positioning stages.

For imaging and alignment, this setup makes use of a 92:8 beam splitter (oriented to pass 92% of the cw pump light) as shown in Figure B.2. Between the beamsplitter and IR camera there is an adjustable polarizer and collimating tube lens. The polarizer enables the image intensity and camera saturation to be controlled. It is often helpful to cross-polarize to the pump light in order to better image the exact center of the beam spot on the sample surface. The tube lens is necessary to ensure that the camera is initially focused at infinity, so that the image plane (beyond the 20x objective) coincides with the focal plane of the pump laser. Fine adjustments to tube-threading are required to properly position the tube lens a focal length away from the camera's CCD. Once this has been properly done, no further adjustments are required. Thus it is a good idea to dedicate these

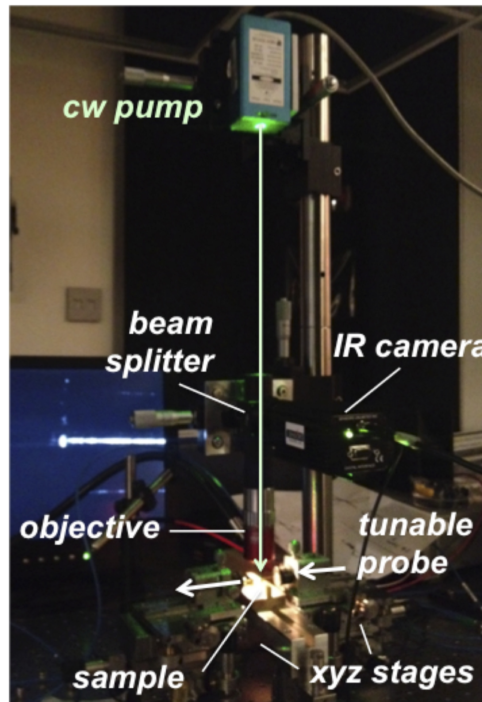

Figure B.1: Photograph of the measurement setup used to characterize hybrid Si/VO_2 devices under photothermal excitation.

particular tubes and polarizer for imaging at infinity. The same method is used to achieve proper focusing of the nanosecond pump laser.

Performing measurements with this setup requires proper alignment and focusing of the pump laser. After ensuring that pump light is delivered straight downward and into the center of the beamsplitter and objective, coarse manual adjustments to the xyz position of the imaging optics must be performed. These adjustments should be performed in iteration with adjustments to the xy position of the pump laser in order to bring the focal spot close to the device of interest. Rapidly sweeping through the focus with +z and -z adjustments, while independently making small x or y changes, is a very helpful technique for ensuring a well-centered and circular focal spot is achieved.

B.1.2 Nanosecond Pump-Probe Measurements

Figure B.3 shows a photograph of the optical setup illustrated in Fig. 5.1.c. Overall, the basic setup is very similar to the photothermal testing configuration discussed above. However, delivery of the

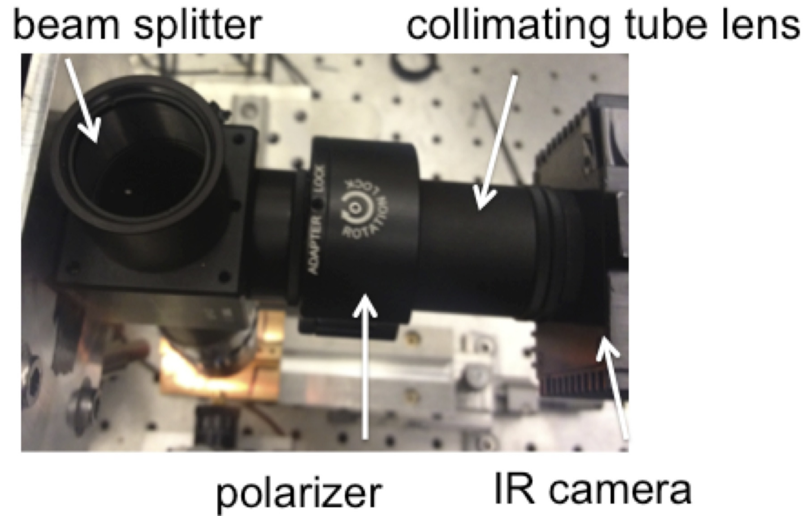

Figure B.2: Close up view of the beamsplitter, polarizer, tube system, and IR camera.

pump beam is constrained by the geometry of the nanosecond pump laser. Thus, two broadband dielectric mirrors are used to direct the pump light upward and over toward the tube system and imaging optics. As the pump light enters the tube system, it first encounters an adjustable polarizer which is used to tune the input pump intensity. This polarizer is similar to the one shown in Fig. B.2. Pump light then encounters the first beam splitter which splits 50% of the light downward into microscope objective and allows the other 50% to be transmitted toward the photo-diode and power meter. The power meter averages the optical power reading over many seconds, and can be used to determine the pump pulse energy if the pulse repetition rate is known (typically set to 10Hz) and the additional losses through the microscope objective and imaging polarizer have been calibrated. This method of power monitoring may not work well for all repetition rates and pump fluences. In such situations an alternative technique is recommended, such as the use of additional attenuators or switching to a thermopile detector.

Probe light is coupled to/from Si bus waveguides using tapered lensed fibers. The output signal is then sent to a high speed, fiber coupled avalanche photodiode (Newport 1647). Before using this detector it is important to read through the Newport 1647 manual, as there are a number of considerations which should be taken into account to avoid damaging the detector and ensuring quality

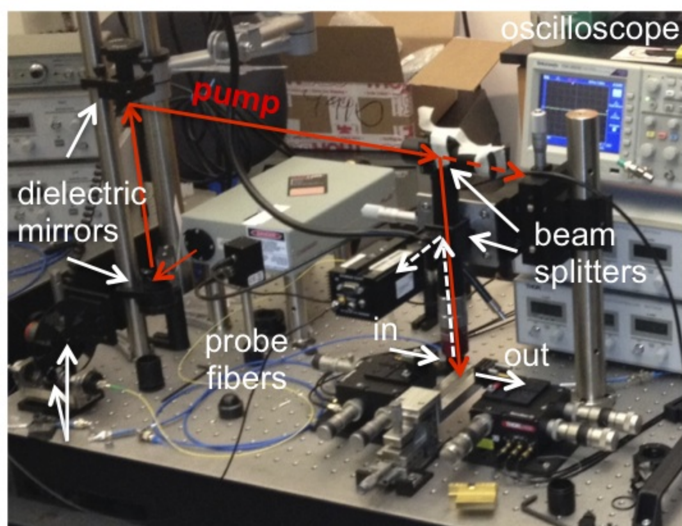

Figure B.3: Photograph of the measurement setup used to characterize hybrid Si/VO_2 devices under nanosecond pulsed optical pumping.

measurement. The primary consideration is to never direct too much power into the detector. After probe light has been coupled into the bus waveguides and monitored using a separate fiber coupled detector and power meter, the output fiber can be switched to the Newport 1647. This detector requires the use of a triple output power supply which should be set to $\sim$ 15V, as described in the manual. The power supply should be turned on at least 30 min to 1 hr before making quantitative measurements in order to ensure measurement stability. The detector offers a differential output (+/-) which can be sent to the primary channels of the the oscilloscope (i.e., Ch1/Ch2). Before performing pump-probe measurements, it is important to test detection of the probe light, by turning on the chopper. The chopper modulates the probe signal at a low $\sim$kHz frequency, which is below the low-frequency cutoff of the high-speed detector. Thus, the observed signal appears not as a square wave, but as a periodic signal of + and - pulses (equivalent to the derivative of the square wave). After finding the signal and triggering on Ch1 or Ch2 at the appropriate level, the xyz piezo stages can be adjusted to maximize the probe signal. Importantly, this detector generally requires a minimum power of $\sim 0.7\ \mu$W (even at a gain setting of 7) for any signal to be detected. For the pump-probe measurements, the oscilloscope should be triggered off of the laser.

As with the photothermal measurement setup, these measurements utilize a beamsplitter (BS2), polarizer, tube lens, and IR camera for imaging, focusing, and alignment (as in Fig. B.2). Achieving a properly positioned, circular, and well focused spot requires the same careful adjustments recommended above in Sec. B.1.1. However, in this setup the pump laser position is controlled by the dielectric mirrors. Fine adjustments over mirror positioning and alignment should be made while rapidly sweeping through the focus with +z and -z adjustments.

With this setup it is vitally important that the correct microscope objective (5x) is used in the pump-probe experiment, as this focuses the pump pulse and determines the sample fluence (mJ cm^{-2}). Although the 20x objective is convenient for aligning the input/output fibers and coupling probe light through the device, the objective should then be switched to the 5x objective. Note the objectives discussed here are long working distance IR objectives (Mitutoyo). Figure B.4 shows SEM images depicting what can happen to SOI samples if the pump fluence is not properly controlled. These example images correspond to testing done with the 20x objective. Such high magnification typically produces $\sim$J cm^{-2} pump fluence levels which can result in explosive boiling of silicon! Although the damage to the sample may be highly localized, debris may be deposited back on to the sample over larger areas.

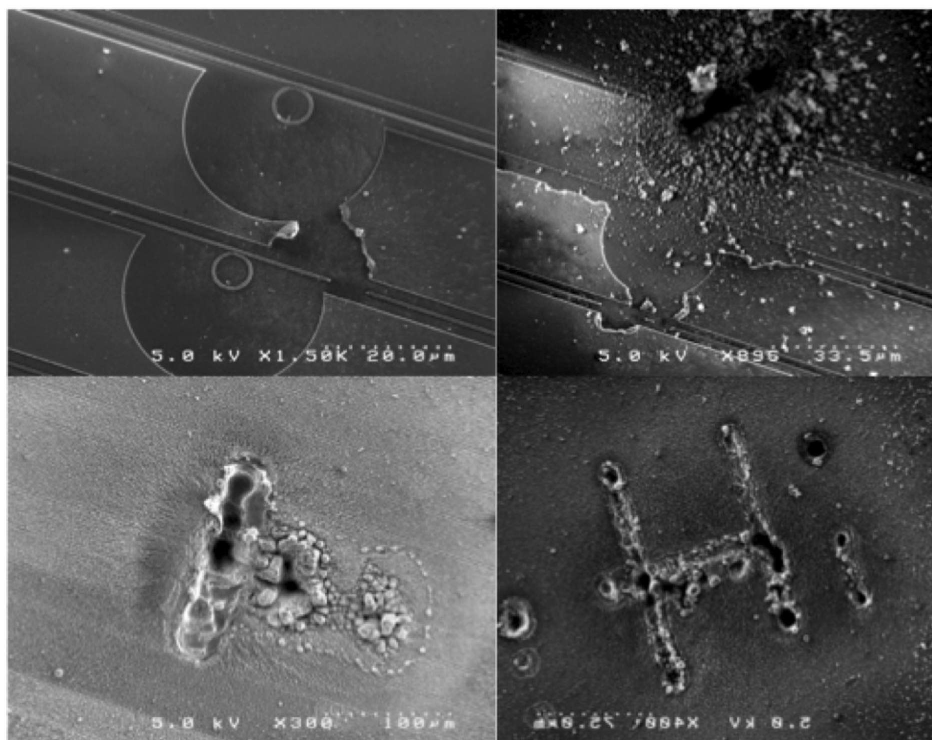

Figure B.4: Example outcomes of using too high a pump fluence ($\sim$J cm^{-2}) with a 20x objective.

BIBLIOGRAPHY

[1] A. P. Li, F. Muller, A. Birner, K. Nielsch, and U. Gosele. Hexagonal pore arrays with a 50-420 nm interpore distance formed by self-organization in anodic alumina. *Journal of Applied Physics*, 84(11):6023, 1998.

[2] Y. Ding, Y. J. Kim, and J. Erlebacher. Nanoporous gold leaf: "ancient technology"/advanced material. *Advanced Materials*, 16(21):1897, 2004.

[3] T. Kasuga, M. Hiramatsu, A. Hoson, T. Sekino, and K. Niihara. Formation of titanium oxide nanotube. *Langmuir*, 14(12):3160, 1998.

[4] R. L. Smith and S. D. Collins. Porous silicon formation mechanisms. *Journal of Applied Physics*, 71(8):R1, 1992.

[5] A. Walcarius, E. Sibottier, M. Etienne, and J. Ghanbaja. Electrochemically assisted self-assembly of mesoporous silica thin films. *Nature Materials*, 6(8):602, 2007.

[6] A. Valance. Theoretical model for early stages of porous silicon formation from n- and p-type silicon substrates. *Physical Review B*, 55(15):9706, 1997.

[7] D. A. G. Bruggeman. Berechnung verschiedener physikalischer konstanten von heterogenen substanzen. i. dielektrizitätskonstanten und leitfähigkeiten der mischkörper aus isotropen substanzen. *Annalen der Physik*, 416(7):636, 1935.

[8] S. M. Weiss. *Tunable Porous Silicon Photonic Bandgap Structures: Mirrors For Optical Interconnects and Optical Switching*. PhD thesis, 2005.

[9] A. Jane, R. Dronov, A. Hodges, and N. H. Voelcker. Porous silicon biosensors on the advance. *Trends in Biotechnology*, 27(4):230, 2009.

[10] X. Wei, C. Kang, M. Liscidini, G. Rong, S. T. Retterer, M. Patrini, J. E. Sipe, and S. M. Weiss. Grating couplers on porous silicon planar waveguides for sensing applications. *Journal of Applied Physics*, 104(12), 2008.

[11] J. D. Ryckman, M. Liscidini, J. E. Sipe, and S. M. Weiss. Porous silicon structures for low-cost diffraction-based biosensing. *Applied Physics Letters*, 96(17), 2010.

[12] A. G. Koutsioubas, N. Spiliopoulos, D. Anastassopoulos, A. A. Vradis, and G. D. Priftis. Nanoporous alumina enhanced surface plasmon resonance sensors. *Journal of Applied Physics*, 103(9), 2008.

[13] H. Ko, S. Chang, and V. V. Tsukruk. Porous substrates for label-free molecular level detection of nonresonant organic molecules. *ACS Nano*, 3(1):181, 2008.

[14] X. Y. Lang, L. H. Qian, P. F. Guan, J. Zi, and M. W. Chen. Localized surface plasmon resonance of nanoporous gold. *Applied Physics Letters*, 98:093701, 2011.

[15] F. Yu, S. Ahl, A. M. Caminade, J. P. Majoral, W. Knoll, and J. Erlebacher. Simultaneous excitation of propagating and localized surface plasmon resonance in nanoporous gold membranes. *Analytical Chemistry*, 78(20):7346, 2006.

[16] E. Tasciotti, X. W. Liu, R. Bhavane, K. Plant, A. D. Leonard, B. K. Price, M. M. C. Cheng, P. Decuzzi, J. M. Tour, F. Robertson, and M. Ferrari. Mesoporous silicon particles as a multistage delivery system for imaging and therapeutic applications. *Nature Nanotechnology*, 3(3):151, 2008.

[17] J. H. Park, L. Gu, G. von Maltzahn, E. Ruoslahti, S. N. Bhatia, and M. J. Sailor. Biodegradable luminescent porous silicon nanoparticles for in vivo applications. *Nature Materials*, 8 (4):331, 2009.

[18] P. Horcajada, T. Chalati, C. Serre, B. Gillet, C. Sebrie, T. Baati, J. F. Eubank, D. Heurtaux, P. Clayette, C. Kreuz, J. S. Chang, Y. K. Hwang, V. Marsaud, P. N. Bories, L. Cynober, S. Gil,

G. Ferey, P. Couvreur, and R. Gref. Porous metal-organic-framework nanoscale carriers as a potential platform for drug delivery and imaging. *Nature Materials*, 9(2):172, 2010.

[19] F. Cunin, T. A. Schmedake, J. R. Link, Y. Y. Li, J. Koh, S. N. Bhatia, and M. J. Sailor. Biomolecular screening with encoded porous-silicon photonic crystals. *Nature Materials*, 1 (1):39, 2002.

[20] O. K. Varghese, D. W. Gong, M. Paulose, K. G. Ong, E. C. Dickey, and C. A. Grimes. Extreme changes in the electrical resistance of titania nanotubes with hydrogen exposure. *Advanced Materials*, 15(7-8):624, 2003.

[21] S. D. Alvarez, C. P. Li, C. E. Chiang, I. K. Schuller, and M. J. Sailor. A label-free porous alumina interferometric immunosensor. *ACS Nano*, 3(10):3301, 2009.

[22] D. R. Rolison. Catalytic nanoarchitectures - the importance of nothing and the unimportance of periodicity. *Science*, 299(5613):1698, 2003.

[23] A. Wittstock, V. Zielasek, J. Biener, C. M. Friend, and M. Baumer. Nanoporous gold catalysts for selective gas-phase oxidative coupling of methanol at low temperature. *Science*, 327 (5963):319, 2010.

[24] M. Adachi, Y. Murata, M. Harada, and S. Yoshikawa. Formation of titania nanotubes with high photo-catalytic activity. *Chemistry Letters*, (8):942, 2000.

[25] W. Sun, J. E. Puzas, T. J. Sheu, X. Liu, and P. M. Fauchet. Nano- to microscale porous silicon as a cell interface for bone-tissue engineering. *Advanced Materials*, 19(7):921, 2007.

[26] S. P. Low, K. A. Williams, L. T. Canham, and N. H. Voelcker. Evaluation of mammalian cell adhesion on surface-modified porous silicon. *Biomaterials*, 27(26):4538, 2006.

[27] A. Magasinski, P. Dixon, B. Hertzberg, A. Kvit, J. Ayala, and G. Yushin. High-performance lithium-ion anodes using a hierarchical bottom-up approach. *Nature Materials*, 9(4):353, 2010.

[28] J. Biener, G. W. Nyce, A. M. Hodge, M. M. Biener, A. V. Hamza, and S. A. Maier. Nanoporous plasmonic metamaterials. *Advanced Materials*, 20(6):1211, 2008.

[29] S. S. Iyer and Y. H. Xie. Light-emission from silicon. *Science*, 260(5104):40, 1993.

[30] K. D. Hirschman, L. Tsybeskov, S. P. Duttagupta, and P. M. Fauchet. Silicon-based visible light-emitting devices integrated into microelectronic circuits. *Nature*, 384(6607):338, 1996.

[31] O. K. Varghese, M. Paulose, and C. A. Grimes. Long vertically aligned titania nanotubes on transparent conducting oxide for highly efficient solar cells. *Nature Nanotechnology*, 4(9): 592, 2009.

[32] P. N. Ciesielski, A. M. Scott, C. J. Faulkner, B. J. Berron, D. E. Cliffel, and G. K. Jennings. Functionalized nanoporous gold leaf electrode films for the immobilization of photosystem i. *ACS Nano*, 2(12):2465, 2008.

[33] S. Ito, S. M. Zakeeruddin, P. Comte, P. Liska, D. B. Kuang, and M. Gratzel. Bifacial dye-sensitized solar cells based on an ionic liquid electrolyte. *Nature Photonics*, 2(11):693, 2008.

[34] R. Arens-Fischer, M. Kruger, M. Thonissen, V. Ganse, D. Hunkel, M. Marso, and H. Luth. Formation of porous silicon filter structures with different properties on small areas. *Journal of Porous Materials*, 7(1-3):223, 2000.

[35] D. Mangaiyarkarasi, M. B. H. Breese, and Y. S. Ow. Fabrication of three dimensional porous silicon distributed bragg reflectors. *Applied Physics Letters*, 93(22):221905, 2008.

[36] D. J. Sirbuly, G. M. Lowman, B. Scott, G. D. Stucky, and S. K. Buratto. Patterned microstructures of porous silicon by dry-removal soft lithography. *Advanced Materials*, 15(2): 149, 2003.

[37] D. Mangaiyarkarasi, O. Y. Sheng, M. B. Breese, V. L. Fuh, and E. T. Xioasong. Fabrication of large-area patterned porous silicon distributed bragg reflectors. *Optics Express*, 16(17): 12757, 2008.

[38] X. Wei and S. M. Weiss. Guided mode biosensor based on grating coupled porous silicon waveguide. *Optics Express*, 19(12):11330, 2011.

[39] H.-M. Bok, K. L. Shuford, S. Kim, S. K. Kim, and S. Park. Multiple surface plasmon modes for a colloidal solution of nanoporous gold nanorods and their comparison to smooth gold nanorods. *Nano Letters*, 8(8):2265, 2008.

[40] S. Y. Chou, P. R. Krauss, and P. J. Renstrom. Nanoimprint lithography. *Journal of Vacuum Science Technology B*, 14(6):4129, 1996.

[41] S. Zankovych, T. Hoffmann, J. Seekamp, J. U. Bruch, and C. M. S. Torres. Nanoimprint lithography: challenges and prospects. *Nanotechnology*, 12(2):91, 2001.

[42] G. Kumar, H. X. Tang, and J. Schroers. Nanomoulding with amorphous metals. *Nature*, 457 (7231):868, 2009.

[43] J. M. Ji, X. Li, L. T. Canham, and J. L. Coffer. Use of microcontact printing methods to direct pattern formation of calcified mesoporous silicon. *Advanced Materials*, 14(1):41, 2002.

[44] N. F. Mott. Metal-insulator transition. *Reviews of Modern Physics*, 40(4):677, 1968.

[45] T. M. Rice and D. B. Mcwhan. Metal-insulator transition in transition metal oxides. *Bulletin of the American Physical Society*, 15(2):155, 1970.

[46] M. Imada, A. Fujimori, and Y. Tokura. Metal-insulator transitions. *Reviews of Modern Physics*, 70(4):1039, 1998.

[47] M. Wuttig and N. Yamada. Phase-change materials for rewriteable data storage. *Nature Materials*, 6(11):824, 2007.

[48] S. R. Ovshinsky. Reversible electrical switching phenomena in disordered structures. *Physical Review Letters*, 21:1450, 1968.

[49] F. J. Morin. Oxides which show a metal-to-insulator transition at the neel temperature. *Physical Review Letters*, 3:34, 1959.

[50] K. Appavoo and R. F. Haglund. Detecting nanoscale size dependence in VO_2 phase transition using a split-ring resonator metamaterial. *Nano Letters*, 11(3):1025, 2011.

[51] V. Eyert. The metal-insulator transitions of VO_2: a band theoretical approach. *Ann. Phys. (Leipzig)*, 9:650, 2002.

[52] J. Nag and R. F. Haglund. Synthesis of vanadium dioxide thin films and nanoparticles. *Journal of Physics-Condensed Matter*, 20(26):264016, 2008.

[53] R. Lopez, R. F. Haglund, L. C. Feldman, L. A. Boatner, and T. E. Haynes. Optical nonlinearities in VO_2 nanoparticles and thin films. *Applied Physics Letters*, 85(22):5191, 2004.

[54] M. Rini, A. Cavalleri, R. W. Schoenlein, R. Lopez, L. C. Feldman, R. F. Haglund, L. A. Boatner, and T. E. Haynes. Photoinduced phase transition in VO_2 nanocrystals: ultrafast control of surface-plasmon resonance. *Optics Letters*, 30(5):558, 2005.

[55] G. Rampelberg, M. Schaekers, K. Martens, Q. Xie, D. Deduytsche, B. De Schutter, N. Blasco, J. Kittl, and C. Detavernier. Semiconductor-metal transition in thin VO_2 films grown by ozone based atomic layer deposition. *Applied Physics Letters*, 98(16), 2011.

[56] M. Nakano, K. Shibuya, D. Okuyama, T. Hatano, S. Ono, M. Kawasaki, Y. Iwasa, and Y. Tokura. Collective bulk carrier delocalization driven by electrostatic surface charge accumulation. *Nature*, 487(7408):459, 2012.

[57] K. Shibuya, M. Kawasaki, and Y. Tokura. Metal-insulator transition in epitaxial $V_{1-x}W_xO_2$ ($0 \leq x \leq 0.33$) thin films. *Applied Physics Letters*, 96(2):022102, 2010.

[58] I. P. Parkin and T. D. Manning. Intelligent thermochromic windows. *Journal of Chemical Education*, 83(3):393, 2006.

[59] M. A. Richardson and J. A. Coath. Infrared optical modulators for missile testing. *Optics Laser Technology*, 30(2):137, 1998.

[60] M. B. Cortie, A. Dowd, N. Harris, and M. J. Ford. Core-shell nanoparticles with self-regulating plasmonic functionality. *Physical Review B*, 75(11):113405, 2007.

[61] M. J. Dicken, K. Aydin, I. M. Pryce, L. A. Sweatlock, E. M. Boyd, S. Walavalkar, J. Ma, and H. A. Atwater. Frequency tunable near-infrared metamaterials based on VO_2 phase transition. *Optics Express*, 17(20):18330, 2009.

[62] V. G. Golubev, V. Y. Davydov, N. F. Kartenko, D. A. Kurdyukov, A. V. Medvedev, A. B. Pevtsov, A. V. Scherbakov, and E. B. Shadrin. Phase transition-governed opal–VO_2 photonic crystal. *Applied Physics Letters*, 79(14):2127, 2001.

[63] G. T. Reed, G. Mashanovich, F. Y. Gardes, and D. J. Thomson. Silicon optical modulators. *Nature Photonics*, 4(8):518, 2010.

[64] Q. F. Xu, B. Schmidt, S. Pradhan, and M. Lipson. Micrometre-scale silicon electro-optic modulator. *Nature*, 435(7040):325, 2005.

[65] A. S. Liu, R. Jones, L. Liao, D. Samara-Rubio, D. Rubin, O. Cohen, R. Nicolaescu, and M. Paniccia. A high-speed silicon optical modulator based on a metal-oxide-semiconductor capacitor. *Nature*, 427(6975):615, 2004.

[66] J. Teng, P. Dumon, W. Bogaerts, H. B. Zhang, X. G. Jian, X. Y. Han, M. S. Zhao, G. Morthier, and R. Baets. Athermal silicon-on-insulator ring resonators by overlaying a polymer cladding on narrowed waveguides. *Optics Express*, 17(17):14627, 2009.

[67] W. N. Ye, J. Michel, and L. C. Kimerling. Athermal high-index-contrast waveguide design. *IEEE Photonics Technology Letters*, 20(9-12):885, 2008.

[68] S. Manipatruni, R. K. Dokania, B. Schmidt, N. Sherwood-Droz, C. B. Poitras, A. B. Apsel, and M. Lipson. Wide temperature range operation of micrometer-scale silicon electro-optic modulators. *Optics Letters*, 33(19):2185, 2008.

[69] F. Y. Gardes, G. T. Reed, N. G. Emerson, and C. E. Png. A sub-micron depletion-type photonic modulator in silicon on insulator. *Optics Express*, 13(22):8845, 2005.

[70] Y. H. Kuo, Y. K. Lee, Y. S. Ge, S. Ren, J. E. Roth, T. I. Kamins, D. A. B. Miller, and J. S. Harris. Strong quantum-confined stark effect in germanium quantum-well structures on silicon. *Nature*, 437(7063):1334, 2005.

[71] L. Liu, J. Van Campenhout, G. Roelkens, R. A. Soref, D. Van Thourhout, P. Rojo-Romeo, P. Regreny, C. Seassal, J. M. Fedeli, and R. Baets. Carrier-injection-based electro-optic modulator on silicon-on-insulator with a heterogeneously integrated iii-v microdisk cavity. *Optics Letters*, 33(21):2518, 2008.

[72] H. W. Chen, Y. H. Kuo, and J. E. Bowers. 25Gb/s hybrid silicon switch using a capacitively loaded traveling wave electrode. *Optics Express*, 18(2):1070, 2010.

[73] M. Liu, X. Yin, E. Ulin-Avila, B. Geng, T. Zentgraf, L. Ju, F. Wang, and X. Zhang. A graphene-based broadband optical modulator. *Nature*, 474(7349):64, 2011.

[74] M. Hochberg, T. Baehr-Jones, G. X. Wang, M. Shearn, K. Harvard, J. D. Luo, B. Q. Chen, Z. W. Shi, R. Lawson, P. Sullivan, A. K. Y. Jen, L. Dalton, and A. Scherer. Terahertz all-optical modulation in a silicon-polymer hybrid system. *Nature Materials*, 5(9):703, 2006.

[75] R. M. Briggs, I. M. Pryce, and H. A. Atwater. Compact silicon photonic waveguide modulator based on the vanadium dioxide metal-insulator phase transition. *Optics Express*, 18(11): 11192, 2010.

[76] M. Iqbal, M. A. Gleeson, B. Spaugh, F. Tybor, W. G. Gunn, M. Hochberg, T. Baehr-Jones, R. C. Bailey, and L. C. Gunn. Label-free biosensor arrays based on silicon ring resonators and

high-speed optical scanning instrumentation. *IEEE Journal of Selected Topics in Quantum Electronics*, 16(3):654, 2010.

[77] http://genalyte.com.

[78] M. S. Luchansky and R. C. Bailey. High-Q optical sensors for chemical and biological analysis. *Analytical Chemistry*, 84(2):793, 2012.

[79] P. B. Deotare, I. Bulu, I. W. Frank, Q. M. Quan, Y. N. Zhang, R. Ilic, and M. Loncar. All optical reconfiguration of optomechanical filters. *Nature Communications*, 3:846, 2012.

[80] J. D. Ryckman, V. Diez-Blanco, J. Nag, R. E. Marvel, B. K. Choi, R. F. Haglund, and S. M. Weiss. Photothermal optical modulation of ultra-compact hybrid Si-VO_2 ring resonators. *Optics Express*, 20(12):13215, 2012.

[81] S. Strauf, N. G. Stoltz, M. T. Rakher, L. A. Coldren, P. M. Petroff, and D. Bouwmeester. High-frequency single-photon source with polarization control. *Nature Photonics*, 1(12): 704, 2007.

[82] T. J. Kippenberg and K. J. Vahala. Cavity optomechanics: Back-action at the mesoscale. *Science*, 321(5893):1172, 2008.

[83] J. Leuthold, C. Koos, and W. Freude. Nonlinear silicon photonics. *Nature Photonics*, 4(8): 535, 2010.

[84] M. Pollinger, D. O'Shea, F. Warken, and A. Rauschenbeutel. Ultrahigh-Q tunable whispering-gallery-mode microresonator. *Physical Review Letters*, 103(5), 2009.

[85] H. Lee, T. Chen, J. Li, K. Y. Yang, S. Jeon, O. Painter, and K. J. Vahala. Chemically etched ultrahigh-Q wedge-resonator on a silicon chip. *Nature Photonics*, 6(6):369, 2012.

[86] X. L. Zhu, J. S. Zhang, J. Xu, H. Li, X. S. Wu, Z. M. Liao, Q. Zhao, and D. P. Yu. Dispersion control in plasmonic open nanocavities. *ACS Nano*, 5(8):6546, 2011.

[87] Q. M. Quan and M. Loncar. Deterministic design of wavelength scale, ultra-high Q photonic crystal nanobeam cavities. *Optics Express*, 19(19):18529, 2011.

[88] P. B. Deotare, M. W. McCutcheon, I. W. Frank, M. Khan, and M. Loncar. High quality factor photonic crystal nanobeam cavities. *Applied Physics Letters*, 94(12), 2009.

[89] J. D. Ryckman and S. M. Weiss. Low mode volume slotted photonic crystal single nanobeam cavity. *Applied Physics Letters*, 101(7):071104, 2012.

[90] D. K. Gramotnev and S. I. Bozhevolnyi. Plasmonics beyond the diffraction limit. *Nature Photonics*, 4(2):83, 2010.

[91] J. N. Anker, W. P. Hall, O. Lyandres, N. C. Shah, J. Zhao, and R. P. Van Duyne. Biosensing with plasmonic nanosensors. *Nature Materials*, 7(6):442, 2008.

[92] J. Vuckovic, M. Loncar, H. Mabuchi, and A. Scherer. Optimization of the Q factor in photonic crystal microcavities. *IEEE Journal of Quantum Electronics*, 38(7):850, 2002.

[93] Y. Akahane, T. Asano, B. S. Song, and S. Noda. High-Q photonic nanocavity in a two-dimensional photonic crystal. *Nature*, 425(6961):944, 2003.

[94] M. Notomi, E. Kuramochi, and H. Taniyama. Ultrahigh-Q nanocavity with 1d photonic gap. *Optics Express*, 16(15):11095, 2008.

[95] T. Asano, B. S. Song, Y. Akahane, and S. Noda. Ultrahigh-Q nanocavities in two-dimensional photonic crystal slabs. *IEEE Journal of Selected Topics in Quantum Electronics*, 12(6):1123, 2006.

[96] A. R. M. Zain, N. P. Johnson, M. Sorel, and R. M. De la Rue. Ultra high quality factor one dimensional photonic crystal/photonic wire micro-cavities in silicon-on-insulator (SOI). *Optics Express*, 16(16):12084, 2008.

[97] E. Kuramochi, H. Taniyama, T. Tanabe, K. Kawasaki, Y. G. Roh, and M. Notomi. Ultrahigh-Q one-dimensional photonic crystal nanocavities with modulated mode-gap barriers on SiO_2 claddings and on air claddings. *Optics Express*, 18(15):15859, 2010.

[98] J. S. Foresi, P. R. Villeneuve, J. Ferrera, E. R. Thoen, G. Steinmeyer, S. Fan, J. D. Joannopoulos, L. C. Kimerling, H. I. Smith, and E. P. Ippen. Photonic-bandgap microcavities in optical waveguides. *Nature*, 390(6656):143, 1997.

[99] S. Y. Chou, C. Keimel, and J. Gu. Ultrafast and direct imprint of nanostructures in silicon. *Nature*, 417(6891):835, 2002.

[100] J. L. Gong, D. J. Lipomi, J. D. Deng, Z. H. Nie, X. Chen, N. X. Randall, R. Nair, and G. M. Whitesides. Micro- and nanopatterning of inorganic and polymeric substrates by indentation lithography. *Nano Letters*, 10(7):2702, 2010.

[101] J. D. Ryckman, M. Liscidini, J. E. Sipe, and S. M. Weiss. Direct imprinting of porous substrates: A rapid and low-cost approach for patterning porous nanomaterials. *Nano Letters*, 11(5):1857, 2011.

[102] P. J. Blau and B. R. Lawn. *Microindentation Techniques in Materials Science and Engineering: A Symposium Sponsored by ASTM Committee E-4 on Metallography and by the International Metallographic Society*. American Society for Testing Materials, 1986.

[103] S. P. Duttagupta, X. L. Chen, S. A. Jenekhe, and P. M. Fauchet. Microhardness of porous silicon films and composites. *Solid State Communications*, 101(1):33, 1997.

[104] Z.-q. Fang, M. Hu, W. Zhang, X.-r. Zhang, and H.-b. Yang. Mechanical properties of porous silicon by depth-sensing nanoindentation techniques. *Thin Solid Films*, 517(9):2930, 2009.

[105] Y. Jiao, J. D. Ryckman, P. N. Ciesielski, C. A. Escobar, G. K. Jennings, and S. M. Weiss. Patterned nanoporous gold as an effective sers template. *Nanotechnology*, 22:295302, 2011.

[106] S. Zanotto, M. Liscidini, and L. C. Andreani. Light trapping regimes in thin-film silicon solar cells with a photonic pattern. *Optics Express*, 18(5):4260, 2010.

[107] X. Wei and S. M. Weiss. Grating coupled waveguide biosensor based on porous silicon. *MRS Proceedings Online Library*, 1301(03), 2011.

[108] P. N. Prasad. *Introduction to Biophotonics*. Wiley, New York, 2003.

[109] J. B. Goh, R. W. Loo, R. A. McAloney, and M. C. Goh. Diffraction-based assay for detecting multiple analytes. *Analytical and bioanalytical chemistry*, 374(1):54, 2002.

[110] M. Liscidini and J. E. Sipe. Enhancement of diffraction for biosensing applications via bloch surface waves. *Applied Physics Letters*, 91(25), 2007.

[111] M. Liscidini and J. E. Sipe. Analysis of Bloch-surface-wave assisted diffraction-based biosensors. *Journal of the Optical Society of America B-Optical Physics*, 26(2):279, 2009.

[112] F. Yu and W. Knoll. Immunosensor with self-referencing based on surface plasmon diffraction. *Analytical Chemistry*, 76(7):1971, 2004.

[113] E. Guillermain, V. Lysenko, R. Orobtchouk, T. Benyattou, S. Roux, A. Pillonnet, and P. Perriat. Bragg surface wave device based on porous silicon and its application for sensing. *Applied Physics Letters*, 90(24), 2007.

[114] G. Rong, J. D. Ryckman, R. L. Mernaugh, and S. M. Weiss. Label-free porous silicon membrane waveguide for dna sensing. *Applied Physics Letters*, 93(16):161109, 2008.

[115] L. Pavesi. Porous silicon dielectric multilayers and microcavities. *Rivista Del Nuovo Cimento*, 20(10):1, 1997.

[116] C. B. Burckhardt. Efficiency of a dielectric grating. *Journal of the Optical Society of America*, 57(5):601, 1967.

[117] G. Hermanson. *Bioconjugate Techniques*. Academic, New York, 1996.

[118] H. Ouyang, C. C. Striemer, and P. M. Fauchet. Quantitative analysis of the sensitivity of porous silicon optical biosensors. *Applied Physics Letters*, 88(16), 2006.

[119] D. M. Whittaker and I. S. Culshaw. Scattering-matrix treatment of patterned multilayer photonic structures. *Physical Review B*, 60(4):2610, 1999.

[120] G. Gaur, D. Koktysh, and S. M. Weiss. Integrating colloidal Quantum dots with porous silicon for high sensitivity biosensing. *MRS Online Proceedings Library*, 1301:null, 2011.

[121] J. L. Lawrie, Y. Jiao, and S. M. Weiss. Size-dependent infiltration and optical detection of nucleic acids in nanoscale pores. *IEEE Transactions on Nanotechnology*, 9(5):596, 2010.

[122] X. Wei, J. W. Mares, Y. Gao, D. Li, and S. M. Weiss. Biomolecule kinetics measurements in flow cell integrated porous silicon waveguides. *Biomedical Optics Express*, 3(9):1993, 2012.

[123] A. del Campo and E. Arzt. Fabrication approaches for generating complex micro- and nanopatterns on polymeric surfaces. *Chemical Reviews*, 108(3):911, 2008.

[124] M. Geissler and Y. Xia. Patterning: Principles and some new developments. *Advanced Materials*, 16(15):1249, 2004.

[125] C. Guo, S. Cao, P. Jiang, Y. Fang, J. Zhang, Y. Fan, Y. Wang, W. Xu, Z. Zhao, and Q. Liu. Grayscale photomask fabricated by laser direct writing in metallic nano-films. *Optics Express*, 17(22):19981, 2009.

[126] Y. Q. Fu, N. K. A. Bryan, and O. N. Shing. Diffractive optical elements with continuous relief fabricated by focused ion beam for monomode fiber coupling. *Optics Express*, 7(3):141, 2000.

[127] W. X. Yu and X. C. Yuan. Fabrication of refractive microlens in hybrid SiO_2/TiO_2 sol-gel glass by electron beam lithography. *Optics Express*, 11(8):899, 2003.

[128] U. Levy, B. Desiatov, I. Goykhman, T. Nachmias, A. Ohayon, and S. E. Meltzer. Design, fabrication, and characterization of circular dammann gratings based on grayscale lithography. *Optics Letters*, 35(6):880, 2010.

[129] K. S. Urquhart, R. Stein, and S. H. Lee. Computer-generated holograms fabricated by direct write of positive electron-beam resist. *Optics Letters*, 18(4):308, 1993.

[130] J. C. Yang, H. W. Gao, J. Y. Suh, W. Zhou, M. H. Lee, and T. W. Odom. Enhanced optical transmission mediated by localized plasmons in anisotropic, three-dimensional nanohole arrays. *Nano Letters*, 10(8):3173, 2010.

[131] T. Zentgraf, Y. Liu, M. H. Mikkelsen, J. Valentine, and X. Zhang. Plasmonic luneburg and eaton lenses. *Nature Nanotechnology*, 6(3):151, 2011.

[132] C. Waits, M. A., and R. Ghodssi. Investigation of gray-scale technology for large area 3d silicon mems structures. *Journal of Micromechanics and Microengineering*, 13:170, 2003.

[133] G. Ruffato, F. Romanato, D. Garoli, and S. Cattarin. Nanoporous gold plasmonic structures for sensing applications. *Optics Express*, 19(14):13164, 2011.

[134] Y. N. Xia, E. Kim, X. M. Zhao, J. A. Rogers, M. Prentiss, and G. M. Whitesides. Complex optical surfaces formed by replica molding against elastomeric masters. *Science*, 273(5273): 347, 1996.

[135] B. D. Gates, Q. B. Xu, M. Stewart, D. Ryan, C. G. Willson, and G. M. Whitesides. New approaches to nanofabrication: Molding, printing, and other techniques. *Chemical Reviews*, 105(4):1171, 2005.

[136] L. J. Guo. Nanoimprint lithography: Methods and material requirements. *Advanced Materials*, 19(4):495, 2007.

[137] J. Zaumseil, M. A. Meitl, J. W. P. Hsu, B. R. Acharya, K. W. Baldwin, Y. L. Loo, and J. A. Rogers. Three-dimensional and multilayer nanostructures formed by nanotransfer printing. *Nano Letters*, 3(9):1223, 2003.

[138] K. H. Hsu, P. L. Schultz, P. M. Ferreira, and N. X. Fang. Electrochemical nanoimprinting with solid-state superionic stamps. *Nano Letters*, 7(2):446, 2007.

[139] A. Schleunitz, V. A. Guzenko, A. Schander, M. Vogler, and H. Schift. Selective profile transformation of electron-beam exposed multilevel resist structures based on a molecular weight dependent thermal reflow. *Journal of Vacuum Science Technology B*, 29(6):F302, 2011.

[140] J. D. Ryckman, Y. Jiao, and S. M. Weiss. Three-dimensional patterning and morphological control of porous nanomaterials by gray-scale direct imprinting. *Sci. Rep.*, 3(1502), 2013.

[141] H. M. Bok, K. L. Shuford, S. Kim, S. K. Kim, and S. Park. Multiple surface plasmon modes for a colloidal solution of nanoporous gold nanorods and their comparison to smooth gold nanorods. *Nano Letters*, 8(8):2265, 2008.

[142] N. Sardana, F. Heyroth, and J. Schilling. Propagating surface plasmons on nanoporous gold. *Journal of the Optical Society of America B-Optical Physics*, 29(7):1778, 2012.

[143] L. H. Qian, X. Q. Yan, T. Fujita, A. Inoue, and M. W. Chen. Surface enhanced Raman scattering of nanoporous gold: Smaller pore sizes stronger enhancements. *Applied Physics Letters*, 90(15):153120, 2007.

[144] X. Y. Lang, L. Y. Chen, P. F. Guan, T. Fujita, and M. W. Chen. Geometric effect on surface enhanced Raman scattering of nanoporous gold: Improving Raman scattering by tailoring ligament and nanopore ratios. *Applied Physics Letters*, 94(21):213109, 2009.

[145] N. I. Zheludev and Y. S. Kivshar. From metamaterials to metadevices. *Nature Materials*, 11 (11):917, 2012.

[146] M. Bosman, G. R. Anstis, V. J. Keast, J. D. Clarke, and M. B. Cortie. Light splitting in nanoporous gold and silver. *ACS Nano*, 6(1):319, 2012.

[147] W. Freese, T. Kämpfe, E.-B. Kley, and A. Tünnermann. Design of binary subwavelength multiphase level computer generated holograms. *Optics Letters*, 35(5):676, 2010.

[148] S. Larouche, Y.-J. Tsai, T. Tyler, N. Jokerst, and D. Smith. Infrared metamaterial phase holograms. *Nature Materials*, 11(5):450, 2012.

[149] M. Gharghi, C. Gladden, T. Zentgraf, Y. Liu, X. Yin, J. Valentine, and X. Zhang. A carpet cloak for visible light. *Nano Letters*, 11(7):2825, 2011.

[150] J. Valentine, J. Li, T. Zentgraf, G. Bartal, and X. Zhang. An optical cloak made of dielectrics. *Nature Materials*, 8(7):568, 2009.

[151] T. Zentgraf, J. Valentine, N. Tapia, J. Li, and X. Zhang. An optical "Janus" device for integrated photonics. *Advanced Materials*, 22(23):2561, 2010.

[152] T. Sondergaard, S. M. Novikov, T. Holmgaard, R. L. Eriksen, J. Beermann, Z. H. Han, K. Pedersen, and S. I. Bozhevolnyi. Plasmonic black gold by adiabatic nanofocusing and absorption of light in ultra-sharp convex grooves. *Nature Communications*, 3(969):969, 2012.

[153] S. Lee, J. Shin, Y. H. Lee, and J. K. Park. Fabrication of the funnel-shaped three-dimensional plasmonic tip arrays by directional photofluidization lithography. *ACS Nano*, 4(12):7175, 2010.

[154] V. R. Almeida, C. A. Barrios, R. R. Panepucci, and M. Lipson. All-optical control of light on a silicon chip. *Nature*, 431(7012):1081, 2004.

[155] Q. F. Xu and M. Lipson. All-optical logic based on silicon micro-ring resonators. *Optics Express*, 15(3):924, 2007.

[156] Q. F. Xu, B. Schmidt, J. Shakya, and M. Lipson. Cascaded silicon micro-ring modulators for WDM optical interconnection. *Optics Express*, 14(20):9430, 2006.

[157] M. Liu, X. B. Yin, E. Ulin-Avila, B. S. Geng, T. Zentgraf, L. Ju, F. Wang, and X. Zhang. A graphene-based broadband optical modulator. *Nature*, 474(7349):64, 2011.

[158] J. Cao, E. Ertekin, V. Srinivasan, W. Fan, S. Huang, H. Zheng, J. W. L. Yim, D. R. Khanal, D. F. Ogletree, J. C. Grossmanan, and J. Wu. Strain engineering and one-dimensional organization of metal-insulator domains in single-crystal vanadium dioxide beams. *Nature Nanotechnology*, 4(11):732, 2009.

[159] G. Stefanovich, A. Pergament, and D. Stefanovich. Electrical switching and Mott transition in VO_2. *Journal of Physics-Condensed Matter*, 12(41):8837, 2000.

[160] D. Ruzmetov, G. Gopalakrishnan, J. D. Deng, V. Narayanamurti, and S. Ramanathan. Electrical triggering of metal-insulator transition in nanoscale vanadium oxide junctions. *Journal of Applied Physics*, 106(8):083702, 2009.

[161] A. Cavalleri, C. Toth, C. W. Siders, J. A. Squier, F. Raksi, P. Forget, and J. C. Kieffer. Femtosecond structural dynamics in VO_2 during an ultrafast solid-solid phase transition. *Physical Review Letters*, 87(23):237401, 2001.

[162] A. Pashkin, C. Kubler, H. Ehrke, R. Lopez, A. Halabica, R. F. Haglund, R. Huber, and A. Leitenstorfer. Ultrafast insulator-metal phase transition in VO_2 studied by multiterahertz spectroscopy. *Physical Review B*, 83(19):195120, 2011.

[163] Q. F. Xu, D. Fattal, and R. G. Beausoleil. Silicon microring resonators with 1.5-mu m radius. *Optics Express*, 16(6):4309, 2008.

[164] J. Nag, E. A. Payzant, K. L. More, and R. F. Haglund. Enhanced performance of room-temperature-grown epitaxial thin films of vanadium dioxide. *Applied Physics Letters*, 98 (25):251916, 2011.

[165] R. E. Marvel, K. Appavoo, B. K. Choi, J. Nag, and J. Haglund, R. F. Electron-beam deposition of vanadium dioxide thin films. *Applied Physics A*, pages 1–7, 2012.

[166] J. Y. Suh, R. Lopez, L. C. Feldman, and J. R. F. Haglund. Semiconductor to metal phase transition in the nucleation and growth of VO_2 nanoparticles and thin films. *Journal of Applied Physics*, 96(2):1209, 2004.

[167] M. S. Nawrocka, T. Liu, X. Wang, and R. R. Panepucci. Tunable silicon microring resonator with wide free spectral range. *Applied Physics Letters*, 89(07):1110, 2006.

[168] T. Ben-Messaoud, G. Landry, J. P. Gariepy, B. Ramamoorthy, P. V. Ashrit, and A. Hache. High contrast optical switching in vanadium dioxide thin films. *Optics Communications*, 281(24):6024, 2008.

[169] G. Cocorullo, F. G. Della Corte, I. Rendina, and P. M. Sarro. Thermo-optic effect exploitation in silicon microstructures. *Sensors and Actuators a-Physical*, 71(1-2):19, 1998.

[170] A. S. Liu, R. Jones, L. Liao, D. Samara-Rubio, D. Rubin, O. Cohen, R. Nicolaescu, and M. Paniccia. A high-speed silicon optical modulator based on a metal-oxide-semiconductor capacitor. *Nature*, 427(6975):615, 2004.

[171] J. T. Robinson, L. Chen, and M. Lipson. On-chip gas detection in silicon optical microcavities. *Optics Express*, 16(6):4296, 2008.

[172] J. D. Ryckman and S. M. Weiss. Localized field enhancements in guided and defect modes of a periodic slot waveguide. *IEEE Photonics Journal*, 3(6):986, 2011.

[173] E. Dulkeith, F. Xia, L. Schares, W. M. J. Green, and Y. A. Vlasov. Group index and group velocity dispersion in silicon-on-insulator photonic wires. *Optics Express*, 14(9):3853, 2006.

[174] C. Pacholski, C. Yu, G. M. Miskelly, D. Godin, and M. J. Sailor. Reflective interferometric fourier transform spectroscopy: a self-compensating label-free immunosensor using double-layers of porous sio2. *J Am Chem Soc*, 128(13):4250–4252, Apr 2006.

[175] B. Soller, D. Gifford, M. Wolfe, and M. Froggatt. High resolution optical frequency domain reflectometry for characterization of components and assemblies. *Optics Express*, 13(2): 666–674, 2005.

[176] S. Manipatruni, K. Preston, L. Chen, and M. Lipson. Ultra-low voltage, ultra-small mode volume silicon microring modulator. *Optics Express*, 18(17):18235, 2010.

[177] C. Batten, A. Joshi, J. Orcutt, A. Khilo, B. Moss, C. Holzwarth, M. Popovic, L. Hanqing, H. Smith, J. Hoyt, F. Kartner, R. Ram, V. Stojanovic, and K. Asanovic. Building manycore processor-to-dram networks with monolithic silicon photonics. In *16th IEEE Symposium on High Performance Interconnects*, page 21, 2008.

[178] A. S. Liu, R. Jones, L. Liao, D. Samara-Rubio, D. Rubin, O. Cohen, R. Nicolaescu, and M. Paniccia. A high-speed silicon optical modulator based on a metal-oxide-semiconductor capacitor. *Nature*, 427(6975):615, 2004.

[179] M. Li, W. H. P. Pernice, C. Xiong, T. Baehr-Jones, M. Hochberg, and H. X. Tang. Harnessing optical forces in integrated photonic circuits. *Nature*, 456(7221):480, 2008.

[180] M. Bagheri, M. Poot, M. Li, W. P. H. Pernice, and H. X. Tang. Dynamic manipulation of nanomechanical resonators in the high-amplitude regime and non-volatile mechanical memory operation. *Nature Nanotechnology*, 6(11):726, 2011.

[181] N. N. Feng, D. Z. Feng, S. R. Liao, X. Wang, P. Dong, H. Liang, C. C. Kung, W. Qian, J. Fong, R. Shafiiha, Y. Luo, J. Cunningham, A. V. Krishnamoorthy, and M. Asghari. 30GHz ge electro-absorption modulator integrated with 3μm silicon-on-insulator waveguide. *Optics Express*, 19(8):7062, 2011.

[182] J. Clark and G. Lanzani. Organic photonics for communications. *Nature Photonics*, 4(7): 438, 2010.

[183] C. Koos, P. Vorreau, T. Vallaitis, P. Dumon, W. Bogaerts, R. Baets, B. Esembeson, I. Biaggio, T. Michinobu, F. Diederich, W. Freude, and J. Leuthold. All-optical high-speed signal processing with silicon-organic hybrid slot waveguidesx. *Nature Photonics*, 3(4):216, 2009.

[184] H. W. Verleur, A. S. Barker, and C. N. Berglund. Optical properties of VO_2 between 0.25 and 5 eV. *Physical Review*, 172(3):788, 1968.

[185] M. Liu, H. Y. Hwang, H. Tao, A. C. Strikwerda, K. Fan, G. R. Keiser, A. J. Sternbach, K. G. West, S. Kittiwatanakul, J. Lu, S. A. Wolf, F. G. Omenetto, X. Zhang, K. A. Nelson, and R. D. Averitt. Terahertz-field-induced insulator-to-metal transition in vanadium dioxide metamaterial. *Nature*, 487:345, 2012.

[186] J. Wei, H. Ji, W. Guo, A. H. Nevidomskyy, and D. Natelson. Hydrogen stabilization of metallic vanadium dioxide in single-crystal nanobeams. *Nature Nanotechnology*, 7(6):357, 2012.

[187] M. Hada, D. Zhang, A. Casandruc, R. J. D. Miller, Y. Hontani, J. Matsuo, R. E. Marvel, and J. Haglund, Richard F. Hot electron injection driven phase transitions. *Physical Review B*, 86(13):134101, 2012.

[188] A. Cavalleri, T. Dekorsy, H. H. W. Chong, J. C. Kieffer, and R. W. Schoenlein. Evidence for a structurally-driven insulator-to-metal transition in VO_2: A view from the ultrafast timescale. *Physical Review B*, 70(16):161102, 2004.

[189] T. Driscoll, H.-T. Kim, B.-G. Chae, B.-J. Kim, Y.-W. Lee, N. M. Jokerst, S. Palit, D. R. Smith, M. Di Ventra, and D. N. Basov. Memory metamaterials. *Science*, 325(5947):1518, 2009.

[190] J. M. Choi, R. K. Lee, and A. Yariv. Control of critical coupling in a ring resonator fiber configuration: application to wavelength-selective switching, modulation, amplification, and oscillation. *Optics Letters*, 26(16):1236, 2001.

[191] C. Kubler, H. Ehrke, R. Huber, R. Lopez, A. Halabica, R. F. Haglund, and A. Leitenstorfer. Coherent structural dynamics and electronic correlations during an ultrafast insulator-to-metal phase transition in VO_2. *Physical Review Letters*, 99(11):116401, 2007.

[192] S. Wall, D. Wegkamp, L. Foglia, K. Appavoo, J. Nag, R. F. Haglund, J. Stahler, and M. Wolf. Ultrafast changes in lattice symmetry probed by coherent phonons. *Nature Communications*, 3:721, 2012.

[193] Z. S. Tao, T. R. T. Han, S. D. Mahanti, P. M. Duxbury, F. Yuan, C. Y. Ruan, K. Wang, and J. Q. Wu. Decoupling of structural and electronic phase transitions in VO_2. *Physical Review Letters*, 109(16):166406, 2012.

[194] T. K. Liang, L. R. Nunes, T. Sakamoto, K. Sasagawa, T. Kawanishi, M. Tsuchiya, G. R. A. Priem, D. Van Thourhout, P. Dumon, R. Baets, and H. K. Tsang. Ultrafast all-optical switching by cross-absorption modulation in silicon wire waveguides. *Optics Express*, 13(19):7298, 2005.

[195] M. M. Qazilbash, M. Brehm, B. G. Chae, P. C. Ho, G. O. Andreev, B. J. Kim, S. J. Yun, A. V. Balatsky, M. B. Maple, F. Keilmann, H. T. Kim, and D. N. Basov. Mott transition in VO_2 revealed by infrared spectroscopy and nano-imaging. *Science*, 318(5857):1750, 2007.

[196] S. Lysenko, A. Rua, V. Vikhnin, F. Fernandez, and H. Liu. Insulator-to-metal phase transition and recovery processes in VO_2 thin films after femtosecond laser excitation. *Physical Review B*, 76(3), 2007.

[197] Y. Zhang and S. Ramanathan. Analysis of ”on” and ”off” times for thermally driven VO_2 metal-insulator transition nanoscale switching devices. *Solid-State Electronics*, 62(1):161, 2011.

[198] P. Dong, W. Qian, H. Liang, R. Shafiiha, D. Z. Feng, G. L. Li, J. E. Cunningham, A. V. Kr-

ishnamoorthy, and M. Asghari. Thermally tunable silicon racetrack resonators with ultralow tuning power. *Optics Express*, 18(19):20298, 2010.

[199] J. Nag, J. Richard F. Haglund, E. A. Payzant, and K. L. More. Non-congruence of thermally driven structural and electronic transitions in VO_2. *Journal of Applied Physics*, 112(10): 103532, 2012.

[200] T. L. Cocker, L. V. Titova, S. Fourmaux, G. Holloway, H. C. Bandulet, D. Brassard, J. C. Kieffer, M. A. El Khakani, and F. A. Hegmann. Phase diagram of the ultrafast photoinduced insulator-metal transition in vanadium dioxide. *Physical Review B*, 85(15):155120, 2012.

[201] H. S. Rong, R. Jones, A. S. Liu, O. Cohen, D. Hak, A. Fang, and M. Paniccia. A continuous-wave Raman silicon laser. *Nature*, 433(7027):725, 2005.

[202] V. R. Almeida, Q. F. Xu, C. A. Barrios, and M. Lipson. Guiding and confining light in void nanostructure. *Optics Letters*, 29(11):1209, 2004.

[203] F. Dell'Olio and V. M. N. Passaro. Optical sensing by optimized silicon slot waveguides. *Optics Express*, 15(8):4977, 2007.

[204] C. A. Barrios, K. B. Gylfason, B. Sanchez, A. Griol, H. Sohlstroem, M. Holgado, and R. Casquel. Slot-waveguide biochemical sensor. *Optics Letters*, 32(21):3080, 2007.

[205] Y. Li, J. J. Zheng, J. Gao, J. Shu, M. S. Aras, and C. W. Wong. Design of dispersive optomechanical coupling and cooling in ultrahigh-Q/V slot-type photonic crystal cavities. *Optics Express*, 18(23):23844, 2010.

[206] M. Li, W. H. P. Pernice, and H. X. Tang. Ultrahigh-frequency nano-optomechanical resonators in slot waveguide ring cavities. *Applied Physics Letters*, 97(18), 2010.

[207] C. Koos, L. Jacome, C. Poulton, J. Leuthold, and W. Freude. Nonlinear silicon-on-insulator waveguides for all-optical signal processing. *Optics Express*, 15(10):5976, 2007.

[208] T. Vallaitis, S. Bogatscher, L. Alloatti, P. Dumon, R. Baets, M. L. Scimeca, I. Biaggio, F. Diederich, C. Koos, W. Freude, and J. Leuthold. Optical properties of highly nonlinear silicon-organic hybrid (SOH) waveguide geometries. *Optics Express*, 17(20):17357, 2009.

[209] J.-M. Brosi, C. Koos, L. C. Andreani, M. Waldow, J. Leuthold, and W. Freude. High-speed low-voltage electro-optic modulator with a polymer-infiltrated silicon photonic crystal waveguide. *Optics Express*, 16(6):4177, 2008.

[210] T. Baehr-Jones, M. Hochberg, G. X. Wang, R. Lawson, Y. Liao, P. A. Sullivan, L. Dalton, A. K. Y. Jen, and A. Scherer. Optical modulation and detection in slotted silicon waveguides. *Optics Express*, 13(14):5216, 2005.

[211] J. H. Wulbern, J. Hampe, A. Petrov, M. Eich, J. D. Luo, A. K. Y. Jen, A. Di Falco, T. F. Krauss, and J. Bruns. Electro-optic modulation in slotted resonant photonic crystal heterostructures. *Applied Physics Letters*, 94(24), 2009.

[212] C. Koos, P. Vorreau, T. Vallaitis, P. Dumon, W. Bogaerts, R. Baets, B. Esembeson, I. Biaggio, T. Michinobu, F. Diederich, W. Freude, and J. Leuthold. All-optical high-speed signal processing with silicon-organic hybrid slot waveguidesx. *Nature Photonics*, 3(4):216, 2009.

[213] A. H. J. Yang, S. D. Moore, B. S. Schmidt, M. Klug, M. Lipson, and D. Erickson. Optical manipulation of nanoparticles and biomolecules in sub-wavelength slot waveguides. *Nature*, 457(7225):71, 2009.

[214] A. H. J. Yang, T. Lerdsuchatawanich, and D. Erickson. Forces and transport velocities for a particle in a slot waveguide. *Nano Letters*, 9(3):1182, 2009.

[215] Z. Gaburro. A design for a photonic syringe with multimode coupled slot waveguides. *Optics Express*, 18(1):288, 2010.

[216] S. G. Johnson, A. Mekis, S. H. Fan, and J. D. Joannopoulos. Molding the flow of light. *Computing in Science Engineering*, 3(6):38, 2001.

[217] J. T. Robinson, C. Manolatou, L. Chen, and M. Lipson. Ultrasmall mode volumes in dielectric optical microcavities. *Physical Review Letters*, 95(14):143901, 2005.

[218] A. Gondarenko and M. Lipson. Low modal volume dipole-like dielectric slab resonator. *Optics Express*, 16(22):17689, 2008.

[219] F. Riboli, P. Bettotti, and L. Pavesi. Band gap characterization and slow light effects in one dimensional photonic crystals based on silicon slot-waveguides. *Optics Express*, 15(19): 11769, 2007.

[220] T. Yamamoto, M. Notomi, H. Taniyama, E. Kuramochi, Y. Yoshikawa, Y. Torii, and T. Kuga. Design of a high-Q air-slot cavity based on a width-modulated line-defect in a photonic crystal slab. *Optics Express*, 16(18):13809, 2008.

[221] J. Gao, J. F. McMillan, M. C. Wu, J. J. Zheng, S. Assefa, and C. W. Wong. Demonstration of an air-slot mode-gap confined photonic crystal slab nanocavity with ultrasmall mode volumes. *Applied Physics Letters*, 96(5), 2010.

[222] A. Taflove and S. C. Hagness. *Computational Electrodynamics: The Finite-Difference Time-Domain Method*. Artech, Norwood, MA, 2000.

[223] V. A. Mandelshtam and H. S. Taylor. Harmonic inversion of time signals and its applications. *Journal of Chemical Physics*, 107(17):6756, 1997.

[224] A. F. Oskooi, D. Roundy, M. Ibanescu, P. Bermel, J. D. Joannopoulos, and S. G. Johnson. Meep: A flexible free-software package for electromagnetic simulations by the FDTD method. *Computer Physics Communications*, 181(3):687, 2010.

[225] A. Farjadpour, D. Roundy, A. Rodriguez, M. Ibanescu, P. Bermel, J. D. Joannopoulos, S. G. Johnson, and G. W. Burr. Improving accuracy by subpixel smoothing in the finite-difference time domain. *Optics Letters*, 31(20):2972, 2006.

[226] S. H. Fan, J. N. Winn, A. Devenyi, J. C. Chen, R. D. Meade, and J. D. Joannopoulos. Guided and defect modes in periodic dielectric waveguides. *Journal of the Optical Society of America B-Optical Physics*, 12(7):1267, 1995.

[227] C. Kang, C. T. Phare, Y. A. Vlasov, S. Assefa, and S. M. Weiss. Photonic crystal slab sensor with enhanced surface area. *Optics Express*, 18(26):27930, 2010.

[228] Y. Akahane, T. Asano, B. S. Song, and S. Noda. High-Q photonic nanocavity in a two-dimensional photonic crystal. *Nature*, 425(6961):944, 2003.

[229] S. Gary, E. Bryan, P. Jan, A. M. Marie, S. Tomas, H. James, E. H. Eugene, and J. Vuckovic. Nanobeam photonic crystal cavity light-emitting diodes. *Applied Physics Letters*, 99:071105, 2011.

[230] S. H. Fan, J. N. Winn, A. Devenyi, J. C. Chen, R. D. Meade, and J. D. Joannopoulos. Guided and defect modes in periodic dielectric wave-guides. *Journal of the Optical Society of America B-Optical Physics*, 12(7):1267, 1995.

[231] Z. C. Wang, N. Zhu, Y. B. Tang, L. Wosinski, D. X. Dai, and S. L. He. Ultracompact low-loss coupler between strip and slot waveguides. *Optics Letters*, 34(10):1498, 2009.

[232] P. Yu, B. A. Qi, X. Q. Jiang, M. H. Wang, and J. Y. Yang. Ultrasmall-v high-Q photonic crystal nanobeam microcavities based on slot and hollow-core waveguides. *Optics Letters*, 36(8):1314, 2011.

[233] B. Desiatov, I. Goykhman, and U. Levy. Parabolic tapered photonic crystal cavity in silicon. *Applied Physics Letters*, 100(4):041112, 2012.

[234] Q. M. Quan, P. B. Deotare, and M. Loncar. Photonic crystal nanobeam cavity strongly coupled to the feeding waveguide. *Applied Physics Letters*, 96(20):203102, 2010.

[235] Y. Y. Gong, A. Rundquist, A. Majumdar, and J. Vuckovic. Low power resonant optical excitation of an optomechanical cavity. *Optics Express*, 19(2):1429, 2011.

[236] M. L. Cooper, G. Gupta, J. S. Park, M. A. Schneider, I. B. Divliansky, and S. Mookherjea. Quantitative infrared imaging of silicon-on-insulator microring resonators. *Optics Letters*, 35(5):784, 2010.

[237] Q. Quan, I. B. Burgess, S. K. Y. Tang, D. L. Floyd, and M. Loncar. High-q, low index-contrast polymeric photonic crystal nanobeam cavities. *Optics Express*, 19(22):22191, 2011.

[238] Y. Jiao. *A Study of Improved Sensing Performances Based on Nanoscale Porous Substrates*. PhD thesis, Vanderbilt University, 2013.

[239] M. Eichenfield, R. Camacho, J. Chan, K. Vahala, and O. Painter. A picogram- and nanometre-scale photonic-crystal optomechanical cavity. *Nature*, 459(7246):550, 2009.

[240] J. Chan, M. Eichenfield, R. Camacho, and O. Painter. Optical and mechanical design of a ”zipper” photonic crystal optomechanical cavity. *Optics Express*, 17(5):3802, 2009.

[241] F. Kevin, L. Loic, C. Benoit, P. Emmanuel, P. David, F. Frederique de, and H. Emmanuel. An air-slotted nanoresonator relying on coupled high Q small V Fabry-Perot nanocavities. *Applied Physics Letters*, 94:251111, 2009.

[242] I. W. Frank, P. B. Deotare, M. W. McCutcheon, and M. Loncar. Programmable photonic crystal nanobeam cavities. *Optics Express*, 18(8):8705, 2010.

[243] S. Lin, E. Schonbrun, and K. Crozier. Optical manipulation with planar silicon microring resonators. *Nano Letters*, 10(7):2408, 2010.

[244] S. Mandal, X. Serey, and D. Erickson. Nanomanipulation using silicon photonic crystal resonators. *Nano Letters*, 10(1):99, 2010.

[245] X. Serey, S. Mandal, and D. Erickson. Comparison of silicon photonic crystal resonator designs for optical trapping of nanomaterials. *Nanotechnology*, 21(30), 2010.

[246] C. A. Barrios and M. Lipson. Electrically driven silicon resonant light emitting device based on slot- waveguide. *Optics Express*, 13(25):10092, 2005.

[247] M. M. Orosco, C. Pacholski, and M. J. Sailor. Real-time monitoring of enzyme activity in a mesoporous silicon double layer. *Nature Nanotechnology*, 4(4):255–258, 04 2009.